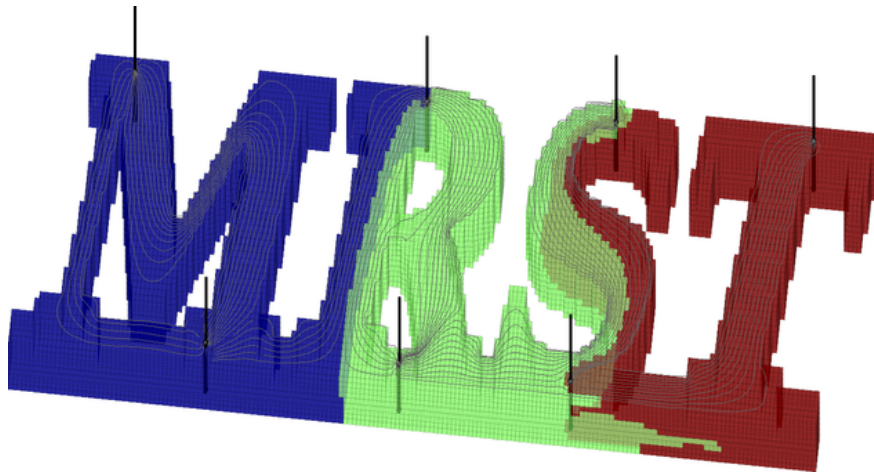


Knut-Andreas Lie

An Introduction to Reservoir Simulation Using MATLAB

User Guide for the Matlab Reservoir Simulation
Toolbox (MRST)

December 16, 2015



SINTEF ICT, Departement of Applied Mathematics
Oslo, Norway

Contents

1	Introduction	3
1.1	Petroleum production	5
1.2	Reservoir simulation	9
1.3	Outline of the book	11
2	The MATLAB Reservoir Simulation Toolbox	15
2.1	The first encounter with MRST	16
2.2	Downloading and installing the software	17
2.3	Terms of usage	20
2.4	Getting started with the software	21
2.5	More advanced solvers and workflow tools	25
2.6	Rapid prototyping using MATLAB and MRST	28
2.7	Automatic differentiation in MRST	31

Part I Geological Models and Grids

3	Modelling Reservoir Rocks	39
3.1	Formation of sedimentary rocks	39
3.2	Creation of crude oil and natural gas	44
3.3	Multiscale modelling of permeable rocks	47
3.3.1	Macroscopic models	48
3.3.2	Representative elementary volumes	50
3.3.3	Microscopic models: The pore scale	51
3.3.4	Mesosopic models	53
3.4	Modelling rock properties	54
3.4.1	Porosity	55
3.4.2	Permeability	56
3.4.3	Other parameters	58
3.5	Property modelling in MRST	59
3.5.1	Homogeneous models	60

3.5.2	Random and lognormal models	60
3.5.3	10 th SPE Comparative Solution Project: Model 2	62
3.5.4	The Johansen Formation	65
3.5.5	SAIGUP: shallow-marine reservoirs	66
4	Grids in Subsurface Modeling	77
4.1	Structured grids	79
4.2	Unstructured grids	85
4.2.1	Delaunay tessellation	85
4.2.2	Voronoi diagrams	88
4.2.3	Other types of tessellations	91
4.2.4	Using an external mesh generator	93
4.3	Stratigraphic grids	96
4.3.1	Corner-point grids	96
4.3.2	2.5D unstructured grids	107
4.4	Grid structure in MRST	109
4.5	Examples of more complex grids	119
5	Grid Coarsening	131
5.1	Partition vectors	132
5.1.1	Uniform partitions	133
5.1.2	Connected partitions	133
5.1.3	Composite partitions	134
5.2	Coarse grid representation in MRST	137
5.2.1	Subdivision of coarse faces	138
5.3	Coarsening of realistic reservoir models	141
5.3.1	The Johansen aquifer	141
5.3.2	The SAIGUP model	144
5.4	General advice and simple guidelines	148

Part II Incompressible Single-Phase Flow

6	Mathematical Models and Basic Discretizations	153
6.1	Fundamental concept: Darcy's law	153
6.2	General flow equations for single-phase flow	155
6.3	Auxiliary conditions and equations	160
6.3.1	Boundary and initial conditions	160
6.3.2	Injection and production wells	161
6.3.3	Field lines and time-of-flight	165
6.3.4	Tracers and volume partitions	167
6.4	Basic finite-volume discretizations	168
6.4.1	Two-point flux-approximation	169
6.4.2	Discrete div and grad operators	173
6.4.3	Time-of-flight and tracer	178

7 Incompressible Solvers 181

7.1 Basic data structures in a simulation model 182

7.1.1 Fluid properties 182

7.1.2 Reservoir states 183

7.1.3 Fluid sources 183

7.1.4 Boundary conditions 184

7.1.5 Wells 186

7.2 Incompressible two-point pressure solver 188

7.3 Upwind solver for time-of-flight and tracer 191

7.4 Simulation examples 194

7.4.1 Quarter five-spot 195

7.4.2 Boundary conditions 199

7.4.3 Structured versus unstructured stencils 203

7.4.4 Using Peaceman well models 208

8 Consistent Discretizations on Polyhedral Grids 213

8.1 The mixed finite-element method 216

8.1.1 Continuous formulation 216

8.1.2 Discrete formulation 218

8.1.3 Hybrid formulation 221

8.2 Consistent methods on mixed hybrid form 223

8.3 The mimetic method 227

8.3.1 General family of inner products 228

8.3.2 General parametric family 230

8.3.3 Two-point type methods 230

8.3.4 Raviart–Thomas type inner product 233

8.3.5 Default inner product in MRST 234

8.3.6 Local-flux mimetic method 235

8.3.7 Monotonicity 236

9 Flow Diagnostics 239

9.1 Flow patterns and volumetric connections 240

9.1.1 Volumetric partitions 242

9.1.2 Time-of-flight per tracer region: improved accuracy 244

9.1.3 Well-allocation factors 244

9.2 Measures of dynamic heterogeneity 245

9.2.1 Flow and storage capacity 246

9.2.2 Lorenz coefficient and sweep efficiency 248

9.2.3 Summary of diagnostic curves and measures 250

9.3 Case studies 252

9.3.1 Tarbert formation: volumetric connections 252

9.3.2 Layers of SPE10: heterogeneity and sweep improvement 256

9.4 Interactive flow diagnostics tools 261

9.4.1 Simple 2D example 264

9.4.2 SAIGUP: flow patterns and volumetric connections 268

10 Upscaling Petrophysical Properties	271
10.1 Upscaling for reservoir simulation	273
10.2 Upscaling additive properties	275
10.3 Upscaling absolute permeability	277
10.3.1 Averaging methods	278
10.3.2 Flow-based upscaling	284
10.4 Upscaling transmissibility	289
10.5 Global and local-global upscaling	292
10.6 Upscaling examples	295
10.6.1 Flow diagnostics quality measure	295
10.6.2 Model with two rock types	296
10.6.3 SPE10 with six wells	299
10.6.4 General advice and simple guidelines	303

Part III Incompressible Multiphase Flow

11 Mathematical Models for Multiphase Flow	307
11.1 New physical properties and phenomena	308
11.1.1 Saturation	308
11.1.2 Wettability	310
11.1.3 Capillary pressure	311
11.1.4 Relative permeability	316
11.2 Flow equations for multiphase flow	319
11.2.1 Single-component phases	319
11.2.2 Multicomponent phases	321
11.2.3 Black-oil models	322
11.3 Model reformulations for immiscible two-phase flow	324
11.3.1 Pressure formulation	324
11.3.2 Fractional flow formulation in phase pressure	325
11.3.3 Fractional flow formulation in global pressure	330
11.3.4 Fractional flow formulation in phase potential	331
11.3.5 Richards' equation	332
11.4 The Buckley–Leverett theory of 1D displacements	334
11.4.1 Horizontal displacement	334
11.4.2 Gravity segregation	338

Part IV Compressible Flow

12 Single-Phase Flow and Rapid Prototyping	341
12.1 Implicit discretization	342
12.2 A simulator based on automatic differentiation	343
12.2.1 Model setup and initial state	344
12.2.2 Discrete operators and equations	345

12.2.3 Well model	347
12.2.4 The simulation loop	348
12.3 Pressure-dependent viscosity	352
12.4 Non-Newtonian fluid	354
12.5 Thermal effects	360
References	369

Preface

There are many books that describe mathematical models for flow in porous media and present numerical methods that can be used to discretize and solve the corresponding systems of partial differential equations; a comprehensive list can be found in the bibliography. However, neither of these books fully describe how you should implement these models and numerical methods to form a robust and efficient simulator. Some books may present algorithms and data structures, but most leave it up to you to figure out all the nitty-gritty details you need to get your implementation up and running. Likewise, you may read papers that present models or computational methods that may be exactly what you need for your work. After the first enthusiasm, however, you very often end up quite disappointed, or at least, I do when I realize that the authors have not presented all the details of their model, or that it will probably take me months to get my own implementation working.

In this book, I try to be a bit different and give a reasonably self-contained introduction to the simulation of flow and transport in porous media that also discusses how to implement the models and algorithms in a robust and efficient manner. In the presentation, I have tried to let the discussion of models and numerical methods go hand in hand with numerical examples that come fully equipped with codes and data, so that you can rerun and reproduce the results by yourself and use them as a starting point for your own research and experiments. All examples in the book are based on the Matlab Reservoir Simulation Toolbox (MRST), which has been developed by my group and published online as free open-source code under the GNU General Public License since 2009.

The book can alternatively be seen as a comprehensive user-guide to MRST. Over the years, MRST has become surprisingly popular (the latest releases typically have from a thousand to fifteen hundred unique downloads each) and has expanded rapidly with new features. Unfortunately, the manuscript has not been able to keep pace. The current version is up-to-date with respect to the latest development in data structures and syntax, but only includes material on single-phase flow, some workflow tools like upscal-

ing and flow diagnostics, and a basic introduction to multiphase flow. However, more material is being added whenever I have time or inspiration, and the manuscript will hopefully be expanded to cover simulation of multiphase flow and examples of more realistic simulations in the not too distant future.

I would like to thank my current and former colleagues at SINTEF with whom I have collaborated over many year to develop MRST; primarily Bård Skaflestad, Halvor Møll Nilsen, Jostein R. Natvig, Odd Andersen, Olav Møyner, Stein Krogstad, and Xavier Raynaud. The chapter on flow diagnostics is the result of many discussions with Brad Mallison from Chevron. I am also grateful to the University of Bergen and the Norwegian University of Science and Technology for funding through my Professor II positions. Victor Calo and Yalchin Efendiev invited me to KAUST, where important parts of the chapters on grids and petrophysics were written. Likewise, Margot Gerritsen invited me to Stanford and gave me the opportunity to develop Jolts videos that complement the material in the book. Last, but not least, I would like to thank colleagues and students who have given suggestions, pointed out errors and misprints, and given me inspiration to continue working. Even though your name is not mentioned here, I have not forgotten all your important contributions.

Finally to the reader: I hereby grant you permission to use the manuscript and the accompanying example scripts for your own educational purpose, but please do not reuse or redistribute this material as a whole, or in parts, without explicit permission. Moreover, notice that *the current manuscript is a snapshot of work in progress and is far from complete*. Every now and then you may encounter some text that has been marked in dark red color to indicate that it needs editing. The text may also contain a number of misprints and errors, and I would be grateful if you help to improve the manuscript by sending me an email. Suggestions for other improvement are also much welcome.

Oslo,
December 16, 2015

Knut-Andreas Lie
Knut-Andreas.Lie@sintef.no

Introduction

Modelling of flow processes in the subsurface is important for many applications. In fact, subsurface flow phenomena cover some of the most important technological challenges of our time. The road toward sustainable use and management of the earth's groundwater reserves necessarily involves modelling of groundwater hydrological systems. In particular, modelling is used to acquire general knowledge of groundwater basins, quantify limits of sustainable use, monitor transport of pollutants in the subsurface, and appraise schemes for groundwater remediation.

A perhaps equally important problem is how to reduce emission of greenhouse gases, such as CO₂, into the atmosphere. Carbon sequestration in porous media has been suggested as a possible means. The primary concern related to storage of CO₂ in subsurface rock formations is how fast the stored CO₂ will escape back to the atmosphere. Repositories do not need to store CO₂ forever, just long enough to allow the natural carbon cycle to reduce the atmospheric CO₂ to near pre-industrial level. Nevertheless, making a qualified estimate of the leakage rates from potential CO₂ storage facilities is a nontrivial task, and demands interdisciplinary research and software based on state-of-the-art numerical methods for modelling subsurface flow. Other questions of concern is whether the stored CO₂ will leak into fresh-water aquifers or migrate to habitated or different legislative areas.

A third challenge is petroleum production. The civilized world will very likely continue to depend on the utilization of petroleum resources both as an energy carrier and as a raw material for consumer products in the foreseeable future. In recent years, conventional petroleum production has declined and the rate of new major discoveries has been significantly reduced: Optimal utilization of current fields and new discoveries is therefore of utter importance to meet the demands for petroleum and lessen the pressure on exploration in vulnerable areas like in the arctic regions. Likewise, there is a strong need to understand how unconventional petroleum resources can be produced in an economic way that minimizes the harm to the environment.

Reliable computer modeling of subsurface flow is much needed to overcome these three challenges, but is also needed to exploit deep geothermal energy, ensure safe storage of nuclear waste, improve remediation technologies to remove contaminants from the subsurface, etc. Indeed, the need for tools that help us understand flow processes in the subsurface is probably greater than ever, and increasing. More than fifty years of prior research in this area has led to some degree of agreement in terms of how subsurface flow processes can be modelled adequately with numerical simulation technology. Herein, we will mainly focus on modelling flow in oil and gas reservoirs, which is often referred to as reservoir simulation. However, the general modelling framework and the numerical methods that are discussed also apply to modelling other types of flow in consolidated and saturated porous media.

In the book, we will introduce and discuss basic physical properties and mathematical models that are used to represent porous rocks and describe flow processes on a macroscopic scale. The presentation will focus primarily on physical processes that take place during hydrocarbon production. What this means is that even though the mathematical models, numerical methods, and software implementations presented can be applied to any of the applications outlined above, the specific examples use vocabulary, physical scales, and balances of driving forces that are specific to petroleum production. As an example of vocabulary, we can consider the ability of a porous medium to transmit fluids. In petroleum engineering this is typically given in terms of the 'permeability', which is a pure rock property, whereas one in water resource engineering is more concerned with the 'hydraulic conductivity' that also takes the viscosity and density of the fluid into account; in CO₂ sequestration you can see both quantities used. As an example of physical scales, let us compare oil production by water flooding and the question of long-term geological storage of CO₂. The hydrocarbons that make up petroleum resources can only accumulate when their natural upward movement relative to water is prevented by confinements in the overlying rocks, and hence the fluid flow in a petroleum reservoir takes place in a relatively closed system. Hydrocarbons will typically be produced for tens of years, during which the main driving mechanism is viscous forces induced by the pressure difference between the points where water is injected and oil is produced, which cause water to displace oil over distances of hundred to thousands of meters. Huge aquifer systems that stretch out for hundreds of kilometers are currently the most promising candidates for large-scale geological storage. During the injection phase, the flow processes of CO₂ storage are almost identical to those of petroleum production, albeit the operational constraints may differ, but as the CO₂ moves into the aquifer and the effects of the injection pressure ceases, the fluid movement will be dominated by buoyant forces that will cause the lighter CO₂ phase to migrate upward in the open aquifer system, and potentially continue to do so for thousands of years. In both cases, the governing equations of the basic flow physics are the same, but the balances between

physical forces are different, which should be accounted for when formulating the overall mathematical models and appropriate numerical methods.

Techniques developed to study subsurface flow are also applicable to other natural and man-made porous media such as soils, biological tissues and plants, filters, fuel cells, concrete, textiles, polymer composites, etc. A particular interesting example is in-tissue drug delivery, where the challenge is to minimize the volume swept by the injected fluid. This is the complete opposite of the challenge in petroleum production, in which one seeks to maximize the volumetric sweep of the injected fluid to push as much petroleum out as possible.

1.1 Petroleum production

To provide context for the discussion that will follow later in the book, we will briefly outline the various ways by which hydrocarbon can be produced from a subsurface reservoir. Good reservoir rocks have large void spaces between the mineral grains forming networks of connected pores that can store and transmit large amounts of fluids. Conceptually, one can think of a hydrocarbon reservoir as a bent, rigid sponge that is confined inside an insulating material and has all its pores filled with hydrocarbons that may appear in the form of oil or gas as illustrated in Figure 1.1. Natural gas will be dissolved in oil under high pressure like carbon-dioxide inside a soda can. If the pressure inside the pristine reservoir is below the bubble point, the oil is undersaturated and still able to dissolve more gas. If the pressure is above the bubble point, the oil will be fully saturated with gas and any excess gas will form a gas cap on top of the oil since it is lighter. To extract oil from the reservoir, one drills a well into the oil zone. The pristine pressure inside the reservoir may be sufficient to push hydrocarbons up to the surface. Alternatively, one may have to pump to lower the pressure beyond the point where oil starts flowing. How large the pressure differential needs to be for oil to flow will depend on the permeability of the rock; the higher the permeability is, the easier the hydrocarbons will flow towards the well.

As oil is extracted, the pressure inside the reservoir will decay and the production will gradually decline. However, declining pressure will often induce physical processes that contribute to maintain the production:

- In a *water drive*, the pore space below the hydrocarbons is filled with salt water that is slightly compressible, and hence will expand a little as the reservoir pressure is lowered. If the total water volume is large compared with the oil zone, even a small expansion will create significant water volumes that will push oil towards the well and hence contribute to maintain pressure. Sometimes the water is part of a large aquifer system that has a natural influx that replenishes the extracted oil by water and maintains pressure.

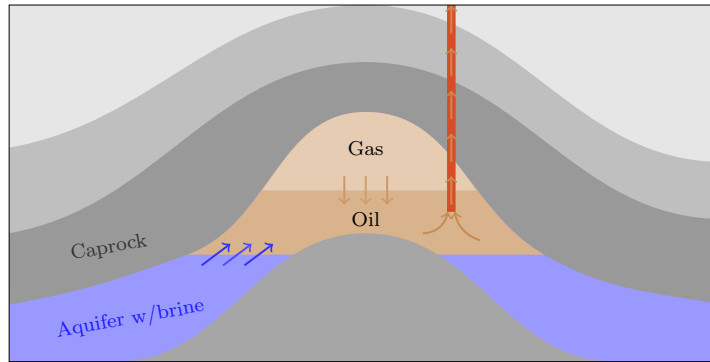


Fig. 1.1. Conceptual illustration of a petroleum reservoir during primary production. Over millions of years, hydrocarbons have accumulated under a caprock that has low ability to transmit fluids and therefore prevents their upward movement. Inside the trap, the fluids will be distributed according to density, with light gas on top, oil in the middle, and brine at the bottom. If the difference in pressure between the oil zone and the well is sufficiently high, the oil will flow naturally out of the reservoir. As oil is produced, the pressure inside the reservoir will decline, which in turn may introduce other mechanisms that contribute to maintain pressure and push more oil out of the well.

- *Solution gas drive* works like when you shake and open a soda can. Initially, the pristine oil will be in a pure liquid state and contain no free gas. The extraction of fluids will gradually lower the reservoir pressure below the bubble point, which causes free gas to develop and form expanding gas bubbles that force oil into the well. Inside the well, the gas bubble rise with the oil and make the combined fluid lighter and hence easier to push upward to the surface. At a certain point, however, the bubbles may reach a critical volume fraction and start to flow as a single gas phase that has lower viscosity than the oil and hence moves faster. This rapidly depletes the energy stored inside the reservoir and causes the production to falter. Gas coming out of solution can also migrate to the top of the structure and form a gas cap above the oil that pushes down on the liquid oil and hence contributes to maintain pressure.
- In a *gas cap drive*, the reservoir contains more gas than what can be dissolved in the oil. When pressure is lowered the gas cap expands and pushes oil into the well. Over time, the gas cap will gradually infiltrate the oil and cause the well to produce increasing amounts of gas.
- If a reservoir is highly permeable, gravity will force oil to move downward relative to gas and upward relative to water. This is called *gravity drive*.
- In a *combination drive* there is water below the oil zone and a gas cap above that both will push oil to the well at the same time as the reservoir pressure is reduced.

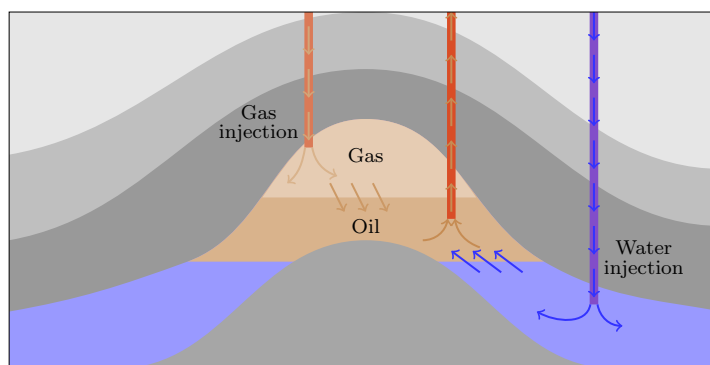


Fig. 1.2. Conceptual illustration of voidage replacement, which is an example of a secondary production strategy in which gas and/or water is injected to maintain the reservoir pressure.

These natural (or primary) drive mechanisms will only be able to maintain the pressure for a limited period and the production will gradually falter as the reservoir pressure declines. How fast the pressure declines and how much oil one can extract before the production ceases, varies with the drive mechanism. Solution gas drives can have a relatively rapid decline, whereas water and gas cap drives are able to maintain production for longer periods. Normally only 30% of the oil can be extracted using primary drive mechanisms.

To keep up the production and increase the recovery factor, most reservoirs will use some kind of engineered drive mechanisms. Figure 1.2 illustrates two examples of voidage replacement in which water and/or gas is injected to support pressure in the reservoir. Water can also be injected to sweep the reservoir, displace the oil, and push it towards the wells. In some cases, one may choose to inject produced formation water that is contaminated with hydrocarbons and solid particles and hence must be disposed of in some manner. Alternatively, one can extract formation water from a nearby aquifer. In offshore production it is also common to inject seawater. A common problem for all waterflooding methods is to maximize the sweep efficiency so that water does not move rapidly through high-flow zones in the reservoir and leaves behind large volumes of unswept, mobile oil. Maintaining good sweep efficiency is particularly challenging for reservoirs containing high-viscosity oil. If injected water has low viscosity, it will tend to form viscous fingers that rapidly expand through the oil and cause early water breakthrough in the production wells. (Think of water being poured into a cup of honey). To improve the sweep efficiency, one can add polymers to the water to increase its viscosity and improve the mobility ratio between the injected and displaced fluid. Polymers have also been used to create flow diversions by plugging high-flow zones so that the injected fluid contacts and displaces more oil. For heavy

oils, adverse mobility ratios can be improved by using steam injection or some other thermal method to heat the oil to reduce its viscosity.

Water flooding, polymer injection, and steam injection are all examples of methods for so-called enhanced oil recovery (EOR). Another example is miscible and chemical injection, where one uses a solvent or surfactant that mixes with the oil in the reservoir to make it flow more readily. The solvent may be a gas such as carbon dioxide or nitrogen. However, the most common approach is to inject natural gas produced from the reservoir when there is no market that will accept the gas. Surfactants are similar to detergents used for laundry. Alkaline or caustic solutions, for instance, can react with organic acids occurring naturally in the reservoir to produce soap. The effect of all these substances is that they reduce the interfacial tension between water and oil, which enables small droplets of oil that were previously immobile to flow (more) freely. This is the same type of process that takes place when you use detergent to remove waxy and greasy stains from textiles. A limiting factor of these methods is that the chemicals are quickly adsorbed and lost into the reservoir rock

Often, one will want to combine methods that improve the sweep efficiency of mobile oil with methods that mobilize immobile oil. Miscible gas injection, for instance, can be used after a waterflood to flush out residually trapped oil and establish new pathways to the production wells. Water-alternating-gas (WAG) is the most successful and widely used EOR method. Injecting large volumes of gas is expensive, and by injecting alternating slugs of water, one reduces the injected volume of gas required to maintain pressure. Similarly, presence of mobile water reduces the tendency of the injected gas to finger through the less mobile oil. In polymer flooding, it is common to add surfactants to mobilize immobile oil by reducing or removing the interface tension between oil and water, and likewise, add alkaline solutions to reduce the adsorption of chemicals onto the rock faces.

While the mechanisms of all the above methods for enhanced oil recovery are reasonably well studied and understood, there are other methods whose mechanisms are much debated. This includes injection of low-salinity water, which is not well understood even though it has proved to be highly effective in certain cases. Another example is microbial enhanced oil recovery which relies on microbes that digest long hydrocarbon molecules to form biosurfactants or emit carbon dioxide that will reduce interfacial tension and mobilize immobile oil. Microbial activity can either be achieved by injecting bacterial cultures mixed with a food source, or by injecting nutrients that will activate microbes that already reside in the reservoir.

Use of secondary recovery mechanisms has been highly successful. On the Norwegian Continental Shelf, for instance, the average recovery factor is now almost 50%, which can be attributed mainly to water flooding and miscible gas injection. In other parts of the world, chemical methods have proved to be very efficient for onshore reservoirs having relatively short distances between wells. For offshore fields, however, the potential benefits of using chemical

methods are much debated. First of all, it is not obvious that such methods will be effective for reservoirs characterized by large inter-well distances as rapid adsorption onto the pore walls generally makes it difficult to transport the active ingredients long distances into a reservoir. Chemicals are also costly, need to be transported in large quantities, and may consume space on the platforms.

Even small improvements in recovery rates can lead to huge economic benefits for the owners of a petroleum asset and for this reason much research and engineering work is devoted to improve the understanding of mobilization and displacement mechanisms and to design improved methods for primary and enhanced oil recovery. Mathematical modeling and numerical reservoir simulation play key roles in this endeavor.

1.2 Reservoir simulation

Reservoir simulation is the means by which we use a numerical model of the petrophysical characteristics of a hydrocarbon reservoir to analyze and predict fluid behavior in the reservoir over time. Simulation of petroleum reservoirs started in the mid 1950's and has become an important tool for qualitative and quantitative prediction of the flow of fluid phases. Reservoir simulation is a complement to field observations, pilot field and laboratory tests, well testing and analytical models and is used to estimate production characteristics, calibrate reservoir parameters, visualize reservoir flow patterns, etc. The main purpose of simulation is to provide an information database that can help oil companies position and manage wells and well trajectories to maximize recovery of oil and gas. Generally, the value of simulation studies depends on what kind of extra monetary or other profit they will lead to, e.g., by increasing the recovery from a given reservoir. However, even though reservoir simulation can be an invaluable tool to enhance oil-recovery, the demand for simulation studies depends on many factors. For instance, petroleum discoveries vary in size from small pockets of hydrocarbon that may be buried just a few meters beneath the surface of the earth and can easily be produced, to huge reservoirs¹ stretching out several square kilometers beneath remote and stormy seas, for which extensive simulation studies are inevitable to avoid making suboptimal and costly decisions.

To describe the subsurface flow processes mathematically, two types of models are needed. First, one needs a mathematical model that describes how fluids flow in a porous medium. These models are typically given as a set of partial differential equations describing the mass-conservation of fluid phases, accompanied by a suitable set of constitutive relations that describe the relationship among different physical quantities. Second, one needs a geological

¹ The largest reservoir in the world is found in Ghawar in the Saudi Arabian desert and is approximately 230 km long, 30 km wide, and 90 m thick.

model that describes the given porous rock formation (the reservoir). The geological model is realized as a grid populated with petrophysical properties that are used as input to the flow model, and together they make up the reservoir simulation model.

Unfortunately, obtaining an accurate prediction of reservoir flow scenarios is a difficult task. One reason is that we can never get a complete and accurate characterization of the rock parameters that influence the flow pattern. Even if we did, we would not be able to run simulations that exploit all available information, since this would require a tremendous amount of computer resources that far exceed the capabilities of modern multi-processor computers. On the other hand, we do not need, nor do we seek a simultaneous description of the flow scenario on all scales down to the pore scale. For reservoir management it is usually sufficient to describe the general trends in the reservoir flow pattern.

In the early days of the computer, reservoir simulation models were built from two-dimensional slices with 10^2 – 10^3 Cartesian grid cells representing the whole reservoir. In contrast, contemporary reservoir characterization methods can model the porous rock formations by the means of grid-blocks down to the meter scale. This gives three-dimensional models consisting of millions of cells. Stratigraphic grid models, based on extrusion of 2D areal grids to form volumetric descriptions, have been popular for many years and are the current industry standard. However, more complex methods based on unstructured grids are gaining in popularity.

Despite an astonishing increase in computer power, and intensive research on computation techniques, commercial reservoir simulators can seldom run simulations directly on geological grid models. Instead, coarse grid models with grid-blocks that are typically ten to hundred times larger are built using some kind of upscaling of the geophysical parameters. How one should perform this upscaling is not trivial. In fact, upscaling has been, and probably still is, one of the most active research areas in the oil industry. This effort reflects the general opinion that with the ever increasing size and complexity of the geological reservoir models one cannot generally expect to run simulations directly on geological models in the foreseeable future.

Along with the development of better computers, new and more robust upscaling techniques, and more detailed reservoir characterizations, there has also been an equally significant development in the area of numerical methods. State-of-the-art simulators employ numerical methods that can take advantage of multiple processors, distributed memory workstations, adaptive grid refinement strategies, and iterative techniques with linear complexity. For the simulation, there exists a wide variety of different numerical schemes that all have their pros and cons. With all these techniques available we see a trend where methods are being tuned to a special set of applications and mathematical models, as opposed to traditional methods that were developed for a large class of differential equations.

1.3 Outline of the book

The book is intended to serve several purposes. First of all, you can use the book as a self-contained introduction to the basic theory of flow in porous media and the numerical methods used to solve the underlying differential equations. Hopefully, the book will also give you a hands-on introduction to practical modeling of flow in porous media, focusing in particular on models and problems that are relevant to the petroleum industry. The discussion of mathematical models and numerical methods is accompanied by a large number of illustrative examples, ranging from idealized and highly simplified examples to cases involving models of real-life reservoirs.

All examples in the book have been created using the MATLAB Reservoir Simulation Toolbox (MRST), which we will discuss in more detail in Chapter 2. MRST is an open-source software that can either be used as a set of gray-box reservoir simulators and workflow tools you can modify to suit your own purposes, or as a collection of flexible and efficient software libraries and data structures you can use to design your own simulators or computational workflows. The use of MRST permeates more traditional textbook material, and the book can therefore be seen as a user guide to MRST, or alternatively as a discussion, in terms of a large number of detailed examples, of how a scripting language like MATLAB can for be used for rapid prototyping, testing, and verification on realistic problems with a high degree of complexity. Through the many examples, we also try to gradually teach you some of the techniques and programming concepts that have been used to create MRST, which you can use to ensure flexibility and high efficiency in your own programs.

The first part of the book discusses how to represent a geological medium as a discrete model that can subsequently be used to study the flow of one or more fluid phases. The resulting volumetric grid, in which each cell is equipped with a set of petrophysical properties, is used as input to the mathematical models that describe the macroscopic physics of one or more fluid phases flowing through the microscopic network of pores and throats between mineral grains in the porous rock. As part of this discussion, you will be introduced to the data structures for unstructured grids and petrophysical. Understanding these data structures is fundamental if you want to use MRST to create your own computational methods or understand the inner workings of a majority of the routines implemented in the software. Through the many examples, you will also be introduced to various functionality in MRST for plotting data associated with cells and faces (interface between two neighboring cells).

In the second part of the book, we discuss the special case of incompressible fluids flowing in a completely rigid medium. We start by considering the single-phase case, for which the pressure distribution can be modeled by a Poisson-type partial differential equation (PDE) with a varying coefficient that describes the interaction between the rigid rock and the flowing fluid. To form a full model, this second-order, elliptic PDE must be equipped

with extra equations describing the external forces that drive the fluid flow; these can either be boundary conditions and/or wells that inject or produce fluids. To better understand the complex flow patterns that arise even for steady-state flow, the basic model can be extended to include equations for non-physical quantities like time-of-flight, which defines natural time lines in the porous medium, and steady-state distribution of numerical tracers, which can be used to determine communication patterns and delineate the reservoir into sub-regions that can be uniquely associated with distinct parts of the inflow/outflow boundaries. To discretize the mathematical models, we introduce a classical two-point finite-volume method, which is the current industry standard. Although the mathematical model and the numerical discretizations are quite simple, computing accurate solutions can be quite challenging. Primarily this can be attributed to the strongly heterogeneous structure of the porous rocks, which introduces a multiscale structure in the elliptic equation so that the variable coefficient spans many orders of magnitude and has a wide spectrum of spatial correlation lengths. A second challenge comes from the grids that are used to describe real reservoirs, which typically have an unstructured topology with irregular cells with high aspect ratios. To improve the spatial discretization, we introduce and discuss a few recent methods for consistent discretization on general polyhedral grids that are still being researched by academia. We also describe upscaling methods that can be used to develop reduced models by coarsening the grid and computing new effective properties on a coarser scale. We end the second part of the book by discussing how the multiphase effects can be incorporated into the incompressible models using the so-called fractional-flow formulation and simulated using sequential methods in which pressure effects and transport of fluid saturations and/or component concentrations are computed in separate steps.

The third part of the book is devoted to compressible, transient flow. We start by discussing compressible single-phase flow, which in the general case is modelled by a nonlinear, time-dependent, parabolic PDE. Using this relatively simple model, we introduce many of the concepts that will later be used to develop multiphase simulators of full industry-standard complexity. To discretize the single-phase equation, we combine the two-point method introduced for incompressible flow with an implicit temporal discretization. The standard approach for solving the nonlinear system of discrete equations arising from complex multiphase models is to compute the Jacobian matrix of first derivatives for the nonlinear system and use Newton's method to successively find a better approximations to the solution. Deriving and implementing analytic expressions for Jacobian matrices is both error-prone and time-consuming, in particular if the flow equations contain complex fluid model, well descriptions, thermodynamical behavior, etc.

In MRST, we have chosen to construct Jacobian matrices using automatic differentiation, which is a technique to numerically evaluate the derivatives of functions specified by a computer program to working precision accuracy. Combining automatic differentiation with discrete averaging and differential

operators enables you to write very compact simulator codes in which the flow models are implemented almost in the same form as they are written in the corresponding mathematical equations. This opens up for a simple way of writing new simulators: all the user has to do is to implement the new model equations in residual form and specify which variables should be used in the linearization of the resulting nonlinear system, and then the software computes the corresponding derivatives and assemble them into a correct block matrix. To demonstrate the utility and power the resulting framework, we show how one can quickly change functional dependencies in the single-phase pressure solver and extend it to include thermal and non-Newtonian fluid effects. Once this is done, we move on to discuss more advanced multiphase flow models, focusing primarily on the black-oil formulation and extensions thereof for enhanced oil recovery that can be found in contemporary commercial simulators.

In the introductory examples in the book, we present and discuss in detail the code lines necessary to produce the numerical results and figures presented. We have tried to make these examples as self-contained as possible, but sometimes we omit minor details that either have been discussed elsewhere or should be part of your basic MATLAB repertoire. As we move to more complex examples, in particular for multiphase flow, it is no longer expedient to discuss MATLAB scripts in full details. In most cases, however, complete scripts that contain all code lines necessary to run the examples can be found in a dedicated `book` module that is part MRST. We strongly encourage you to use your own computer to run the examples in the book and other examples and tutorials that are distributed with the software. Your understanding will be further enhanced if you also modify the examples, e.g., by changing the input parameters, or extend them to solve problems that are related, but (slightly) different. MRST is an open-source software, and if reading this book gives you ideas about new functionality, or you discover things that are not working as they should or could, you are welcome to contribute to improve the toolbox and extend it in new directions.

The MATLAB Reservoir Simulation Toolbox

Practical computer modeling of porous media constitutes an important part of the book and is presented through a series of examples that are intermingled with more traditional textbook material. All examples discussed in the book rely on the MATLAB Reservoir Simulation Toolbox (MRST), which is an open-source software that can be used for any purpose under the GNU General Public License (GPLv3). The basic part of MRST contains a comprehensive set of data structures and routines for representing and manipulating the primary input parameters that make up a simulation model of a porous medium: grids representing geometry of the porous domain, petrophysical rock properties, properties, and forcing terms such as gravity, boundary conditions, source terms, and well models. In addition, there are routines for reading and processing input files and plotting quantities defined over cells and cell interfaces, as well as functionality for automatic differentiation. On top of this, MRST provides a set of add-on modules that supply a wide range of discretizations, solvers, simulators, and workflow tools that can be combined to perform various tasks in reservoir modeling. By carefully documenting and releasing this software as free, open source, we hope to contribute to give a head start to students about to embark on a master or PhD project, as well as to researchers working on similar problems.

This chapter will provide you with a brief overview of MRST and the philosophy underlying its design. We show you how to obtain and install the software and explain its terms of use, as well as how we recommend that you use the software as a companion to the textbook. We also briefly discuss how you can use a scripted, numerical programming environment like MATLAB to increase the productivity of your experimental programming and give a few examples of tricks and ways of working with MATLAB that we have found particularly useful. We end the chapter by introducing you to automatic differentiation, which is one of the key aspects that make MRST a powerful tool for rapid prototyping and enable us to write compact and quite self-explanatory codes that are well suited for pedagogical purposes. As a complement to the material presented in this chapter, you should also

consult the first section [113] of the just-in-time online learning tools (Jolts) developed in collaboration with Stanford University. This Jolt gives a brief overview of the software, tells you why and how it was created, and shows you how to download and install it on your computer. If you are not interested in programming at all, you can jump directly to Chapter 3. However, if you choose to not work with the software alongside the textbook material, be warned, you might miss a lot of valuable insight.

Before we dive into more details about the MATLAB Reservoir Simulation Toolbox, we present a simple example that will give you a first a taste of simulating flow in porous media and a feel of the software

2.1 The first encounter with MRST

The purpose of this first example is to show the basic steps for setting up, solving, and visualizing a simple flow problem using MRST. To this end, we will compute a known analytical solution: the linear pressure solution describing hydrostatic equilibrium for an incompressible, single-phase fluid. The basic model in subsurface flow consists of an equation expressing conservation of mass and a constitutive relation called Darcy’s law that relates the volumetric flow rate to the gradient of flow potential

$$\nabla \cdot \vec{v} = 0, \quad \vec{v} = -\frac{K}{\mu} [\nabla p + \rho g \nabla z], \quad (2.1)$$

where the unknowns are the pressure p and the flow velocity \vec{v} . By eliminating \vec{v} , we can reduce (2.1) to the elliptic Poisson equation. In (2.1), the rock is characterized by the permeability K that gives the rock’s ability to transmit fluid. Here, K is set to 100 millidarcy (mD). The fluid has a density ρ of 1000 kg/m³ and viscosity μ equal one centipoise (cP), g is the gravity constant, and z is the depth. More details on these flow equations, the rock and fluid parameters, the computational method, and its MATLAB implementation will be given throughout the book.

The computational domain is a square column, $[0, 1] \times [0, 1] \times [0, 30]$ m³, which we discretize using a regular $1 \times 1 \times 30$ Cartesian grid. The simulation model is set up by constructing a grid and assigning the rock permeability, and setting boundary conditions:

```
gravity reset on
G = cartGrid([1, 1, 30], [1, 1, 30]*meter^3);
G = computeGeometry(G);
rock.perm = repmat(0.1*darcy(), [G.cells.num, 1]);
```

MRST works in SI units and we must therefore be careful to specify the correct units for all physical quantities. To solve (2.1), we will use a standard two-point finite-volume scheme, that relates the flux between cells to their pressure difference, $v_{ij} = -T_{ij}(p_i - p_j)$. For Cartesian grids, this scheme

coincides with the classical seven-point scheme for Poisson’s problem and is the only discretization that is available in the basic parts of MRST. More advanced discretizations can be found in the add-on modules. To define the two-point discretization, we compute therefore compute the transmissibilities T_{ij} , which can be defined independent of the particular flow model once we have defined the grid and petrophysical parameters:

```
T = computeTrans(G, rock);
```

Since we are solving (2.1) on a finite domain, we must also describe conditions on all boundaries. To this end, we prescribe $p = 100$ bar at the top of the column and no-flow conditions ($\vec{v} \cdot \vec{n} = 0$) elsewhere:

```
bc = pside([], G, 'TOP', 100.*barsa());
```

The next thing we need to define is the fluid properties. Unlike grids, petrophysical data, and boundary conditions, data structures for representing fluid properties are not part of the basic functionality of MRST. The reason is that the way fluid properties are specified is tightly coupled with the mathematical and numerical formulation of the flow equations, and may differ a lot between different types of simulators. Here, we have assumed incompressible flow and can therefore use fluid models from the `incomp` add-on module,

```
mrstModule add incomp;
fluid = initSingleFluid('mu', 1*centi*poise, ...
                       'rho', 1014*kilogram/meter^3);
```

As a final step, we use the transmissibilities, the fluid object, and the boundary conditions to assemble and solve the discrete system:

```
sol = incompTPFA(initResSol(G, 0.0), G, T, fluid, 'bc', bc);
```

Having computed the solution, we plot the pressure given in units 'bar', which equals 0.1 mPa and is referred to as 'barsa' in MRST since 'bar' is a built-in command in MATLAB:

```
plotFaces(G, 1:G.faces.num, convertTo(sol.facePressure, barsa()));
set(gca, 'ZDir', 'reverse'), title('Pressure [bar]')
view(3), colorbar, set(gca, 'DataAspect', [1 1 10])
```

From the plot shown in Figure 2.1, we see that our solution correctly reproduces the linear pressure increase with depth one would expect to find inside a column consisting of a single fluid phase.

2.2 Downloading and installing the software

The main parts of MRST are hosted as a collection of private software repositories on Bitbucket. Public releases are provided as self-contained archive files that can be downloaded from the webpage:

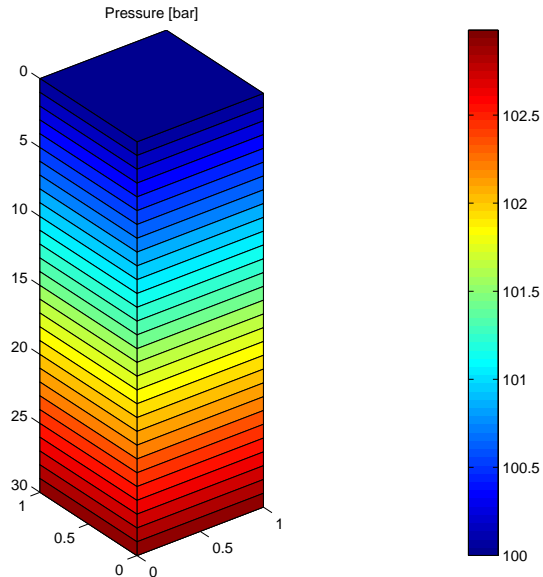


Fig. 2.1. Hydrostatic pressure distribution in a gravity column computed by MRST. This is example is taken from the MRST tutorial `gravityColumn.m`

<http://www.sintef.no/MRST/>

Assuming that you have downloaded the tarball of one of the recent releases, here we will use MRST R2015a as an example, issuing the following command

```
untar mrst-2015a.tar.gz
```

in MATLAB will create a new directory `mrst-2015a` in you current working director that contains all parts of the software. Once MRST has been extracted to some directory, which we henceforth will refer to as the MRST root directory, you must navigate MATLAB there, either using the built-in file browser, or by using the `cd` command. Assuming that the files were extracted to the home directory, this would amount to the following on Linux/Mac OS,

```
cd /home/username/mrst-2015a/      % on Linux/Mac OS
cd C:\Users\username\mrst-2015a\  % on Windows
```

Once you are in the directory that contains the software, you need to run the following command to activate it

```
startup;
```

The whole procedure of downloading and installing MRST, step by step, can be seen in the first MRST Jolt [113].

At this point, a word of caution is probably in order. Throughout the book, we will refer to the software as a toolbox. By this we mean that MRST

is a collection of data structures and routines that can be used alongside with MATLAB. It is, however, *not* a toolbox in the same sense as those that can be purchased from the official vendors of MATLAB. This means, for instance, that MRST is not automatically loaded unless you start MATLAB from the MRST root directory, or make this directory your standing directory and manually issue the `startup` command. Alternatively, if do not want to navigate to the MRST root directory, for instance in an automated script, you can call startup directly

```
run /home/username/mrst-2015b/startup
```

To verify that MRST is active, you can run the simple example discussed in the previous section by writing `gravityColumn`. This should produce the same plot as shown in Figure 2.1.

The minimal requirement is MATLAB version 7.4 (R2007a). However, certain parts of the software use features that were not present in R2007a:

- The functionality for automatic differentiation uses new-style classes (`classdef`) that were introduced in R2008a.
- Various scripts and examples use new syntax for random numbers introduced in R2007b.
- Some script may use the tilde operator to ignore return values (e.g., `[~,i]=max(X,1)`) that was introduced in R2009b.
- Some routines, like the fully-implicit simulators for black-oil models, rely on accessing sub-blocks of large sparse matrices. Although these routines will run on any version from R2007a and onward, they may not be efficient on versions older than R2011b.

Large parts of MRST can also be used with GNU Octave, which is an open-source numerical programming environment that is designed to be compatible with MATLAB. However, there are two main difficulties: GNU Octave has less (stable) functionality for 3D visualization, which is used a lot throughout this book, and does not yet offer the new-style classes (`classdef`) used in the implementation of automatic differentiation.

Although MRST is designed to only use functionality available in standard MATLAB, there are a few third-party packages and libraries that we have found to be quite useful:

- **MATLAB-BGL**: MATLAB does not yet have extensive support for graph algorithms. The Boost Graph Library (BGL) is a generic interface for traversing graphs. The MATLAB Boost Graph Library contains binaries for useful algorithms in BGL such as depth-first search, computation of connected components, etc. MATLAB-BGL is freely available under the BSD License from the Mathwork File Exchange¹. MRST has a particular module, see Section 2.5, that downloads and installs this library.

¹ <http://www.mathworks.com/matlabcentral/fileexchange/10922>

- **METIS**: is a widely used library for partitioning graphs, partitioning finite element meshes, and producing fill reducing orderings for sparse matrices [97]. The library is released² under a permissive Apache License 2.0.
- **AGMG**: For large problems, the linear solvers available in MATLAB are not always sufficient, and it may be necessary to use an iterative algebraic multigrid method. AGMG [150] has MATLAB bindings included and was originally published as free open-source. The latest releases have unfortunately only offered free licenses for academic research and teaching³.

MATLAB-BGL is required by several of the more advanced solvers that are not part of the basic functionality in MRST. Installing the other two packages is recommended by not required. When installing extra libraries or third-party toolboxes that you want to integrate with MRST, you must make the software aware of them. To this end, you should add a new script called `startup_user.m` and use the built-in command `mrstPath` to make sure that they are on the search path used by MRST and MATLAB to find functions and scripts.

2.3 Terms of usage

The MRST software is distributed as free, open-source software under the GNU Public License (GPLv3)⁴. This license is a widely used example of a so-called copyleft license that offers the right to distribute copies and modified versions of copyrighted creative work, provided the same rights are preserved in modified and extended versions of the work. For MRST, this means that you can use the software for any purpose, share it with anybody, modify it to suit your needs, and share the changes you make. However, if you share any version of the software, modified or unmodified, you must grant others the same rights to distribute and modify it as in the original version. By distributing MRST as free software under the GPLv3 license, the developers of MRST have made sure that the software will stay free, no matter who changes or distributes it.

The development of the MRST toolbox has to a large extent been funded by strategic research grants awarded from the Research Council of Norway. Dissemination of research results is an important evaluation criterion for these types of research grants. To provide us with an overview of some usage statistics for the software, you are kindly asked to register your affiliation/country upon download. This information is only used when reporting impact of the creative work to agencies co-funding the development of MRST. If you also leave an email address, we will notify you when a new releases or critical bugfixes are available. Your e-mail address will under no circumstances be shared with any third party.

² <http://glaros.dtc.umn.edu/gkhome/metis/metis/overview>

³ <http://homepages.ulb.ac.be/~ynotay/AGMG/>

⁴ See <http://www.gnu.org/licenses/gpl.html> for more details.

Finally, if you use MRST in any scholar work, we require that the creative work of the MRST developers is courteously and properly acknowledged by referring to the MRST webpage or by citing this book or one of the overview papers that describe MRST [115, 112, 104].

2.4 Getting started with the software

The open-source MRST toolbox was originally developed to support research on consistent discretization and multiscale solvers on unstructured, polyhedral grids, but has over the years developed into an efficient platform for rapid prototyping and efficient testing of new mathematical models and simulation methods. A particular aim of MRST is to accelerate the process of moving from simplified and conceptual testing to validation and verification on problems with a high degree of realism, and in many cases, full industry-standard complexity.

To make the software as flexible as possible, MRST is organized quite similar to MATLAB and consists of a collection of core routines and a set of add-on modules, see Figure 2.2. The core contains routines and data structures for creating and manipulating grids and physical properties, utilities for performing automatic differentiation (you write the formulas and specify the independent variables, the software computes the corresponding Jacobians), as well as a few routines for plotting cell and face data defined over a grid. The functionality in the core module is considered to be stable and not expected to change significantly in future releases. The introductory parts of the book relies almost entirely on general routines from the core module. In addition, we will sometimes use functionality from the `incomp` add-on module that implements basic solvers for incompressible, immiscible, single-phase and two-phase flow.

Routines in the core and `incomp` modules are generally well documented in a format that follows the MATLAB standard, see Figure 2.3. In addition, there are several worked tutorials highlighting key functionality that will be needed by most users; the tutorials are distributed as part of the MRST release and a subset of the tutorials are also available on the MRST webpage. These examples are designed using cell-mode scripts, which can be seen as a type of “MATLAB workbook” that allows you break the scripts down into smaller pieces that can be run individually to perform a specific task such as creating parts of a model or making an illustrative plot; see Figure 2.4 for an illustration. In our opinion, the best way to understand the examples is to go through the corresponding scripts, evaluating one cell at the time. Alternatively, you can set a breakpoint on the first line, and step through the script in debug mode, e.g., as shown in the fourth video of the first MRST Jolt [113]. Some of the example scripts in MRST contain quite a lot of text and are designed to make easily published documents. If you are not familiar

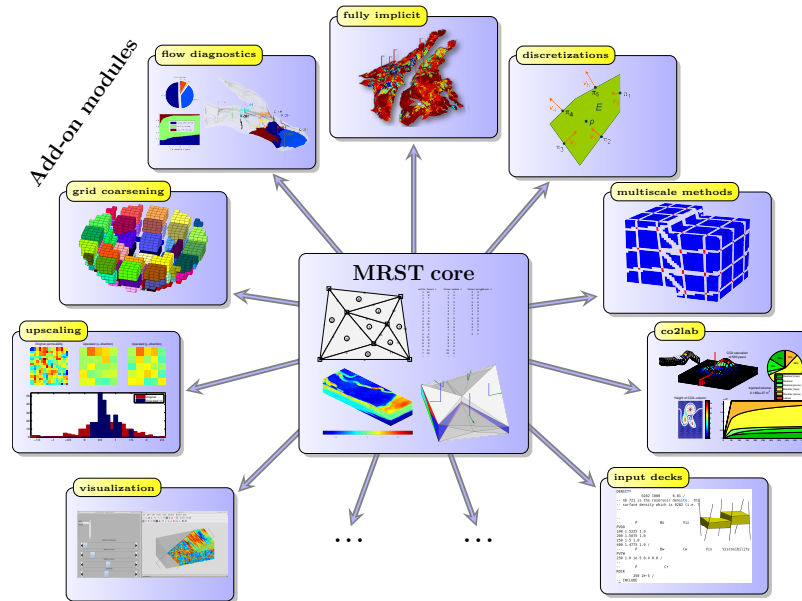


Fig. 2.2. The Matlab Reservoir Simulation Toolbox consists of a core module that provides basic data structures and utility functions, and a set of add-on modules that offer discretizations and solvers, simulators for incompressible and compressible flow, and various workflow tools such as flow diagnostics, grid coarsening, upscaling, visualization of simulation output, and so on.

with cell-mode scripts, or debug mode, we strongly urge you to learn these useful features in MATLAB as soon as possible.

Over the last few years, key parts of MRST have become relatively mature and well tested. This has enabled a stable release policy with two releases per year, one in the spring and one in the fall. Throughout the releases, the basic functionality like grid structures has remained largely unchanged, except for occasional and inevitable bugfixes, and the primary focus has been on expanding functionality by maturing and releasing in-house prototype modules. However, MRST is mainly developed and maintained as an efficient prototyping tool to support contract research carried out by SINTEF for the energy-resource industry and public research agencies. Fundamental changes will therefore occur from time to time, e.g., like when automatic differentiation was introduced in 2012. Likewise, parts of the software may sometimes be reorganized like when the basic incompressible solvers were taken out of MRST core and put in a separate module in 2015. In writing this, we (regretfully) acknowledge the fact that specific code details and examples in books that describe evolving software tend to become somewhat outdated. To countermand this, complete codes for almost all examples presented in the book

```

>> help computeTrans
Compute transmissibilities.

SYNOPSIS:
    T = computeTrans(G, rock)
    T = computeTrans(G, rock, 'pn', pv, ...)

PARAMETERS:
    G - Grid structure as described by grid_structure.

    rock - Rock data structure with valid field 'perm'. The permeability
    is assumed to be in measured in units of metres squared (m^2).
    Use function 'darcy' to convert from darcies to m^2, e.g.,
        perm = convertFrom(perm, milli*darcy)
    if the permeability is provided in units of millidarcies.
    :
    :

RETURNS:
    T - half-transmissibilities for each local face of each grid cell
    in the grid. The number of half-transmissibilities equals
    the number of rows in G.cells.faces.

COMMENTS:
    PLEASE NOTE: Face normals are assumed to have length equal to
    the corresponding face areas. . .

SEE ALSO:
    computeGeometry, computeMimeticIP, darcy, permTensor.
    
```

Fig. 2.3. Most functions in MRST are documented in a standard format that gives a one-line summary of what the function does, specifies the synopsis (e.g., how the function should be called), explains the input and out parameters, and points to related functions.

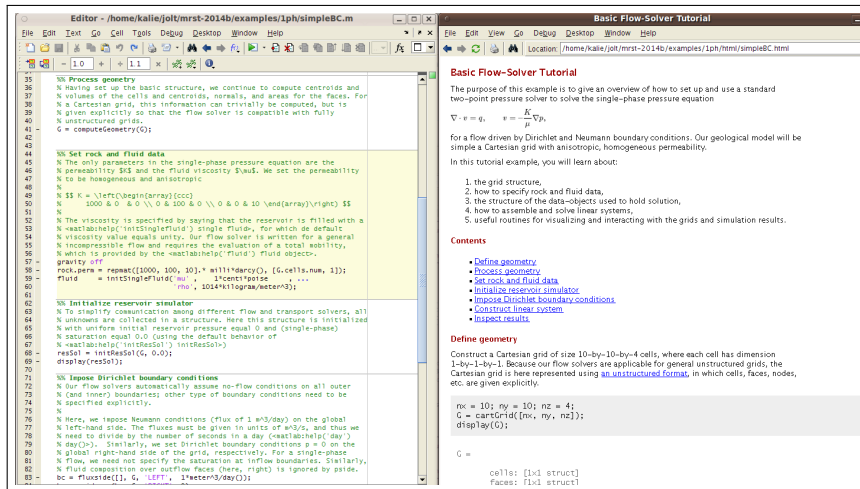


Fig. 2.4. Illustration of the MATLAB workbook concept. The editor window shows part of the source code for the simpleBC tutorial. Notice how cells are separated by horizontal lines and how each cell has a header and a text that describes what the cell does. The exception is the first cell, which summarizes the content of the whole tutorial. The right window shows the result of publishing the workbook as a webpage.

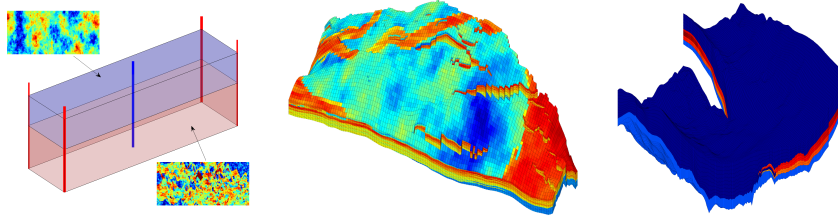


Fig. 2.5. Volumetric grids for three standard data sets used in the book: SPE10, SAIGUP, and Johansen.

are contained in a separate `book` module that accompanies MRST 2015a and later releases.

These examples either use MRST to create their input data or rely on public data sets that can be downloaded freely from the internet – examples of such data sets are shown in Figure 2.5. Herein, we use the convention that such data sets are stored in sub-directories of a standard path, which you can retrieve by issuing the following query

```
mrstDataDirectory()
```

We recommend that you adhere to this convention when using the software as a supplement to the book. If you insist on placing standard data sets elsewhere, we suggest that you use `mrstDataDirectory()` to reset the default data path. To simplify the process dataset management, MRST offers a graphical user interface, `mrstDatasetGUI`, that lists all public data sets known MRST, gives a short description of each, and provides functionality for downloading and unpacking them to the correct sub-directory of the standard path. For some data sets, you may have to register your email address or fill in a license form, and in this case we provide a link to the correct webpage. In addition standard datasets, the book contains a few examples, particularly in Chapter 4, that are based on data that cannot be publicly disclosed. For these examples, we only discuss the salient points and do not supply full details of the corresponding source codes.

At this point, we should also add a word of caution about exact reproducibility of the examples. Whereas the grid-factory routines in MRST are mostly deterministic and should enable you to create the exact same grids that are discussed in the book, the routines for generating petrophysical data rely on random numbers and will not give the same results in repeated runs. Hence, you can only expect to reproduce plots and numbers that are qualitatively similar whenever these are used.

COMPUTER EXERCISES:

1. Download and install the software
2. Run the `gravityColumn` tutorial from the command line to verify that your installation is working

3. Load the `gravityColumn` tutorial in the editor (`edit gravityColumn.m`) and run it in cell model (evaluating one cell at the time). Use `help` or `doc` to inspect the documentation for the various functions that are used in the script.
4. Run the `gravityColumn` tutorial line-by-line: Set a breakpoint on the first executable line by clicking on the small symbol next to line 27, push the 'play button', and then use the 'step' button to advance a single line at the time. Change the grid size to $10 \times 10 \times 25$ and .
5. Examine the `simpleBC` tutorial in the same way as you did for `gravityColumn`. Publish the workbook to reproduce the contents of Figure 2.4.
6. Replace the constant permeability in the `simpleBC` tutorial by a random permeability field

```
rock.perm = logNormLayers(G.cartDims,[100 10 100])*milli*darcy;
```

Can you explain the changes in the pressure field?

2.5 More advanced solvers and workflow tools

Most of the material presented in the book relies on functionality that is either found in the core module of MRST or in the `incomp` module that implements flow and transport solvers for incompressible fluid models based on standard two-point discretizations. Notable exceptions are Chapters 5 and 8, which discuss grid coarsening and consistent discretizations, respectively, and are based on functionality that can be found in other the add-on modules. These modules contain routines and functionality that extend, complement, and override existing MRST features, typically in the form of specialized or more advanced solvers and workflow tools like upscaling, grid coarsening, etc. In addition, there are modules that contain support for special input formats, Octave support, C-acceleration of selected routines from the core module, etc. Some of these modules are robust, well-documented, and contain features that will likely not change in future releases. As such, they could have been included in the core module if we had not decided to keep it as small as possible. Examples of such modules are:

- consistent discretizations on general polyhedral grids (mimetic and MPFA-0 methods) as discussed in [112] and Chapter 8;
- a small module for downloading and setting up flow models based on the SPE10 data set [49], which are commonly used benchmarks encountered in a multitude of papers;
- upscaling, including methods for flow-based single-phase upscaling as well as steady-state methods for two-phase upscaling, see e.g., [82];

- extended data structures for representing coarse grids as well as routines for partitioning grids with an underlying Cartesian topology, as discussed in Chapter 5;
- agglomeration-based grid coarsening [79, 78, 117]: methods for defining coarse grids that adapt to geological features, flow patterns, etc;
- multiscale mixed finite-element methods for incompressible flow on stratigraphic and unstructured grids [46, 1, 2, 3, 5, 101, 141, 13, 117, 152];
- multiscale finite-volume methods for incompressible flow [92], which extends the original operator formulation [122] from Cartesian grids to stratigraphic and unstructured grids that are not too complex [130, 133];
- a simplified reader that can take data describing the input parameters for a simulation given in the industry-standard ECLIPSE format, convert physical quantities to SI units, and construct MRST objects for grids, fluids, rock properties, and wells;
- C-acceleration of grid processing and basic solvers for incompressible flow;
- GUI-based tools for interactive visualization of geological models and simulation results.

Other modules and workflow tools, on the other hand, are constantly changing to support ongoing research:

- fully-implicit solvers based on automatic differentiation [104]: rapid prototyping of flow models of industry-standard complexity;
- flow diagnostics [137, 162]: simple, controlled numerical experiments that are run to probe a reservoir model and establish connections and basic volume estimates to compare, rank, and cluster models, or used as simplified flow proxies
- a numerical CO₂ laboratory [171] that offers a chain of simulation tools of increasing complexity [147, 118, 16, 119, 17]: geometrical methods for identifying structural traps [148], percolation type methods for identifying potential spill paths, and vertical-equilibrium methods that can efficiently simulate structural, residual, and solubility trapping in a thousand-year perspective [15, 145, 146];
- adjoint equations for computing gradients and sensitivities that can e.g., be used for optimization of well rates, well placement, etc

All these modules are distributed as part of the standard MRST release and have some kind of documentation on the webpage. To find out which modules that are part of your current installation, you use the function

```
mrstPath
```

which will list all modules that MRST is aware of and can load. This function can be used to search for specific modules, register new ones, etc. To *load* a particular module, you use the function `mrstModule`. As an example, calling

```
mrstModule add mimetic mpfa
```

will load the two modules that contain the consistent discretization methods discussed in Chapter 8. The software also provides a graphical interface, `moduleGUI`, for those who prefer to load and unload modules using check-boxes.

In addition to the modules that are part of the official MRST releases, there are several third-party modules that are available courtesy of their developers, as well as in-house prototype modules and workflow examples that are available upon request:

- two-point and multipoint solvers for discrete fracture-matrix systems [167, 179], including multiscale methods, developed by researchers at the University of Bergen;
- an ensemble Kalman filter module developed by researchers at TNO [109, 108] that contains EnKF and EnRML schemes, localization, inflation, asynchronous data, production and seismic data, updating of conventional and structural parameters;
- multiscale finite-volume methods for simulation of 'full physics' on stratigraphic and unstructured grids [132, 131, 134, 135, 136];
- polymer flooding based on a Todd–Longstaff model with adsorption and dead pore space, permeability reduction, shear thinning, near-well (radial) and standard grids;
- geochemistry with conventional and structural parameters and without chemical equilibrium and coupling with fluid flow;
- geomechanics discretized by virtual element methods and multipoint finite-volume discretizations;

Discussing all these modules in detail is beyond the scope of the book.

As should be evident from the overview of current modules, MRST does not have strict requirements on what becomes a module and what does not. The concept of semi-independent modules is simply a way to organize the software development that promotes software reuse. If you start to make what should eventually become a module, you will probably be a bit more careful to distinguish parts of your development that have generic value from parts that are case specific or of temporary value only. Moreover, the fact that others or your future self may want to reuse your functionality will hopefully also motivate you to put in the extra effort on documenting your routines and making examples and tutorials that later decided whether somebody wants to use or continue to develop the functionality you have implemented or not.

COMPUTER EXERCISES:

7. Try to run the following tutorials and examples from various modules
 - `simpleBCmimetic` from the `mimetic` module.
 - `simpleUpscaleExample` from the `upscaling` module
 - `gravityColumnMS` from the `msmfem` module
 - `example2` from the `diagnostics` module
 - `firstTrappingExample` from the `co2lab` module (notice that this example does not work unless you have `MATLAB–BGL` installed).

2.6 Rapid prototyping using MATLAB and MRST

How can you reduce the time span from the moment you get a new idea to when you have demonstrated that it works well for realistic reservoir engineering problems?

In our experience, prototyping and validating new numerical methods is painstakingly slow. There are many reasons for this. First of all, there is often a strong disconnect between the mathematical abstractions and equations used to express models and numerical algorithms and the syntax of the computer language you use to implement your algorithms. This is particularly true for compiled languages, where you typically end up spending most of your time writing and tweaking loops that perform operations on individual members of arrays or matrices. Object-oriented languages like C++ offer powerful functionality that can be used to make abstractions that are both flexible and computationally efficient and enable you to design your algorithms using high-level mathematical constructs. However, these advanced features are usually alien and unintuitive to those who do not have extensive training in computer sciences. If you are familiar with such concepts and are in the possession of a flexible framework, you still face the never-ending frustration caused by different versions of compilers and (third-party) libraries that seems to be an integral part of working with compiled languages.

Based on the experience of a large number of researchers and students over the past twenty years, we claim that using a numerical computing environment based on a scripting language like MATLAB (or Python) to prototype, test, and verify new models and computational algorithms is significantly more efficient than using a compiled language like Fortran, C, and C++. Not only is the syntax intuitive and simple, but there are many mechanisms that help to boost your productivity and you avoid some of the frustrations that come with compiled languages: there is no complicated build process or handling of external libraries and your implementation is inherently cross-platform compatible.

MATLAB, for instance, provides mathematical abstractions for vectors and matrices and built-in functions for numerical computations, data analysis, and visualization that enable you to quickly write codes that are not only compact and readable, but also efficient and robust. On top of this, MRST provides additional functionality that has been developed especially for computational modeling of flow in porous media:

- an unstructured grid format that enables you to implement algorithms without knowing the specifics of the grid;
- discrete operators, mappings, and forms that are not tied to specific flow equations, and hence can be precomputed independently and used to write discretized flow equations in a very compact form that is close to the mathematical formulations of the same;
- automatic differentiation which enables you to compute the values of gradients, Jacobians, and sensitivities of any programmed function without

having to compute the necessary partial derivatives analytically; this can, in particular, be used to automate the formulation of fully implicit discretizations of time-dependent and coupled systems of equations

- data structures that provide unified access and enable you to hide specific details of constitutive laws, fluid and rock properties, boundary conditions, wells, etc;

This functionality will be gradually introduced and described in detail throughout the book.

An equally important aspect of using a numerical environment like MATLAB is that you can develop your program differently than what you would do in a compiled language. Using the interactive environment, you can interactively analyse, change and extend data objects, try out each operation, include new functionality, and build your program as you go. This feature is essential in a debugging process, when one tries to understand why a given numerical method fails to produce the results one expects it to give. In fact, you can easily continue to change and extend your program during a test run: the debugger enables you to run the code line by line and inspect and change variables at any point. You can also easily step back and rerun parts of the code with changed parameters that may possibly change the program flow. Since MATLAB uses dynamic type-checking you can also add new behavior and data members while executing a program. However, how to do this in practice is difficult to teach in a textbook. Instead, you should run and modify the various examples that come with MRST and the book. We also recommend that you try to solve the computer exercises that are suggested at the end of several of the chapters and sections in the book.

Unfortunately, all this flexibility and productivity comes at a price: it is very easy to develop programs that are not very efficient. In the book, we therefore try to teach programming concepts that can be used to ensure flexibility and high efficiency of your programs. These include, in particular, powerful mechanisms for traversing data structures like vectorization, indirection maps, and logical indexes, as well as use of advanced MATLAB functions like `accumarray`, `bsxfun`, etc. Although these will be presented in the context of reservoir simulation, we think the techniques should be of interest for readers working with lower-order finite-volume discretizations on general polyhedral grids. As an illustration of the type of MATLAB programming that will be used, let us consider a simple example. The following code generates one million random points in 3D and counts the number of points that lie inside each of the eight octants:

```
n = 1000000;
pt = randn(n,3);
I = sum(bsxfun(@times, pt>0, [1 2 4]),2)+1;
num = accumarray(I,1);
```

The third line computes the sign of the x , y , and z coordinates and maps each of the resulting one million triples of logical values to an integer number between 1 and 8 that represents each of the octants. To count the number of points inside each octant, we use the function `accumarray` that groups elements from a data set and applies a function to each group. The default function is summation, and by setting a unit value in each element, we count the entries.

Next, let us compute the mean point inside each octant. A simple loop-based solution could be something like:

```
avg = zeros(8,3);
for i=1:1000000
    quad = sum((pt(i,:)>0).*[1 2 4])+1;
    avg(quad,:) = avg(quad:)+pt(i,:);
end
avg = bsxfun(@rdivide, avg, num);
```

Use of loops should generally be avoided since they tend to be slow in MATLAB. On the author's computer, it took 0.09 seconds to count the number of points within each octant, but 2.6 seconds to compute the mean points. So let us try to do something more clever and utilize vectorization. The `accumarray` function cannot be used since it only works for scalar values. Instead, we can build a sparse matrix that we multiply with the `pt` array to sum the coordinates of the points. The matrix will have one row per octant and one column per point. Now, all we have to do is to use our indicator `I` to assign a unit value in the correct row for each column use `bsxfun` to divide the sum of the coordinates with the number of points inside each octant:

```
avg = bsxfun(@rdivide, sparse(I,1:n,1)*pt, num);
```

On the author's computer this operation took 0.05 seconds, which is fifty times faster than the loop-based solution. In fact, summing all coordinates inside each octant is faster than counting the number of points. Let us try to utilize this to speed up the computation of mean points. This is quite simple: we expand each coordinate to a quadruple $(x, y, z, 1)$, multiply by the same sparse matrix, and use `bsxfun` to divide the first three columns by the fourth column to compute the average:

```
avg = sparse(I,1:n,1)*[pt, ones(n,1)];
avg = bsxfun(@rdivide, avg(:,1:end-1), avg(:,end));
```

The overall operation ran in 0.07 seconds, which not only is two times faster than our previous solution, but perhaps also a bit more elegant.

Hopefully, this simple example has inspired you to learn a bit more about efficient programming tricks if you do not already speak MATLAB fluently. MRST is generally full of tricks like this, and in the book we will occasionally show a few of them. However, if you really want to learn the tricks of the trade, the best way is to dig deep into the actual codes.

2.7 Automatic differentiation in MRST

Automatic differentiation is a technique that exploits the fact that any computer code, regardless of complexity, can be broken down to a limited set of arithmetic operations (+, −, *, /, etc), and, in our case, more or less elementary MATLAB functions (`exp`, `sin`, `power`, `interp`, etc). In automatic differentiation (AD) the key idea is to keep track of quantities and their derivatives simultaneously; every time an operation is applied to a quantity, the corresponding differential operation is applied to its derivative. Consider a scalar primary variable x and a function $f = f(x)$. Their AD-representations would then be the pairs $\langle x, 1 \rangle$ and $\langle f, f_x \rangle$, where 1 is the derivative dx/dx and f_x is the numerical value of the derivative df/dx . Accordingly, the action of the elementary operations and functions must be defined for such pairs, e.g.,

$$\begin{aligned}\langle f, f_x \rangle + \langle g, g_x \rangle &= \langle f + g, f_x + g_x \rangle, \\ \langle f, f_x \rangle * \langle g, g_x \rangle &= \langle fg, fg_x + f_xg \rangle, \\ \langle f, f_x \rangle / \langle g, g_x \rangle &= \left\langle \frac{f}{g}, \frac{f_xg - fg_x}{g^2} \right\rangle \\ \exp(\langle f, f_x \rangle) &= \langle \exp(f), \exp(f)f_x \rangle, \\ \sin(\langle f, f_x \rangle) &= \langle \sin(f), \cos(f)f_x \rangle.\end{aligned}$$

In addition to this, one needs to use the chain rule to accumulate derivatives; that is, if $f(x) = g(h(x))$, then $f_x(x) = \frac{dg}{dh}h_x(x)$. This more or less summarizes the key idea behind automatic differentiation, the remaining and difficult part is how to implement the idea as efficient computer code that has a low user-threshold and minimal computational overhead.

As the above example illustrates, it is straightforward to write down all elementary rules needed to differentiate a program or piece of code. To be useful, however, these rules should not be implemented as standard functions, so that you need to write something like `myPlus(a, myTimes(b,c))` when you want to evaluate $a + bc$. An elegant solution is to instead use classes and operator overloading. When MATLAB encounters an expression `a+b`, the software will choose one out of several different addition functions depending on the data types of `a` and `b`. All we now have to do is introduce new addition functions for the various classes of data types that `a` and `b` may belong to. Neidinger [143] gives a nice introduction to how to implement this in MATLAB. .

There are many automatic differentiation libraries for MATLAB, e.g., ADi-Mat [173, 29], ADMAT [38, 181], MAD [176, 169, 71], or from MATLAB Central [70, 128]. The AD class in MRST uses operator overloading as suggested in [143] and uses a relatively simple forward accumulation, but differs from other libraries in a subtle, but important way. Instead of working with a single Jacobian of the full discrete system as one matrix, MRST uses a list of matrices that represent the derivatives with respect to different variables that will constitute sub-blocks in the Jacobian of the full system. The reason for

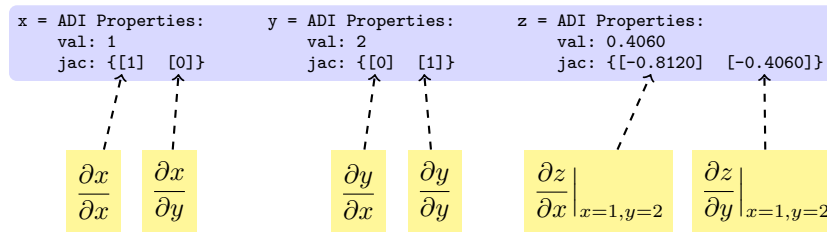
this choice is two-fold: computational performance and user utility. In typical simulation, and particularly for complex model, the mathematical model will consist of several equations (continuum equations, Darcy’s law, equations of state, other constitutive relationships, control equations for wells, etc) that have different characteristics and play different roles in the overall equation system. In typical cases, we will use fully-implicit discretizations in which one seeks to solve for all state variables simultaneously, but we may still want to manipulate parts of the full equation system that represents specific sub-equations. This is not practical if the Jacobian of the system is represented as a single matrix; manipulating subsets of large sparse matrices is currently not very efficient in MATLAB, and keeping track of the necessary index sets may also be quite cumbersome from a user’s point-of-view. Accordingly, our current choice is to let the MRST AD-class represent the derivatives of different primary variable as a list of matrices.

In the rest of the section, we will go through two simple examples that demonstrate how the AD class works. Later in the book we demonstrate how automatic differentiation can be used to set up simulations in a (surprisingly) few number of code lines.

Example 2.1. As a first example, let us say we want to compute the expression $z = 3e^{-xy}$ and its partial derivatives $\partial z/\partial x$ and $\partial z/\partial y$ for the values $x = 1$ and $y = 2$. This is done with the following two lines:

```
[x,y] = initVariablesADI(1,2);
z = 3*exp(-x*y)
```

The first line tells MRST that x and y are independent variables and initializes their values. The second line is what you normally would write in MATLAB to evaluate the given expression. After the second line has been executed, you have three AD variables (pairs of values and derivatives):



If we now go on computing with these variables, each new computation will lead to a result that contains the value of the computation as well as the derivatives with respect to x and y .

Let us look a bit in detail on what happens behind the curtain. We start by observing that the operation $3*\exp(-x*y)$ in reality consists of a sequence of elementary operations: $-$, $*$, \exp , and $*$, executed in that order. In MATLAB, this corresponds to the following sequence of call to elementary functions

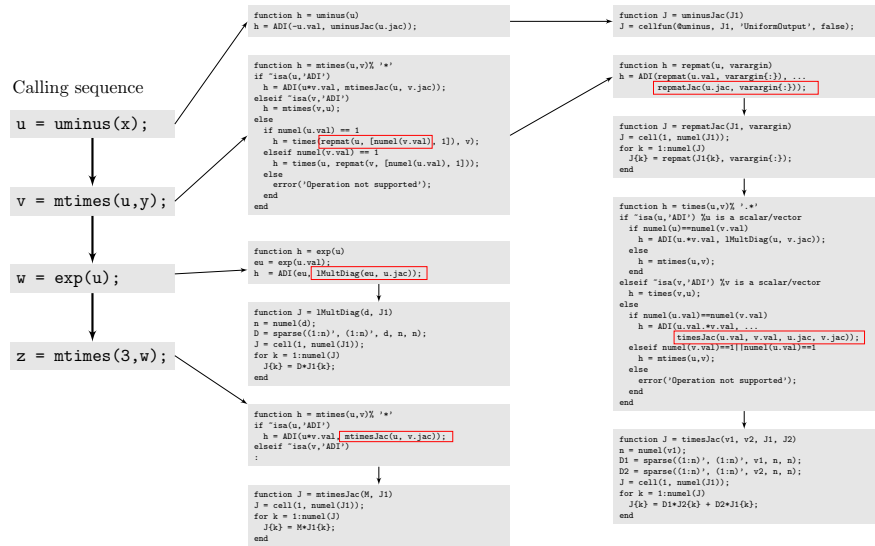


Fig. 2.6. Complete set of functions invoked to evaluate $3 \cdot \exp(-x \cdot y)$ when x and y are AD variables. For brevity, we have not included details of the constructor function `ADI(val,Jac)`, which constructs an AD pair with the value `val` and list of Jacobi matrices `Jac`.

```

u = uminus(x);
v = mtimes(u,y);
w = exp(u);
z = mtimes(3,w);
    
```

To see this, you can enter the command into a file, set a breakpoint in front of the assignment to `z`, and use the 'Step in' button to step through all details. The AD class overloads these three functions by new functions that have the same names, but operate on an AD pair for `uminus` and `exp`, and on two AD pairs or a combination of a double and an AD pair for `mtimes`. Figure 2.6 gives an overview of the sequence of calls that are invoked within the AD implementation to evaluate $3 \cdot \exp(-x \cdot y)$ when x and y are AD variables⁵.

As you can see from the above example, use of automatic differentiation will give rise to a whole new set of function calls that are not executed if one only wants to evaluate a mathematical expression and not find its derivatives. Apart from the cost of the extra code lines one has to execute, user-defined classes are fairly new in MATLAB and there is still some overhead in using

⁵ The observant reader may notice that some computational saving could have been obtained if we had been careful to replace the call to matrix multiply (`*=mtimes`) by a call to vector multiply (`+.*=times`), which are mathematically equivalent for scalar quantities.

class objects and accessing their properties (e.g., `val` and `jac`) compared to the built-in `struct`-class. The reason why AD still pays off in most examples, is that the cost of generating derivatives is typically much smaller than the cost of the solution algorithms they will be used in, in particular when working with equations systems consisting of large sparse matrices with more than one row per cell in the computational grid. However, one should still seek to limit the number of calls involving AD-class functions (including the constructor). We let the following example be a reminder that vectorization is of particular importance when using AD classes in MRST:

Example 2.2. To investigate the efficiency of vectorization versus serial execution of the AD objects in MRST, we consider the inner product of two vectors

```
z = x.*y;
```

We will compare the cost of computing z , $\partial z/\partial x$, and $\partial z/\partial y$ using four different approaches:

1. analytical expressions $z_x = y$ and $z_y = x$ and standard MATLAB vectors of doubles,
2. the overloaded vector multiply (`.*`) with AD-vectors for x and y
3. a loop over all vector elements with matrix multiply (`*=mtimes`) and x and y represented as scalar AD variables
4. same as 3, but with vector multiply (`.*=times`)

This is implemented as follows:

```
[n,t1,t2,t3,t4] = deal(zeros(m,1));
for i = 1:m
    n(i) = 2^(i-1);
    xv = rand(n(i),1); yv=rand(n(i),1);
    [x,y] = initVariablesADI(xv,yv);
    tic, z = xv.*yv; zx=yv; zy = xv;          t1(i)=toc;
    tic, z = x.*y;                            t2(i)=toc;
    tic, for k =1:n(i), z(k)=x(k)*y(k); end;  t3(i)=toc;
    tic, for k =1:n(i), z(k)=x(k).*y(k); end; t4(i)=toc;
end
```

Figure 2.7 shows a plot of the corresponding runtimes as function of the number elements in the vector. For this simple function, using AD is a factor 20-40 times more expensive than using direct evaluation of z and the analytical expressions for z_x and z_y . Using a loop will on average be more than three orders more expensive than using vectorization. Since the inner iterations multiplies scalars, many programmers would implement it using matrix multiply `*` without a second thought. Replacing `*` by vector multiply `.*` reduces the cost by 30% on average, but the factor diminishes as the number of elements increases in the vector.

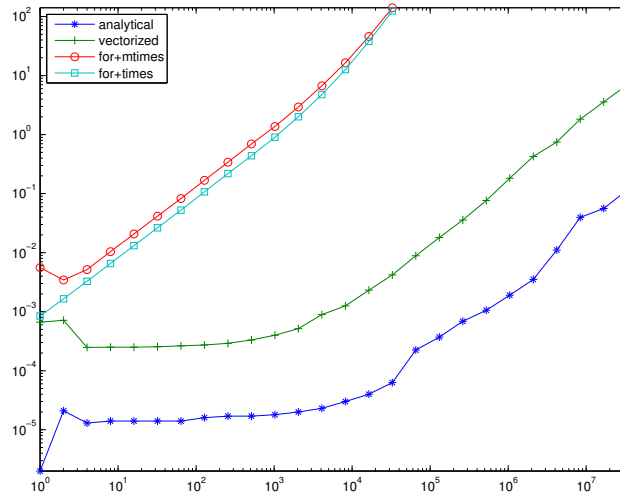


Fig. 2.7. Comparison of the time required for computing $z=x.*y$ and derivatives as function of the number of elements in the vectors x and y .

While `for`-loops in many cases will be quite efficient in MATLAB (contrary to common belief), one should always try to avoid loops that call functions with non-negligible overhead. The AD class in MRST has been designed to work on long vectors and lists of (sparse) Jacobian matrices and has not been optimized for scalar variables. As a result, there is considerable overhead when working with small AD objects.

Beyond the examples and the discussion above, we will not go more into details about the technical considerations that lie behind the implementation of AD in MRST. If you want a deeper understanding of how the AD class works, the source code is fully open, so you are free to dissect the details to the level of your own choice.

COMPUTER EXERCISES:

8. As an alternative to using automatic differentiation, one can use finite differences, $f'(x) \approx [f(x+h) - f(x)]/h$, or a complex extension to compute $f'(x) \approx \text{Im}(f(x+ih))/h$. Use automatic differentiation and the function


```
f = @(x) exp((x-.05).*(x-.4).*(x-.5).*(x-.7).*(x-.95));
```

 to assess how accurate the two methods approximate $f'(x)$ at n equidistant points in the interval $x \in [0, 1]$ for different values of h .
9. While the AD class supports `log` and `exp`, it does not yet support `log2`, `log10`, and `logm`. Study `ADI.m` and see if you can implement the missing functions. What about trigonometric functions?
10. Can automatic differentiation be used to compute higher-order derivatives? How or why not?

Geological Models and Grids

Modelling Reservoir Rocks

Aquifers and natural petroleum reservoirs consist of a subsurface body of sedimentary rock having sufficient porosity and permeability to store and transmit fluids. In this chapter, we will give an overview of how such rocks are modelled to become part of a simulation model. We start by describing briefly how sedimentary rocks and hydrocarbons are formed. In doing so, we introduce some geological concepts that you may encounter while working with subsurface modelling. We then move on to describe how rocks that contain hydrocarbons or aquifer systems are modelled. Finally, we discuss how rock properties are represented in MRST and show several examples of rock models with varying complexity, ranging from an idealized shoe-box rock body with homogeneous properties, via the widely used SPE 10 model, to two realistic models, one synthetic and one representing a large-scale aquifer from the North Sea.

3.1 Formation of sedimentary rocks

Sedimentary rocks are created by mineral or organic particles that are deposited and accumulated on the Earth's surface or within bodies of water to create layer upon layer of sediments. The sedimentary rocks that are found in reservoirs come from sedimentary basins, inside which large-scale sedimentation processes have taken place. Sedimentary basins are formed as the result of stretching and breaking of the continental crust. As the crust is stretched, hot rocks deeper in the earth come closer to the surface. When the stretching stops, the hot rocks start to cool, which causes the crustal rock to gradually subside and move downward to create a basin. Such processes are also taking place today. The Great Rift Valley of Africa is a good example of a so-called rift basin, where a rift splits the continental plate so that opposite sides of the valley are moving a millimeter apart each year. This gradually creates a basin inside which a new ocean may appear over the next hundred million years.

3.3 Multiscale modelling of permeable rocks

All sedimentary rocks consist of a solid matrix with an interconnected void. The void pore space allows the rocks to store and transmit fluids. The ability to store fluids is determined by the volume fraction of pores (the rock porosity), and the ability to transmit fluids (the rock permeability) is given by the interconnection of the pores.

Rock formations found in natural petroleum reservoirs are typically heterogeneous at all length scales, from the micrometer scale of pore channels between the solid particles making up the rock to the kilometer scale of a full reservoir formation. On the scale of individual grains, there can be large variation in grain sizes, giving a broad distribution of void volumes and interconnections. Moving up a scale, laminae may exhibit large contrasts on the mm-cm scale in the ability to store and transmit fluids because of alternating layers of coarse and fine-grained material. Laminae are stacked to form beds, which are the smallest stratigraphic units. The thickness of beds varies from millimeters to tens of meters, and different beds are separated by thin layers with significantly lower permeability. Beds are, in turn, grouped and stacked into parasequences or sequences (parallel layers that have undergone similar geologic history). Parasequences represent the deposition of marine sediments, during periods of high sea level, and tend to be somewhere in the range from 1–100 meters thick and have a horizontal extent of several kilometers.

The trends and heterogeneity of parasequences depend on the depositional environment. For instance, whereas shallow-marine deposits may lead to rather smoothly varying permeability distributions with correlation lengths in the order 10–100 meters, fluvial reservoirs may contain intertwined patterns of sand bodies on a background with high clay content, see Figure 3.12. The reservoir geology can also consist of other structures like for instance shale layers (impermeable clays), which are the most abundant sedimentary rocks. Fractures and faults, on the other hand, are created by stresses in the rock and may extend from a few centimeters to tens or hundreds of meters. Faults may have a significantly higher or lower ability to transmit fluids than the surrounding rocks, depending upon whether the void space has been filled with clay material.

All these different length scales can have a profound impact on fluid flow. However, it is generally not possible to account for all pertinent scales that impact the flow in a single model. Instead, one has to create a hierarchy of models for studying phenomena occurring at reduced spans of scales. This is illustrated in Figure 3.7. Microscopic models represent the void spaces between individual grains and are used to provide porosity, permeability, electrical and elastic properties of rocks from core samples and drill cuttings. Mesoscopic models are used to upscale these basic rock properties from the mm/cm-scale of internal laminations, through the lithofacies scale (~ 50 cm), to the macroscopic facies association scale (~ 100 m) of geological models. In this book, we will primarily focus on another scale, simulation models, which represent

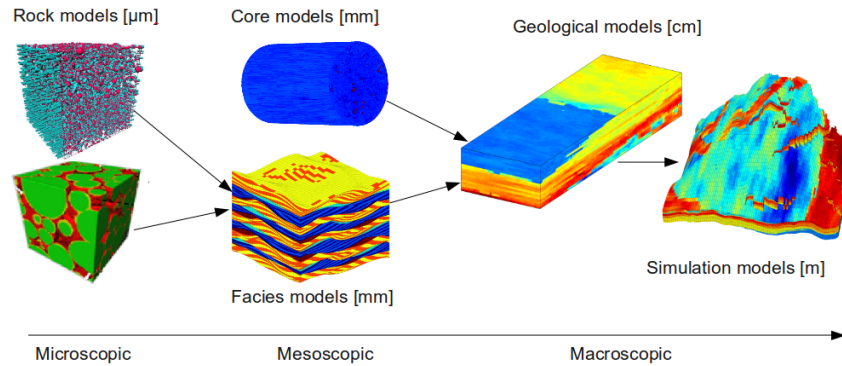


Fig. 3.7. Illustration of the hierarchy of flow models used in subsurface modeling. The length scales are the vertical sizes of typical elements in the models.

the last scale in the model hierarchy. Simulation models are obtained by up-scaling geological models and are either introduced out of necessity because geological models contain more details than a flow simulator can cope with, or out of convenience to provide faster calculation of flow responses.

3.3.1 Macroscopic models

To model a reservoir on a macroscopic scale, we basically need to represent its geology at a level of detail that is sufficient for the purpose the model is built to serve: to visualize how different experts perceive the reservoir, to provide estimates of hydrocarbon volumes, to assist well planning and geosteering, or as input to geophysical analysis (seismic modeling, rock mechanics) or flow simulations. For flow simulation, which is our primary concern in this book, we need a volumetric description that decomposes the reservoir into a set of grid cells (small 3D polygonal volumes) that are petrophysically and/or geometrically distinct from each other. With a slight abuse of terminology, we will in the following refer to this as the *geological model*, which we will distinguish from the models that describe the reservoir fluids and the forces that cause their movement.

Geological models are generally built in a sequence of steps, using a combination of stratigraphy (the study of rock layers and layering), sedimentology (study of sedimentary rocks), structural geology (the study of how rock layers are deformed over time by geological activity), diagenesis (the study of chemical, physical, and biological processes that transform sediments to rock), and interpretation of measured data. The starting point is usually a seismic interpretation, from which one obtains a representation of faults and geological horizons that bound different geological units. The seismic interpretation is used alongside a conceptual model in which geologists express how they believe the reservoir looks like based on studies of geological history

and geological outcrops. The result can be expressed as a geometric model that consists of vertical or inclined surfaces representing faults and horizontal or slightly sloping surfaces representing horizons that subdivide the reservoir volume into different geological units (zones). This zonation is obtained by combining seismic interpretation that describes the gross geometry of the reservoir with stratigraphic modelling and thickness information (isochores) obtain from well logs that defines the internal layering. Once a model of the structural and stratigraphic architecture of the reservoir is established, the surface description can be turned into a 3D grid that is populated with cell and face properties that reflect the geological framework.

Unfortunately, building a geological model for a reservoir is like finishing a puzzle where most of the pieces are missing. The amount of data available is limited due to the costs of acquiring them, and the data that is obtained is measured on scales that may be quite disparate from the geological features one needs to model. Seismic surveys give a sort of X-ray image of the reservoir, but are both expensive and time consuming and can only give limited resolution; you cannot expect to see structures thinner than ten meters from seismic data. Information on finer scales is available from various measuring tools lowered into the wells to gather information of the rock in near-well region, e.g., by radiating the reservoir and measuring the response. Well-logs have quite limited resolution, rarely down to centimeter scale. The most detailed information is available from rock samples (cores) extracted from the well. The industry uses X-ray, CT-scan, as well as electron microscopes to gather high resolution information from the cores, and the data resolution is only limited by the apparatus at hand. However, information from cores and well-logs can only tell you how the rock looks like near the well, and extrapolating this information to the rest of the reservoir is subject to great uncertainty. Moreover, due to high costs, one cannot expect well-logs and cores to be taken from every well. All these techniques give separately small contributions that can help build a geological model. However, in the end we still have very limited information available considering that a petroleum reservoir can have complex geological features that span across all types of length scales from a few millimeters to several kilometers.

In summary, the process of making a geological model is generally strongly under-determined. It is therefore customary to use a combination of deterministic and probabilistic modeling to estimate the subsurface characteristics between the wells. Deterministic modeling is used to specify large-scale structures such as faults, correlation, trends, and layering, which are used as input and controls to geostatistical techniques that build detailed grid models satisfying statistical properties assumed for the petrophysical heterogeneity. Since trends and heterogeneity in petrophysical properties depend strongly on the structure of sedimentary deposits, high-resolution petrophysical realizations are in many cases not built directly. Instead, one starts by building a *rock model* that is based on the structural model and consists of a set of discrete rock bodies (facies) that are specified to improve petrophysical classification

and spatial shape. For carbonates, the modelled facies are highly related to diagenesis, while the facies modelled for sandstone reservoirs are typically derived from the depositional facies. By supplying knowledge of the depositional environment (fluvial, shallow marine, deep marine, etc.) and conditioning to observed data, one can determine the geometry of the facies and how they are mixed.

To populate the modelled facies with properties it is common to use stochastic simulation techniques that simulate multiple realizations of the petrophysical properties represented as cell and face properties in high-resolution grid models. Each grid model has a plausible heterogeneity and can contain from a hundred thousand to a hundred million cells. The collection of all realizations gives a measure of the uncertainty involved in the modelling. Hence, if the sample of realizations (and the upscaling procedure that converts the geological models into simulation models) is unbiased, then it is possible to supply predicted production characteristics, such as the cumulative oil production, obtained from simulation studies with a measure of uncertainty.

This cursory overview of different models is all that is needed for what follows in the next few chapters, and the reader can therefore skip to Section 3.4 which discusses macroscopic modelling of reservoir rocks. The remains of this section will discuss microscopic and mesoscopic modelling in some more detail. First, however, we will briefly discuss the concept of representative elementary volumes, which underlies the continuum models used to describe subsurface flow and transport.

3.3.2 Representative elementary volumes

Choosing appropriate modelling scales is often done by intuition and experience, and it is hard to give very general guidelines. An important concept in choosing model scales is the notion of representative elementary volumes (REVs), which is the smallest volume over which a measurement can be made and be representative of the whole. This concept is based on the idea that petrophysical flow properties are constant on some intervals of scale, see Figure 3.8. Representative elementary volumes, if they exist, mark transitions between scales of heterogeneity, and present natural length scales for modelling.

To identify a range of length scales where REVs exist, e.g., for porosity, we move along the length-scale axis from the micrometer-scale of pores toward the kilometer-scale of the reservoir. At the pore scale, the porosity is a rapidly oscillating function equal to zero (in solid rock) or one (in the pores). Hence, obviously no REVs can exist at this scale. At the next characteristic length scale, the core scale level, we find laminae deposits. Because the laminae consist of alternating layers of coarse and fine grained material, we cannot expect to find a common porosity value for the different rock structures. Moving further along the length-scale axis, we may find long thin layers, perhaps

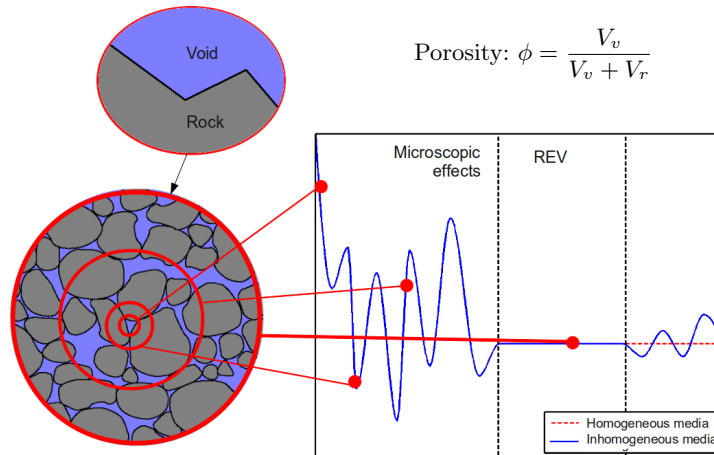


Fig. 3.8. The concept of a representative elementary volume (REV), here illustrated for porosity which measures the fraction of void space to bulk volume.

extending throughout the entire horizontal length of the reservoirs. Each of these individual layers may be nearly homogeneous because they are created by the same geological process, and probably contain approximately the same rock types. Hence, at this scale it sounds reasonable to speak of an REV. If we move to the high end of the length-scale axis, we start to group more and more layers into families with different sedimentary structures, and REVs for porosity will probably not exist.

The previous discussion gives some grounds to claim that reservoir rock structures contain scales where REVs may exist. From a general point of view, however, the existence of REVs in porous media is highly disputable. A faulted reservoir, for instance, can have faults distributed continuously both in length and aperture throughout the reservoir, and will typically have no REVs. Moreover, no two reservoirs are identical, so it is difficult to capitalize from previous experience. Indeed, porous formations in reservoirs may vary greatly, also in terms of scales. Nevertheless, the concept of REVs can serve as a guideline when deciding what scales to model.

3.3.3 Microscopic models: The pore scale

Pore-scale model, as illustrated to the left in Figure 3.7, may be about the size of a sugar cube and are based on measurements from core plugs obtained from well trajectories during drilling. These rock samples are necessarily confined (in dimension) by the radius of the well, although they lengthwise are only confined by the length of the well. Three such rock samples are shown in Figure 3.9. The main methods for obtaining pore-scale models from a rock sample is by studying thin slices using an electron microscope with micrometer



Fig. 3.9. Three core plugs with diameter of one and a half inches, and a height of five centimeters.

resolution or by CT-scans. In the following, we will give a simplified overview of flow modelling on this scale.

At the pore scale, the porous medium is either represented by a volumetric grid or by a graph (see e.g., [151]). A graph is a pair (V, E) , where V is a set whose elements are called vertices (or nodes), and E is a subset of $V \times V$ whose elements are called edges. The vertices are taken to represent pores, and the edges represent pore-throats (i.e., connections between pores).

The flow process, in which one fluid invades the void space filled by another fluid, is generally described as an invasion-percolation process. This process is mainly dominated by capillary forces, although gravitational forces can still be important. In the invasion, a fluid phase can invade a pore only if a neighboring pore is already invaded. For each pore, there is an entry pressure, i.e., the threshold pressure needed for the invading phase to enter the pore, that depends on the size and shape of pores, the size of pore throats, as well as other rock properties. The invading phase will first invade the neighboring pore that has the lowest threshold pressure. This gives a way of updating the set of pores that are neighbors to invaded ones. Repeating the process establishes a recursive algorithm to determine the flow pattern of the invading phase. In the invasion process, we are interested in whether a phase has a path through the model, i.e., percolates, or not, and the time variable is often not modelled at all. For pore networks, this is misleading because we are also interested in modelling the flow after the first path through the model has been established. After a pore has been invaded, the saturations in the pore will vary with pressures and saturations in the neighboring pores (as well as in the pore itself). New pores may also be invaded after the first path is formed, so that we may get several paths through the model through which the invading phase can flow. Once the invading phase percolates (i.e., has a path through the model), one can start estimating flow properties. As the

simulation progresses, the saturation of the invading phase will increase, which can be used to estimate flow properties at different saturation compositions in the model.

In reality, the process is more complicated than explained above because of wettability. When two immiscible fluids (such as oil and water) contact a solid surface (such as the rock), one of them tends to spread on the surface more than the other. The fluid in a porous medium that preferentially contacts the rock is called the wetting fluid. Note that wettability conditions are usually changing throughout a reservoir. The flow process where the invading fluid is non-wetting is called drainage and is typically modelled with invasion-percolation. The flow process where the wetting fluid displaces the non-wetting fluid is called imbibition, and is more complex, involving effects termed film flow and snap-off.

Another approach to multiphase modelling is through the use of the lattice Boltzmann method that represents the fluids as a set of particles that propagate and collide according to a set of rules defined for interactions between particles of the same fluid phase, between particles of different fluid phases, and between the fluids and the walls of the void space. A further presentation of pore-scale modelling is beyond the scope here, but the interested reader is encouraged to consult, e.g., [151] and references therein.

From an analytical point of view, pore-scale modelling is very important as it represents flow at the fundamental scale (or more loosely, where the flow really takes place), and hence provides the proper framework for understanding the fundamentals of porous media flow. From a practical point of view, pore-scale modelling has a huge potential. Modelling flow at all other scales can be seen as averaging of flow at the pore scale, and properties describing the flow at larger scales are usually a mixture of pore-scale properties. At larger scales, the complexity of flow modelling is often overwhelming, with large uncertainties in determining flow parameters. Hence being able to single out and estimate the various factors determining flow parameters is invaluable, and pore-scale models can be instrumental in this respect. However, to extrapolate properties from the pore scale to an entire reservoir is very challenging, even if the entire pore space of the reservoir was known (of course, in real life you will not be anywhere close to knowing the entire pore space of a reservoir).

3.3.4 Mesoscopic models

Models based on flow experiments on core plugs is by far the most common mesoscopic models. The fundamental equations describing flow are continuity of fluid phases and Darcy's law, which basically states that flow rate is proportional to pressure drop. The purpose of core-plug experiments is to determine capillary pressure curves and the proportionality constant in Darcy's law that measures the ability to transmit fluids, see (2.1) in Section 2.1. To this end, the sides of the core are insulated and flow is driven through the

core. By measuring the flow rate versus pressure drop, one can estimate the proportionality constant for both single-phase or multi-phase flows.

In conventional reservoir modelling, the effective properties from core-scale flow experiments are extrapolated to the macroscopic geological model, or directly to the simulation model. Cores should therefore ideally be representative for the heterogeneous structures that one may find in a typical grid block in the geological model. However, flow experiments are usually performed on relatively homogeneous cores that rarely exceed one meter in length. Cores can therefore seldom be classified as representative elementary volumes. For instance, cores may contain a shale barrier that blocks flow inside the core, but does not extend much outside the well-bore region, and the core was slightly wider, there would be a passage past the shale barrier. Flow at the core scale is also more influenced by capillary forces than flow on a reservoir scale.

As a supplement to core-flooding experiments, it has in recent years become popular to build 3D grid models to represent small-scale geological details like the bedding structure and lithology (composition and texture). One example of such a model is shown in Figure 3.7. Effective flow properties for the 3D model can now be estimated in the same way as for core plugs by replacing the flow experiment by flow simulations using rock properties that are e.g., based on the input from microscopic models. This way, one can incorporate fine-scale geological details from lamina into the macroscopic reservoir models.

This discussion shows that the problem of extrapolating information from cores to build a geological model is largely under-determined. Supplementary pieces of information are also needed, and the process of gathering geological data from other sources is described next.

3.4 Modelling rock properties

Describing the flow through a porous rock structure is largely a question of the scale of interest, as we saw in the previous section. The size of the rock bodies forming a typical petroleum reservoir will be from ten to hundred meters in the vertical direction and several hundred meters or a few kilometers in the lateral direction. On this modelling scale, it is clearly impossible to describe the storage and transport in individual pores and pore channels as discussed in Section 3.3.3 or the through individual lamina as in Section 3.3.4. To obtain a description of the reservoir geology, one builds models that attempt to reproduce the true geological heterogeneity in the reservoir rock at the macroscopic scale by introducing macroscopic petrophysical properties that are based on a continuum hypothesis and volume averaging over a sufficiently large representative elementary volume (REV), as discussed in Section 3.3.2. These petrophysical properties are engineering quantities that are used as input to flow simulators and are not geological or geophysical properties of the underlying media.

A geological model is a conceptual, three-dimensional representation of a reservoir, whose main purpose is therefore to provide the distribution of petrophysical parameters, besides giving location and geometry of the reservoir. The rock body itself is modelled in terms of a volumetric grid, in which the layered structure of sedimentary beds and the geometry of faults and large-scale fractures in the reservoir are represented by the geometry and topology of the grid cells. The size of a cell in a typical geological grid-model is in the range of 0.1–1 meters in the vertical direction and 10–50 meters in the horizontal direction. The petrophysical properties of the rock are represented as constant values inside each grid cell (porosity and permeability) or as values attached to cell faces (fault multipliers, fracture apertures, etc). In the following, we will describe the main rock properties in more detail. More details about the grid modelling will follow in Chapter 4.

3.4.1 Porosity

The porosity ϕ of a porous medium is defined as the fraction of the bulk volume that is occupied by void space, which means that $0 \leq \phi < 1$. Likewise, $1 - \phi$ is the fraction occupied by solid material (rock matrix). The void space generally consists of two parts, the interconnected pore space that is available to fluid flow, and disconnected pores (dead-ends) that is unavailable to flow. Only the first part is interesting for flow simulation, and it is therefore common to introduce the so-called “effective porosity” that measures the fraction of connected void space to bulk volume.

For a completely rigid medium, porosity is a static, dimensionless quantity that can be measured in the absence of flow. Porosity is mainly determined by the pore and grain-size distribution. Rocks with nonuniform grain size typically have smaller porosity than rocks with a uniform grain size, because smaller grains tend to fill pores formed by larger grains. Similarly, for a bed of solid spheres of uniform diameter, the porosity depends on the packing, varying between 0.2595 for a rhomboidal packing to 0.4764 for cubic packing. When sediments are first deposited in water, they usually have a porosity of approximately 0.5, but as they are buried, the water is gradually squeezed out and the void space between the mineral particles decreases as the sediments are consolidated into rocks. For sandstone and limestone, ϕ is in the range 0.05–0.5, although values outside this range may be observed on occasion. Sandstone porosity is usually determined by the sedimentological process by which the rock was deposited, whereas for carbonate porosity is mainly a result of changes taking place after deposition. Increase compaction (and cementation) causes porosity to decrease with depth in sedimentary rocks. The porosity can also be reduced by minerals that are deposited as water moves through the pore spaces. For sandstone, the loss in porosity is small, whereas shales lose their porosity very quickly. Shales are therefore unlikely to be good reservoir rocks, and will instead act like caprocks having porosities that

are orders of magnitude lower than those found in good sandstone and carbonates.

For non-rigid rocks, the porosity is usually modelled as a pressure-dependent parameter. That is, one says that the rock is *compressible*, having a rock compressibility defined by

$$c_r = \frac{1}{\phi} \frac{d\phi}{dp} = \frac{d \ln(\phi)}{dp}, \quad (3.1)$$

where p is the overall reservoir pressure. Compressibility can be significant in some cases, e.g., as evidenced by the subsidence observed in the Ekofisk area in the North Sea. For a rock with constant compressibility, (3.1) can be integrated to give

$$\phi(p) = \phi_0 e^{c_r(p-p_0)}, \quad (3.2)$$

and for simplified models, it is common to use a linearization so that:

$$\phi = \phi_0 [1 + c_r(p - p_0)]. \quad (3.3)$$

Because the dimension of the pores is very small compared to any interesting scale for reservoir simulation, one normally assumes that porosity is a piecewise continuous spatial function. However, ongoing research aims to understand better the relation between flow models on pore scale and on reservoir scale.

3.4.2 Permeability

The *permeability* is the basic flow property of a porous medium and measures its ability to transmit a single fluid when the void space is completely filled with this fluid. This means that permeability, unlike porosity, is a parameter that cannot be defined apart from fluid flow. The precise definition of the (absolute, specific, or intrinsic) permeability K is as the proportionality factor between the flow rate and an applied pressure or potential gradient $\nabla\Phi$,

$$\vec{u} = -\frac{K}{\mu} \nabla\Phi. \quad (3.4)$$

This relationship is called Darcy's law after the french hydrologist Henry Darcy, who first observed it in 1856 while studying flow of water through beds of sand [51]. In (3.4), μ is the fluid viscosity and \vec{u} is the superficial velocity, i.e., the flow rate divided by the cross-sectional area perpendicular to the flow. This should not be confused with the interstitial velocity $\vec{v} = \phi^{-1}\vec{u}$, i.e., the rate at which an actual fluid particle moves through the medium. We will come back to a more detailed discussion of Darcy's law in Section 6.2.

The SI-unit for permeability is m^2 , which reflects the fact that permeability is determined entirely by the geometric characteristics of the pores. However, it is more common to use the unit 'darcy' (D). The precise definition of $1\text{D} \approx 0.987 \cdot 10^{-12} \text{ m}^2$ involves transmission of a 1 cP fluid through

a homogeneous rock at a speed of 1 cm/s due to a pressure gradient of 1 atm/cm. Translated to reservoir conditions, 1 D is a relatively high permeability and it is therefore customary to specify permeabilities in millidarcys (mD). Rock formations like sandstones tend to have many large or well-connected pores and therefore transmit fluids readily. They are therefore described as permeable. Other formations, like shales, may have smaller, fewer or less interconnected pores and are hence described as impermeable. Conventional reservoirs typically have permeabilities ranging from 0.1 mD to 20 D for liquid flow and down to 10 mD for gases. In recent years, however, there has been an increasing interest in unconventional resources, that is, gas and oil locked in extraordinarily impermeable and hard rocks, with permeability values ranging from 0.1 mD and down to 1 μ D or lower. 'Tight' reservoirs are defined as those having permeability less than 0.1 mD. Compared with conventional resources, the potential volumes of tight gas, shale gas, shale oil are enormous, but cannot be easily produced at economic rates unless stimulated, e.g., using a pressurized fluid to fracture the rock (hydraulic fracturing). In this book, our main focus will be on simulation of conventional resources.

In (3.4), we tacitly assumed that the permeability K is a scalar quantity. However, the permeability will generally be a full tensor,

$$\mathbf{K} = \begin{bmatrix} K_{xx} & K_{xy} & K_{xz} \\ K_{yx} & K_{yy} & K_{yz} \\ K_{zx} & K_{zy} & K_{zz} \end{bmatrix}. \quad (3.5)$$

Here, the diagonal terms $\{K_{xx}, K_{yy}, K_{zz}\}$ represent how the flow rate in one axial direction depends on the pressure drop in the same direction. The off-diagonal terms $\{K_{xy}, K_{xz}, K_{yx}, K_{yz}, K_{zx}, K_{zy}\}$ account for dependence between flow rate in one axial direction and the pressure drop in perpendicular directions. A full tensor is needed to model local flow in directions at an angle to the coordinate axes. Let us for instance consider a layered system, for which the dominant direction of flow will generally be along the layers. However, if the layers form an angle to the coordinate axes, a pressure drop in one coordinate direction will produce flow at an angle to this direction. This type of flow can only be modelled correctly with a permeability tensor with nonzero off-diagonal terms. If the permeability can be represented by a scalar function $K(\vec{x})$, we say that the permeability is *isotropic* as opposed to the *anisotropic* case where we need a full tensor $\mathbf{K}(\vec{x})$. To model a physical system, the anisotropic permeability tensor must be symmetric because of the Onsager principle of reciprocal relations and positive definite because the flow component parallel to the pressure drop should be in the same direction as the pressure drop. As a result, a full-tensor permeability \mathbf{K} may be diagonalized by a change of basis.

Since the porous medium is formed by deposition of sediments over thousands of years, there is often a significant difference between permeability in the vertical and lateral directions, but no difference between the permeabilities in the two lateral directions. The permeability is obviously also a function of

porosity. Assuming a laminar flow (low Reynolds numbers) in a set of capillary tubes, one can derive the Carman–Kozeny relation,

$$K = \frac{1}{8\tau A_v^2} \frac{\phi^3}{(1-\phi)^2}, \quad (3.6)$$

which relates permeability to porosity ϕ , but also shows that the permeability depends on local rock texture described by tortuosity τ and specific surface area A_v . The tortuosity is defined as the squared ratio of the mean arc-chord length of flow paths, i.e., the ratio between the length of a flow path and the distance between its ends. The specific surface area is an intrinsic and characteristic property of any porous medium that measures the internal surface of the medium per unit volume. Clay minerals, for instance, have large specific surface areas and hence low permeability. The quantities τ and A_v can be calculated for simple geometries, e.g., for engineered beds of particles and fibers, but are seldom measured for reservoir rocks. Moreover, the relationship in (3.6) is highly idealized and only gives satisfactory results for media that consist of grains that are approximately spherical and have a narrow size distribution. For consolidated media and cases where rock particles are far from spherical and have a broad size-distribution, the simple Carman–Kozeny equation does not apply. Instead, permeability is typically obtained through macroscopic flow measurements.

Permeability is generally heterogeneous in space because of different sorting of particles, degree of cementation (filling of clay), and transitions between different rock formations. Indeed, the permeability may vary rapidly over several orders of magnitude, local variations in the range 1 mD to 10 D are not unusual in a typical field. The heterogeneous structure of a porous rock formation is a result of the deposition and geological history and will therefore vary strongly from one formation to another, as we will see in a few of the examples in Section 3.5.

Production of fluids may also change the permeability. When temperature and pressure is changed, microfractures may open and significantly change the permeability. Furthermore, since the definition of permeability involves a certain fluid, different fluids will experience different permeability in the same rock sample. Such rock-fluid interactions are discussed in Chapter 11.

3.4.3 Other parameters

Not all rocks in a reservoir zone are reservoir rocks. To account for the fact that some portion of a cell may consist of impermeable shale, it is common to introduce the so-called “net-to-gross” (N/G) property, which is a number in the range 0 to 1 that represents the fraction of reservoir rock in the cell. To get the effective porosity of a given cell, one must multiply the porosity and N/G value of the cell. (The N/G values also act as multipliers for lateral transmissibilities, which we will come back to later in the book). A zero value

means that the corresponding cell only contains shale (either because the porosity, the N/G value, or both are zero), and such cells are by convention typically not included in the active model. Inactive cells can alternatively be specified using a dedicated field (called 'actnum' in industry-standard input formats).

Faults can either act as conduits for fluid flow in subsurface reservoirs or create flow barriers and introduce compartmentalization that severely affects fluid distribution and/or reduces recovery. On a reservoir scale, faults are generally volumetric objects that can be described in terms of displacement and petrophysical alteration of the surrounding host rock. However, lack of geological resolution in simulation models means that fault zones are commonly modelled as surfaces that explicitly approximate the faults' geometrical properties. To model the hydraulic properties of faults, it is common to introduce so-called multipliers that alter the ability to transmit fluid between two neighboring cells. Multipliers are also used to model other types of subscale features that affect communication between grid blocks, e.g., thin mud layers resulting from flooding even which may partially cover the sand bodies and reduce vertical communication. It is also common to (ab)use multipliers to increase or decrease the flow in certain parts of the model to calibrate the simulated reservoir responses to historic data (production curves from wells, etc). More details about multipliers will be given later in the book.

3.5 Property modelling in MRST

All flow and transport solvers in MRST assume that the rock parameters are represented as fields in a structure. Our naming convention is that this structure is called `rock`, but this is not a requirement. The fields for porosity and permeability, however, must be called `poro` and `perm`, respectively. The porosity field `rock.poro` is a vector with one value for each active cell in the corresponding grid model. The permeability field `rock.perm` can either contain a single column for an isotropic permeability, two or three columns for a diagonal permeability (in two and three spatial dimensions, respectively), or six columns for a symmetric, full-tensor permeability. In the latter case, cell number i has the permeability tensor

$$\mathbf{K}_i = \begin{bmatrix} K_1(i) & K_2(i) \\ K_2(i) & K_3(i) \end{bmatrix}, \quad \mathbf{K}_i = \begin{bmatrix} K_1(i) & K_2(i) & K_3(i) \\ K_2(i) & K_4(i) & K_5(i) \\ K_3(i) & K_5(i) & K_6(i) \end{bmatrix},$$

where $K_j(i)$ is the entry in column j and row i of `rock.perm`. Full-tensor, non-symmetric permeabilities are currently not supported in MRST. In addition to porosity and permeability, MRST supports a field called `ntg` that represents the net-to-gross ratio and consists of either a scalar or a single column with one value per active cell.

In the rest of the section, we present a few examples that demonstrate how to generate and specify permeability and porosity values. In addition, we will briefly discuss a few models with industry-standard complexity. Through the discussion, you will also be exposed to a lot of the visualization capabilities of MRST. Complete scripts necessary to reproduce the results and the figures presented can be found in various scripts in the `rock` subdirectory of the software module that accompanies the book.

3.5.1 Homogeneous models

Homogeneous models are very simple to specify, as is illustrated by a simple example. We consider a square 10×10 grid model with a uniform porosity of 0.2 and isotropic permeability equal 200 mD:

```
G = cartGrid([10 10]);
rock.poro = repmat(0.2, [G.cells.num,1]);
rock.perm = repmat(200*milli*darcy, [G.cells.num,1]);
```

Because MRST works in SI units, it is important to convert from the field units 'darcy' to the SI unit 'meters²'. Here, we did this by multiplying with `milli` and `darcy`, which are two functions that return the corresponding conversion factors. Alternatively, we could have used the conversion function `convertFrom(200, milli*darcy)`. Homogeneous, anisotropic permeability can be specified in the same way:

```
rock.perm = repmat([100 100 10].*milli*darcy, [G.cells.num,1]);
```

3.5.2 Random and lognormal models

Given the difficulty of measuring rock properties, it is common to use geostatistical methods to make realizations of porosity and permeability. MRST contains two *very* simplified methods for generating geostatistical realizations. For more realistic geostatistics, the reader should use GSLIB [56] or a commercial geomodelling software.

In our first example, we will generate the porosity ϕ as a Gaussian field. To get a crude approximation to the permeability-porosity relationship, we assume that our medium is made up of uniform spherical grains of diameter $d_p = 10 \mu\text{m}$, for which the specific surface area is $A_v = 6/d_p$. Using the Carman–Kozeny relation (3.6), we can then calculate the isotropic permeability K from

$$K = \frac{1}{72\tau} \frac{\phi^3 d_p^2}{(1 - \phi)^2},$$

where we further assume that $\tau = 0.81$. As a simple approximation to a Gaussian field, we generate a field of independent normally distributed variables and convolve it with a Gaussian kernel.

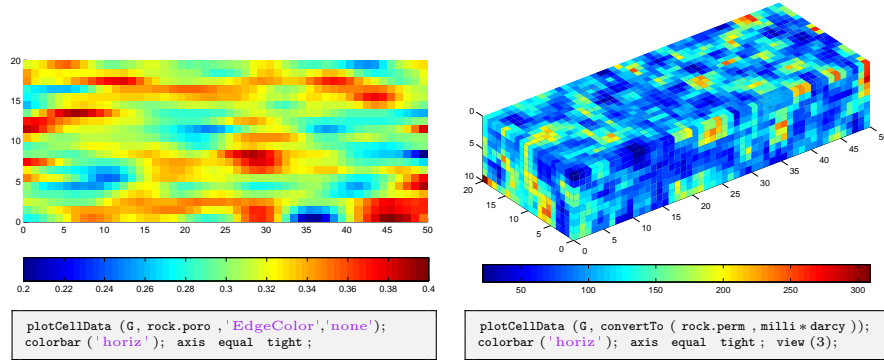


Fig. 3.10. The left plot shows a 50×20 porosity field generated as a Gaussian field with a larger filter size in x -direction than in the y -direction. The right plot shows the permeability field computed from the Carman–Kozeny relation for a similar $50 \times 20 \times 10$ porosity realization computed with filter size $[3, 3, 3]$.

```
G = cartGrid([50 20]);
p = gaussianField(G.cartDims, [0.2 0.4], [11 3], 2.5);
K = p.^3.*(1e-5)^2./(0.81*72*(1-p).^2);
rock.poro = p(:);
rock.perm = K(:);
```

The resulting porosity field is shown in the left plot of Figure 3.10. The right plot shows the permeability obtained for a 3D realization generated in the same way.

In the second example, we use the same methodology as above to generate layered realizations, for which the permeability in each geological layer is independent of the other layers and lognormally distributed. Each layer can be represented by several grid cells in the vertical direction. Rather than using a simple Cartesian grid, we will generate a stratigraphic grid with wavy geological faces and a single fault. Such grids will be described in more detail in Chapter 4.

```
G = processGRDECL(simpleGrdecl([50 30 10], 0.12));
K = logNormLayers(G.cartDims, [100 400 50 350], 'indices', [1 2 5 7 11]);
```

Here, we have specified four geological layers of different thickness. From top to bottom (stratigraphic grids are often numbered from the top and downward), the first layer is one cell thick and has a mean permeability value of 100 mD, the second layer is three cells thick and has mean permeability of 400 mD, the third layer is two cells thick and has mean value 50 mD, and the fourth layer is four cells thick and has mean value 350 mD. To specify this, we have used an indirection map. That is, if \mathbf{K}_m is the n -vector of mean permeabilities and \mathbf{L} is the $(n + 1)$ -vector of indices, the value $\mathbf{K}_m(i)$ is assigned to vertical layers number $\mathbf{L}(i)$ to $\mathbf{L}(i+1)-1$. The resulting permeability is shown in Figure 3.11.

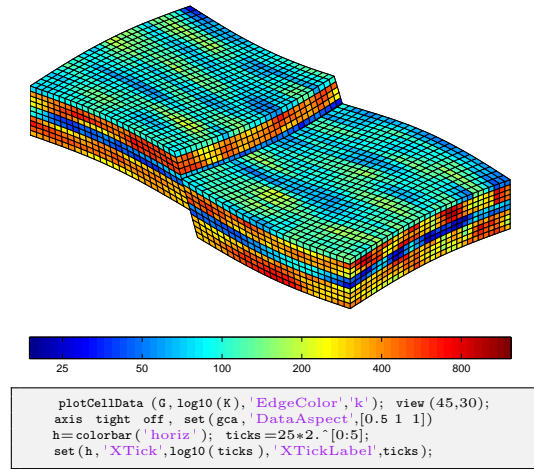


Fig. 3.11. A stratigraphic grid with a single fault and four geological layers, each with a lognormal permeability distribution.

3.5.3 10th SPE Comparative Solution Project: Model 2

Society of Petroleum Engineers (SPE) has developed a series of benchmarks that can be used to independently compare computational methods and simulators. The first nine benchmarks focus on black-oil, compositional, dual-porosity, thermal, and miscible simulations, as well as horizontal wells and gridding techniques. The 10th SPE Comparative Solution Project [49] was posed as a benchmark for upscaling methods, but the second data set of this benchmark has later become very popular within the academic community as a benchmark for comparing different computational methods. The data set is a 3-D geostatistical realization from the Jurassic Upper Brent formations, in which one can find the giant North Sea fields of Statfjord, Gullfaks, Oseberg, and Snorre. The main feature of the model is a permeability and porosity fields given on a $60 \times 220 \times 85$ Cartesian grid, in which each cells is of size $20\text{ft} \times 10\text{ft} \times 2\text{ft}$. In this specific model, the top 35 cell layers having a total height of 70 ft represent the shallow-marine Tarbert formation and the lower 50 layers having a height of 100 ft represent the fluvial Ness formation. The model is structurally simple but is highly heterogeneous, and, for this reason, some describe it as a 'simulator-killer'. On the other hand, the fact that the flow is dictated by the strong heterogeneity means that streamline methods will be particularly efficient for this model [2].

The SPE 10 data set is used in a large number of publications and is publicly available from the SPE website

<http://www.spe.org/web/csp/>

MRST supplies a module called `spe10` that downloads, reorganizes, and stores the data set in a file for later use. The module also contains routines that extract (subsets of) the petrophysical data and set up simulation models and appropriate data structures representing grids and wells. Alternatively, the data set can be downloaded using `mrstDatasetGUI`.

Because the geometry is a simple Cartesian grid, we can use standard MATLAB functionality to visualize the heterogeneity in the permeability and porosity (full details can be found in the script `rocks/showSPE10.m`)

```
% load SPE 10 data set
mrstModule add spe10;
rock = SPE10_rock(); p=rock.poro; K=rock.perm;

% show p
slice( reshape(p,60,220,85), [1 220], 60, [1 85]);
shading flat, axis equal off, set(gca,'zdir','reverse'), box on;
colorbar('horiz');

% show Kx
slice( reshape(log10(K(:,1)),60,220,85), [1 220], 60, [1 85]);
shading flat, axis equal off, set(gca,'zdir','reverse'), box on;
h=colorbar('horiz');
set(h,'XTickLabel',10.^[get(h,'XTick')]);
set(h,'YTick',mean(get(h,'YLim')),'YTickLabel','mD');
```

Figure 3.12 shows porosity and permeability; the permeability tensor is diagonal with equal permeability in the two horizontal coordinate directions. Both formations are characterized by large permeability variations, 8–12 orders of magnitude, but are qualitatively different. The Tarbert consists of sandstone, siltstone, and shales and comes from a tidally influenced, transgressive, shallow-marine deposit; in other words, a deposit that has taken place close to the coastline, see Figure 3.1. The formation has good communication in the vertical and horizontal directions. The fluvial Ness formation has been deposited by rivers or running water in a delta-plain continental environment (see Figures 3.1 and 3.2), leading to a spaghetti of well-sorted high-permeable sandstone channels with good communication (long correlation lengths) imposed on a low-permeable background of shales and coal, which gives low communication between different sand bodies. The porosity field has a large span of values and approximately 2.5% of the cells have zero porosity and should be considered as being inactive.

Figure 3.13 shows histograms of the porosity and the logarithm of the horizontal and vertical permeabilities. The nonzero porosity values and the horizontal permeability of the Tarbert formation appear to follow a normal and lognormal distribution, respectively. The vertical permeability follows a bi-modal distribution. For the Ness formation, the nonzero porosities and the horizontal permeability follow bi-modal normal and lognormal distributions, respectively, as is to be expected for a fluvial formation. The vertical permeability is trimodal.

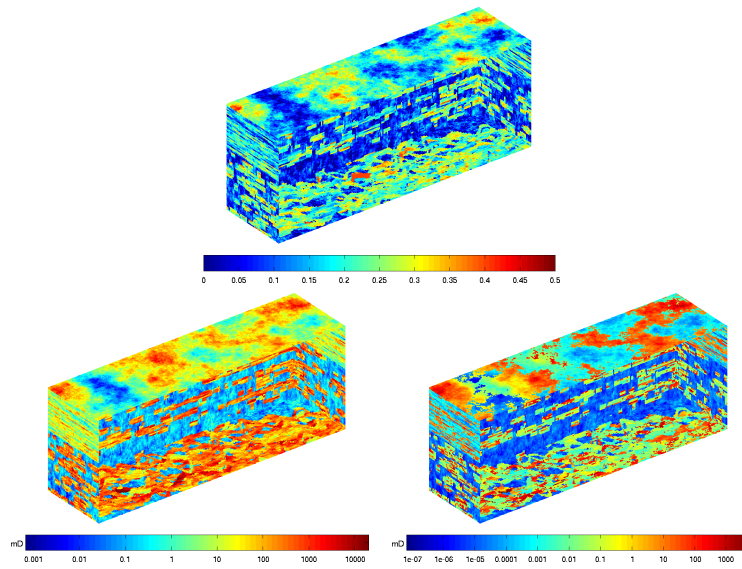


Fig. 3.12. Rock properties for the SPE 10 model. The upper plot shows the porosity, the lower left the horizontal permeability, and the lower right the vertical permeability. (The permeabilities are shown using a logarithmic color scale).

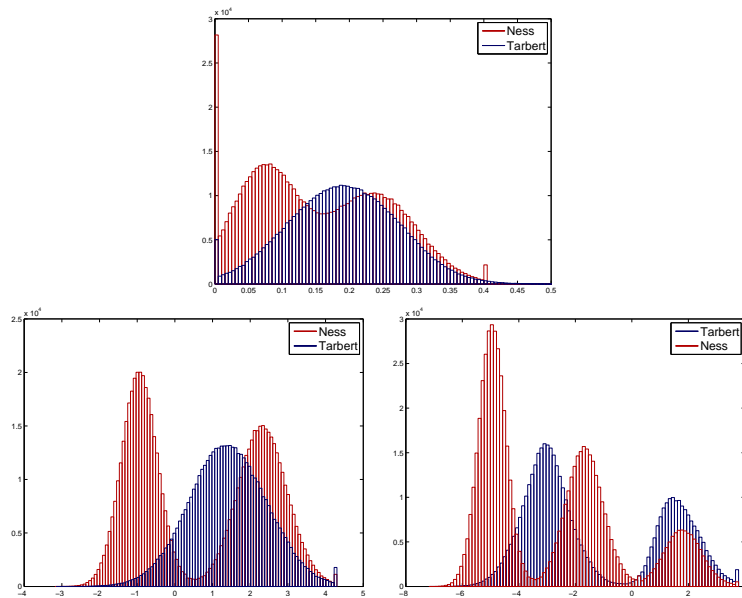


Fig. 3.13. Histogram of rock properties for the SPE 10 model: ϕ (upper plot), $\log K_x$ (lower left), and $\log K_z$ (lower right) The Tarbert formation is shown in blue and the Ness formation in red.

3.5.4 The Johansen Formation

The Johansen formation is located in the deeper part of the Sognefjord delta, 40–90 km offshore Mongstad on the west coast of Norway. A few years ago, a gas-power plant with carbon capture and storage was planned at Mongstad and the water-bearing Johansen formation was a possible candidate for storing the captured CO₂. The Johansen formation is part of the Dunlin group, and is interpreted as a large sandstone delta 2200–3100 meters below sea level that is limited above by the Dunlin shale and below by the Amundsen shale. The average thickness of the formation is roughly 100 m and the lateral extensions are up to 100 km in the north-south direction and 60 km in the east-west direction. The aquifer has good sand quality and lies at a depth where CO₂ would undoubtedly be in supercritical phase, and would thus be ideal for carbon storage. With average porosities of approximately 25 percent, this implies that the theoretical storage capacity of the Johansen formation is more than one gigatonne of CO₂ [65]. The Troll field, one of the largest gas fields in the North Sea, is located some 500 meters above the north-western parts of the Johansen formation. A set of geological models of Johansen is publicly available from the url:

<http://www.sintef.no/Projectweb/MatMorA/Downloads/Johansen/>

and can be downloaded using the `mrstDatasetGUI` function. Altogether, there are five models: one full-field model (149 × 189 × 16 grid), three homogeneous sector models (100 × 100 × n for $n = 11, 16, 21$), and one heterogeneous sector model (100 × 100 × 11). Herein, we consider the latter. All statements used to analyze the model are found in the script `rocks/showJohansenNPD5.m`.

The grid consists of hexahedral cells and is given on the industry-standard corner-point format, which will be discussed in details in Section 4.3.1. A more detailed discussion of how to input the grid will be given in the next section. The rock properties are given as plain ASCII files, with one entry per cell. In the model, the Johansen formation is represented by five grid layers, the low-permeable Dunlin shale above is represented by five layers, and the Amundsen shale below is represented as one layer. The Johansen formation consists of approximately 80% sandstone and 20% claystone, whereas the Amundsen formation consists of siltstones and shales, see [65, 64, 11] for more details.

We start by loading the data and visualizing the porosity, which is straightforward once we remember to use `G.cells.indexMap` to extract rock properties only for active cells in the model.

```
G = processGRDECL(readGRDECL('NPD5.grdecl'));
p = load('NPD5_Porosity.txt'); p = p(G.cells.indexMap);
```

Figure 3.14 shows the porosity field of the model. The left plot shows the Dunlin shale, the Johansen sand, and the Amundsen shale, where the Johansen sand is clearly distinguished as a wedge shape that is pinched out in the front part of the model and splits the shales laterally in two at the back. In the

right plot, we only plot the good reservoir rocks distinguished as the part of the porosity field that has values larger than 0.1.

The permeability tensor is assumed to be diagonal with the vertical permeability equal one-tenth of the horizontal permeability. Hence, only the x -component \mathbf{K}_x is given in the data file

```
K = load('NPD5_Permeability.txt'); K=K(G.cells.indexMap);
```

Figure 3.15 shows three different plots of the permeability. The first plot shows the logarithm of whole permeability field. In the second plot, we have filtered out the Dunlin shale above Johansen but not the Amundsen shale below. The third plot shows the permeability in the Johansen formation using a linear color scale, which clearly shows the depth trend that was used to model the heterogeneity.

3.5.5 SAIGUP: shallow-marine reservoirs

Most commercial simulators use a combination of an 'input language' and a set of data files to describe and set up a simulation model of a reservoir. However, although the principles for the input description has much in common, the detail syntax is obviously unique to each simulator. Herein, we will mainly focus on the ECLIPSE input format, which has emerged as an industry standard for describing static and dynamic properties of a reservoir system, from the reservoir rock, via production and injection wells and up to connected top-side facilities. ECLIPSE input decks use keywords to signify and separate the different data elements that comprise a full model. These keywords define a detailed language that can be used to specify how the data elements

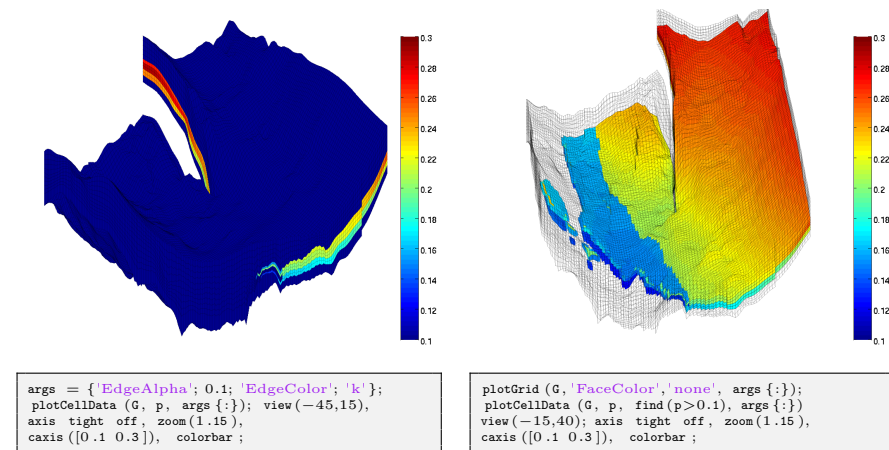


Fig. 3.14. Porosity for the Johansen data set 'NPD5'. The left plot shows porosity for the whole model, whereas in the right plot we have masked the low-porosity cells in the Amundsen and Dunlin formations.

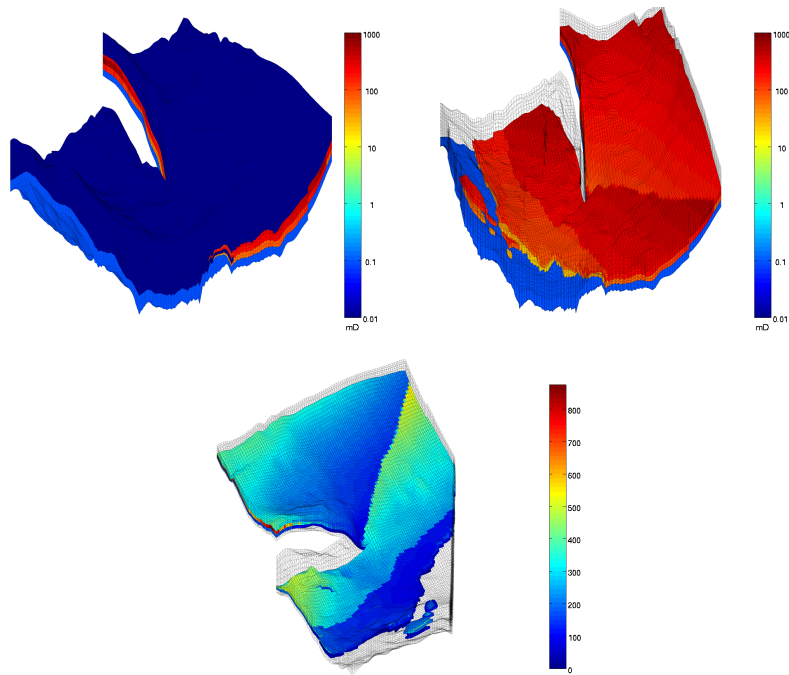


Fig. 3.15. Permeability for the Johansen data set 'NPD5'. The upper-left plot shows the permeability for the whole model, the upper-right plot shows the Johansen sand and the Amundsen shale, whereas the lower plot only shows the permeability of the Johansen sand.

should be put together, and modify each other, to form a full spatio-temporal model of a reservoir. In the most general form, an ECLIPSE input file consists of eight sets of keywords, which are organized into eight sections that must come in a prescribed order. However, some of the sections are optional and may not always be present. The order of the keywords within each section is arbitrary, except in the section that defines wells and gives operating schedule, etc. Altogether, the ECLIPSE format consists of thousands of keywords, and describing them all is far beyond the scope of this book.

In the following, we will instead briefly outline some of the most common keywords used in the GRID section that describes the reservoir geometry and petrophysical properties. The purpose is to provide you with a basic understanding of the required input for simulations of real-life reservoir models. Our focus is mainly on the ingredients of a model and not on the specific syntax. For brevity, we will therefore not go through all MATLAB and MRST statements used to visualize the different data elements. All details necessary to reproduce the results can be found in the script `rocks/showSAIGUP.m`.

As our primary example of a realistic petroleum reservoir, we will use a model from the SAIGUP study [124], whose purpose was to conduct a sensitiv-

ity analysis of the impact of geological uncertainties on production forecasting in clastic hydrocarbon reservoirs. As part of this study, a broad suite of geo-statistical realizations and structural models were generated to represent a wide span of shallow-marine sedimentological reservoirs. The SAIGUP models mainly focus on shoreface reservoirs in which the deposition of sediments is caused by variation in sea level, so that facies are forming belts in a systematic pattern (river deposits create curved facies belts, wave deposits create parallel belts, etc). Sediments are in general deposited when the sea level is increasing. No sediments are deposited during decreasing sea levels; instead, the receding sea may affect the appearing shoreline and cause the creation of a barrier. All models are synthetic, but contain representative examples of the complexities seen in real-life reservoirs.

One of the many SAIGUP realizations is publicly available from:

<http://www.sintef.no/MRST>

The specific realization comes in the form of a GZip-compressed TAR file (`SAIGUP.tar.gz`) that contains the structural model as well as petrophysical parameters, represented in the ECLIPSE format. The data set can be downloaded using the `mrstDatasetGUI` function. Here, however, we unpack the data set manually for completeness of presentation. Assuming that the archive file `SAIGUP.tar.gz` that contains the model realization has been downloaded as described on the webpage, we extract the data set and place it in a standardized path relative to the root directory of MRST:

```
untar('SAIGUP.tar.gz', fullfile(ROOTDIR, 'examples', 'data', 'SAIGUP'))
```

This will create a new directory containing seventeen data files that comprise the structural model, various petrophysical parameters, etc:

```
028_A11.EDITNNC    028.MULTX  028.PERMX  028.SATNUM    SAIGUP.GRDECL
028_A11.EDITNNC.001 028.MULTY  028.PERMY  SAIGUP_A1.ZCORN
028_A11.TRANK      028.MULTZ  028.PERMZ  SAIGUP.ACTNUM
028_A11.TRANY      028.NTG    028.PORO   SAIGUP.COORD
```

The main file is `SAIGUP.GRDECL`, which lists the sequence of keywords that specifies how the data elements found in the other files should be put together to make a complete model of the reservoir rock. The remaining files represent different keywords: the grid geometry is given in files `SAIGUP_A1.ZCORN` and `SAIGUP.COORD`, the porosity in `028.PORO`, the permeability tensor in the three `028.PERM*` files, net-to-gross properties in `028.NTG`, the active cells in `SAIGUP.ACTNUM`, transmissibility multipliers that modify the flow connections between different cells in the model are given in `028.MULT*`, etc. For now, we will rely entirely on MRST's routines for reading ECLIPSE input files; more details about corner-point grids and the ECLIPSE input format will follow later in the book, starting in Chapter 4.

The `SAIGUP.GRDECL` file contains seven of the eight possible sections that may comprise a full input deck. The `deckformat` module in MRST contains a comprehensive set of input routines that enable the user to read the most

important keywords and options supported in these sections. Here, however, it is mainly the sections describing static reservoir properties that contain complete and useful information, and we will therefore use the much simpler function `readGRDECL` from MRST core to read and interprets the GRID section of the input deck:

```
grdecl = readGRDECL(fullfile(ROOTDIR, 'examples', ...
    'data', 'SAIGUP', 'SAIGUP.GRDECL'));
```

This statement parses the input file and stores the content of all keywords it recognizes in the structure `grdecl`:

```
grdecl =
  cartDims: [40 120 20]
  COORD: [29766x1 double]
  ZCORN: [768000x1 double]
  ACTNUM: [96000x1 int32]
  PERMX: [96000x1 double]
  PERMY: [96000x1 double]
  PERMZ: [96000x1 double]
  MULTX: [96000x1 double]
  MULTY: [96000x1 double]
  MULTZ: [96000x1 double]
  PORO: [96000x1 double]
  NTG: [96000x1 double]
  SATNUM: [96000x1 double]
```

The first four data fields describe the grid, and we will come back to these in Chapter 4.3.1. In the following, we will focus on the next eight data fields, which contain the petrophysical parameters. We will also briefly look at the last data field, which delineates the reservoir into different (user-defined) rock types that can be used to associate different rock-fluid properties.

Recall that MRST uses the strict SI conventions in all of its internal calculations. The SAIGUP model, however, is provided using the ECLIPSE 'METRIC' conventions (permeabilities in mD and so on). We use the functions `getUnitSystem` and `convertInputUnits` to assist in converting the input data to MRST's internal unit conventions.

```
usys = getUnitSystem('METRIC');
grdecl = convertInputUnits(grdecl, usys);
```

Having converted the units properly, we generate a space-filling grid and extract petrophysical properties

```
G = processGRDECL(grdecl);
G = computeGeometry(G);
rock = grdecl2Rock(grdecl, G.cells.indexMap);
```

The first statement takes the description of the grid geometry and constructs an unstructured MRST grid represented with the data structure outlined in Section 4.4. The second statement computes a few geometric primitives like cell volumes, centroids, etc., as discussed on page 116. The third statement constructs a rock object containing porosity, permeability, and net-to-gross.

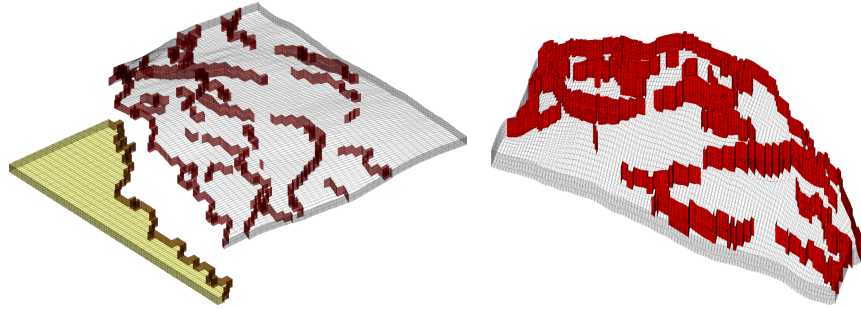


Fig. 3.16. The structural SAIGUP model. The left plot shows the full model with faults marked in red and inactive cells marked in yellow, whereas the right plot shows only the active parts of the model seen from the opposite direction.

For completeness, we first show a bit more details of the structural model in Figure 3.16. The left plot shows the whole $40 \times 120 \times 20$ grid model¹, where we in particular should note the disconnected cells marked in yellow that are not part of the active model. The relatively large fault throw that disconnects the two parts is most likely a modelling artifact introduced to clearly distinguish the active and inactive parts of the model. A shoreface reservoir is bounded by faults and geological horizons, but faults also appear inside the reservoir as the right plot in Figure 3.16 shows. Faults and barriers will typically have a pronounced effect on the flow pattern, and having an accurate representation is important to produce reliable flow predictions.

The petrophysical parameters for the model were generated on a regular $40 \times 120 \times 20$ Cartesian grid, as illustrated in the left plot of Figure 3.17, and then mapped onto the structural model, as shown in the plot to the right. A bit simplified, one can view the Cartesian grid model as representing the rock body at geological 'time zero' when the sediments have been deposited and have formed a stack of horizontal grid layers. From geological time zero and up to now, geological activity has introduced faults and deformed the layers, resulting in the structural model seen in the left plot of Figure 3.17.

Having seen the structural model, we continue to study the petrophysical parameters. The grid cells in our model are thought to be larger than the laminae of our imaginary reservoir and hence each grid block will generally contain both reservoir rock (with sufficient permeability) and impermeable shale. This is modelled using the net-to-gross ratio, `rock.ntg`, which is shown in Figure 3.18 along with the horizontal and vertical permeability. The plotting routines are exactly the same as for the porosity in Figure 3.17, but with different data and slightly different specification of the colorbar. From the figure, we clearly see that the model has a large content of shale and thus low

¹ To not confuse the reader, we emphasize that only the active part of the model is read with the MRST statements given above. How to also include the inactive part, will be explained in more details in Chapter 4.

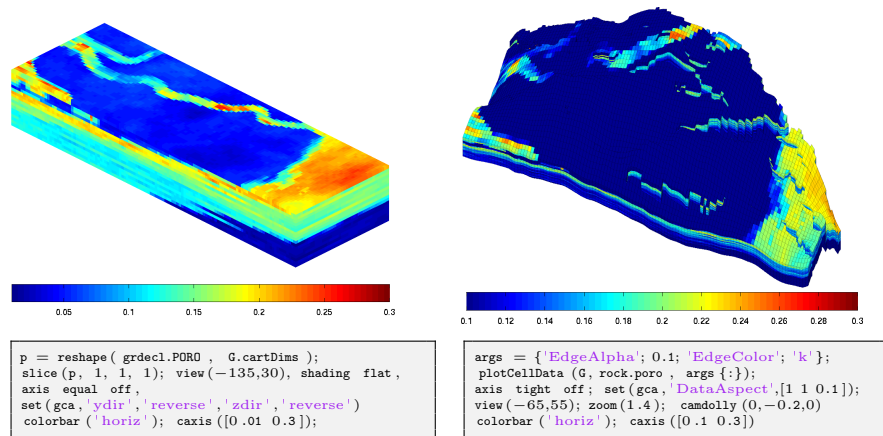


Fig. 3.17. Porosity for the SAIGUP model. The left plot shows porosity as generated by geostatistics in logical ijk space. The right plot shows the porosity mapped to the structural model shown in Figure 3.16.

permeability along the top. However, we also see high-permeable sand bodies that cut through the low-permeable top. In general, the permeabilities seem to correlate well with the sand content given by the net-to-gross parameter.

Some parts of the sand bodies are partially covered by mud that strongly reduces the vertical communication, most likely because of flooding events. These mud-draped surfaces occur on a sub-grid scale and are modelled through a multiplier value (MULTZ) associated with each cell, which takes values between zero and one and can be used to manipulate the effective communication (the transmissibility) between a given cell (i, j, k) and the cell immediately above $(i, j, k + 1)$. For completeness, we remark that the horizontal multiplier values (MULTX and MULTY) play a similar role for vertical faces, but are equal one in (almost) all cells for this particular realization.

To further investigate the heterogeneity of the model, we next look at histograms of the porosity and the permeabilities, as we did for the SPE 10 example (the MATLAB statements are omitted since they are almost identical). In Figure 3.19, we clearly see that the distributions of porosity and horizontal permeability are multi-modal in the sense that five different modes can be distinguished, corresponding to the five different facies used in the petrophysical modelling.

It is common modelling practice that different rock types are assigned different rock-fluid properties (relative permeability and capillary functions), more details about such properties will be given later in the book. In the ECLIPSE input format, these different rock types are represented using the SATNUM keyword. By inspection of the SATNUM field in the input data, we see that the model contains six different rock types as depicted in Figure 3.20. For completeness, the figure also shows the permeability distribution inside

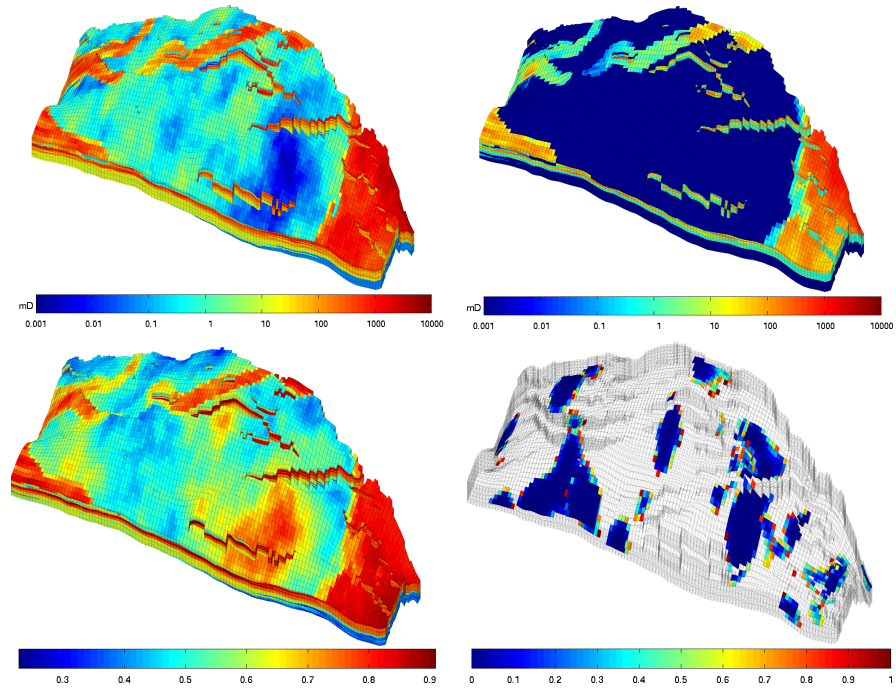


Fig. 3.18. The upper plots show the permeability for the SAIGUP model, using a logarithmic color scale, with horizontal permeability to the left and vertical permeability to the right. The lower-left plot shows net-to-gross, i.e., the fraction of reservoir rock per bulk volume. The lower-right plot shows regions of the reservoir where reduced vertical communication is modelled by vertical multiplier values less than unity.

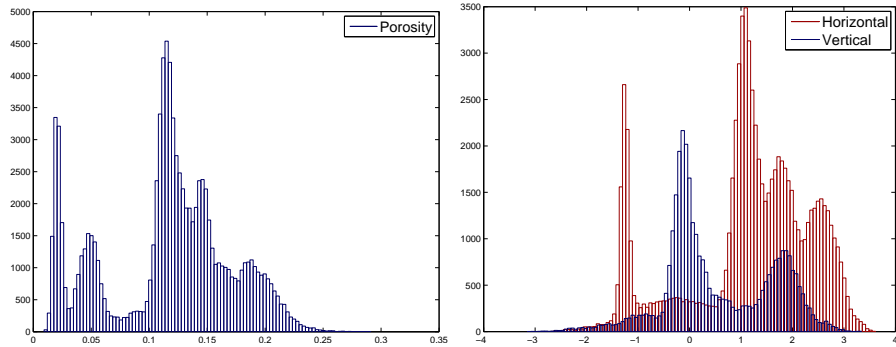


Fig. 3.19. Histogram of the porosity (left) and the logarithm of the horizontal and vertical permeability (right) for the shallow-marine SAIGUP model. Since the reservoir contains five different facies, the histograms are multi-modal. See also Figure 3.20.

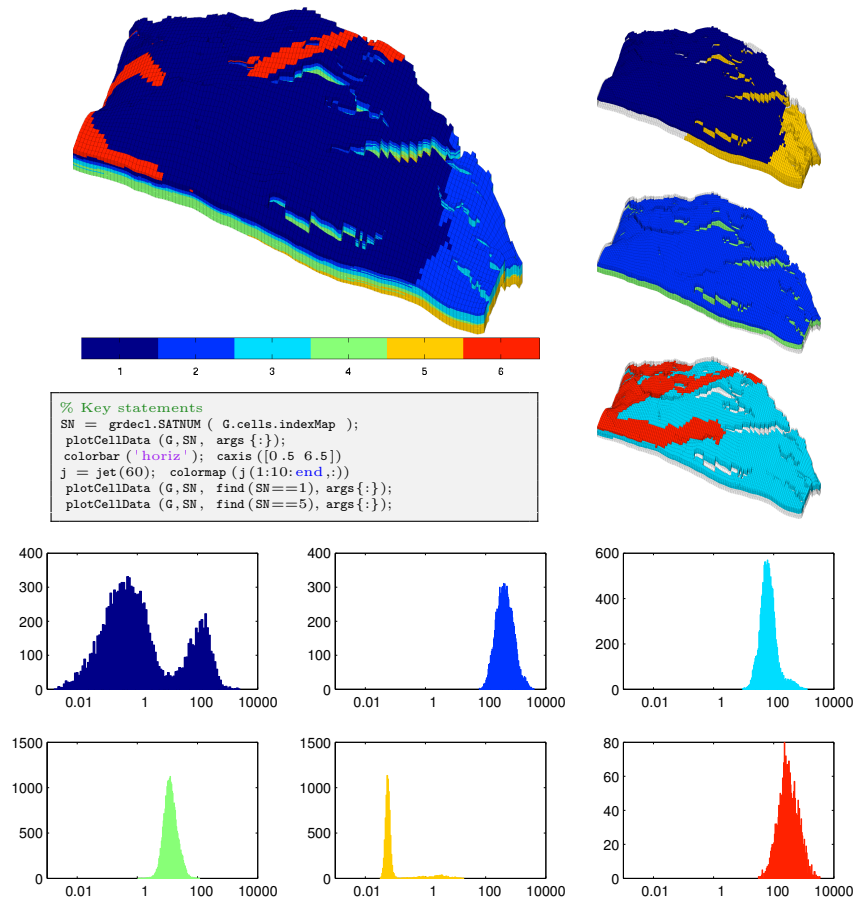


Fig. 3.20. The upper-left plot shows the rock type distribution for the SAIGUP model. The right column shows the six rock types grouped in pairs; from top to bottom, rock types number 1 and 5, 2 and 4, and 3 and 6. The bottom part of the figure shows histograms of the lateral permeability in units [mD] for each of the six rock types found in the SAIGUP model.

each rock type. Interestingly, the permeability distribution is multi-modal for at least two of the rock types.

Finally, to demonstrate the large difference in heterogeneity resulting from different depositional environment, we compare the realization we have studied above with another realization. In Figure 3.21 we show porosities and rock-type distributions. Whereas our original realization seems to correspond to a depositional environment with a flat shoreline, the other realization corresponds to a two-lobed shoreline, giving distinctively different facies belts. The figure also clearly demonstrates how the porosity (which depends on the

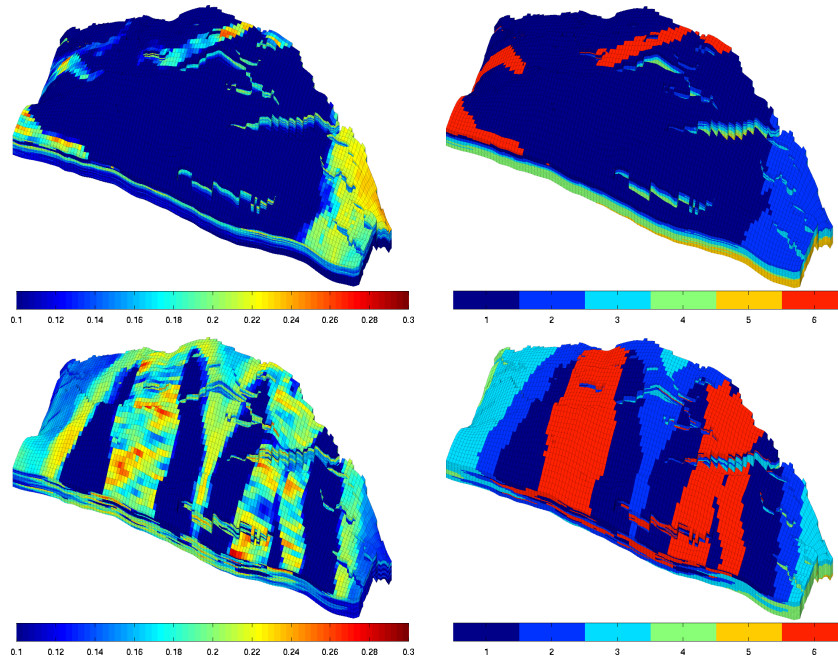


Fig. 3.21. Comparison of porosity (left) and the distribution of rock types (right) for two different SAIGUP realizations.

grain-size distribution and packing) varies with the rock types. This can be confirmed by a quick analysis:

```
for i=1:6, pavg(i) = mean(rock.poro(SN==i));
           navg(i) = mean(rock.ntg(SN==i)); end
```

```
pavg = 0.0615    0.1883    0.1462    0.1145    0.0237    0.1924
navg = 0.5555    0.8421    0.7554    0.6179    0.3888    0.7793
```

In other words, rock types two and six are good sands with high porosity, three and four have intermediate porosity, whereas one and five correspond to less quality sand with a high clay content and hence low porosity.

COMPUTER EXERCISES:

11. Look at the correlation between the porosity and the permeability for the SPE 10 data set. Do you see any artifacts, and if so, how would you explain them? (Hint: plot ϕ versus $\log K$)
12. Download the `CaseB4` models that represent a simple box geometry with intersecting faults. Pick at least one of the model realizations and try to set homogeneous and random petrophysical data as discussed in Sections 3.5.1 and 3.5.2.

13. The permeability field given in `rock1.mat` in the book module contains an unusual geological structure. Can you find what it is?
14. Download the `BedModels1` and `BedModel2` data sets that represent sedimentary beds similar to the facies model shown in Figure 3.7. Use the techniques introduced in Sections 3.5.3 to 3.5.5 to familiarize yourself with these models:
 - look at porosities and permeabilities in physical space
 - compare with the same quantities in ijk space
 - find models that have facies information and look at the distribution of petrophysical properties inside each facies
15. Modify the `simpleGravityColumn` example from Section 2.1 so that it uses the geometry and petrophysical data in the `mortarTestModel` or `periodicTilted` models from the `BedModels1` data set instead. Can you explain what you observe?

Grids in Subsurface Modeling

The basic geological description of a petroleum reservoir or an aquifer system will typically consist of two sets of surfaces. Geological horizons are lateral surfaces that describe the bedding planes that delimit the rock strata, whereas faults are vertical or inclined surfaces along which the strata may have been displaced by geological processes. In this chapter, we will discuss how to turn the basic geological description into a discrete model that can be used to formulate various computational methods, e.g., for solving the equations that describe fluid flow.

A *grid* is a tessellation of a planar or volumetric object by a set of contiguous simple shapes referred to as *cells*. Grids can be described and distinguished by their *geometry*, reflected by the shape of the cells that form the grid, and their *topology* that tells how the individual cells are connected. In 2D, a cell is in general a closed polygon for which the geometry is defined by a set of *vertices* and a set of *edges* that connect pairs of vertices and define the interface between two neighboring cells. In 3D, a cell is a closed polyhedron for which the geometry is defined by a set of vertices, a set of edges that connect pairs of vertices, and a set of *faces* (surfaces delimited by a subset of the edges) that define the interface between two different cells, see Figure 4.1. Herein, we will assume that all cells in a grid are non-overlapping, so that each point in the planar/volumetric object represented by the grid is either inside a single cell, lies on an interface or edge, or is a vertex. Two cells that share a common face are said to be connected. Likewise, one can also define connections based on edges and vertices. The topology of a grid is defined by the total set of connections, which is sometimes also called the *connectivity* of the grid.

When implementing grids in modeling software, one always has the choice between generality and efficiency. To represent an arbitrary grid, it is necessary to explicitly store the geometry of each cell in terms of vertices, edges, and faces, as well as storing the connectivity among cells, faces, edges, and vertices. However, as we will see later, huge simplifications can be made for particular classes of grids by exploiting regularity in the geometry and structures in the topology. Consider, for instance, a planar grid consisting of rectangular

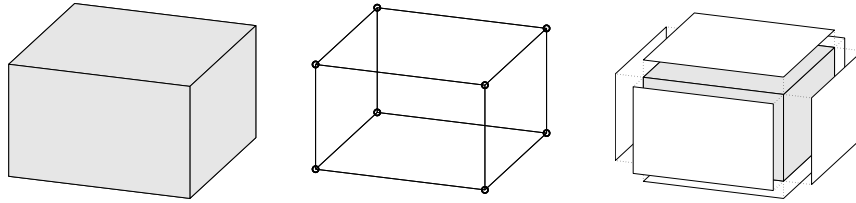


Fig. 4.1. Illustration of a single cell (left), vertices and edges (middle), and cell faces (right).

cells of equal size. Here, the topology can be represented by two indices and one only needs to specify a reference point and the two side lengths of the rectangle to describe the geometry. This way, one ensures minimal memory usage and optimal efficiency when accessing the grid. On the other hand, exploiting the simplified description explicitly in your flow or transport solver inevitably means that the solver must be reimplemented if you later decide to use another grid format.

The most important goal for our development of MRST is to provide a toolbox that both allows *and* enables the use of various grid types. To avoid having a large number of different, and potentially incompatible, grid representations, we have therefore chosen to store *all grid types* using a general unstructured format in which cells, faces, vertices, and connections between cells and faces are explicitly represented. This means that we, for the sake of generality, have sacrificed some of the efficiency one can obtain by exploiting special structures in a particular grid type and instead have focused on obtaining a flexible grid description that is not overly inefficient. Moreover, our grid structure can be extended by other properties that are required by various discretization schemes for flow and transport simulations. A particular discretization may need the *volume* or the *centroid* (grid-point, midpoint, or generating point) of each cell. Likewise, for cell faces one may need to know the face areas, the face normals, and the face centroids. Although these properties can be computed from the geometry (and topology) of the grid, it is often useful to precompute and include them explicitly in the grid representation.

The first third of this chapter is devoted to standard grid formats that are available in MRST. We introduce examples of structured grids, including regular Cartesian, rectilinear, and curvilinear grids, and briefly discuss unstructured grids, including Delaunay triangulations and Voronoi grids. The purpose of our discussion is to demonstrate the basic grid functionality in MRST and show some key principles that can be used to implement new structured and unstructured grid formats. In the second part of the chapter, we discuss industry-standard grid formats for stratigraphic grids that are based on extrusion of 2D shapes (corner-point, prismatic, and 2.5D PEBI grids). Although these grids have an inherent logical structure, representation of faults, erosion, pinch-outs, and so on lead to cells that can have quite ir-

regular shapes and an (almost) arbitrary number of faces. In the last part of the chapter, we discuss how the grids introduced in the first two parts of the chapter can be partitioned to form flexible coarse descriptions that preserve the geometry of the underlying fine grids. The ability to represent a wide range of grids, structured or unstructured on the fine and/or coarse scale, is a strength of MRST compared to the majority of research codes arising from academic institutions.

A number of videos that complement the material presented in this chapter can be found in the second MRST Jolt [114]. This Jolt introduces different types of grids, discusses how such grids can be represented, and outlines functionality in MRST you can use to generate your own grids.

4.1 Structured grids

As we saw above, a grid is a tessellation of a planar or volumetric object by a set of simple shapes. In a *structured* grid, only one basic shape is allowed and this basic shape is laid out in a regular repeating pattern so that the topology of the grid is constant in space. The most typical structured grids are based on quadrilaterals in 2D and hexahedrons in 3D, but in principle it is also possible to construct grids with a fixed topology using certain other shapes. Structured grids can be generalized to so-called multiblock grids (or hybrid grids), in which each block consists of basic shapes that are laid out in a regular repeating pattern.

Regular Cartesian grids

The simplest form of a structured grid consists of unit squares in 2D and unit cubes in 3D, so that all vertices in the grid are integer points. More generally, a regular Cartesian grid can be defined as consisting of congruent rectangles in 2D and rectilinear parallelepipeds in 3D, etc. Hence, the vertices have coordinates $(i_1\Delta x_1, i_2\Delta x_2, \dots)$ and the cells can be referenced using the multi-index (i_1, i_2, \dots) . Herein, we will only consider finite Cartesian grids that consist of a finite number $n_2 \times n_2 \times \dots \times n_k$ of cells that cover a bounded domain $[0, L_1] \times [0, L_2] \times \dots \times [0, L_k]$.

Regular Cartesian grids can be represented very compactly by storing n_i and L_i for each dimension. In MRST, however, Cartesian grids are represented as if they were fully unstructured using a general grid structure that will be described in more detail in Section 4.4. Cartesian grids therefore have special constructors,

```
G = cartGrid([nx, ny], [Lx Ly]);
G = cartGrid([nx, ny, nz], [Lx Ly Lz]);
```

that set up the data structures representing the basic geometry and topology of the grid. The second argument is optional.

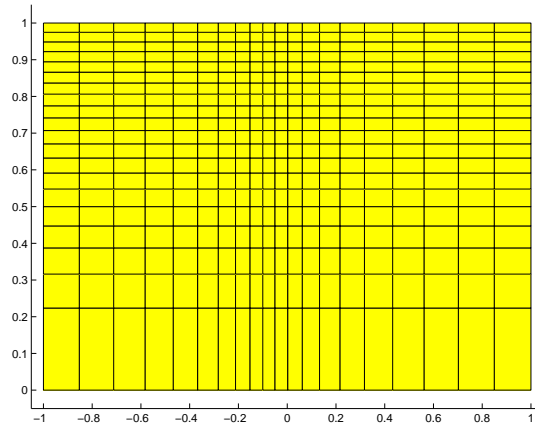


Fig. 4.2. Example of a rectilinear grid.

Rectilinear grids

A rectilinear grid (also called a tensor grid) consists of rectilinear shapes (rectangles or parallelepipeds) that are not necessarily congruent to each other. In other words, whereas a regular Cartesian grid has a uniform spacing between its vertices, the grid spacing can vary along the coordinate directions in a rectilinear grid. The cells can still be referenced using a multi-index (i_1, i_2, \dots) but the mapping from indices to vertex coordinates is nonuniform.

In MRST, one can construct a rectilinear grid by specifying the vectors with the grid vertices along the coordinate directions:

```
G = tensorGrid(x, y);
G = tensorGrid(x, y, z);
```

This syntax is the same as for the MATLAB functions `meshgrid` and `ndgrid`.

As an example of a rectilinear grid, we construct a 2D grid that covers the domain $[-1, 1] \times [0, 1]$ and is graded toward $x = 0$ and $y = 1$ as shown in Figure 4.2.

```
dx = 1-0.5*cos((-1:0.1:1)*pi);
x = -1.15+0.1*cumsum(dx);
y = 0:0.05:1;
G = tensorGrid(x, sqrt(y));
plotGrid(G); axis([-1.05 1.05 -0.05 1.05]);
```

Curvilinear grids

A curvilinear grid is a grid with the same topological structure as a regular Cartesian grid, but in which the cells are quadrilaterals rather than rectangles

in 2D and cuboids rather than parallelepipeds in 3D. The grid is given by the coordinates of the vertices but there exists a mapping that will transform the curvilinear grid to a uniform Cartesian grid so that each cell can still be referenced using a multi-index (i_1, i_2, \dots) .

For the time being, MRST has no constructor for curvilinear grids. Instead, the user can create curvilinear grids by first instantiating a regular Cartesian or a rectilinear grid and then manipulating the vertices, as we will demonstrate next. This method is quite simple as long as there is a one-to-one mapping between the curvilinear grid in physical space and the logically Cartesian grid in reference space. The method will *not* work if the mapping is not one-to-one so that vertices with different indices coincide in physical space. In this case, the user should create an Eclipse input file with keywords `COORD[XYZ]`, see Section 4.3.1, and use the function `buildCoordGrid` to create the grid.

To illustrate the discussion, we show two examples of how to create curvilinear grids. In the first example, we create a rough grid by perturbing all internal nodes of a regular Cartesian grid (see Figure 4.3):

```

nx = 6; ny=12;
G = cartGrid([nx, ny]);
subplot(1,2,1); plotGrid(G);
c = G.nodes.coords;
I = any(c==0,2) | any(c(:,1)==nx,2) | any(c(:,2)==ny,2);
G.nodes.coords(~I,:) = c(~I,:) + 0.6*rand(sum(~I),2)-0.3;
subplot(1,2,2); plotGrid(G);

```

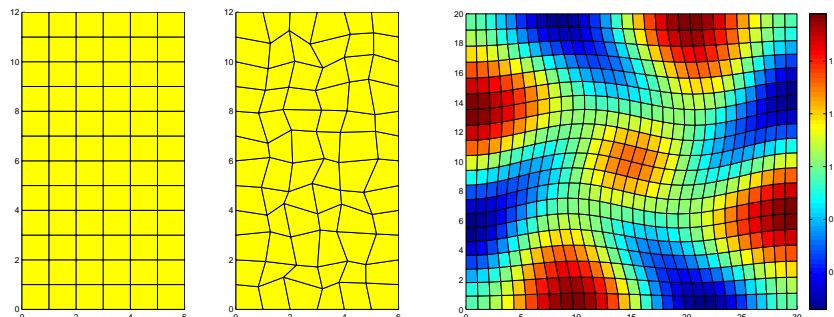


Fig. 4.3. The middle plot shows a rough grid created by perturbing all internal nodes of the regular 6×12 Cartesian grid in the left plot. The right plot shows a curvilinear grid created using the function `twister` that uses a combination of sin functions to perturb a rectilinear grid. The color is determined by the cell volumes.

In the second example, we use the MRST example routine `twister` to perturb the internal vertices. The function maps the grid back to the unit square, perturbs the vertices according to the mapping

$$(x_i, y_i) \mapsto (x_i + f(x_i, y_i), y_i - f(x_i, y_i)), \quad f(x, y) = 0.03 \sin(\pi x) \sin(3\pi(y - \frac{1}{2})),$$

and then maps the grid back to its original domain. The resulting grid is shown in the right plot of Figure 4.3. To illuminate the effect of the mapping, we have colored the cells according to their volume, which has been computed using the function `computeGeometry`, which we will come back to below.

```
G = cartGrid([30, 20]);
G.nodes.coords = twister(G.nodes.coords);
G = computeGeometry(G);
plotCellData(G, G.cells.volumes, 'EdgeColor', 'k'), colorbar
```

Fictitious domains

One obvious drawback with Cartesian and rectilinear grids, as defined above, is that they can only represent rectangular domains in 2D and cubic domains in 3D. Curvilinear grids, on the other hand, can represent more general shapes by introducing an appropriate mapping, and can be used in combination with rectangular/cubic grids in multiblock grids for efficient representation of realistic reservoir geometries. However, finding a mapping that conforms to a given boundary is often difficult, in particular for complex geologies, and using a mapping in the interior of the domain will inadvertently lead to cells with rough geometries that deviate far from being rectilinear. Such cells may in turn introduce problems if the grid is to be used in a subsequent numerical discretization, as we will see later.

As an alternative, complex geometries can be easily modelled using structured grids by a so-called fictitious domain method. In this method, the complex domain is embedded into a larger "fictitious" domain of simple shape (a rectangle or cube) using, e.g., a boolean indicator value in each cell to tell whether the cell is part of the domain or not. The observant reader will notice that we already have encountered the use of this technique for the SAIGUP dataset (Figure 3.16) and the Johansen dataset in Chapter 3. In some cases, one can also adapt the structured grid by moving the nearest vertices to the domain boundary.

MRST has support for fictitious domain methods through the function `removeCells`, which we will demonstrate in the next example, where we create a regular Cartesian grid that fills the volume of an ellipsoid:

```
x = linspace(-2,2,21);
G = tensorGrid(x,x,x);
subplot(1,2,1); plotGrid(G);view(3); axis equal

subplot(1,2,2); plotGrid(G,'FaceColor','none');
G = computeGeometry(G);
c = G.cells.centroids;
r = c(:,1).^2 + 0.25*c(:,2).^2+0.25*c(:,3).^2;
G = removeCells(G, r>1);
plotGrid(G); view(-70,70); axis equal;
```

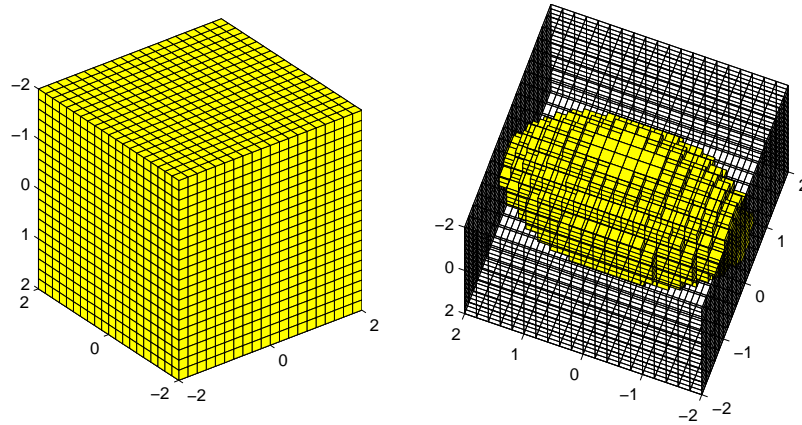


Fig. 4.4. Example of a regular Cartesian grid representing a domain in the form of an ellipsoid. The underlying logical Cartesian grid is shown in the left plot and as a wireframe in the right plot. The active part of the model is shown in yellow color in the right plot.

Worth observing here is the use of `computeGeometry` to compute cell centroids which are not part of the basic geometry representation in MRST. Plots of the grid before and after removing the inactive parts are shown in Figure 4.4. Because of the fully unstructured representation used in MRST, calling `computeGeometry` actually removes the inactive cells from the grid structure, but from the outside, the structure behaves as if we had used a fictitious domain method.

You can find more examples of how you can make structured grids and populate them with petrophysical properties in the fourth video of the second MRST Jolt [114].

COMPUTER EXERCISES:

16. Make the grid shown below:

Hint: the grid spacing in the x -direction is given by $\Delta x(1 - \frac{1}{2} \cos(\pi x))$ and the colors signify cell volumes.

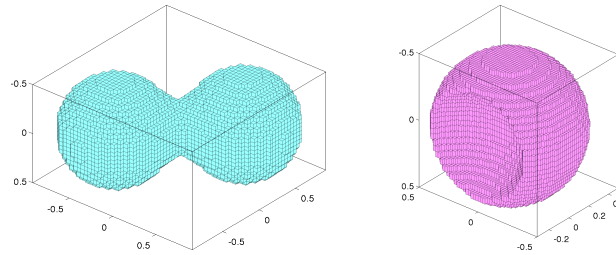
17. Metaballs are commonly used in computer graphics to generate organic-looking objects. Each metaball is defined as a smooth function that has finite support. One example is

$$m(\vec{x}, r) = \left[1 - \min\left(\frac{|\vec{x}|^2}{r^2}, 1\right) \right]^4.$$

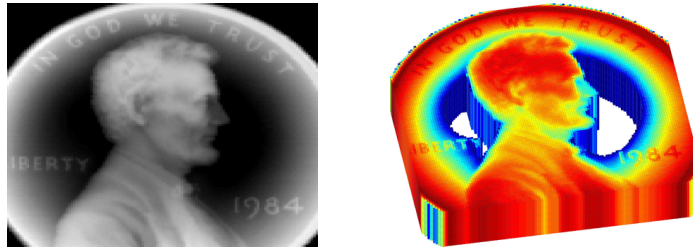
Metaballs can be used to define objects implicitly, e.g., as all the points \vec{x} that satisfy

$$\sum_i m(\vec{x} - \vec{x}_i, r_i) \leq C, \quad C \in \mathbb{R}^+$$

Use this approach and try to make grids similar to the ones shown below:



18. A simple way to make test models with funny geometries is to use the method of fictitious and let an image define the domain of interest. In the example below, the image was taken from `penny`, which is one of the standard data sets that are distributed with MATLAB, and then used to define the geometry of the grid and assign permeability values



Pick your own favorite image or make one in a drawing program and use `imread` to load the image into MATLAB as a 3D array, which you can use to define your geometry and petrophysical values. If you do not have an image at hand, you can use `penny` or `spine`. For `penny`, in particular, you may have to experiment a bit with the threshold used to define your domain to ensure that all cells are connected, i.e., that the grid you obtain consists of only one piece.

4.2 Unstructured grids

An unstructured grid consists of a set of simple shapes that are laid out in an irregular pattern so that any number of cells can meet at a single vertex. The topology of the grid will therefore change throughout space. An unstructured grid can generally consist of a combination of polyhedral cells with varying number of faces, as we will see below. However, the most common forms of unstructured grids are based on triangles in 2D and tetrahedrons in 3D. These grids are very flexible and are relatively easy to adapt to complex domains and structures or refine to provide increased local resolution.

Unlike structured grids, unstructured grids cannot generally be efficiently referenced using a structured multi-index. Instead, one must describe a list of connectivities that specifies the way a given set of vertices make up individual element and element faces, and how these elements are connected to each other via faces, edges, and vertices.

To understand the properties and construction of unstructured grids, we start by a brief discussion of two concepts from computational geometry: Delaunay tessellation and Voronoi diagrams. Both these concepts are supported by standard functionality in MATLAB.

4.2.1 Delaunay tessellation

A tessellation of a set of generating points $\mathcal{P} = \{x_i\}_{i=1}^n$ is defined as a set of simplices that completely fills the convex hull of \mathcal{P} . The convex hull H of \mathcal{P} is the convex minimal set that contains \mathcal{P} and can be described constructively as the set of convex combinations of a finite subset of points from \mathcal{P} ,

$$H(\mathcal{P}) = \left\{ \sum_{i=1}^{\ell} \lambda_i x_i \mid x_i \in \mathcal{P}, \lambda_i \in \mathbb{R}, \lambda_i \geq 0, \sum_{i=1}^{\ell} \lambda_i = 1, 1 \leq \ell \leq n \right\}.$$

Delaunay tessellation is by far the most common method of generating a tessellation based on a set of generating points. In 2D, the Delaunay tessellation consists of a set of triangles defined so that three points form the corners of a Delaunay triangle only when the circumcircle that passes through them contains no other points, see Figure 4.5. The definition using circumcircles can readily be generalized to higher dimensions using simplices and hyperspheres.

The center of the circumcircle is called the circumcenter of the triangle. We will come back to this quantity when discussing Voronoi diagrams in the next subsection. When four (or more) points lie on the same circle, the Delaunay triangulation is not unique. As an example, consider four points defining a rectangle. Using either of the two diagonals will give two triangles satisfying the Delaunay condition.

The Delaunay triangulation can alternatively be defined using the so-called max-min angle criterion, which states that the Delaunay triangulation is the one that maximizes the minimum angle of all angles in a triangulation, see

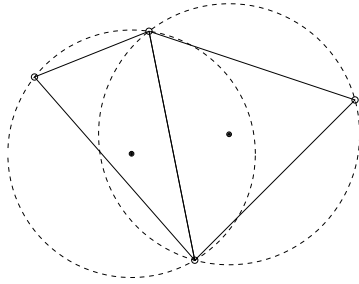


Fig. 4.5. Two triangles and their circumcircles.

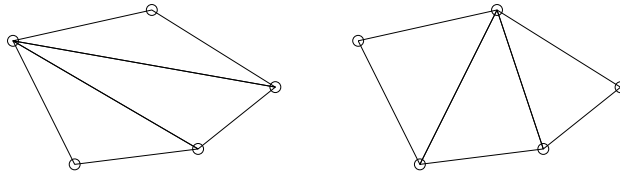


Fig. 4.6. Example of two triangulations of the same five points; the triangulation to the right satisfies the min-max criterion.

Figure 4.6. Likewise, the Delaunay triangulation minimizes the largest circum-circle and minimizes the largest min-containment circle, which is the smallest circle that contains a given triangle. Additionally, the closest two generating points are connected by an edge of a Delaunay triangulation. This is called the closest-pair property, and such two neighboring points are often referred to as natural neighbors. This way, the Delaunay triangulation can be seen as the natural tessellation of a set of generating points.

Delaunay tessellation is a popular research topic and there exists a large body of literature on theoretical aspects and computer algorithms. Likewise, there are a large number of software implementations available on the net. For this reason, MRST does not have any routines for generating tessellations based on simplexes. Instead, we have provided simple routines for mapping a set of points and edges, as generated by MATLAB's Delaunay triangulation routines, to the internal data structure used to represent grids in MRST. How they work, will be illustrated in terms of a few simple examples.

In the first example, we use routines from MATLAB's `polyfun` toolbox to triangulate a rectangular mesh and convert the result using the MRST routine `triangleGrid`:

```
[x,y] = meshgrid(1:10,1:8);
t = delaunay(x(:),y(:));
G = triangleGrid([x(:) y(:)],t);
plot(x(:),y (:), 'o', 'MarkerSize',8);
plotGrid(G,'FaceColor','none');
```

Depending on what version you have of MATLAB, the 2D Delaunay routine `delaunay` will produce one of the triangulations shown in Figure 4.7. In older versions of MATLAB, the implementation of `delaunay` was based on 'QHULL' (see <http://www.qhull.org>), which produces the unstructured triangulation shown in the right plot. MATLAB 7.9 and newer has improved routines for 2-D and 3-D computational geometry, and here `delaunay` will produce the structured triangulation shown in the left plot. However, the n-D tessellation routine `delaunayn(x(:) y (:))` is still based on 'QHULL' and will generally produce an unstructured tessellation, as shown in the right plot.

If the set of generating points is structured, e.g., as one would obtain by calling either `meshgrid` or `ndgrid`, it is straightforward to make a structured triangulation. The following skeleton of a function makes a 2D triangulation and can easily be extended by the interested reader to 3D:

```
function t = mesh2tri(n,m)
[I,J]=ndgrid(1:n-1, 1:m-1); p1=sub2ind([n,m],I(:),J(:));
[I,J]=ndgrid(2:n , 1:m-1); p2=sub2ind([n,m],I(:),J (:));
[I,J]=ndgrid(1:n-1, 2:m ); p3=sub2ind([n,m],I (:),J (:));
[I,J]=ndgrid(2:n , 1:m-1); p4=sub2ind([n,m],I (:),J (:));
[I,J]=ndgrid(2:n , 2:m ); p5=sub2ind([n,m],I (:),J (:));
[I,J]=ndgrid(1:n-1, 2:m ); p6=sub2ind([n,m],I (:),J (:));
t = [p1 p2 p3; p4 p5 p6];
```

In Figure 4.8, we have used the demo case `seamount` that is supplied with MATLAB as an example of a more complex unstructured grid

```
load seamount;
plot(x(:),y (:), 'o');
G = triangleGrid([x(:) y (:)]);
plotGrid(G,'FaceColor',[.8 .8 .8]); axis off;
```

The observant reader will notice that here we do not explicitly generate a triangulation before calling `triangleGrid`; if the second argument is omitted, the routine uses MATLAB's built-in `delaunay` triangulation as default.

For 3D grids, MRST supplies a conversion routine `tetrahedralGrid(P, T)` that constructs a valid grid definition from a set of points P ($m \times 3$ array

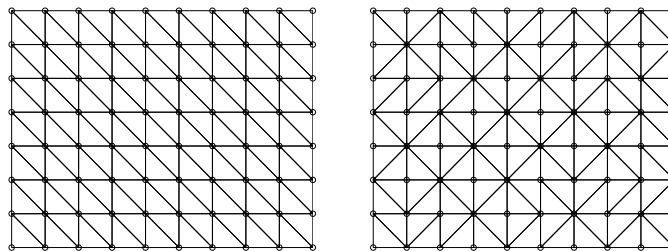


Fig. 4.7. Two different Delaunay tessellations of a rectangular point mesh.

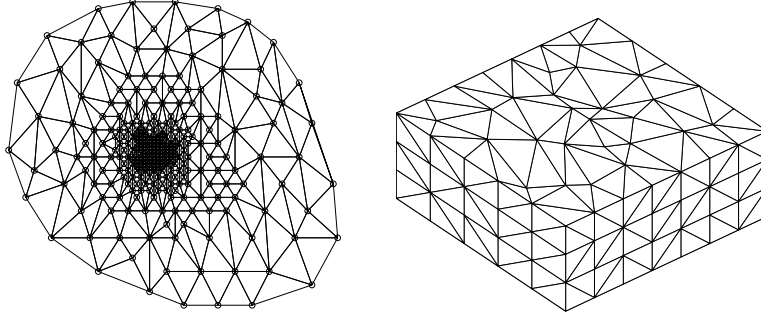


Fig. 4.8. The left plot shows the triangular grid from the `seamount` demo case. The right plot shows a tetrahedral tessellation of a 3D point mesh.

of node coordinates) and a tetrahedron list T (n array of node indices). The tetrahedral tessellation shown to the right in Figure 4.8 was constructed from a set of generating points defined by perturbing a regular hexahedral point mesh:

```
N=7; M=5; K=3;
[x,y,z] = ndgrid(0:N,0:M,0:K);
x(2:N,2:M,:) = x(2:N,2:M,:) + 0.3*randn(N-1,M-1,K+1);
y(2:N,2:M,:) = y(2:N,2:M,:) + 0.3*randn(N-1,M-1,K+1);
G = tetrahedralGrid([x(:) y(:) z(:)]);
plotGrid(G, 'FaceColor',[.8 .8 .8]); view(-40,60); axis tight off
```

4.2.2 Voronoi diagrams

The Voronoi diagram of a set of points $\mathcal{P} = \{x_i\}_{i=1}^n$ is the partitioning of Euclidean space into n (possibly unbounded) convex polytopes¹ such that each polytope contains exactly one generating point x_i and every point inside the given polytope is closer to its generating point than any other point in \mathcal{P} . The convex polytopes are called Voronoi cells (or Voronoi regions). Mathematically, the Voronoi cell $V(x_i)$ of generating point x_i in \mathcal{P} can be defined as

$$V(x_i) = \left\{ x \mid \|x - x_i\| < \|x - x_j\| \forall j \neq i \right\}. \quad (4.1)$$

A Voronoi region is not closed in the sense that a point that is equally close to two or more generating points does not belong to the region defined by (4.1). Instead, these points are said to lie on the Voronoi segments and can be included in the Voronoi cells by defining the closure of $V(x_i)$, using “ \leq ” rather than “ $<$ ” in (4.1).

¹ A polytope is a generic term that refers to a polygon in 2D, a polyhedron in 3D, and so on.

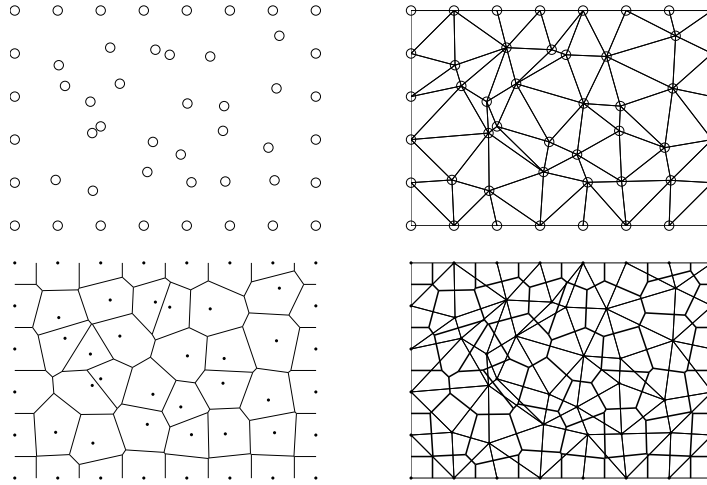


Fig. 4.9. Duality between Voronoi diagrams and Delaunay triangulation. From top left to bottom right: generating points, Delaunay triangulation, Voronoi diagram, and Voronoi diagram (thick lines) and Delaunay triangulation (thin lines).

The Voronoi cells for all generating points lying at the convex hull of \mathcal{P} are unbounded, all other Voronoi cells are bounded. For each pair of two points x_i and x_j , one can define a hyperplane with co-dimension one consisting of all points that lie equally close to x_i and x_j . This hyperplane is the perpendicular bisector to the line segment between x_i and x_j and passes through the midpoint of the line segment. The Voronoi diagram of a set of points can be derived directly as the *dual* of the Delaunay triangulation of the same points. To understand this, we consider the planar case, see Figure 4.9. For every triangle, there is a polyhedron in which vertices occupy complementary locations:

- The circumcenter of a Delaunay triangle corresponds to a vertex of a Voronoi cell.
- Each vertex in the Delaunay triangulation corresponds to, and is the center of, a Voronoi cell.

Moreover, for locally orthogonal Voronoi diagrams, an edge in the Delaunay triangulation corresponds to a segment in the Voronoi diagram and the two intersect each other orthogonally. However, as we can see in Figure 4.9, this is not always the case. If the circumcenter of a triangle lies outside the triangle itself, the Voronoi segment does not intersect the corresponding Delaunay edge. To avoid this situation, one can perform a constrained Delaunay triangulation and insert additional points where the constraint is not met (i.e., the circumcenter is outside its triangle).

Figure 4.10 shows three examples of planar Voronoi diagrams generated from 2D point lattices using the MATLAB-function `voronoi`. MRST does not

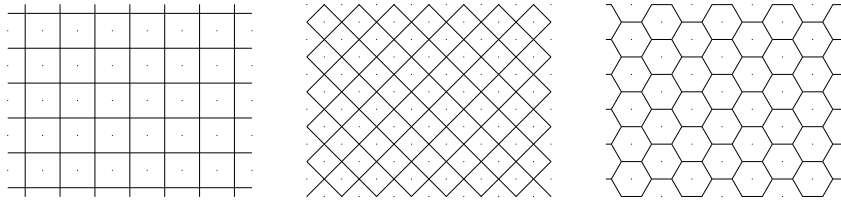


Fig. 4.10. Three examples of Voronoi diagrams generated from 2D point lattices. From left to right: square lattice, square lattice rotated 45 degrees, lattice forming equilateral triangles.

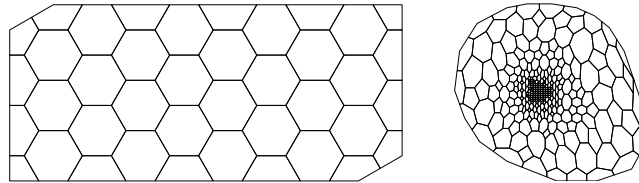


Fig. 4.11. Two examples of Voronoi grids. The left plot shows a honeycombed PEBI grid and the right plot shows the PEBI grid derived from the `seamount` demo case.

yet have a similar function that generates a Voronoi grid from a point set, but offers `V=pebi(T)` that generates a locally orthogonal, 2D Voronoi grid `V` as a dual to a triangular grid `T`. The grids are constructed by connecting the perpendicular bisectors of the edges of the Delaunay triangulation, hence the name perpendicular bisector (PEBI) grids. To demonstrate the functionality, we first generate a honeycombed grid similar to the one shown in the right plot in Figure 4.10

```
[x,y] = meshgrid([0:4]*2*cos(pi/6),0:3);
x = [x(:); x(:)+cos(pi/6)];
y = [y(:); y(:)+sin(pi/6)];
G = triangleGrid([x,y]);
plotGrid(pebi(G), 'FaceColor','none'); axis equal off
```

The result is shown in Figure 4.11. As a second example, we reiterate the `seamount` examples shown in Figure 4.8

```
load seamount
V = pebi(triangleGrid([x y]));
plotGrid(V,'FaceColor',[.8 .8 .8]); axis off;
```

Several of the examples discussed above can also be found in the fifth video of the second MRST Jolt [114]. Since `pebi` is a 2D code, we cannot apply it directly to the 3D tetrahedral grid shown in Figure 4.8 to generate a dual 3D Voronoi grid. In the next section, we discuss a simple approach in geological modeling in which we extrude 2D Voronoi grid to 3D to preserve geological layering. The interested reader should consult [129] and references therein for more discussion of general 3D Voronoi grids.

4.2.3 Other types of tessellations

Tessellations come in many other forms than the Delaunay and Voronoi types discussed in the two previous sections. Tessellations are more commonly referred to as tilings and are patterns made up of geometric forms (tiles) that are repeated over and over without overlapping or leaving any gaps. Such tilings can be found in many patterns of nature, like in honeycombs, giraffe skin, pineapples, snake skin, tortoise shells, to name a few. Tessellations have also been extensively used for artistic purposes since ancient times, from the decorative tiles of Ancient Rome and Islamic art to the amazing artwork of M. C. Esher. For completeness (and fun), MRST offers the function `tessellationGrid` that can take a tessellation consisting of symmetric n -polygons and turn it into a correct grid structure. While this may not be very useful in modeling petroleum reservoirs, it can easily be used to generate irregular grids that can be used to stress-test various discretization methods. Let us first use it to make a standard $n \times m$ Cartesian mesh:

```
[x,y] = meshgrid(linspace(0,1,n+1),linspace(0,1,m+1));
I = reshape(1:(n+1)*(m+1),m+1,n+1);
T = [reshape(I(1:end-1,1:end-1),[],1)'; reshape(I(1:end-1,2:end ),[],1)';
     reshape(I(2:end, 2:end ),[],1)'; reshape(I(2:end, 1:end -1),[],1)'];
G = tessellationGrid([x(:) y(:)], T);
```

Here, the vertices and cells are numbered first in the y direction and then in the x -direction, so that the first two lines in `T` read `[1 m+2 m+3 2; 2 m+3 m+4 3]`, and so on.

There are obviously many ways to make more general tilings. The script `showTessellation` in the `book` module shows two slightly different approaches. To generate the alternating convex/concave hexagonal tiling illustrated in Figure 4.12 we first generate the convex and the concave tiles. These will have symmetry lines that together form a triangle for each tile, which we can use to glue the tiles together. If we glue a convex (blue) to the right edge of the concave (yellow) tile and likewise glue a concave (yellow) tile to the right of the upper convex (blue) tile, we get a dodecagon consisting of two convex and two concave tiles. This composite tile can now be placed on a regular mesh; in Figure 4.12 we have used a 4×2 regular mesh.

To generate the tiling shown in Figure 4.13 we start from an equilateral triangulation (\mathbf{p}, \mathbf{t}) covering a certain part of space. We then extract the endpoints p_1 and p_2 on each edge and compute the angle ϕ the line between them makes with the x -axis. We will use this information to perturb the points. By using this orientation of the lines, we can easily make sure that the original triangles can be turned into matching $3n$ -polygons for $n = 2, 3, \dots$, if we for each triple of new points we add, describe the point added to the original $p_1 p_2$ line on the form (with α and β constants for each triplet):

$$x = p_1 + \alpha |p_2 - p_1| [\cos(\phi + \beta), \sin(\phi + \beta)].$$

Figure 4.13 shows that consecutive addition of four points on each original line segment, thereby turning a triangulation into a pentadecagonal tessellation.

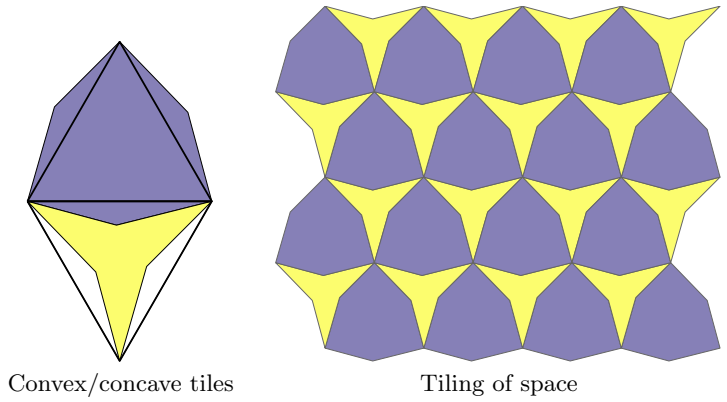


Fig. 4.12. Tiling consisting of alternating convex and concave hexahedrons.

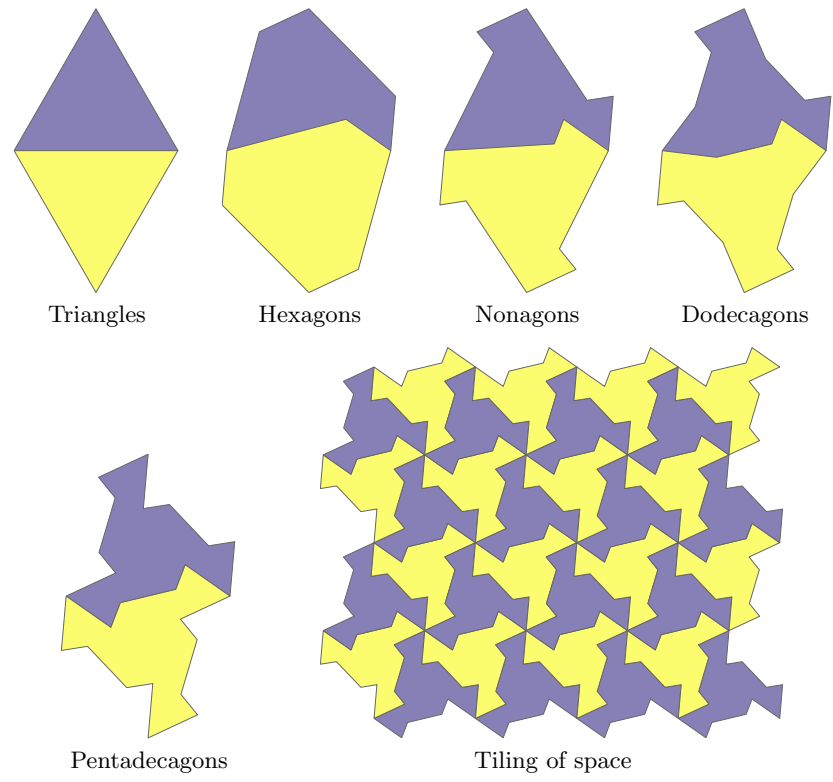


Fig. 4.13. Gradual creation of a tiling consisting of irregular pentadecagons. (Can you see the hen facing left and the man running towards the right?).

4.2.4 Using an external mesh generator

Using a Delaunay triangulation as discussed above, we can generate grids that fit a given set of vertices. However, in most applications, the vertex points are not given *a priori* and all one wants is a reasonable grid that fits an exterior boundary describing the perimeter of the domain and possibly also a set of interior boundaries and/or features, which in the case of subsurface media could be faults or major fractures. To this end, one typically will have to use a mesh generator. There are a large number of mesh generators available online, and in principle any of these can be used in combination with MRST's grid factory routines as long as they produce triangulations on the form outlined above. My personal favorite is `DistMesh` by Persson and Strang [157]. While most mesh generators tend to be complex and quite inaccessible codes, `DistMesh` is a relatively short and simple MATLAB code written in the same spirit as MRST. The performance of the code may not be optimal, but the user can go in and inspect all algorithms and modify them to his or her purpose. In the following, we will use `DistMesh` to generate a few examples of more complex triangular and Voronoi grids in 2D.

`DistMesh` is distributed under the GNU GPL license (which is the same license that MRST uses) and can be downloaded from the software's webpage. The simplest way to integrate `DistMesh` with MRST is to install it as a 3rd-party module. Assuming that you are connected to internet, this is done as follows:

```
path = fullfile(ROOTDIR,'utils','3rdparty','distmesh');
mkdir(path)
unzip('http://persson.berkeley.edu/distmesh/distmesh.zip', path);
mrstPath('reregister', 'distmesh', path);
```

You are now ready to start using the software. If you intend to use `DistMesh` many times, you should copy the last line to the `startup_user.m` file in the MRST root directory.

In `DistMesh`, the perimeter of the domain is represented using a signed distance function $d(x, y)$, which is by definition set to be negative inside the region. The software offers a number of utility functions that makes it simple to describe relatively complex geometries, as we shall see in the following. Let us start with a simple example, which is taken from the `DistMesh` webpage: Consider a square domain $[-1, 1] \times [-1, 1]$ with a circular cutout of radius 0.5 centered at the origin. We start by making a grid that has a uniform target size $h = 0.2$

```
mrstModule add distmesh;
fd=@(p) ddiff(drectangle(p,-1,1,-1,1), dcircle(p,0,0,0.5));
[p,t]=distmesh2d(fd, @huniform, 0.2, [-1,-1;1,1], [-1,-1;-1,1;1,-1;1,1]);
G = triangleGrid(p, t);
```

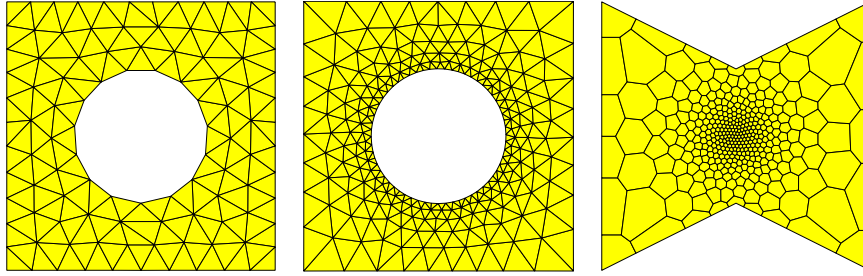


Fig. 4.14. Grids generated by the `DistMesh` grid generator.

Here, we have used utility functions `ddif`, `drectangle` and `dcircle` to compute the signed distance from the outer and the inner perimeter. Likewise, the `uniform` to set enforce uniform cell size equal distance between the points in the initial, which here is 0.2. The fourth argument is the bounding box of our domain, and the fifth argument consist of fixed points that the algorithm is not allowed to move. After the triangulation has been computed by `distmesh2d` we pass it to `triangleGrid` to make a MRST grid structure. The resulting grid is shown to the left in Figure 4.14.

As a second test, let us make a graded grid that has a mesh size of approximately 0.05 at the inner circle and 0.2–0.35 at the outer perimeter. To enforce this, we replace the `uniform` function by another function that gives the correct mesh size distribution

```
fh=@(p) 0.05+0.3*dcircle(p,0,0,0.5);
[p,t]=distmesh2d(fd, fh, 0.05,[-1,-1;1,1], [-1,-1;-1,1;1,-1;1,1]);
```

The resulting grid is shown in the middle plot in Figure 4.14 and has the expected grading from the inner boundary and outwards to the perimeter.

In our last example, we will create a graded triangulation of a polygonal domain and then use `pebi` to compute its Voronoi diagram

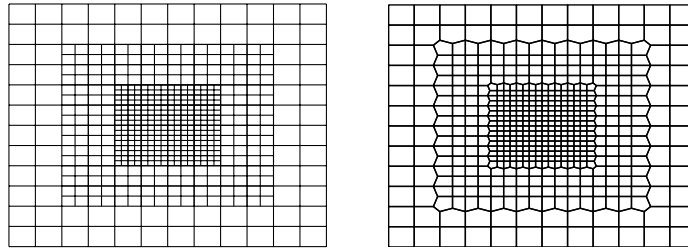
```
pv = [-1 -1; 0 -.5; 1 -1; 1 1; 0 .5; -1 1; -1 -1];
fh = @(p,x) 0.025 + 0.375*sum(p.^2,2);
[p,t] = distmesh2d(@dpoly, fh, 0.025, [-1 -1; 1 1], pv, pv);
G = pebi(triangleGrid(p, t));
```

Here, we use the utility function `dpoly(p,pv)` to compute the signed distance of any point set `p` to the polygon with vertices in `pv`. Notice that `pv` must form a closed path. Likewise, since the signed distance function and the grid density function are assumed to take the same number of arguments, `fh` is created with a dummy argument `x`. The argument sent to these functions are passed as the sixth argument to `distmesh2d`. The resulting grid is shown to the right in Figure 4.14.

`DistMesh` also has routines for creating nD triangulations and triangulations of surfaces, but these are beyond the scope of the current presentation.

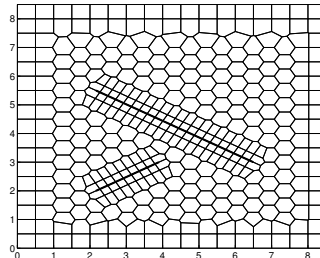
COMPUTER EXERCISES:

19. Create MRST grids from the standard data sets `trimesh2d` and `tetmesh`. How would you assign lognormal petrophysical parameters to these grids so that the spatial correlation is preserved?
20. In MRST all triangular grids are assumed to be planar so that each vertex can be given by a 2D coordinate. However, triangular grids are commonly used to represent non-planar surfaces in 3D. Can you extend the function `triangleGrid` so that it can construct both 2D and 3D grids? You can use the data set `trimesh3d` as an example of a triangulated 3D surface.
21. MRST does not yet have a grid factory routine to generate structured grids with local, nested refinement as shown in the figure to the left below.



Try to use a combination of `triangleGrid` and `pebi` to make a good approximation to such a grid as shown to the right in the figure above. (Hint: to get rid of artifacts, one layer of cells were removed along the outer boundary.)

22. The figure below shows an unstructured hexagonal grid that has been adapted to two faults in the interior of the domain and padded with rectangular cells near the boundary. Try to implement a routine that generates a similar grid.



Hint: in this case, the strike direction of the faults are $\pm 30^\circ$ and the start and endpoints of the faults have been adjusted so that they coincide with the generating points of hexagonal cells.

23. What would you do to fit the tessellations in Figures 4.12 and 4.13 so that they fill a rectangular box without leaving any gaps along the border?
24. Download and install `distmesh` and try to make MRST grids from all the triangulations shown in [157, Fig. 5.1].

4.3 Stratigraphic grids

In the previous chapter, we saw that grid models are used as an important ingredient in describing the geometrical and petrophysical properties of a subsurface reservoir. This means that the grid is closely attached to the parameter description of the flow model and, unlike in many other disciplines, cannot be chosen arbitrarily to provide a certain numerical accuracy. Indeed, the grid is typically chosen by a geologist who tries to describe the rock body by as few volumetric cells as possible and who basically does not care too much about potential numerical difficulties his or her choice of grid may cause in subsequent flow simulations. This statement is, of course, grossly simplified but is important to bear in mind throughout the rest of this chapter.

The industry standard for representing the reservoir geology in a flow simulator is through the use of a stratigraphic grid that is built based on geological horizons and fault surfaces. The volumetric grid is typically built by extruding 2D tessellations of the geological horizons in the vertical direction or in a direction following major fault surfaces. For this reason, some stratigraphic grids, like the PEBI grids that we will meet in Section 4.3.2, are often called 2.5D rather than 3D grids. These grids may be unstructured in the lateral direction, but have a clear structure in the vertical direction to reflect the layering of the reservoir.

Because of the role grid models play in representing geological formations, real-life stratigraphic grids tend to be highly complex and have unstructured connections induced by the displacements that have occurred over faults. Another characteristic feature is high aspect ratios. Typical reservoirs extend several hundred or thousand meters in the lateral direction, but the zones carrying hydrocarbon may be just a few tens of meters in the vertical direction and consist of several layers with (largely) different rock properties. Getting the stratigraphy correct is crucial, and high-resolution geological modeling will typically result in a high number of (very) thin grid layers in the vertical direction, resulting in two or three orders of magnitude aspect ratios.

A full exposition of stratigraphic grids is way beyond the scope of this book. In next two subsections, we will discuss the basics of the two most commonly used forms of stratigraphic grids. A complementary discussion is given in videos 2, 6, and 7 of the second MRST Jolt [114].

4.3.1 Corner-point grids

To model the geological structures of petroleum reservoirs, the industry-standard approach is to introduce what is called a corner-point grid [160], which we already encountered in Chapter 3.5. A corner-point grid consists of a set of hexahedral cells that are topologically aligned in a Cartesian fashion so that the cells can be numbered using a logical ijk index. In its simplest form, a corner-point grid is specified in terms of a set of vertical or inclined pillars defined over an areal Cartesian 2D mesh in the lateral direction. Each

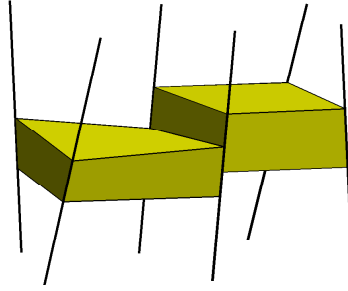


Fig. 4.15. Each cell in the corner-point grid is restricted by four pillars and two points on each pillar.

cell in the volumetric grid has eight *logical* corner points that are restricted by four pillars and specified as two depth-coordinates on each pillar, see Figure 4.15. Each grid consists of $n_x \times n_y \times n_z$ grid cells and the cells are ordered with the i -index (x -axis) cycling fastest, then the j -index (y -axis), and finally the k -index (negative z -direction). All cellwise property data are assumed to follow the same numbering scheme.

As discussed previously, a fictitious domain approach is used to embed the reservoir in a logically Cartesian shoe-box. This means that inactive cells that are not part of the physical model, e.g., as shown in Figure 3.16, are present in the topological ijk -numbering but are indicated by a zero porosity or net-to-gross value, as discussed in Chapter 3.4 or marked by a special boolean indicator (called ACTNUM in the input files).

So far, the topology and geometry of a corner-point grid have not deviated from that of the mapped Cartesian grids studied in the previous section. Somewhat simplified, one may view the logical ijk numbering as a reflection of the sedimentary rock bodies as they may have appeared at geological 'time zero' when all rock facies have been deposited as part of horizontal layers in the grid (i.e., cells with varying i and j but constant k). To model geological features like erosion and pinch-outs of geological layers, the corner-point format allows point-pairs to collapse along pillars. This creates degenerate hexahedral cells that may have less than six faces, as illustrated in Figure 4.16. The corner points can even collapse along all four pillars, so that a cell completely disappears. This will implicitly introduce a new topology, which is sometimes referred to as 'non-neighboring connections', in which cells that are not logical k neighbors can be neighbors and share a common face in physical space. An example of a model that contains both eroded geological layers and fully collapsed cells is shown in Figure 4.17. In a similar manner, (simple) vertical and inclined faults can be easily modelled by aligning the pillars with fault surfaces and displacing the corner points defining the neighboring cells on one or both sides of the fault. This way, one creates non-matching geometries and non-neighboring connections in the underlying ijk topology.

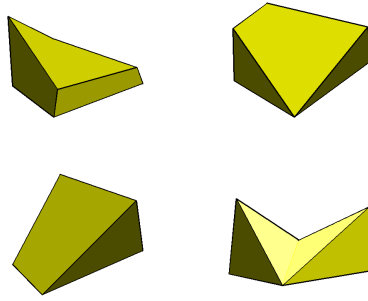


Fig. 4.16. Examples of deformed and degenerate hexahedral cells arising in corner-point grid models.

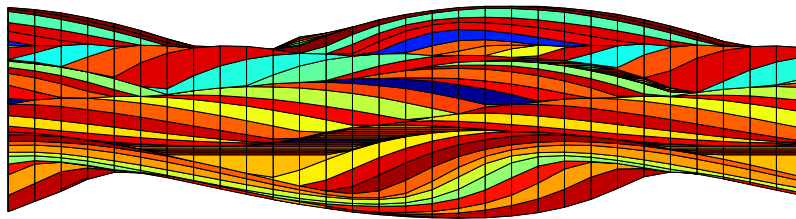


Fig. 4.17. Side view in the xz -plane of corner-point grid with vertical pillars modeling a stack of sedimentary beds (each layer indicated by a different color).

To illustrate the concepts introduced so far, we consider a low-resolution version of the model from Figure 3.11 on page 62 created by the `simpleGrdecl` grid-factory routine, which generates an input stream containing the basic keywords that describe a corner-point grid in the Eclipse input deck

```
grdecl = simpleGrdecl([4, 2, 3], .12, 'flat', true);
```

```
grdecl =
  cartDims: [4 2 3]
  COORD: [90x1 double]
  ZCORN: [192x1 double]
  ACTNUM: [24x1 int32]
```

The 5×3 mesh of pillars are given in terms of a pair of 3D coordinates for each pillar in the `COORD` field, whereas the z -values that determine vertical positions uniquely along each pillar for the eight corner-points of the 24 cells are given in the `ZCORN` field. To extract these data, we use two MRST routines

```
[X,Y,Z] = buildCornerPtPillars(grdecl,'Scale',true);
[x,y,z] = buildCornerPtNodes(grdecl);
```

Having obtained the necessary data, we plot the pillars and the corner-points and mark pillars on which the corner-points of logical ij neighbors do not coincide,

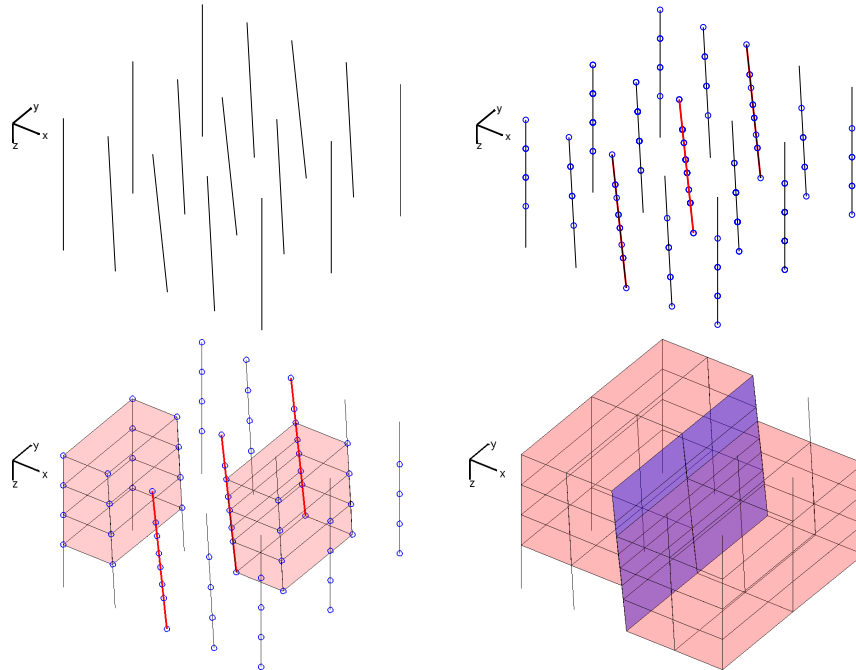


Fig. 4.18. Specification of a corner-point grid. Starting from the pillars (upper left), we add corner-points and identify pillars containing non-matching corner marked in red (upper right). A stack of cells is created for each set of four pillars (lower left), and then the full grid is obtained (lower right). In the last plot, the fault faces have been marked in blue.

```

% Plot pillars
plot3(X',Y',Z', 'k');
set(gca,'zdir','reverse'), view(35,35), axis off, zoom(1.2);

% Plot points on pillars , mark pillars with faults red
hold on; I=[3 8 13];
hpr = plot3(X(I,:),Y(I,:),Z(I,:), 'r', 'LineWidth',2);
hpt = plot3(x(:),y(:),z(:), 'o'); hold off;

```

The resulting plots are shown in the upper row of Figure 4.18, in which we clearly see how the pillars change slope from the east and west side toward the fault in the middle, and how the grid points sit like beads-on-a-string along each pillar.

Cells are now defined by connecting pairs of points from four neighboring pillars that make up a rectangle in the lateral direction. To see this, we plot two vertical stacks of cells and finally the whole grid with the fault surface marked in blue:

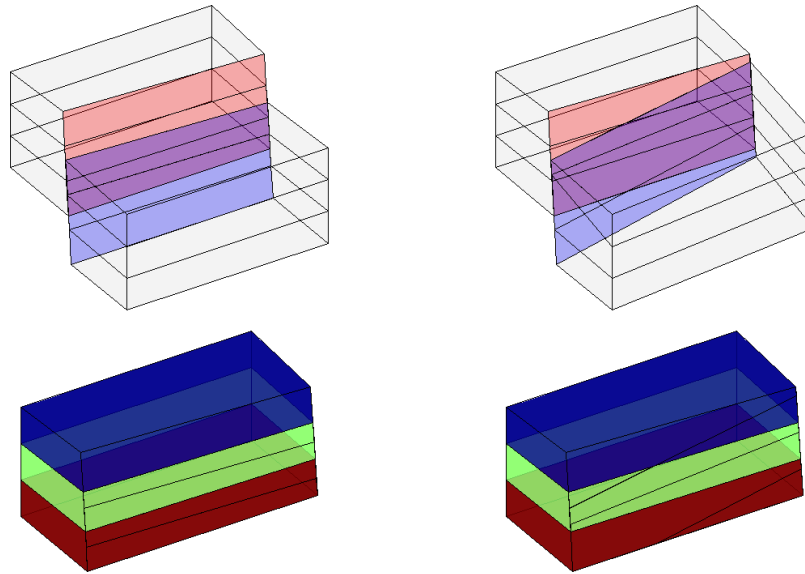


Fig. 4.19. Subdivision of fault face in two three-dimensional models. In the left column, the subfaces are all rectangular. In the right columns they are not. In both the upper plots, the faces marked in red belong only to the cells behind the fault surface, the blue faces belong only to the cells in front of the fault surface, and the magenta ones belong to cells on both sides. The lower plot shows the cells behind the surface, where each cell has been given its own color.

```

% Create grid and plot two stacks of cells
G = processGRDECL(grdecl);
args = {'FaceColor'; 'r'; 'EdgeColor'; 'k'};
hcst = plotGrid(G,[1:8:24 7:8:24], 'FaceAlpha', .1, args{:});

% Plot cells and fault surface
delete([hpt; hpr; hcst]);
plotGrid(G,'FaceAlpha', .15, args{:});
plotFaces(G, G.faces.tag>0,'FaceColor','b','FaceAlpha',.4);

```

The upper-left plot in Figure 4.19 shows the same model sampled with even fewer cells. To highlight the non-matching cell faces along the fault plane we have used different coloring of the cell faces on each side of the fault. In MRST, we have chosen to represent corner-point grids as *matching* unstructured grids obtained by subdividing all non-matching cell faces, instead of using the more compact non-matching hexahedral form. For the model in Figure 4.19, this means that the four cells that have non-neighboring connections across the fault plane will have seven and not six faces. For each such cell, two of the seven faces lie along the fault plane. For the regular model studied here, the

subdivision results in new faces that all have four corners (and are rectangular). However, this is not generally the case, as is shown in the right column of Figure 4.19, where we can see cells with six, seven, eight faces, and faces with three, four, and five corners. Indeed, for real-life models, subdivision of non-matching fault faces can lead to cells that have much more than six faces.

Using the inherent flexibility of the corner-point format it is possible to construct very complex geological models that come a long way in matching the geologist's perception of the underlying rock formations. Because of their many appealing features, corner-point grids have been an industry standard for years and the format is supported in most commercial software for reservoir modeling and simulation.

A synthetic faulted reservoir

In our first example, we consider a synthetic model of two intersecting faults that make up the letter Y in the lateral direction. The two fault surfaces are highly deviated, making an angle far from 90 degrees with the horizontal direction. To model this scenario using corner-point grids, we basically have two different choices. The first choice, which is quite common, is to let the pillars (and hence the extrusion direction) follow the main fault surfaces. For highly deviated faults, like in the current case, this will lead to extruded cells that are far from K -orthogonal and hence susceptible to grid-orientation errors in a subsequent simulation, as will be discussed in more detail in Chapter 8. Alternatively, we can choose a vertical extrusion direction and replace deviated fault surfaces by stair-stepped approximations so that the faults zigzag in direction not aligned with the grid. This will create cells that are mostly K -orthogonal and less prone to grid-orientation errors.

Figure 4.20 shows two different grid models, taken from the CaseB4 data set. In the stair-stepped model, the use of cells with orthogonal faces causes the faults to be represented as zigzag patterns. The pillar grid correctly represents the faults as inclined planes, but has cells with degenerate geometries and cells that deviate strongly from being orthogonal in the lateral direction. Likewise, some pillars have close to 45 degrees inclination, which will likely give significant grid-orientation effects in a standard two-point scheme.

A simulation model of the Norne Field

Norne is an oil and gas field lies located in the Norwegian Sea. The reservoir is found in Jurassic sandstone at a depth of 2500 meter below sea level, and was originally estimated to contain 90.8 million m^3 oil, mainly in the Ile and Tofte formations, and 12.0 billion m^3 in the Garn formation. The field is operated by Statoil and production started in November 1997, using a floating production, storage and offloading (FPSO) ship connected to seven subsea templates at a water depth of 380 meters. The oil is produced with

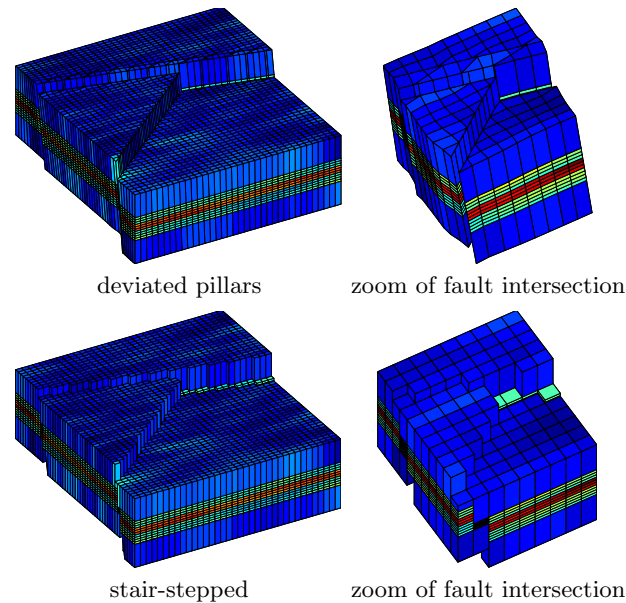


Fig. 4.20. Modeling the intersection of two deviated faults using deviated pillars (top) and stair-stepped approximation (bottom). **CaseB4** grids courtesy of Statoil.

water injection as the main drive mechanisms and the expected ultimate oil recovery is more than 60%, which is very high for a subsea oil reservoir. During thirteen years of production, five 4D seismic surveys of high quality have been recorded. Operator Statoil and partners (ENI and Petoro) have agreed with NTNU to release large amounts of subsurface data from the Norne field for research and education purposes. An important objective of this agreement is to establish a number of international benchmark cases based on real data for the testing of reservoir characterization/history matching and/or production optimization methodologies. More specifically, the Norne Benchmark data sets are hosted and supported by the Center for Integrated Operations in the Petroleum Industry (IO Center) at NTNU:

<http://www.ipt.ntnu.no/~norne/>

Here, we will use the simulation model released as part of “Package 2: Full field model” (2013) as an example of a real reservoir. We emphasize that the view expressed in the following are the views of the author and do not necessarily reflect the views of Statoil and the Norne license partners.

The model consists of a $46 \times 112 \times 22$ corner-point grid, given in the Eclipse format, which can be read as discussed for the SAIGUP model in Chapter 3.5. We start by plotting the whole model, including inactive cells. To this end,

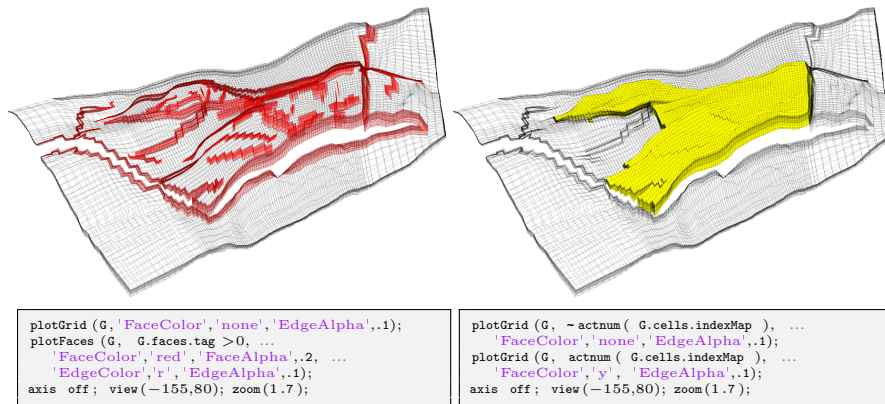


Fig. 4.21. The Norne field, a real model from the Norwegian Sea. The plots show the whole grid with fault faces marked in red (left) and active cells marked in yellow (right).

we need to override² the ACTNUM field before we start processing the input, because if the ACTNUM flag is set, all inactive cells will be ignored when the unstructured grid is built

```

actnum = grdecl.ACTNUM;
grdecl.ACTNUM = ones(prod(grdecl.cartDims),1);
G = processGRDECL(grdecl, 'checkgrid', false);

```

Having obtained the grid in the correct unstructured format, we first plot the outline of the whole model and highlight all faults and the active part of the model, see Figure 4.21. During the processing, all fault faces are tagged with a positive number. This can be utilized to highlight the faults: we simply find all faces with a positive tag, and color them with a specific color as shown in the left box in the figure. We now continue with the active model only. Hence, we reset the ACTNUM field to its original values so that inactive cells are ignored when we process the Eclipse input stream. In particular, we will examine some parts of the model in more detail. To this end, we will use the function `cutGrdecl` that extracts a rectangular box in index space from the Eclipse input stream, e.g., as follows

```

cut_grdecl = cutGrdecl(grdecl, [6 15; 80 100; 1 22]);
g = processGRDECL(cut_grdecl);

```

² At this point we hasten to warn the reader that inactive cells often contain garbage data and may generally not be inspected in this manner. Here, however, most inactive cells are defined in a reasonable way. By not performing basic sanity checks on the resulting grid (option `'checkgrid'=false`), we manage to process the grid and produce reasonable graphical output. In general, however, we strongly advise that `'checkgrid'` remains set in its default state of `true`.

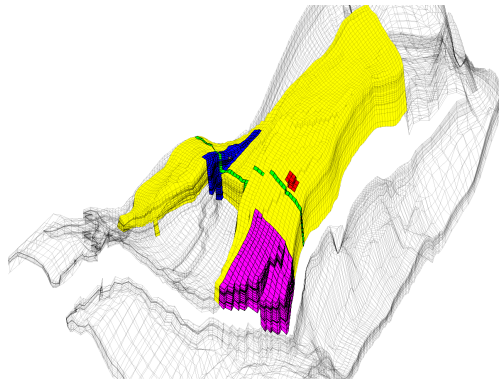
In Figure 4.22, we have zoomed in on four different regions. The first region (red color), is sampled near a laterally stair-stepped fault, which is a curved fault surface that has been approximated by a surface that zigzags in the lateral direction. We also notice how the fault displacement leads to cells that are non-matching across the fault surface and the presence of some very thin layers (the thinnest layers may actually appear to be thick lines in the plot). The thin layers are also clearly seen in the second region (magenta color), which represents a somewhat larger sample from an area near the tip of one of the 'fingers' in the model. Here, we clearly see how similar layers have been strongly displaced across the fault zone. In the third (blue) region, we have colored the fault faces to clearly show the displacement and the hole through the model in the vertical direction, which likely corresponds to a shale layer that has been eliminated from the active model. Gaps and holes, and displacement along fault faces, are even more evident for the vertical cross-section (green region) for which the layers have been given different colors as in Figure 4.17. Altogether, the four views of the model demonstrate typical patterns that can be seen in realistic models.

Extensions, difficulties, and challenges

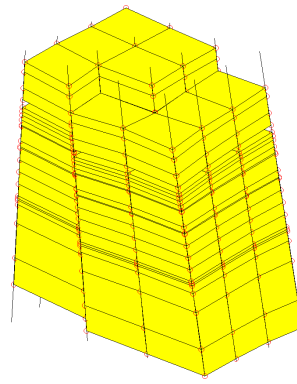
The original corner-point format has been extended in several directions, for instance to enable vertical intersection of two straight pillars in the shape of the letter Y. The pillars may also be piecewise polynomial curves, resulting in what is sometimes called S-faulted grids. Likewise, two neighboring pillars can collapse so that the basic grid shape becomes a prism rather than a hexahedron. However, there are several features that cannot easily be modelled, including multiple fault intersections (e.g., as in the letter 'F') and for this reason, the industry is constantly in search for improved gridding methods. One example will be discussed in the next subsection. First, however, we will discuss some difficulties and challenges, seen from the side of a computational scientist seeking to use corner-point grids for computations.

The flexible cell geometry of the corner-point format poses several challenges for numerical implementations. Indeed, a geocellular grid is typically chosen by a geologist who tries to describe the rock body by as few volumetric cells as possible and who basically does not care too much about potential numerical difficulties his or her choice of geometries and topologies may cause in subsequent flow simulations.

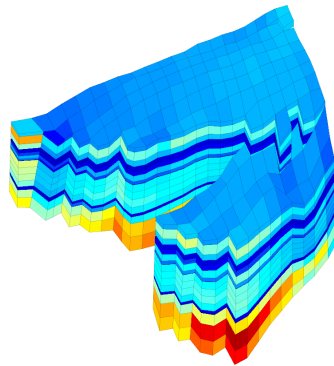
Writing a robust grid-processing algorithm to compute geometry and topology or determine an equivalent matching, polyhedral grid can be quite a challenge. Displacements across faults will lead to geometrically complex, non-conforming grids, e.g., as illustrated in Figure 4.22. Since each face of a grid cell is specified by four (arbitrary) points, the cell interfaces in the grid will generally be bilinear, possibly strongly curved surfaces. Geometrically, this can lead to several complications. Cell faces on different sides of a fault may intersect each other so that cells overlap volumetrically. Cell faces need



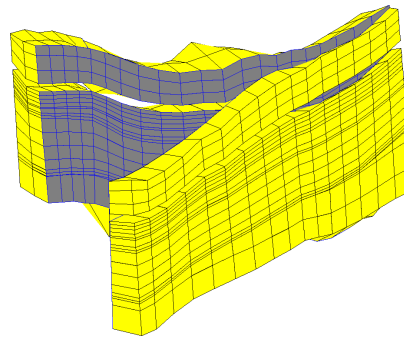
a) The whole model with active and inactive cells and four regions of interest marked in different colors



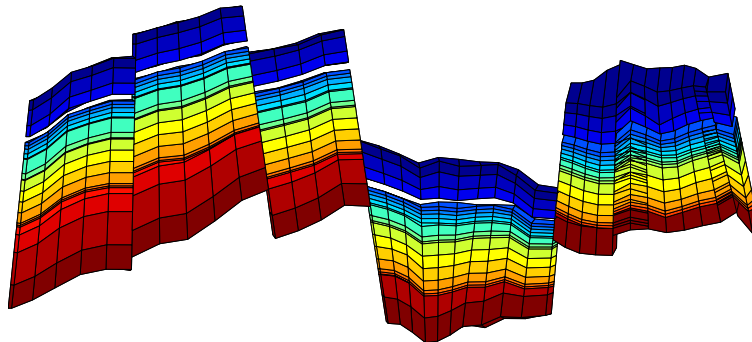
b) Zoom of the red region with pillars and corner-points shown as red circles



c) The magenta region with coloring according to cell volumes, which vary by a factor 700.



d) The blue region in which fault faces have been colored gray and the corresponding grid lines have been colored blue.



e) The green cross-section with coloring according to layer number from top to bottom of the model.

Fig. 4.22. Detailed view of subsets from the Norne simulation model.

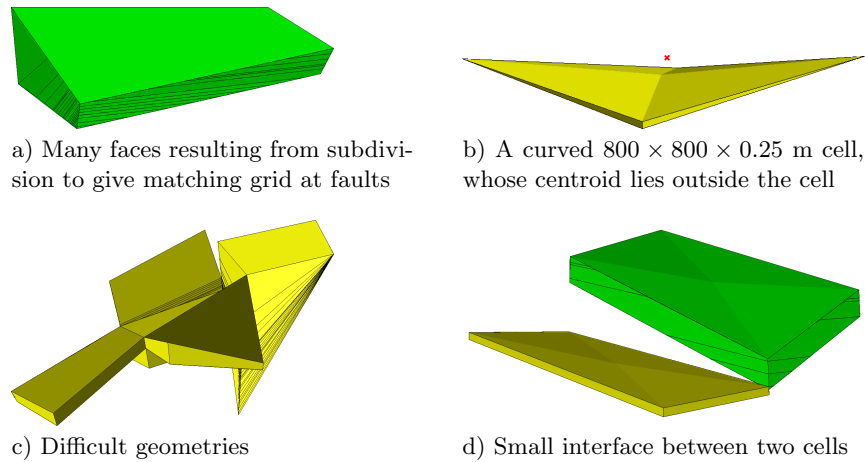


Fig. 4.23. Illustration of difficulties and challenges associated with real-life corner-point geometries.

not be matching, which may leave void spaces. There may be tiny overlap areas between cell faces on different sides a fault, and so on. All these factors contribute to make fault geometries hard to interpret in a consistent way: a subdivision into triangles is, for instance, not unique. Likewise, top and bottom surfaces may intersect for highly curved cells with high aspect ratios, cell centroids may be outside the cell volume, etc.

The presence of degenerate cells, in which the corner-points collapse in pairs, implies that the cells will generally be polyhedral and possibly contain both triangular and bilinear faces (see Figure 4.16). Corner-point cells will typically be non-matching across faults or may have zero volume, which both introduces coupling between non-neighboring cells and gives rise to discretization matrices with complex sparsity patterns. All these facts call for flexible discretizations that are not sensitive to the geometry of each cell or the number of faces and corner points. Although not a problem for industry-standard two-point discretizations, it will pose implementational challenges for more advanced discretization methods that rely on the use of dual grids or reference elements. Figure 4.23 illustrates some geometrical and topological challenges seen in standard grid models.

To adapt to sloping faults, curved horizons and layers, lateral features, and so on, cell geometries may often deviate significantly from being orthogonal, which may generally introduce significant grid-orientation effects, in particular for the industry-standard two-point scheme (as we will see later).

Stratigraphic grids will often have aspect ratios that are two or three orders of magnitude. Such high aspect ratios can introduce severe numerical difficulties because the majority of the flow in and out of a cell occurs across the faces with the smallest area. Similarly, the possible presence of strong

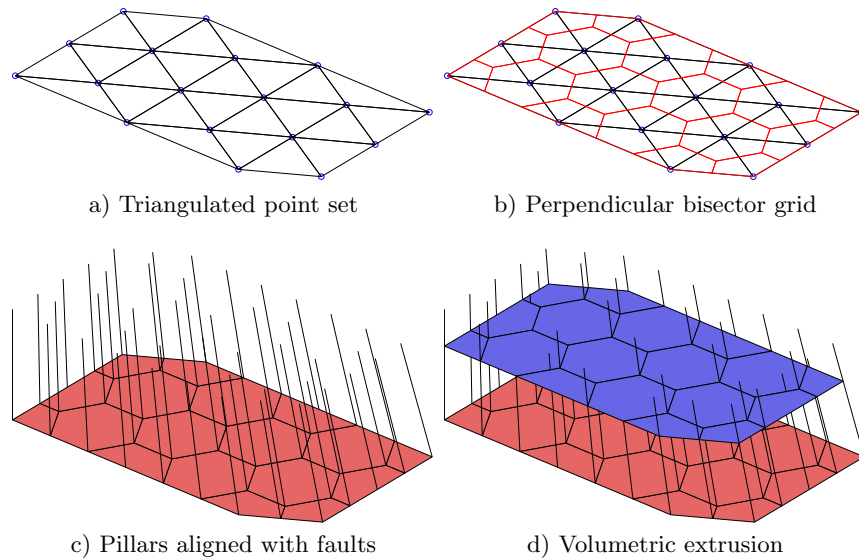


Fig. 4.24. Illustration of a typical process for generating 2.5D PEBI grids.

heterogeneities and anisotropies in the permeability fields, e.g., as seen in the SPE 10 example in Chapter 3, typically introduces large condition numbers in the discretized flow equations.

Corner-point grids generated by geological modeling typically contain too many cells. Once created by the geologist, the grid is handed to a reservoir engineer, whose first job is to reduce the number of cells if he or she is to have any hope of getting the model through a simulator. The generation of good coarse grids for use in upscaling, and the upscaling procedure itself, is generally work-intensive, error prone, and not always sufficiently robust, as we will come back to later in the book.

4.3.2 2.5D unstructured grids

Corner-point grids are well suited to represent stratigraphic layers and faults which laterally coincide with one of the coordinate directions. Although the great flexibility inherent in the corner-point scheme can be used to adapt to areally skewed or curved faults, or other areal features, the resulting cell geometries will typically deviate far from being orthogonal, and hence introduce numerical problems in a subsequent flow simulation, as discussed above.

So-called 2.5D grids are often used to overcome the problem of areal adaptation. These grids have been designed to combine the advantages of two different gridding methods: the (areal) flexibility of unstructured grids and the simple topology of Cartesian grids in the vertical direction. The 2.5D grids are constructed in much the same way as corner-point grids, but instead of defining pillars using a structured areal mesh, the pillars are defined based on

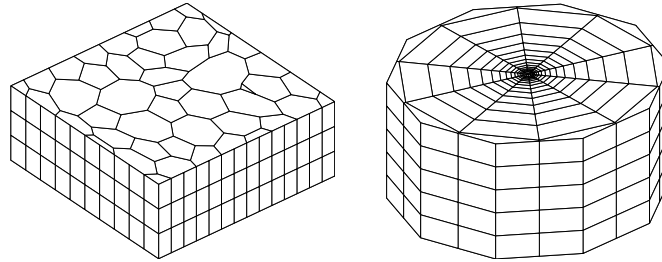


Fig. 4.25. The left plot shows a 2.5D Voronoi grid derived from a perturbed 2D point mesh extruded in the z -direction, whereas the right plot shows a radial grid.

an unstructured lateral grid. To generate such a grid, one starts by defining an areal tessellation on a surface that either aligns with the lateral direction or one of the major geological horizons. Then a pillar is introduced through each vertex in the areal grid. The pillars can either be vertical, inclined to gradually align with major fault planes as shown for the corner-point grid in Figure 4.20, or be defined so that they connect pairs of vertices in two areal tessellations placed above each other, e.g., so that these are aligned with two different geological horizons. Figure 4.24 shows the key steps in the construction of a simple 2.5D PEBI grid. Starting from a set of generating points, an areal tessellation is formed by first computing the Delaunay triangulation and then constructing a perpendicular bisector grid. Through each vertex in the areal tessellation, we define a pillar, whose angle of inclination will change from 90 degrees for vertices on the far left to 45 degrees for vertices on the far right. The pillars are then used to extrude the areal tessellation to a volumetric grid. The resulting volumetric grid is unstructured in the lateral direction, but has a layered structure in the vertical direction (and can thus be indexed using a $[I,K]$ index pair). Because the grid is unstructured in the lateral direction, there is a quite large freedom in choosing the size and shape of the grid cells to adapt to complex features such as curved faults or to improve the areal resolution in near-well zones.

As a first example of a 2.5D grid, we first construct a lateral 2D Voronoi grid from a set of generating points obtained by perturbing the vertices of a regular Cartesian grid, then use the function `makeLayeredGrid` to extrude this Voronoi grid to 3D along vertical pillars in the z -direction.

```
N=7; M=5; [x,y] = ndgrid(0:N,0:M);
x(2:N,2:M) = x(2:N,2:M) + 0.3*randn(N-1,M-1);
y(2:N,2:M) = y(2:N,2:M) + 0.3*randn(N-1,M-1);
aG = pebi(triangleGrid([x(:) y(:)]));
G = makeLayeredGrid(aG, 3);
plotGrid(G, 'FaceColor',[.8 .8 .8]); view(-40,60); axis tight off
```

The resulting grid is shown in the left plot of Figure 4.25 and should be contrasted to the 3D tetrahedral tessellation shown to the right in Figure 4.8

As a second example, we will generate a PEBI grid with radial symmetry, which is graded towards the origin

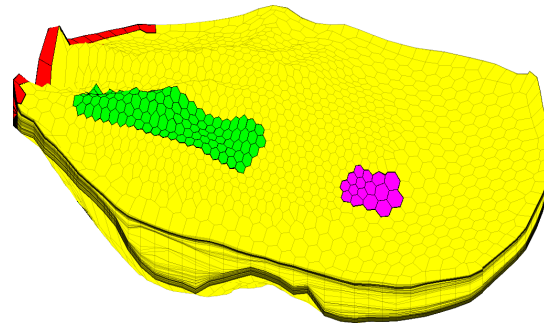
```
P = [];
for r = exp(-3.5:.25:0),
    [x,y,z] = cylinder(r,16); P = [P [x (1,:); y (1,:)]];
end
P = unique([P; 0 0], 'rows');
G = makeLayeredGrid(pebi(triangleGrid(P)), 5);
plotGrid(G, 'FaceColor', [.8 .8 .8]); view(30,50), axis tight off
```

Figure 4.25 shows the resulting grid. Typically, the main difficulty lies in generating a good point set (and a set of pillars). Once this is done, the rest of the process is almost straightforward.

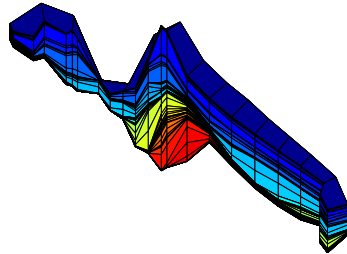
Our third example is a simulation model of a real reservoir. The model shown in Figure 4.26 consists of an unstructured areal grid that has been extruded vertically to model different geological layers. Some of the layers are very thin, which can be seen in particular in Figure 4.26a in which these thin layers appear as if they were thick lines. Figure 4.26b shows part of the perimeter of the model; we notice that the lower layers (yellow to red colors) have been eroded away in most of the grid columns, and although the vertical dimension is strongly exaggerated, we see that the layers contain steep slopes. To a non-geologist looking at the plot in Figure 4.26e, it may appear as if the reservoir was formed by sediments being deposited along a sloping valley that ends in a flat plain. Figures 4.26c and d show more details of the permeability field inside the model. The layering is particularly distinct in plot d, which is sampled from the flatter part of the model. The cells in plot c, on the other hand, show examples of pinch-outs. The layering provides a certain structure in the model, and it is therefore common to add a logical ik index, similar to the logical ijk index for corner-point grids, where i refers to the areal numbering and k to the different layers. Moreover, it is common practice to associate a virtual logically Cartesian grid as an 'overlay' to the 2.5D grid that can be used e.g., to simplify lookup of cells in visualization. In this setup, more than one grid cell may be associated with a cell in the virtual grid.

4.4 Grid structure in MRST

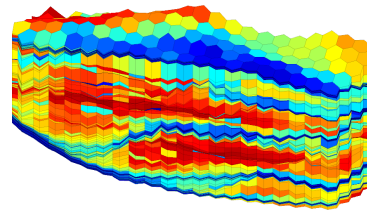
In the two previous sections we have given an introduction to structured and unstructured grid types that can be created using MRST. In this section, we will go into more detail about the internal data structure used to represent various grid types. This data structure is in many ways the most fundamental part of MRST since almost all solvers and visualization routines require an instance of a grid as input argument. By convention, instances of the grid structure are denoted G . Readers who are mainly interested in *using* solvers and visualization routines already available in MRST, need no further knowledge of the grid structure beyond what has been encountered in the examples



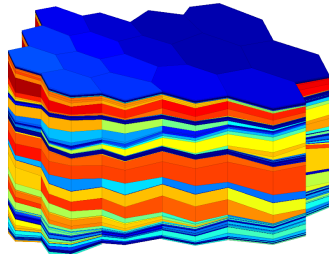
a) The whole model with three areas of interested marked in different colors.



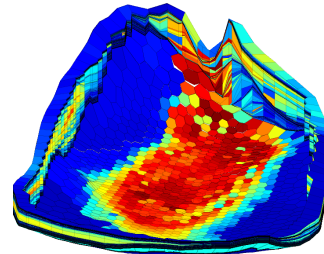
b) Layers 41 to 99 of the red region with colors representing the k -index.



c) Horizontal permeability in the green region of plot a).



d) Horizontal permeability in the magenta region of plot a).



e) Horizontal permeability along the perimeter and bottom of the model.

Fig. 4.26. A real petroleum reservoir modelled by a 2.5D PEBI grid having 1174 cells in the lateral direction and 150 cells along each pillar. Only 90644 out of the 176100 cells are active. The plots show the whole model as well as selected details.

presented so far and can safely skip the remains of this section. For readers who wish to use MRST to prototype new computational methods, however, knowledge of the inner workings of the grid structure is essential. To read the MRST documentation, type

```
help grid_structure
```

This will bring you an overview of all the grid structure and all its members.

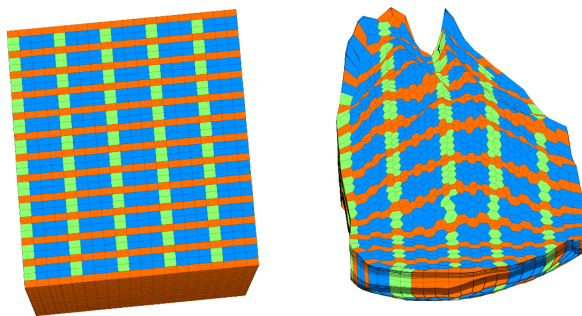


Fig. 4.27. Example of a virtual grid used for fast lookup in a 2.5D PEBI grid. The virtual grid has dimensions $37 \times 20 \times 150$ while the PEBI grid has ik dimensions 1174×150 .

As was stated in the introduction to the chapter, we have chosen to store all grid types using a general unstructured grid format that represents cells, faces, vertices, and connections between cells and faces. To this end, the main grid structure \mathbf{G} contains three fields—`cells`, `faces`, and `nodes`—that specify individual properties for each individual cell/face/vertex in the grid. Grids in MRST can either be volumetric or lie on a 2D or 3D surface. The field `griddim` is used to distinguish volumetric and surface grids; all cells in a grid are polygonal surface patches if `griddim=2` and polyhedral volumetric entities otherwise. In addition, the grid contains a field `type` consisting of a cell array of strings describing the history of grid-constructor and modifier functions through which a particular grid structure has been defined, e.g., `'tensorGrid'`. For grids that have an underlying logical Cartesian structure, we also include the field `cartDims`.

The cell structure, $\mathbf{G.cells}$, consists of the following mandatory fields:

- `num`: the number n_c of cells in the global grid.
- `facePos`: an indirection map of size `[num+1,1]` into the `faces` array. Specifically, the face information of cell i is found in the submatrix

$$\mathbf{faces}(\mathbf{facePos}(i) : \mathbf{facePos}(i+1)-1, :)$$

The number of faces of each cell may be computed using the statement `diff(facePos)` and the total number of faces is given as $n_f = \mathbf{facePos}(\mathbf{end})-1$.

- `faces`: an $n_f \times 3$ array that gives the global faces connected to a given cell. Specifically, if `faces(i,1)==j`, the face with global number `faces(i,2)` is connected to cell number j . The last component, `faces(i,3)`, is optional and can for certain types of grids contain a tag used to distinguish face directions: `East`, `West`, `South`, `North`, `Bottom`, `Top`.

The first column of `faces` is redundant: it consists of each cell index j repeated `facePos(j+1)-facePos(j)` times and can therefore be reconstructed by decompressing a run-length encoding with the cell indices `1:num` as encoded vector and the number of faces per cell as repetition vector. Hence,

to conserve memory, only the last two columns of `faces` are stored, while the first column can be reconstructed using the statement:

```
rldecode(1:G.cells.num, diff(G.cells.facePos), 2) .'
```

This construction is used a lot throughout MRST and has therefore been implemented as a utility function inside `mrst-core/utis/gridtools`

```
f2cn = gridCellNo(G);
```

- `indexMap`: an optional $n_c \times 1$ array that maps internal cell indices to external cell indices. For models with no inactive cells, `indexMap` equals $1 : n_c$. For cases with inactive cells, `indexMap` contains the indices of the active cells sorted in ascending order. An example of such a grid is the ellipsoid in Figure 4.4 that was created using a fictitious domain method. For logically Cartesian grids, a map of cell numbers to logical indices can be constructed using the following statements in 2D:

```
[ij{1:2}] = ind2sub(dims, G.cells.indexMap(:));
ij        = [ij{:}];
```

and likewise in 3D:

```
[ijk{1:3}] = ind2sub(dims, G.cells.indexMap(:));
ijk        = [ijk{:}];
```

In the latter case, `ijk(i:)` is the global (I, J, K) index of cell i .

In addition, the cell structure can contain the following optional fields that typically will be added by a call to `computeGeometry`:

- `volumes`: an $n_c \times 1$ array of cell volumes
- `centroids`: an $n_c \times d$ array of cell centroids in \mathbb{R}^d

The face structure, `G.faces`, consists of the following mandatory fields:

- `num`: the number n_f of global faces in the grid.
- `nodePos`: an indirection map of size `[num+1,1]` into the `nodes` array. Specifically, the node information of face i is found in the submatrix

```
nodes(nodePos(i) : nodePos(i+1)-1, :)
```

The number of nodes of each face may be computed using the statement `diff(nodePos)`. Likewise, the total number of nodes is given as $n_n = \text{nodePos}(\text{end}) - 1$.

- `nodes`: an $N_n \times 2$ array of vertices in the grid. If `nodes(i,1)==j`, the local vertex i is part of global face number j and corresponds to global vertex `nodes(i,2)`. For each face the nodes are assumed to be oriented such that a right-hand rule determines the direction of the face normal. As for `cells.faces`, the first column of `nodes` is redundant and can be easily reconstructed. Hence, to conserve memory, only the last column is stored, while the first column can be constructed using the statement:

```
rldecode(1:G.faces.num, diff(G.faces.nodePos), 2) .'
```

- **neighbors**: an $n_f \times 2$ array of neighboring information. Global face i is shared by global cells `neighbors(i,1)` and `neighbors(i,2)`. One of the entries in `neighbors(i,:)`, but not both, can be zero, to indicate that face i is an external face that belongs to only one cell (the nonzero entry).

In addition to the mandatory fields, `G.faces` has optional fields that are typically added by a call to `computeGeometry` and contain geometry information:

- **areas**: an $n_f \times 1$ array of face areas.
- **normals**: an $n_f \times d$ array of **area weighted**, directed face normals in \mathbb{R}^d . The normal on face i points from cell `neighbors(i,1)` to cell `neighbors(i,2)`.
- **centroids**: an $n_f \times d$ array of face centroids in \mathbb{R}^d .

Moreover, `G.faces` can sometimes contain an $n_f \times 1$ (int8) array, `G.faces.tag`, that can contain user-defined face indicators, e.g., to specify that the face is part of a fault.

The vertex structure, `G.nodes`, consists of two fields:

- **num**: number N_n of global nodes (vertices) in the grid,
- **coords**: an $N_n \times d$ array of physical nodal coordinates in \mathbb{R}^d . Global node i is at physical coordinate `coords(i,:)`.

To illustrate how the grid structure works, we consider two examples. We start by considering a regular 3×2 grid, where we take away the second cell in the logical numbering,

```
G = removeCells( cartGrid([3,2]), 2)
```

This produces the output

```
G =
  cells: [1x1 struct]
  faces: [1x1 struct]
  nodes: [1x1 struct]
cartDims: [3 2]
  type: {'tensorGrid' 'cartGrid' 'removeCells'}
griddim: 2
```

Examining the output from the call, we notice that the field `G.type` contains three values, 'cartGrid' indicates the creator of the grid, which again relies on 'tensorGrid', whereas the field 'removeCells' indicates that cells have been removed from the Cartesian topology. The resulting 2D geometry consists of five cells, twelve nodes, and sixteen faces. All cells have four faces and hence `G.cells.facePos = [1 5 9 13 17 21]`. Figure 4.28 shows³ the geometry and topology of the grid, including the content of the fields `cells.faces`,

³ To create the plot in Figure 4.28, we first called `plotGrid` to plot the grid, then called `computeGeometry` to compute cell and face centroids, which were used to place a marker and a text label with the cell/face number in the correct position.

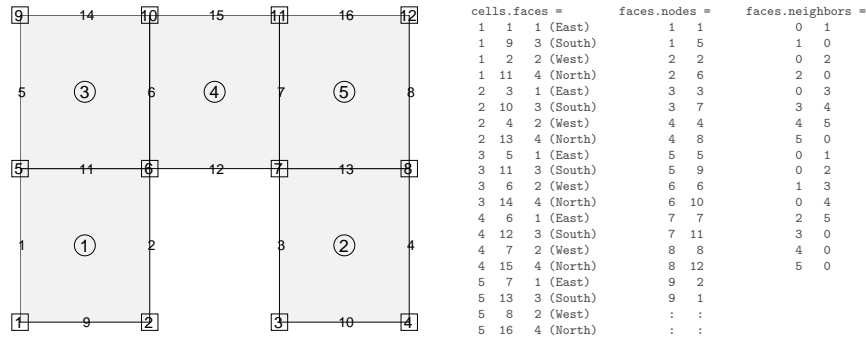


Fig. 4.28. Illustration of the `cell` and `faces` fields of the grid structure: cell numbers are marked by circles, node numbers by squares, and face numbers have no marker.

`faces.nodes`, and `faces.neighbors`. We notice, in particular, that all interior faces (6, 7, 11, and 13) are represented twice in `cells.faces` as they belong to two different cells. Likewise, for all exterior faces, the corresponding row in `faces.neighbors` has one zero entry. Finally, being logically Cartesian, the grid structure contains a few optional fields:

- `G.cartDims` equals `[3 2]`,
- `G.cells.indexMap` equals `[1 3 4 5 6]` since the second cell in the logical numbering has been removed from the model, and
- `G.cells.faces` contains a third column with tags that distinguish global directions for the individual faces.

As a second example, we consider an unstructured triangular grid given by seven points in 2D:

```
p = [ 0.0, 1.0, 0.9, 0.1, 0.6, 0.3, 0.75; ...
      0.0, 0.0, 0.8, 0.9, 0.2, 0.6, 0.45]'; p = sortrows(p);
G = triangleGrid(p)
```

which produces the output

```
G =
  faces: [1x1 struct]
  cells: [1x1 struct]
  nodes: [1x1 struct]
  type: {'triangleGrid'}
  griddim: 2
```

Because the grid contains no structured parts, `G` only consists of the three mandatory fields `cells`, `faces`, and `nodes` that are sufficient to determine the geometry and topology of the grid, the `type` tag naming its creator, and `griddim` giving that it is a surface grid. Altogether, the grid consists of eight cells, fourteen faces, and seven nodes, which are shown in Figure 4.29 along with the contents of the fields `cells.faces`, `faces.nodes`, and `faces.neighbors`.

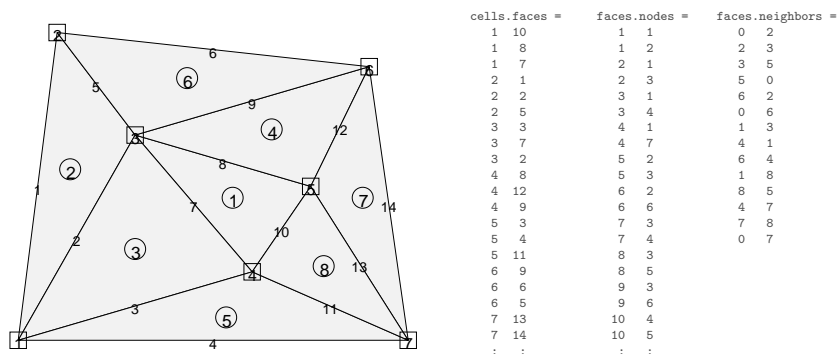


Fig. 4.29. Illustration of the `cell` and `faces` fields of the grid structure: cell numbers are marked by circles, node numbers by squares, and face numbers have no marker. squares.

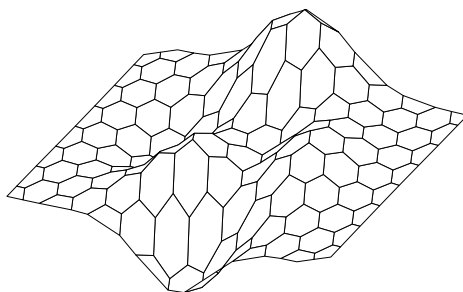


Fig. 4.30. Example of a surface grid: 2D PEBI grid draped over the `peaks` surface.

Notice, in particular, the absence of the third column in `cells.faces`, which generally does not make sense for a (fully) unstructured grid. Likewise, the `cells` structure does not contain any `indexMap` as all cells in the model are active.

Surface grids do not necessary have to follow a planar surface in 2D, but can generally be draped over a (continuous) surface in 3D. In MRST, such grids are used in the `co2lab` module for simulating CO_2 storage in deep saline aquifers using vertically-integrated models that describe the thickness of a supercritical CO_2 plume under a sealing caprock. To demonstrate the basic feature of a surface grid, we generate a 2D PEBI grid and drape it over MATLAB's `peaks` surface.

```
[x,y] = meshgrid([0:6]*2*cos(pi/6),0:7);
x = [x (:); x(:)+cos(pi/6)]; x=(x - mean(x(:)))/2;
y = [y (:); y(:)+sin(pi/6)]; y=(y - mean(y(:)))/2;
G = pebi(triangleGrid([x(:),y(:)]));
G.nodes.coords(:,3) = -peaks(G.nodes.coords(:,1),G.nodes.coords(:,2));
```

The resulting grid is shown in Figure 4.30. Using `computeGeometry`, we can also compute cell and face centroids, cell areas, and face lengths. Face normals, however, are generally not uniquely defined and are therefore only computed as projections onto the horizontal plane. Likewise, it does not make sense to use this grid together with any of the standard flow and transport solvers in MRST, since neither of these contain discretizations that properly account for processes taking place on non-planar surfaces.

Computing geometry information

All grid factory routines in MRST generate the basic geometry and topology of a grid, that is, how nodes are connected to make up faces, how faces are connected to form cells, and how cells are connected over common faces. Whereas this information is sufficient for many purposes, more geometrical information may be required in many cases. As explained above, such information is provided by the routine `computeGeometry`, which computes cell centroids and volumes and face areas, centroids, and normals. Whereas computing this information is straightforward for simplexes and Cartesian grids, it is not so for general polyhedral grids that may contain curved polygonal faces. In the following we will therefore go through how it is done in MRST.

For each cell, the basic grid structure provides us with a list of vertices, a list of cell faces, etc, as shown in the upper-left plots of Figures 4.31 and 4.32. The routine starts by computing face quantities (areas, centroids, and normals). To utilize MATLAB efficiently, the computations are programmed using vectorization so that each derived quantity is computed for all points, all faces, and all cells in one go. To keep the current presentation as simple as possible, we will herein only give formulas for a single face and a single cell. Let us consider a single face given by the points $\vec{p}(i_1), \dots, \vec{p}(i_m)$ and let $\alpha = (\alpha_1, \dots, \alpha_m)$ denote a multi-index that describes how these points are connected to form the perimeter of the faces. For the face with global number j , the multi-index is given by the vector

$$\mathbf{G.faces.nodes}(\mathbf{G.faces.nodePos}(j):\mathbf{G.faces.nodePos}(j+1)-1)$$

Let us consider two faces. Global face number two in Figure 4.31 is planar and consists of points $\vec{p}(2), \vec{p}(4), \vec{p}(6), \vec{p}(8)$ with the ordering $\alpha = (2, 4, 8, 6)$. Likewise, we consider global face number one in Figure 4.32, which is curved and consists of points $\vec{p}(1), \dots, \vec{p}(5)$ with the ordering $\alpha = (4, 3, 2, 1, 5)$. For curved faces, we need to make a choice of how to interpret the surface spanned by the node points. In MRST (and some commercial simulators) this is done as follows: We start by defining a so-called *hinge point* \vec{p}_h , which is often given as part of the input specification of the grid. If not, we use the m points that make up the face and compute the hinge point as the center point of the face, $\vec{p}_h = \sum_{k=1}^m \vec{p}(\alpha_k)/m$. The hinge point can now be used to tessellate the face into m triangles, as shown to the upper right in Figures 4.31 and 4.32. The triangles are defined by the points $\vec{p}(\alpha_k), \vec{p}(\alpha_{\text{mod}(k,m)+1})$, and \vec{p}_h .

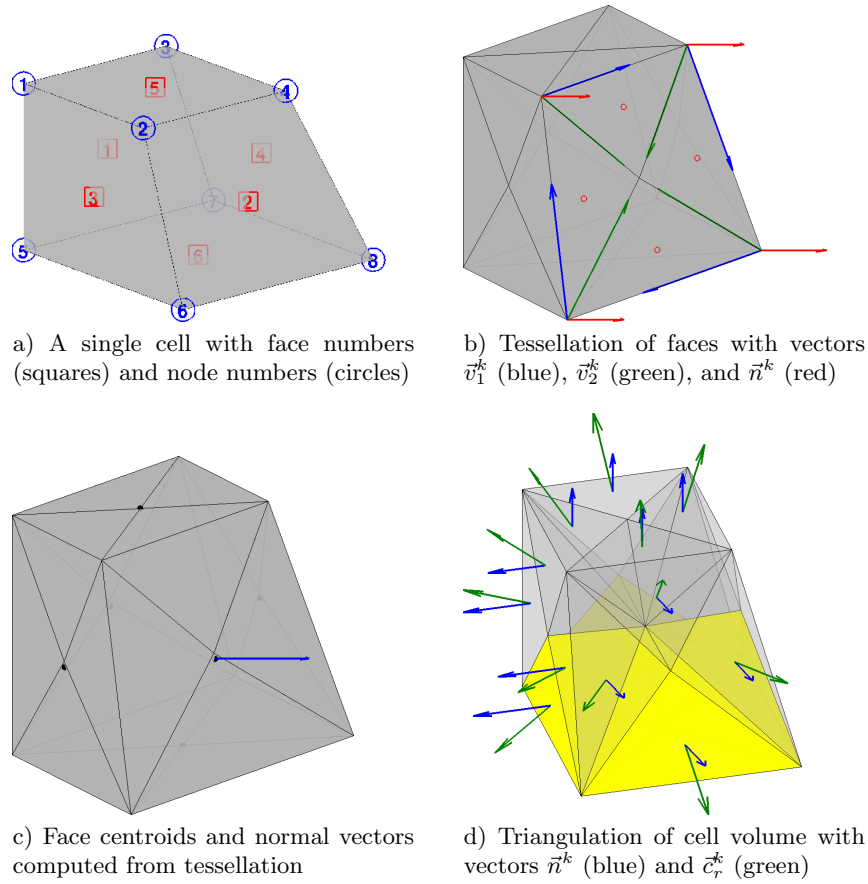


Fig. 4.31. Steps in the computation of geometry information for a single corner-point cell using `computeGeometry`.

for $k = 1, \dots, m$. Each triangle has a center point \vec{p}_c^k defined in the usual way as the average of its three vertices and a normal vector and area given by

$$\vec{n}^k = (\vec{p}(\alpha_{\text{mod}(k,m)+1}) - \vec{p}(\alpha_k)) \times (\vec{p}_h - \vec{p}(\alpha_k)) = \vec{v}_1^k \times \vec{v}_2^k$$

$$A^k = \sqrt{\vec{n}^k \cdot \vec{n}^k}.$$

The face area, centroid, and normal are now computed as follows

$$A_f = \sum_{k=1}^m A^k, \quad \vec{c}_f = (A_f)^{-1} \sum_{k=1}^m \vec{p}_c^k A^k, \quad \vec{n}_f = \sum_{k=1}^m \vec{n}^k. \quad (4.2)$$

The result is shown to the lower left in Figures 4.31, where the observant reader will see that the centroid \vec{c}_f does not coincide with the hinge point \vec{p}_h unless the planar face is a square. This effect is more pronounced for the curved faces of the PEBI cell in Figure 4.32.

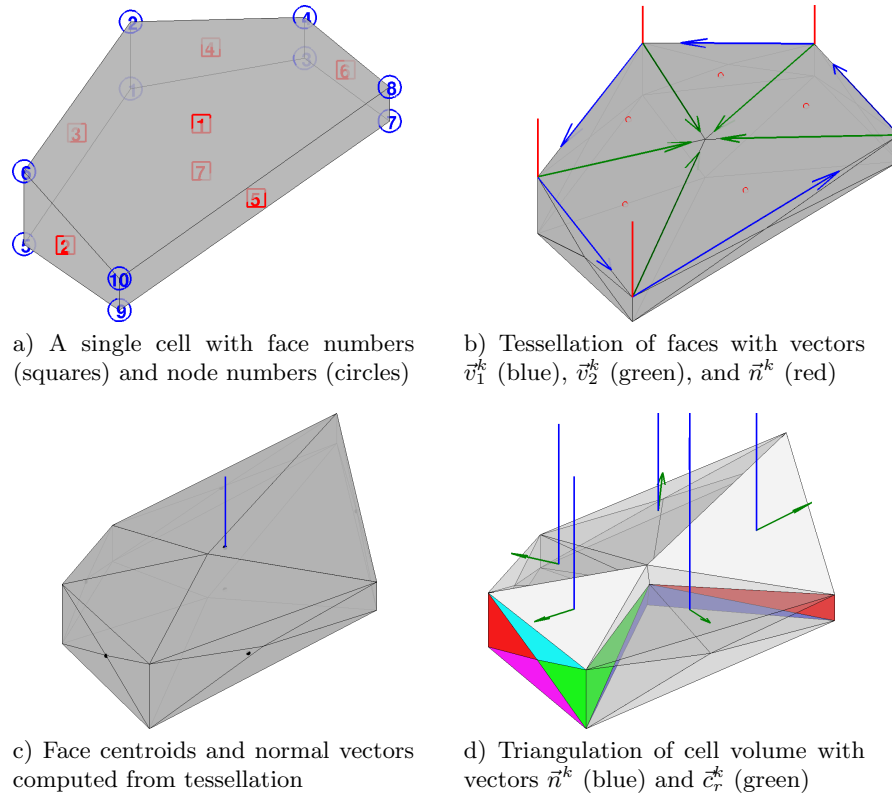


Fig. 4.32. Steps in the computation of geometry information for a single PEBI cell using `computeGeometry`.

The computation of centroids in (4.2) requires that the grid does not have faces with zero area, because otherwise the second formula would involve a division by zero and hence incur centroids with NaN values. The reader interested in creating his/her own grid-factory routines for grids that may contain degenerate (pinched) cells should be aware of this and make sure that all faces with zero area are removed in a preprocessing step.

To compute the cell centroid and volume, we start by computing the centre point \vec{c}_c of the cell, which we define as the average of the face centroids, $\vec{c}_c = \sum_{k=1}^{m_f} \vec{c}_f / m_f$, where m_f is the number of faces of the cell. By connecting this centre point to the m_t face triangles, we define a unique triangulation of the cell volume, as shown to the lower right in Figures 4.31 and 4.32. For each tetrahedron, we define the vector $\vec{c}_r^k = \vec{p}_c^k - \vec{c}_c$ and compute the volume (which may be negative if the centre point \vec{c}_c lies outside the cell)

$$V^k = \frac{1}{3} \vec{c}_r^k \cdot \vec{n}^k.$$

The triangle normals \vec{n}^k will point outward or inward depending upon the orientation of the points used to calculate them, and to get a correct computation we therefore must modify the triangle normals so that they point outward. Finally, we can define the volume and the centroid of the cell as follows

$$V = \sum_{k=1}^{m_t} V^k, \quad \vec{c} = \vec{c}_c + \frac{3}{4V} \sum_{k=1}^{m_t} V^k \vec{c}_r^k. \quad (4.3)$$

In MRST, all cell quantities are computed inside a loop, which may not be as efficient as the computation of the face quantities.

COMPUTER EXERCISES:

25. Go back to Exercise 16 in Section 4.1. What would you do to randomly perturb all nodes in the grid except for those that lie on an outer face whose normal vector has no component in the y -direction?
26. Exercise 20 on page 95 extended the function `triangleGrid` from planar triangulations to triangulated surfaces in 3D. Verify that the function `computeGeometry` computes cell areas, cell centroids, face centroids, and face lengths correctly for general 3D triangulated surfaces.
27. How would you write a function that purges all cells that have an invalid vertex (with value NaN) from a grid?

4.5 Examples of more complex grids

To help the user generate test cases, MRST supplies a routines for generating example grids. We have previously encountered `twister`, which perturbs the x and y coordinates in a grid. Likewise, in Chapter 3.5 we used `simpleGrdecl` to generate a simple Eclipse input stream for a stratigraphic grid describing a wavy structure with a single deviated fault. The routine has several options that allow the user to specify the magnitude of the fault displacement, flat rather than a wavy top and bottom surfaces, and vertical rather than inclined pillars, see Figure 4.33.

Similarly, the routine with the somewhat cryptic name `makeModel3` generates a corner-point input stream that models parts of a dome that is cut through by two faults, see Figure 4.34. Similarly, `extrudedTriangleGrid.m` generates a 2.5D prismatic grid with a laterally curved fault in the middle. Alternatively, the routine can generate a 2.5D PEBI grid in which the curved fault is laterally stair-stepped, see Figure 4.34.

SAIGUP: shallow-marine reservoirs

Having discussed the corner-point format in some detail, it is now time to return to the SAIGUP model. In the following, we will look at the grid representation in more detail and show some examples of how to interact and

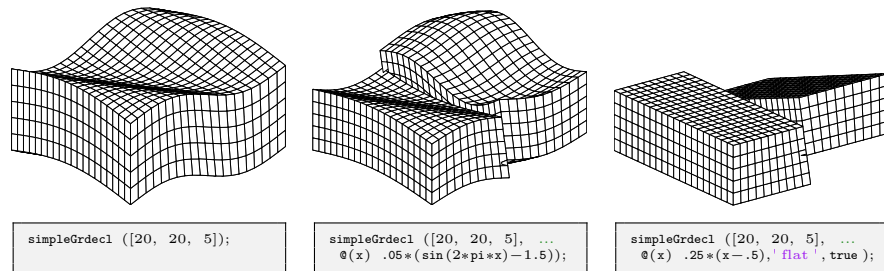


Fig. 4.33. The `simpleGrdecl` routine can be used to produce faulted, two-block grids of different shapes.

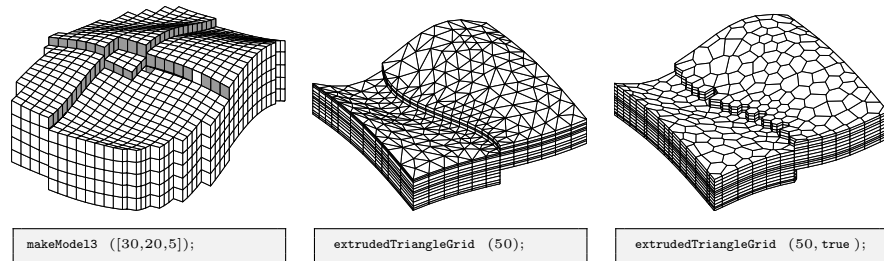


Fig. 4.34. Three different example grids created by the grid example functions `makeModel3` and `extrudedTriangleGrid`.

visualize different features of the grid (see also the last video of the second MRST Jolt on grids and petrophysical data [114]). In Chapter 3.5, we saw that parsing the input file creates the following structure

```
grdecl =
  cartDims: [40 120 20]
  COORD: [29766x1 double]
  ZCORN: [768000x1 double]
  ACTNUM: [96000x1 int32]
  PERMX: [96000x1 double]
  : : :
```

In the following, we will (mostly) use the first four fields:

1. The dimension of the underlying logical Cartesian grid: Eclipse keyword `SPECGRID`, equal $40 \times 120 \times 20$.
2. The coordinates of pillars: Eclipse keyword `COORD`, top and bottom coordinate per vertex in the logical 40×120 areal grid, i.e., $6 \times 41 \times 121$ values.
3. The coordinates along the pillars: Eclipse keyword `ZCORN`, eight values per cell, i.e., $8 \times 40 \times 120 \times 20$ values.
4. The boolean indicator for active cells: Eclipse keyword `ACTNUM`, one value per cell, i.e., $40 \times 120 \times 20$ values.

As we have seen above, we can use the routine `processGRDECL` to process the Eclipse input stream and turn the corner-point grid into MRST's unstructured description. The interested reader may ask the processing routine to display diagnostic output

```
G = processGRDECL(grdecl, 'Verbose', true);
G = computeGeometry(G)
```

and consult the SAIGUP tutorial (`saigupModelExample.m`) or the technical documentation of the processing routine for an explanation of the resulting output.

The model has been created using vertical pillars with lateral resolution of 75 meters and a vertical resolution of 4 meters, giving a typical aspect ratio of 18.75. This can be seen, e.g., by extracting the pillars and corner points and analyzing the results as follows:

```
[X,Y,Z] = buildCornerPtPillars(grdecl,'Scale',true);
dx = unique(diff(X)).'
[x,y,z] = buildCornerPtNodes(grdecl);
dz = unique(reshape(diff(z,1,3),1,[]))
```

The resulting grid has 78 720 cells that are almost equal in size (as can easily be seen by plotting `hist(G.cells.volumes)`), with cell volumes varying between 22 500 m³ and 24 915 m³. Altogether, the model has 264 305 faces: 181 649 vertical faces on the outer boundary and between lateral neighbors, and 82 656 lateral faces on the outer boundary and between vertical neighbors. Most of the vertical faces are not part of a fault and are therefore parallelograms with area equal 300 m². However, the remaining 26–27 000 faces are a result of the subdivision introduced to create a matching grid along the (stair-stepped) faults. Figure 4.35 shows where these faces appear in the model and a histogram of their areas: the smallest face has an area of $5.77 \cdot 10^{-4}$ m² and there are 43, 202, and 868 faces with areas smaller than 0.01, 0.1, and 1 m², respectively. The `processGRDECL` has an optional parameter '`Tolerance`' that sets the minimum distance used to distinguish points along the pillars (the default value is zero). By setting this to parameter to 5, 10, 25, or 50 cm, the area of the smallest face is increased to 0.032, 0.027, 0.097, or 0.604 m², respectively. In general, we advice against aggressive use of this tolerance parameter; one should instead develop robust discretization schemes and, if necessary, suitable post-processing methods that eliminate or ignore faces with small areas.

Next, we will show a few examples of visualizations of the grid model that will highlight various mechanisms for interacting with the grid and accessing parts of it. As a first example, we start by plotting the layered structure of the model. To this end, we use a simple trick: create a matrix with ones in all cells of the logical Cartesian grid and then do a cumulative summation in the vertical direction to get increasing values,

```
val = cumsum(ones(G.cartDims),3);
```

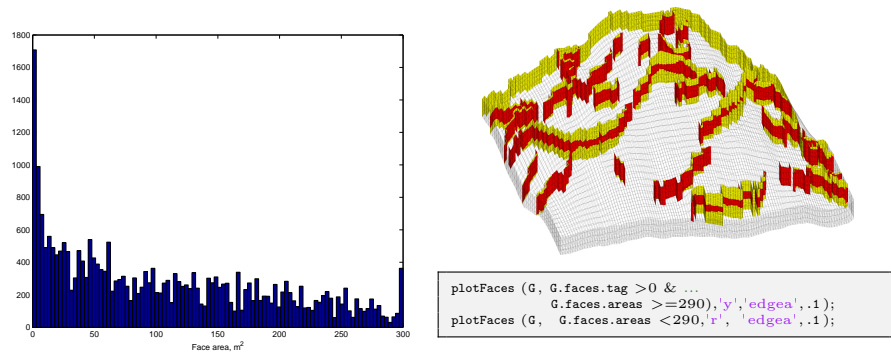


Fig. 4.35. Faces that have been subdivided for the SAIGUP mode. The left plot shows a histogram of the faces areas. The right plot shows all fault faces (yellow) and fault faces having area less than 290 m² (red).

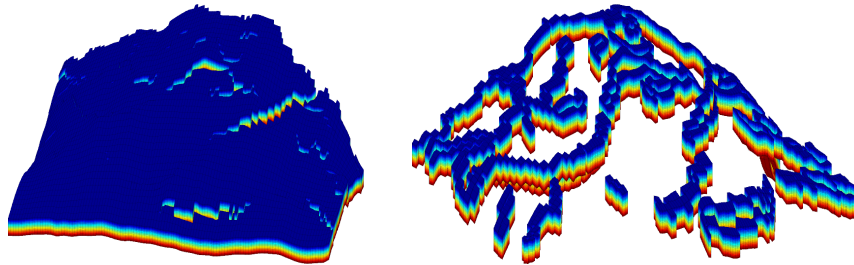


Fig. 4.36. Visualizing the layered structure of the SAIGUP model.

which we then plot using a standard call to `plotCellData`, see the left plot in Figure 4.36. Unfortunately, our attempt at visualizing the layered structure was not very successful. We therefore try to extract and visualize only the cells that are adjacent to a fault:

```

cellList = G.faces.neighbors(G.faces.tag>0, :);
cells    = unique(cellList(cellList>0));

```

In the first statement, we go through all faces and extract the neighbors of all faces that are marked with a tag (i.e., lies at a fault face). The list may have repeated entries if a cell is attached to more than one fault face and contain zeros if a fault face is part of the outer boundary. We get rid of these in the second statement, and can then plot the result using `plotCellData(G, val(G.cells.indexMap), cells)`, giving the result in the right plot of Figure 4.36. Let us inspect the fault structure in the lower-right corner of the plot. If we disregard using `cutGrdecl` as discussed on page 103, there are basically two ways we can extract parts of the model, that both rely on the construction of a map of cell numbers of logical indices. In the first method,

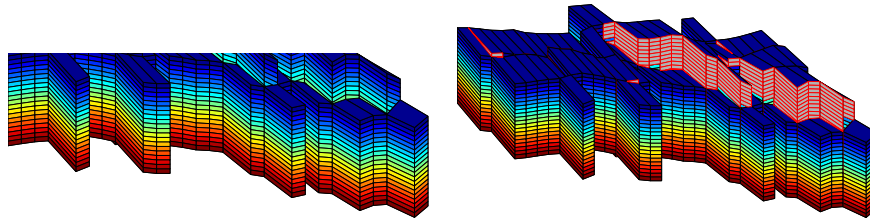


Fig. 4.37. Details from the SAIGUP model showing a zoom of the fault structure in the lower-right corner of the right plot in Figure 4.36. The left plot shows the cells attached to the fault faces, and in the right plot the fault faces have been marked with gray color and red edges.

we first construct a logical set for the cells in a logically Cartesian bounding box and then use the built-in function `ismember` to extract the members of `cells` that lie within this bounding box:

```
[ijk{1:3}] = ind2sub(G.cartDims, G.cells.indexMap); ijk = [ijk{:}];
[I,J,K] = meshgrid(1:9,1:30,1:20);
bndBox = find(ismember(ijk,[I(:), J(:), K(:)], 'rows'));
inspect = cells(ismember(cells,bndBox));
```

The `ismember` function has an operational count of $\mathcal{O}(n \log n)$. A faster alternative is to use logical operations having an operational count of $\mathcal{O}(n)$. That is, we construct a vector of boolean numbers that are `true` for the entries we want to extract and `false` for the remaining entries

```
[ijk{1:3}] = ind2sub(G.cartDims, G.cells.indexMap);

I = false(G.cartDims(1),1); I(1:9)=true;
J = false(G.cartDims(2),1); J(1:30)=true;
K = false(G.cartDims(3),1); K(1:20)=true;

pick = I(ijk{1}) & J(ijk{2}) & K(ijk{3});
pick2 = false(G.cells.num,1); pick2(cells) = true;
inspect = find(pick & pick2);
```

Both approaches produce the same index set; the resulting plot is shown in Figure 4.37. To mark the fault faces in this subset of the model, we do the following steps

```
cellno = rldecode(1:G.cells.num, diff(G.cells.facePos), 2) .';
faces = unique(G.cells.faces(pick(cellno), 1));
inspect = faces(G.faces.tag(faces)>0);
plotFaces(G, inspect, [.7 .7 .7], 'EdgeColor','r');
```

The first statement constructs a list of all cells in the model, the second extracts a unique list of face numbers associated with the cells in the logical vector `pick` (which represents the bounding box in logical index space), and the

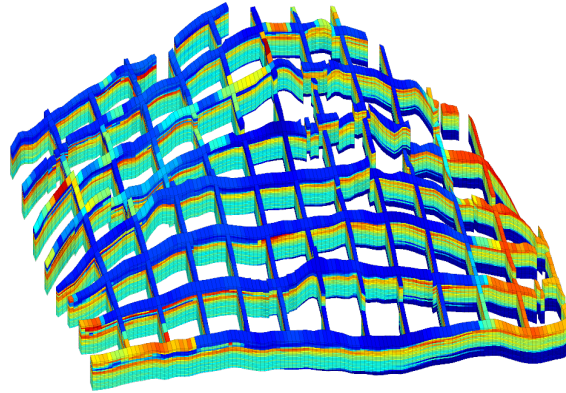


Fig. 4.38. A 'sieve' plot of the porosity in the SAIGUP model. Using this technique, one can more easily see the structure in the interior of the model.

third statement extracts the faces within this bounding box that are marked as fault faces.

Logical operations are also useful in other circumstances. As an example, we will extract a subset of cells forming a sieve that can be used to visualize the petrophysical quantities in the interior of the model:

```
% Every fifth cell in the x-direction
I = false(G.cartDims(1),1); I(1:5:end)=true;
J = true(G.cartDims(2),1);
K = true(G.cartDims(3),1);
pickX = I(ijk{1}) & J(ijk{2}) & K(ijk{3});

% Every tenth cell in the y-direction
I = true(G.cartDims(1),1);
J = false(G.cartDims(2),1); J(1:10:end) = true;
pickY = I(ijk{1}) & J(ijk{2}) & K(ijk{3});

% Combine the two picks
plotCellData(G,rock.poro, pickX | pickY, 'EdgeColor','k','EdgeAlpha',.1);
```

Composite grids

One advantage of an unstructured grid description is that it easily allows the use of composite grids consisting of geometries and topologies that vary throughout the model. That is, different grid types of cells or different grid resolution may be used locally to adapt to well trajectories and flow and geological constraints, see e.g., [77, 129, 72, 123, 32, 57, 177] and references therein.

You may already have encountered a composite grid if you did Exercise 22 on page 95, where we sought an unstructured grid that adapted to two skew

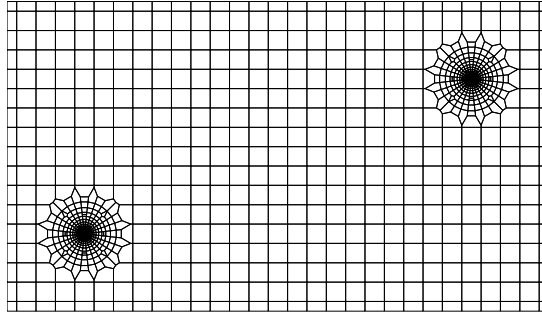


Fig. 4.39. A composite grid consisting of a regular Cartesian mesh with radial refinement around two well positions.

faults and was padded with rectangular cells near the boundary. As another example, we will generate a Cartesian grid that has a radial refinement around two wells in the interior of the domain. This composite grid will be constructed from a set of control points using the `pebi` routine. To this end, we first construct the generating point for a unit refinement, as discussed in Figure 4.25 on page 108

```
Pw = [];
for r = exp(-3.5:.2:0),
    [x,y,z] = cylinder(r,28); Pw = [Pw [x(1,:); y(1,:)]];
end
Pw = [Pw [0; 0]];
```

Then this point set is translated to the positions of the wells and glued into a standard regular point lattice (generated using `meshgrid`):

```
Pw1 = bsxfun(@plus, Pw, [2; 2]);
Pw2 = bsxfun(@plus, Pw, [12; 6]);
[x,y] = meshgrid(0:.5:14, 0:.5:8);
P = unique([Pw1'; Pw2'; x(:) y(:)], 'rows');
G = pebi(triangleGrid(P));
```

The resulting grid is shown in Figure 4.39. To get a good grid, it is important that the number of points around the cylinder has a reasonable match with the density of the points in the regular lattice. If not, the transition cells between the radial and the regular grid may exhibit quite unfeasible geometries. The observant reader will also notice the layer of small cells at the boundary, which is an effect of the particular distribution of the generating points (see the left plot in Figure 4.10 on page 90) and can, if necessary be avoided by a more meticulous choice of points.

In the left plot of Figure 4.40, we have combined these two approaches to generate an areal grid consisting of three characteristic components: Cartesian grid cells at the outer boundary, hexagonal cells in the interior, and a

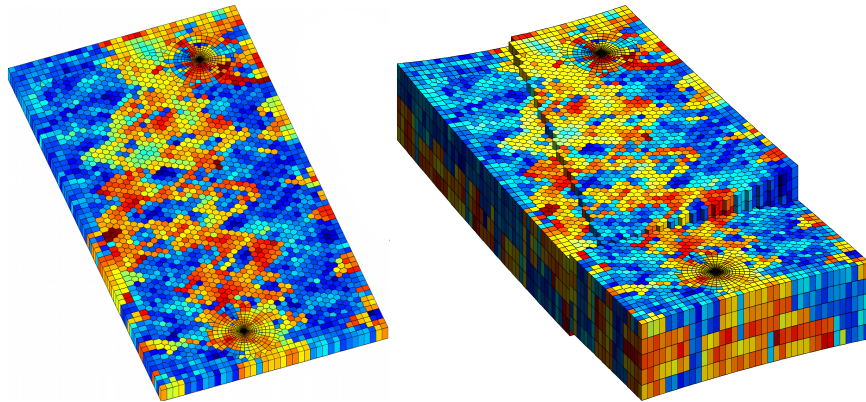


Fig. 4.40. Examples of composite grids. The left plot shows an areal grid consisting of Cartesian, hexagonal, and radial parts. The right plot shows the same grid extruded to 3D with two stair-stepped faults added.

radial grid with exponential radial refinement around two wells. The right plot shows a 2.5D in which the areal Voronoi grid has been extruded to 3D along vertical pillars. In addition, structural displacement has been modelled along two areally stair-stepped faults that intersect near the west boundary. Petrophysical parameters have been sampled from layers 40–44 of the SPE10 data set [49].

Multiblock grids

A somewhat different approach to get grids whose geometry and topology vary throughout the physical domain is to use multiblock grids in which different types of structured or unstructured gridding are glued together. The resulting grid can be non-matching across block interfaces (see e.g., [187, 18, 186]) or have grid lines that are continuous (see e.g., [91, 107]). MRST does not have any grid-factory routine for generating advanced multiblock grids, but offers a the function `glue2DGrid` for gluing together rectangular blocks in 2D. In the following, we will show a few examples of such grids.

As our first example, let us generate a curvilinear grid that has a local refinement at its center as shown in Figure 4.41 (see also Exercise 21 on page 95). To this end, we start by generating three different block types shown in red, green, and blue colors to the left in the figure:

```
G1 = cartGrid([ 5 5],[1 1]);
G2 = cartGrid([20 20],[1 1]);
G3 = cartGrid([15 5],[3 1]);
```

Once these are in place, we can simply translate the blocks and glue them together and then apply the `twister` function to make a curvilinear transformation of each grid line:

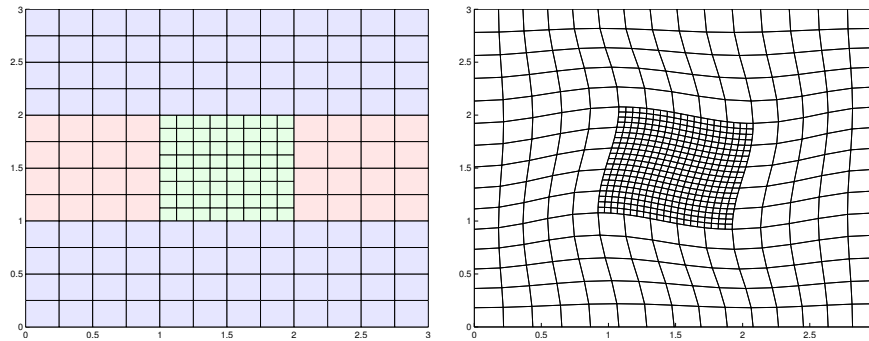


Fig. 4.41. Using a multiblock approach to construct a rectilinear grid with refinement.

```
G = glue2DGrid(G1, translateGrid(G2,[1 0]));
G = glue2DGrid(G, translateGrid(G1,[2 0]));
G = glue2DGrid(G3, translateGrid(G,[0 1]));
G = glue2DGrid(G, translateGrid(G3,[0 2]));
G = twister(G);
```

Let us now replace the central block by a patch consisting of triangular cells. To this end, we start by regenerating G2

```
[N,M]=deal(10,15);
[x,y] = ndgrid( linspace(0,1,N+1), linspace(0,1,M+1));
x(2:N,2:M) = x(2:N,2:M) + 0.3*randn(N-1,M-1)*max(diff(xv));
y(2:N,2:M) = y(2:N,2:M) + 0.3*randn(N-1,M-1)*max(diff(yv));
G2 = computeGeometry(triangleGrid([x(:) y(:)]));
```

The `glue2DGrid` routine relies on face tags as explained in 4.4 on page 111 that can be used to identify the external faces that are facing East, West, North, and South. Generally, such tags does not make much sense for triangular grids and are therefore not supplied. However, to be able to find the correct interface to glue together, we need to supply tags on the perimeter of the triangular patch, where the normal vectors follow the axial directions and tags therefore make sense. To this end, we start by computing the true normal vectors:

```
hf = G2.cells.faces(:,1);
hf2cn = gridCellNo(G2);
sgn = 2*(hf2cn == G2.faces.neighbors(hf, 1)) - 1;
N = bsxfun(@times, sgn, G2.faces.normals(hf,:));
N = bsxfun(@rdivide, N, G2.faces.areas(hf,:));
n = zeros(numel(hf),2); n(:,1)=1;
```

Then, all interfaces that face the East are those whose dot-product with the vector $(1, 0)$ is identical to -1 :

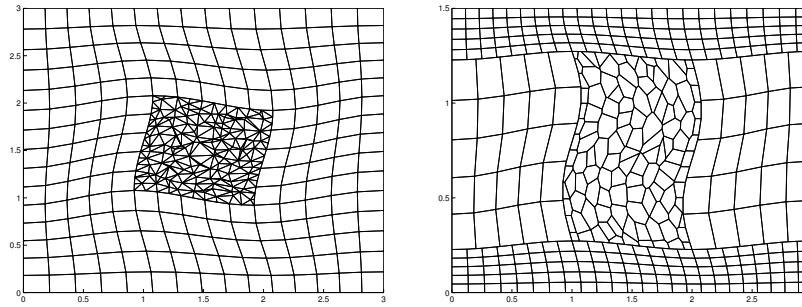


Fig. 4.42. Using a multiblock approach to construct rectilinear grid with triangular and polygonal refinements.

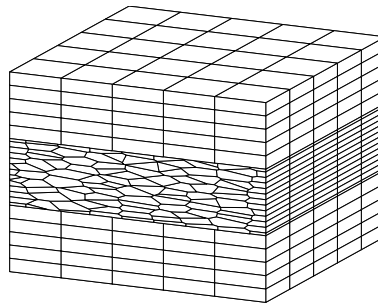


Fig. 4.43. An example of a 3D multiblock grid.

```
G2.cells.faces(:,2) = zeros(size(hf));
i = sum(N.*n,2)==-1; G2.cells.faces(i,2) = 1;
```

Similarly, we can identify all the interfaces facing the West, North, and South. The left plot in Figure 4.42 shows the resulting multiblock grid. Likewise, the right plot shows another multiblock grid where the central refinement is the dual to the triangular patch and $G3$ has been scaled in the y -direction and refined in the x -direction so that the grid lines are no longer matching with the grid lines of $G1$.

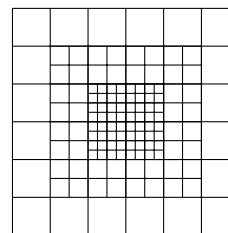
As a last example, let us use this technique to generate a 3D multiblock grid that consists of three blocks in the vertical direction

```
G = glue2DGrid(G1, translateGrid(G2,[0 1]));
G = glue2DGrid(G, translateGrid(G1,[0 2]));
G = makeLayeredGrid(G, 5);
G.nodes.coords = G.nodes.coords(:,[3 1 2]);
```

That is, we first generate an areal grid in the xy -plane, extrude it to 3D along the z direction, and then permute the axis so that their relative orientation is correctly preserved (notice that simply flipping $[1\ 2\ 3] \rightarrow [1\ 3\ 2]$, for instance, will *not* create a functional grid).

COMPUTER EXERCISES:

27. How would you populate the grids shown in Figures 4.33 and 4.34 with petrophysical properties so that spatial correlation and displacement across the fault(s) is correctly accounted for? As an illustrative example, you can try to sample petrophysical properties from the SPE 10 data set.
28. Select at least one of the models in the data sets `BedModel1s1` or `BedModel12` and try to find all inactive cells and then all cells that do not have six faces. Hint: it may be instructive to visualize these models both in physical space and in index space.
29. Extend your function from Exercise 22 on page 95 to also include radial refinement in near-well regions as shown in Figure 4.39.
30. Make a grid similar to the one shown to the right in Figure 4.40. Hint: although it is not easy to see, the grid is matching across the fault, which means that you can use the method of fictitious domain to make the fault structure.
31. As pointed out in Exercise 21 on page 95, MRST does not yet have a grid factory routine to generate structured grids with local nested refinement as shown in the figure to the right. While it is not very difficult to generate the necessary vertices if each refinement patch is rectangular and matches the grid cells on the coarser level, building up the grid structure may prove to be a challenge. Try to develop an efficient algorithm and implement in MRST.



Incompressible Single-Phase Flow

Mathematical Models and Basic Discretizations

If you have read the chapters of the book in chronological order, you have already encountered the equations modeling flow of a single, incompressible fluid through a porous media twice: first in Section 2.1 where we showed how to use MRST to compute vertical equilibrium inside a gravity column, and then in Section 3.4.2, in which we discussed the concept of rock permeability. In this section, we will review the mathematical modeling of single-phase flow in more detail, introduce basic numerical methods for solving the resulting equations, and discuss how these are implemented in MRST and can be combined with the tools introduced in Chapters 3 and 4 to develop efficient simulators for single-phase incompressible flow. Solvers for compressible flow will be discussed in more detail in Chapter 12.

6.1 Fundamental concept: Darcy's law

Mathematical modeling of single-phase flow in porous media started with the work of Henry Darcy, a French hydraulic engineer, who in the middle of the 19th century was engaged to enlarge and modernize the waterworks of the city of Dijon. To understand the physics of flow through the sand filters that were used to clean the water supply, Darcy designed a vertical experimental tank filled with sand, in which water was injected at the top and allowed to flow out at the bottom of the tank; Figure 6.1 shows a conceptual illustration. Once the sand pack is filled with water, and the inflow and outflow rates are equal, the hydraulic head at the inlet and at the outlet can be measured using mercury-filled manometers. The hydraulic head is given as, $h = E/mg = z + p/\rho g$, relative to a fixed datum. As water flows through the porous medium, it will experience a loss of energy. In a series of experiments, Darcy measured the water volumetric flow rate out of the tank and compared this rate with the loss of hydrostatic head from top to bottom of the column. From the experiments, he established that for the same sand pack, the discharge (flow rate) Q [m^3/s] is proportional to the cross-sectional area A [m^2] and the

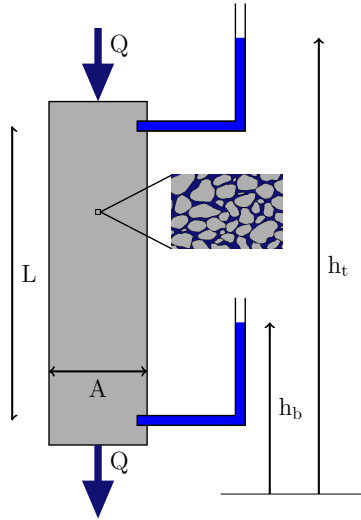


Fig. 6.1. Conceptual illustration of Darcy's experiment.

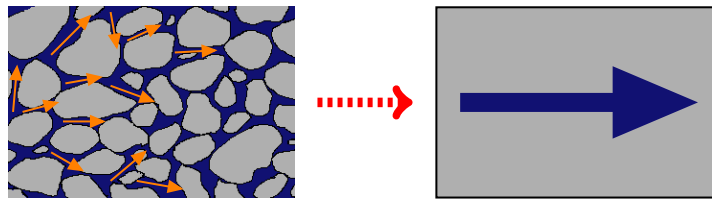


Fig. 6.2. The macroscopic Darcy velocity represents an average of microscopic fluid fluxes.

difference in hydraulic head (height of the water) $h_t - h_b$ [m], and inversely proportional to the flow length of the tank L [m]. Altogether, this can be summarized as

$$\frac{Q}{A} = \kappa \frac{h_t - h_b}{L} \quad (6.1)$$

which was presented in 1856 as an appendix to [51] entitled “Determination of the laws of flow of water through sand” and is what we today call Darcy's law. In (6.1), κ [m/s] denotes the hydraulic conductivity, which is a function both of the medium and the fluid flowing through it. It follows from a dimensional analysis that $\kappa = \rho g K / \mu$, where g [m/s²] is the gravitational acceleration, μ [kg/ms] is the dynamic viscosity, and K [m²] is the intrinsic permeability of a given sand pack.

The specific discharge $v = Q/A$, or Darcy flux, through the sand pack represents the volume of fluid per total area per time and has dimensions [m/s]. Somewhat misleading, v is often referred to as the Darcy velocity. However, since only a fraction of the cross-sectional area is available for flow (the major-

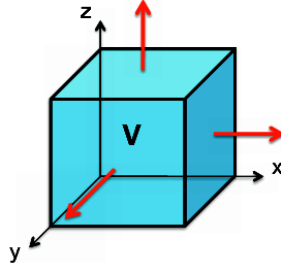


Fig. 6.3. Illustration of a control volume Ω on which one can apply the principle of conservation to derive macroscopic continuity equations.

ity of the area is blocked by sand grains), v is not a velocity in the microscopic sense. Instead, v is the apparent macroscopic velocity obtained by averaging the microscopic fluxes inside representative elementary volumes (REVs) which were discussed in Section 3.3.2. The macroscopic fluid velocity, defined as volume per area occupied by fluid per time, is therefore given by v/ϕ , where ϕ is the porosity associated with the REV.

Henceforth, we will, with a slight abuse of notation, refer to the specific discharge as the Darcy velocity. In modern differential notation, Darcy's law for a single-phase fluid reads,

$$\vec{v} = -\frac{K}{\mu}(\nabla p - g\rho\nabla z), \quad (6.2)$$

where p is the fluid pressure and z is the vertical coordinate. The equation expresses conservation of momentum and was derived from the Navier–Stokes equations by averaging and neglecting inertial and viscous effects by Hubbert [87]. The observant reader will notice that Darcy's law (6.2) is analogous to Fourier's law (1822) for heat conduction, Ohm's law (1827) in the field of electrical networks, or Fick's law (1855) for fluid concentrations in diffusion theory, except that for Darcy there are two driving forces, pressure and gravity. Notice also that Darcy's law assumes a reversible fluid process, which is a special case of the more general physical laws of irreversible processes that were first described by Onsager.

6.2 General flow equations for single-phase flow

To derive a mathematical model for single-phase flow on the macroscopic scale, we first make a continuum assumption based on the existence of REVs as discussed in the previous section and then look at a control volume as shown in Figure 6.3. From the fundamental law of mass conservation, we know that the accumulation of mass inside this volume must equal the net flux over the boundaries,

$$\frac{\partial}{\partial t} \int_{\Omega} \phi \rho d\vec{x} + \int_{\partial\Omega} \rho \vec{v} \cdot \vec{n} ds = \int_{\Omega} \rho q d\vec{x}, \quad (6.3)$$

where ρ is the density of the fluid, ϕ is the rock porosity, \vec{v} is the macroscopic Darcy velocity, \vec{n} denotes the normal at the boundary $\partial\Omega$ of the computational domain Ω , and q denotes fluid sources and sinks, i.e., outflow and inflow of fluids per volume at certain locations. Applying Gauss' theorem, this conservation law can be written on the alternative integral form

$$\int_{\Omega} \left[\frac{\partial}{\partial t} \phi \rho + \nabla \cdot (\rho \vec{v}) \right] d\vec{x} = \int_{\Omega} \rho q d\vec{x}. \quad (6.4)$$

This equation is valid for any volume Ω , and in particular volumes that are infinitesimally small, and hence it follows that the macroscopic behavior of the single-phase fluid must satisfy the continuity equation

$$\frac{\partial(\phi\rho)}{\partial t} + \nabla \cdot (\rho\vec{v}) = \rho q. \quad (6.5)$$

Equation (6.5) contains more unknowns than equations and to derive a closed mathematical model, we need to introduce what is commonly referred to as constitutive equations that give the relationship between different states of the system (pressure, volume, temperature, etc.) at given physical conditions. Darcy's law, discussed in the previous section, is an example of a constitutive relation that has been derived to provide a phenomenological relationship between the macroscale \vec{v} and the fluid pressure p . In Section 3.4.1 we introduced the rock compressibility $c_r = d \ln(\phi)/dp$, which describes the relationship between the porosity ϕ and the pressure p . In a similar way, we can introduce the fluid compressibility to relate the density ρ to the fluid pressure p .

A change in density will generally cause a change in both the pressure p and the temperature T . The usual way of describing these changes in thermodynamics is to consider the change of volume V for a fixed number of particles,

$$\frac{dV}{V} = \frac{1}{V} \left(\frac{\partial V}{\partial p} \right)_T dp + \frac{1}{V} \left(\frac{\partial V}{\partial T} \right)_p dT, \quad (6.6)$$

where the subscripts T and p indicate that the change takes place under constant temperature and pressure, respectively. Since ρV is constant for a fixed number of particles, $d\rho V = \rho dV$, and (6.6) can be written in the equivalent form

$$\frac{d\rho}{\rho} = \frac{1}{\rho} \left(\frac{\partial \rho}{\partial p} \right)_T dp + \frac{1}{\rho} \left(\frac{\partial \rho}{\partial T} \right)_p dT = c_f dp + \alpha_f dT, \quad (6.7)$$

where the c_f denotes the *isothermal compressibility* and α_f denotes the *thermal expansion coefficient*. In many subsurface systems, the density changes slowly so that heat conduction keeps the temperature constant, in which case (6.7) simplifies to

$$c_f = \frac{1}{\rho} \frac{d\rho}{dp} = \frac{d \ln(\rho)}{dp}. \quad (6.8)$$

The factor c_f , which we henceforth will refer to as the fluid compressibility, is non-negative and will generally depend on both pressure and temperature, i.e., $c_f = c_f(p, T)$.

Introducing Darcy's law and fluid and rock compressibilities in (6.5), we obtain the following parabolic equation for the fluid pressure

$$c_t \phi \rho \frac{\partial p}{\partial t} - \nabla \cdot \left[\frac{\rho \mathbf{K}}{\mu} (\nabla p - g \rho \nabla z) \right] = \rho q, \quad (6.9)$$

where $c_t = c_r + c_f$ denotes the total compressibility. Notice that this equation is generally *nonlinear* since both ρ and c_t may depend on p . In the following, we will look briefly at several special cases in which the governing single-phase equation becomes a linear equation for the primary unknown; more extensive discussions can be found in standard textbooks like [155, Chap. 1], [47, Chap. 2]. For completeness, we will also briefly review the concept of an equation-of-state.

Incompressible flow

In the special case of an incompressible rock and fluid (that is, ρ and ϕ are independent of p so that $c_t = 0$), (6.9) simplifies to an elliptic equation with variable coefficients,

$$-\nabla \cdot \left[\frac{\mathbf{K}}{\mu} \nabla (p - g \rho z) \right] = q. \quad (6.10)$$

If we introduce the fluid potential, $\Phi = p - g \rho z$, (6.10) can be recognized as the (generalized) Poisson's equation $-\nabla \cdot \mathbf{K} \nabla \Phi = q$ or as the Laplace equation $\nabla \cdot \mathbf{K} \nabla \Phi = 0$ if there are no volumetric fluid sources or sinks. In the next section, we will discuss in detail how to discretize the second-order spatial Laplace operator $\mathcal{L} = \nabla \cdot \mathbf{K} \nabla$, which is a key technological component that will enter almost any software for simulation of flow in porous rock formations.

Constant compressibility

If the fluid compressibility is constant and independent of pressure, (6.8) can be integrated from a known density ρ_0 at a pressure datum p_0 to give the following equation,

$$\rho(p) = \rho_0 e^{c_f(p-p_0)} \quad (6.11)$$

which applies well to most liquids that do not contain large quantities of dissolved gas. To develop the differential equation, we first assume that the porosity and the fluid viscosity do not depend on pressure. Going back to the definition of fluid compressibility (6.8), it also follows from this equation that $\nabla p = (c_f \rho)^{-1} \nabla \rho$, which we can use to eliminate ∇p from Darcy's law (6.2). Inserting the result into (6.5) gives us the following continuity equation

$$\frac{\partial \rho}{\partial t} - \frac{1}{\mu \phi c_f} \nabla \cdot (\mathbf{K} \nabla \rho - c_f g \rho^2 \mathbf{K} \nabla z) = \rho q, \quad (6.12)$$

which in the absence of gravity forces and source terms is a linear equation for the fluid density that is similar to the classical heat equation with variable coefficients,

$$\frac{\partial \rho}{\partial t} = \frac{1}{\mu \phi c_f} \nabla \cdot (\mathbf{K} \nabla \rho). \quad (6.13)$$

Slightly compressible flow

In the case that the fluid compressibility is small, it is sufficient to use a linear relationship

$$\rho = \rho_0 [1 + c_f(p - p_0)]. \quad (6.14)$$

We further assume that ϕ is a function of \vec{x} only and that μ is constant. For simplicity, we also assume that g and q are both zero. Then, we can simplify (6.9) as follows:

$$(c_f \phi \rho) \frac{\partial p}{\partial t} = \frac{c_f \rho}{\mu} \nabla p \cdot \mathbf{K} \nabla p + \frac{\rho}{\mu} \nabla \cdot (\mathbf{K} \nabla p)$$

If c_f is sufficiently small, in the sense that $c_f \nabla p \cdot \mathbf{K} \nabla p \ll \nabla \cdot (\mathbf{K} \nabla p)$, we can neglect the first term on the right-hand side to derive a linear equation similar to (6.13) for the fluid pressure

$$\frac{\partial p}{\partial t} = \frac{1}{\mu \phi c_f} \nabla \cdot (\mathbf{K} \nabla p). \quad (6.15)$$

Ideal gas

If the fluid is a gas, compressibility can be derived from the gas law, which for an ideal gas can be written in two alternative forms,

$$pV = nRT, \quad \rho = p(\gamma - 1)e. \quad (6.16)$$

In the first form, T is temperature, V is volume, R is the gas constant (8.314 J K⁻¹mol⁻¹), and $n = m/M$ is the amount of substance of the gas in moles, where m is the mass and M is the molecular weight. In the second form, γ is the adiabatic constant, i.e., ratio of specific heat at constant pressure and constant volume, and e is the specific internal energy (internal energy per unit mass). In either case, it follows from (6.8) that $c_f = 1/p$.

If the fluid is a gas, we can neglect gravity, and once again we assume that ϕ is a function of \vec{x} only. Inserting (6.16) into (6.9) gives

$$\frac{\partial(\rho\phi)}{\partial t} = \phi(\gamma - 1)e \frac{\partial p}{\partial t} = \frac{1}{\mu} \nabla \cdot (\rho \mathbf{K} \nabla p) = \frac{(\gamma - 1)e}{\mu} \nabla \cdot (p \mathbf{K} \nabla p)$$

from which it follows that

$$\phi \mu \frac{\partial p}{\partial t} = \nabla \cdot (p \mathbf{K} \nabla p) \quad \Leftrightarrow \quad \frac{\phi \mu}{p} \frac{\partial p^2}{\partial t} = \nabla \cdot (\mathbf{K} \nabla p^2). \quad (6.17)$$

Equation of state

Equations (6.11), (6.14), and (6.16) are all examples of what is commonly referred to as equations of state, which provide constitutive relationships between mass, pressures, temperature, and volumes at thermodynamic equilibrium. Another popular form of these equations are the so-called cubic equations of state, which can be written as cubic functions of the molar volume $V_m = V/n = M/\rho$ involving constants that depend on the pressure p_c , the temperature T_c , and the molar volume V_c at the critical point, i.e., the point at which $(\frac{\partial p}{\partial V})_T = (\frac{\partial^2 p}{\partial V^2})_T \equiv 0$. A few particular examples include the Redlich–Kwong equation of state

$$\begin{aligned} p &= \frac{RT}{V_m - b} - \frac{a}{\sqrt{T} V_m (V_m + b)}, \\ a &= \frac{0.42748 R^2 T_c^{5/2}}{p_c}, \quad b = \frac{0.08662 R T_c}{p_c}, \end{aligned} \quad (6.18)$$

the modified version called Redlich–Kwong–Soave

$$\begin{aligned} p &= \frac{RT}{V_m - b} - \frac{a\alpha}{\sqrt{T} V_m (V_m + b)}, \\ a &= \frac{0.427 R^2 T_c^2}{p_c}, \quad b = \frac{0.08664 R T_c}{p_c}, \\ \alpha &= [1 + (0.48508 + 1.55171\omega - 0.15613\omega^2)(1 - \sqrt{T/T_c})]^2, \end{aligned} \quad (6.19)$$

as well as the Peng–Robinson equation of state,

$$\begin{aligned} p &= \frac{RT}{V_m - b} - \frac{a\alpha}{V_m^2 + 2bV_m - b^2}, \\ a &= \frac{0.4527235 R^2 T_c^2}{p_c}, \quad b = \frac{0.077796 R T_c}{p_c}, \\ \alpha &= [1 + (0.37464 + 1.54226\omega - 0.26992\omega^2)(1 - \sqrt{T/T_c})]^2. \end{aligned} \quad (6.20)$$

Here, ω denotes the acentric factor of the species, which is a measure of the centricity (deviation from spherical form) of the molecules in the fluid. The Peng–Robinson model is much better at predicting the densities of liquids than the Redlich–Kwong–Soave model, which was developed to fit pressure data of hydrocarbon vapor phases. If we introduce

$$A = \frac{a\alpha p}{(RT)^2}, \quad B = \frac{bp}{RT}, \quad Z = \frac{pV}{RT},$$

the Redlich–Kwong–Soave equation (6.19) and the Peng–Robinson equation (6.20) can be written in alternative polynomial forms,

$$0 = Z^3 - Z^2 + Z(A - B - B^2) - AB, \quad (6.21)$$

$$0 = Z^3 - (1 - B)Z^2 + (A - 2B - 3B^2)Z - (AB - B^2 - B^3), \quad (6.22)$$

which illustrates why they are called cubic equations of state.

6.3 Auxiliary conditions and equations

The governing equations for single-phase flow discussed above are all parabolic, except for the incompressible case in which the governing equation is elliptic. For the solution to be well-posed¹ inside a finite domain for any of the equations, one needs to supply boundary conditions that determine the behavior on the external boundary. For the parabolic equations describing unsteady flow, one also needs to impose an initial condition that determines the initial state of the fluid system. In this section, we will discuss these conditions in more detail. We will also discuss models for representing flow in and out of the reservoir rock through wellbores. Because this flow typically takes place on a length scale that is much smaller than the length scales of the global flow inside the reservoir, it is customary to model it using special analytical models. Finally, we also discuss a set of auxiliary equations for describing the movement of fluid elements and/or neutral particles that follow the single-phase flow without affecting it.

6.3.1 Boundary and initial conditions

In reservoir simulation one is often interested in describing closed flow systems that have no fluid flow across its external boundaries. This is a natural assumption when studying full reservoirs that have trapped and contained petroleum fluids for million of years. Mathematically, no-flow conditions across external boundaries are modeled by specifying homogeneous Neumann conditions,

$$\vec{v} \cdot \vec{n} = 0 \quad \text{for } \vec{x} \in \partial\Omega. \quad (6.23)$$

With no-flow boundary conditions, any pressure solution of (6.10) is immaterial and only defined up to an additive constant, unless a datum value is prescribed at some internal point or along the boundary.

It is also common that parts of the reservoir may be in communication with a larger aquifer system that provides external pressure support, which can be modeled in terms of a Dirichlet condition of the form

$$p(\vec{x}) = p_a(\vec{x}, t) \quad \text{for } \vec{x} \in \Gamma_a \subset \partial\Omega. \quad (6.24)$$

The function p_a can, for instance, be given as a hydrostatic condition. Alternatively, parts of the boundary may have a certain prescribed influx, which can be modeled in terms of an inhomogeneous Neumann condition,

$$\vec{v} \cdot \vec{n} = u_a(\vec{x}, t) \quad \text{for } \vec{x} \in \Gamma_a \subset \partial\Omega. \quad (6.25)$$

Combinations of these conditions are used when studying parts of a reservoir (e.g., sector models). There are also cases, e.g., when describing groundwater

¹ A solution is well-posed if it exists, is unique, and depends continuously on the initial and boundary conditions.

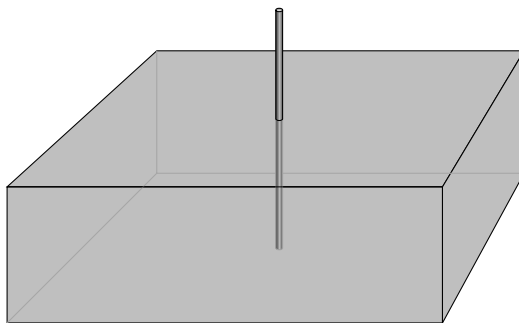


Fig. 6.4. Illustration of a well inside a grid cell. The proportions are not fully to scale: whereas the diameter of a well varies from 5 to 40 inches, a grid block may extend from tens to hundreds of meters in the lateral direction and from a few decimeters to ten meters in the vertical direction.

systems or CO₂ sequestration in saline aquifers, where (parts of) the boundaries are open or the system contains a background flow. More information of how to set boundary conditions will be given in Section 7.1.4. In the compressible case in (6.9), we also need to specify an initial pressure distribution. Typically, this pressure distribution will be hydrostatic, as in the gravity column we discussed briefly in Section 2.1, and hence be given by the ordinary differential equation,

$$\frac{dp}{dz} = \rho g, \quad p(z_0) = p_0. \quad (6.26)$$

6.3.2 Injection and production wells

In a typical reservoir simulation, the inflow and outflow in wells occur on a subgrid scale. In most discretized flow models, the pressure is modelled using a single pressure value inside each grid cell. The size of each grid cell must therefore be chosen so small that the pressure variation inside the cell can be approximated accurately in terms of its volumetric average. Far away from wells, the spatial variations in pressure tend to be relatively slow, at least in certain directions, and one can therefore choose cell sizes in the order of tens or hundreds of meters, which is a reasonable size compared with the extent of the reservoir. Near the well, however, the pressure will have large variations over short distances, and to compute a good approximation of these pressure variations, one would need grid cells that are generally smaller than what is computationally tractable. As a result, one with a setup similar to what is illustrated in Figure 6.4, where the radius of the well is typically between 1/100 and 1/1000 of the horizontal dimensions of the grid cell. The largest percentage of the pressure drop associated with a well occurs near the well and the pressure at the well radius will thus deviate significantly from the volumetric pressure average inside the cell. Special analytical models are

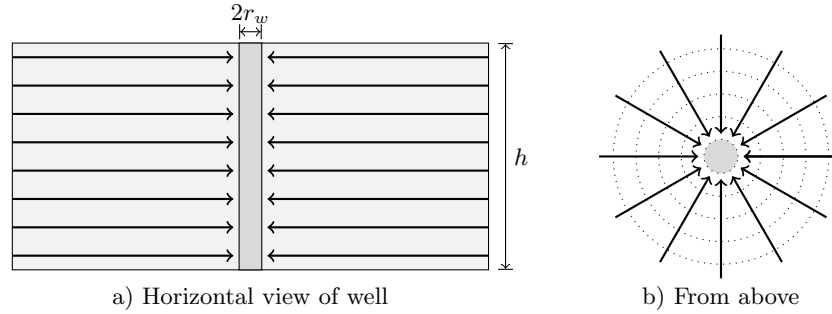


Fig. 6.5. Radial flow used to develop well model

therefore developed to represent the subgrid variations in the particular flow patterns near wells.

Normally, fluids are injected from a well at either constant *surface rate* or at constant *bottom-hole pressure*, which is also called wellbore flowing pressure and refers to the pressure at a certain point inside the wellbore. Similarly, fluids are produced at constant bottom-hole pressure or at constant surface liquid rate. The main purpose of a well model is then to accurately compute the pressure at well radius when the injection or production rate is known, or to accurately compute the flow rate in or out of the reservoir when the pressure at well radius is known. The resulting relation between the bottom-hole pressure and surface flow rate is often called the 'inflow-performance relation' or IPR.

The simplest and most widely used inflow-performance relation is the linear law

$$q_o = J(p_R - p_{bh}), \quad (6.27)$$

which states that the flow rate is directly proportional to the pressure draw-down in the well; that is, flow rate is proportional to the difference between the average reservoir pressure p_R in the grid cell and the bottom-hole pressure p_{bh} in the well. The constant of proportionality J is called the *productivity index* (PI) for production wells or the *well injectivity index* (WI) for injectors and accounts for all rock and fluid properties, as well as geometric factors that affect the flow. In MRST, we do not distinguish between productivity and injectivity indices, and henceforth we will only use the shorthand 'WI'.

The basic linear relation (6.27) can be derived from Darcy's law. Consider a vertical well that drains a rock with uniform permeability K . As an equation of state, we introduce the formation volume factor B defined as the ratio between the volume of the fluid at reservoir conditions and the volume of the fluid at surface conditions. (For incompressible flow, $B \equiv 1$). The well penetrates the rock completely over a height h and is open in the radial direction. Fluids are assumed to only flow in the radial direction and the outer boundary is circular, see Figure 6.5. In other words, we assume a pseudo-steady, radial

flow that can be described by Darcy's law

$$v = \frac{qB}{2\pi rh} = \frac{K}{\mu} \frac{dp}{dr}.$$

Even if several different flow patterns can be expected when fluids flow toward a vertical wellbore, two-dimensional radial flow is considered to be the most representative for vertical oil and gas wells.

We now integrate this equation from the wellbore r_w and to the drainage boundary r_e where the pressure is constant

$$2\pi Kh \int_{p_{bh}}^{p_e} \frac{1}{q\mu B} dp = \int_{r_w}^{r_e} \frac{1}{r} dr.$$

Here, B and μ are pressure-dependent quantities; B decreases with pressure and μ increases. The composite effect is that $(\mu B)^{-1}$ decreases (almost) linearly with pressure. We can therefore approximate μB by $(\mu B)_{avg}$ evaluated at the average pressure $p_{avg} = (p_{bh} + p_e)/2$. For convenience, we drop the subscript in the following. This gives us the pressure as a function of radial distance

$$p_e = p_{bh} + \frac{q\mu B}{2\pi Kh} \ln(r_e/r_w). \quad (6.28)$$

To close the system, we need to know the location of the drainage boundary $r = r_e$ where the pressure is constant. This is often hard to know, and it is customary to relate q to the volumetric average pressure instead. For pseudo-steady flow the volumetric average pressure occurs at $r = 0.472r_e$. Hence,

$$q = \frac{2\pi Kh}{\mu B (\ln(r_e/r_w) - 0.75)} (p_R - p_{bh}). \quad (6.29)$$

The above relation (6.29) was developed for an ideal well under several simplifying assumptions: homogeneous and isotropic formation of constant thickness, clean wellbore, etc. In practice, a well will rarely experience these ideal conditions. Typically the permeability is altered close to the wellbore under drilling and completion, the well will only be partially completed, and so on. The actual pressure performance will therefore deviate from (6.29). To model this, it is customary to include a *skin factor* S to account for extra pressure loss due to alterations in the inflow zone. The resulting equation is

$$q = \frac{2\pi Kh}{\mu B (\ln(r_e/r_w) - 0.75 + S)} (p_R - p_{bh}). \quad (6.30)$$

Often the constant -0.75 is included in the skin factor S , and for stimulated wells the skin factor could be negative. Sometimes h is modified to ch , where c is the completion factor, i.e., a dimensionless number between zero and one describing the fraction of the wellbore open to flow.

To use the radial model in conjunction with a reservoir model, the volumetric average pressure in the radial model must be related to the computed

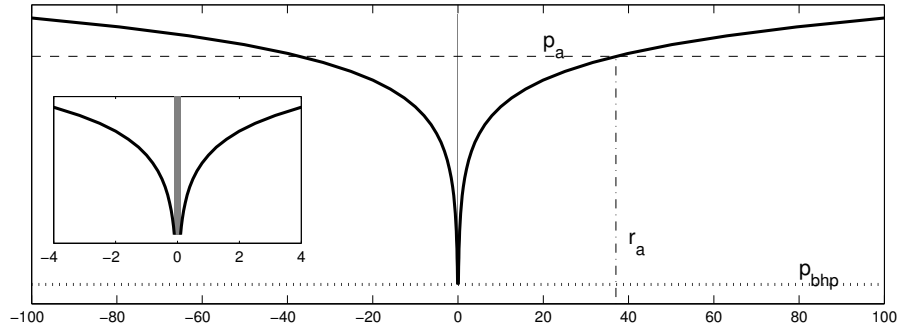


Fig. 6.6. Illustration of the pressure distribution inside a cell computed from (6.28) assuming the well is producing fluids from an infinite domain. Here, p_a is the volumetric pressure average and r_a is the radius at which this value is found. The inset shows a zoom of the near-well zone.

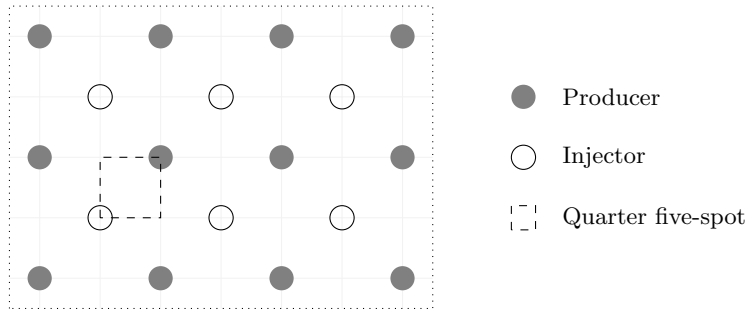


Fig. 6.7. Excerpts of a repeated five-spot pattern.

cell pressure. Analytical solutions are generally not known since real reservoirs have complicated geometries and irregular boundaries. Well models are therefore developed using highly idealized reservoir geometries. One such example is the so-called *repeated five-spot pattern*, which consists of a thin, infinitely large, horizontal reservoir with a staggered pattern of injection and production wells as shown in Figure 6.7 that repeats itself to infinity in all directions. The name comes from the fact that each injector is surrounded by four producers, and vice versa, hence creating tiles of five-spot patterns. If all wells operate at equal rates, the flow pattern has certain symmetries and it is common to only consider a quarter of the five spot, as shown in Figure 6.7, subject to no-flow boundary conditions. An analytical solution for the pressure drop between the injection and production wells was developed by Muskat [138],

$$\Delta p = \frac{q\mu B}{\pi K h} \left(\ln(r_e/r_w) - B \right), \tag{6.31}$$

where d is the distance between the wells, and B is given by an infinite series. Muskat [138] originally used $B = 0.6190$, but a more accurate value, $B =$

0.61738575, was later derived by Peaceman [154], who used (6.31) to determine an equivalent radius r_e at which the cell pressure is equal to the analytical pressure. Assuming isotropic permeabilities, square grid blocks, single-phase flow, and a well at a center of an interior block, Peaceman [156] showed that the equivalent radius is

$$r_e \approx 0.2\sqrt{\Delta x \Delta y}$$

for the two-point discretization that will be discussed in more detail in Section 6.4.1.

This basic model has later been extended to cover a lot of other cases, e.g., off-center wells, multiple wells, non-square grids, anisotropic permeability, horizontal wells; see for instance [14, 67, 7]. For anisotropic permeabilities—and horizontal wells—the equivalent radius is defined as [154]

$$r_e = 0.28 \frac{\left(\sqrt{K_y/K_x} \Delta x^2 + \sqrt{K_x/K_y} \Delta y^2\right)^{1/2}}{\left(K_y/K_x\right)^{1/4} + \left(K_x/K_y\right)^{1/4}}, \quad (6.32)$$

and the permeability is replaced by an effective permeability

$$K_e = \sqrt{K_x K_y}. \quad (6.33)$$

If we include gravity forces in the well and assume hydrostatic equilibrium, the well model thus reads

$$q_i = \frac{2\pi h c K_e}{\ln(r_e/r_w) + S} \frac{1}{\mu_i B_i} (p_R - p_{bh} - \rho_i(z - z_{bh})g), \quad (6.34)$$

where K_e is given by (6.33) and r_e is given by (6.32). For deviated wells, h denotes the length of the grid block in the major direction of the wellbore and *not* the length of the wellbore.

At this point we should add a word of caution. The equivalent radius of a numerical method generally depends on how the method approximates the pressure inside the grid cell containing the well perforation. The formulas given above are strictly seen only valid if you use the specific two-point discretization they were developed for. When using another discretization method, you may have to compute other values for the equivalent radius, e.g., as discussed in [112, 120].

6.3.3 Field lines and time-of-flight

Equation (6.10) together with a set of suitable and compatible boundary conditions is all that one needs to describe the flow of an incompressible fluid inside an incompressible rock. In the remains of this section, we will discuss a few simple concepts and auxiliary equations that have proven useful to visualize, analyze, and understand flow fields.

A simple way to visualize a flow field is to use field lines resulting from the vector field: streamlines, streaklines, and pathlines. In steady flow, the three are identical. However, if the flow is not steady, i.e., when \vec{v} changes with time, they differ. Streamlines are associated with an instant snapshot of the flow field and consists of a family of curves that are everywhere tangential to \vec{v} and show the direction a fluid element will travel at this specific point in time. That is, if $\vec{x}(r)$ is a parametric representation of a single streamline at this instance \hat{t} in time, then

$$\frac{d\vec{x}}{dr} \times \vec{v}(\vec{x}, \hat{t}) = 0, \quad \text{or equivalently,} \quad \frac{d\vec{x}}{dr} = \frac{\vec{v}(\hat{t})}{|\vec{v}(\hat{t})|}. \quad (6.35)$$

In other words, streamlines are calculated instantaneously throughout the fluid from an *instantaneous* snapshot of the flow field. Because two streamlines from the same instance in time cannot cross, there cannot be flow across it, and if we align a coordinate along a bundle of streamlines, the flow through them will be one-dimensional.

Pathlines are the trajectories that individual fluid elements will follow over a certain period. In each moment of time, the path a fluid particle takes will be determined by the streamlines associated with the streamlines at this instance in time. If $\vec{y}(t)$ represents a single path line starting at \vec{y}_0 at time t_0 , then

$$\frac{d\vec{y}}{dt} = \vec{v}(\vec{y}, t), \quad \vec{y}(t_0) = \vec{y}_0. \quad (6.36)$$

A streakline is the line traced out by all fluid particles that have passed through a prescribed point throughout a certain period of time. (Think of dye injected into the fluid at a specific point). If we $\vec{z}(t, s)$ denote a parametrization of a streakline and \vec{z}_0 the specific point through which all fluid particles have passed, then

$$\frac{d\vec{z}}{dt} = \vec{v}(\vec{z}, t), \quad \vec{z}(s) = \vec{z}_0. \quad (6.37)$$

Like streamlines, two streaklines cannot intersect each other.

In summary: streamline patterns change over time, but are easy to generate mathematically. Pathlines and streaklines are recordings of the passage of time and are obtained through experiments.

Within reservoir simulation streamlines are far more used than pathlines and streaklines. Moreover, rather than using the arc length r to parametrize streamlines, it is common to introduce an alternative parametrization called time-of-flight, which takes into account the reduced volume available for flow, i.e., the porosity ϕ . Time-of-flight is defined by the following integral

$$\tau(r) = \int_0^r \frac{\phi(\vec{x}(s))}{|\vec{v}(\vec{x}(s))|} ds, \quad (6.38)$$

where τ expresses the time it takes a fluid particle to travel a distance r along a streamline (in the interstitial velocity field \vec{v}/ϕ). Alternatively, by the fundamental theorem of calculus and the directional derivative,

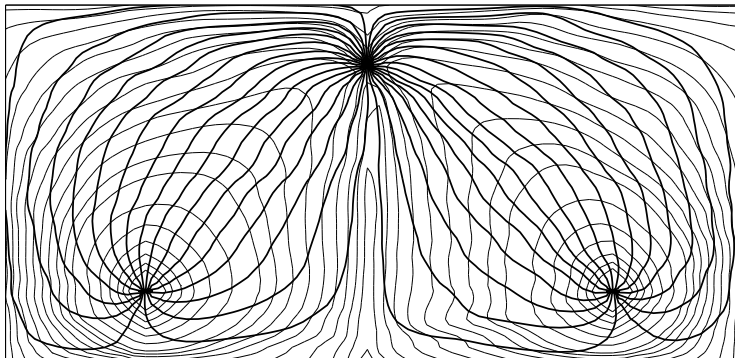


Fig. 6.8. Illustration of time-of-flight, shown as gray isocontour lines, and streamlines shown as thick black lines.

$$\frac{d\tau}{dr} = \frac{\phi}{|\vec{v}|} = \frac{\vec{v}}{|\vec{v}|} \cdot \nabla\tau,$$

from which it follows that τ can be expressed by the following differential equation [52, 53]

$$\vec{v} \cdot \nabla\tau = \phi. \quad (6.39)$$

In lack of a better name, we will refer to this as the time-of-flight equation.

6.3.4 Tracers and volume partitions

Somewhat simplified, tracers can be considered as neutral particles that passively flow with the fluid without altering its flow properties. The concentration of a tracer is given by a continuity equation on the same form as (6.5),

$$\frac{\partial(\phi C)}{\partial t} + \nabla \cdot (\vec{v}C) = q_C. \quad (6.40)$$

Communication patterns within a reservoir can be determined by simulating the evolution of artificial, non-diffusive tracers whose concentration does not change upon fluid compression or expansion. A simple flow diagnostics is to set the tracer concentration equal to one in a particular fluid source or at a certain part of the inflow boundary and compute the solution approached at steady-state conditions from the non-conservative equation,

$$\vec{v} \cdot \nabla C = q_C, \quad C|_{\text{inflow}} = 1. \quad (6.41)$$

The resulting tracer distribution gives the portion of the total fluid volume coming from a certain fluid source, or parts of the inflow boundary, that eventually will reach each point in the reservoir. Likewise, by reversing the sign of the flow field and assigning unit tracers to a particular fluid sink or parts of the outflow, one can compute the portion of the fluid arriving at a

source or outflow boundary that can be attributed to a certain point in the reservoir. By repeating this process for all parts of the inflow, one can easily obtain a partition of the instantaneous flow field.

A more dynamic view can be obtained by utilizing the fact that streamlines and time-of-flight can be used to define an alternative curvilinear and flow-based coordinate system in three dimensions. To this end, we introduce the bi-streamfunctions ψ and χ [23], for which $\vec{v} = \nabla\psi \times \nabla\chi$. In the streamline coordinates (τ, ψ, χ) , the gradient operator is expressed as

$$\nabla_{(\tau, \psi, \chi)} = (\nabla\tau) \frac{\partial}{\partial\tau} + (\nabla\psi) \frac{\partial}{\partial\psi} + (\nabla\chi) \frac{\partial}{\partial\chi}. \quad (6.42)$$

Moreover, a streamline Ψ is defined by the intersection of a constant value for ψ and a constant value for χ . Because \vec{v} is orthogonal to $\nabla\psi$ and $\nabla\chi$, it follows from (6.39) that

$$\vec{v} \cdot \nabla_{(\tau, \psi, \chi)} = (\vec{v} \cdot \nabla\tau) \frac{\partial}{\partial\tau} = \phi \frac{\partial}{\partial\tau}. \quad (6.43)$$

Therefore, the coordinate transformation $(x, y, z) \rightarrow (\tau, \psi, \chi)$ will reduce the three-dimensional transport equation (6.40) to a family of one-dimensional transport equations along each streamline [52, 99], which for incompressible flow reads

$$\frac{\partial C}{\partial t} + \frac{\partial C}{\partial\tau} = 0. \quad (6.44)$$

In other words, there is no exchange of the quantity C between streamlines and each streamline can be viewed as an isolated flow system. Assuming a prescribed concentration history $C_0(t)$ at the inflow, gives a time-dependent boundary-value problem for the concentration at the outflow (6.44). Here, the response is given as (see [52]),

$$C(t) = C_0(t - \tau), \quad (6.45)$$

which is easily verified by inserting the expression into (6.44) and the fact that the solution is unique [83]. For the special case of continuous and constant injection, the solution is particularly simple

$$C(t) = \begin{cases} 0, & t < \tau, \\ C_0, & t > \tau. \end{cases}$$

6.4 Basic finite-volume discretizations

Research on numerical solution of the Laplace/Poisson equation has a long tradition, and there exist a large number of different finite-difference and finite-volume methods, as well as finite-element methods based on standard

Galerkin, mixed, or discontinuous Galerkin formulations, which all have their merits. In Chapter 8, we will discuss consistent discretizations of Poisson-type equations in more detail. We introduce a general framework for formulating such method on general polyhedral grids and present several recent methods that are specially suited for irregular grids with strongly discontinuous coefficients, which are typically seen in realistic reservoir simulation models. In particular, we will discuss multipoint flux-approximation (MPFA) methods and mimetic finite-difference (MFD) methods, which are both available in add-on modules that are part of the standard MRST releases. As a starting point, however, we will in rest of this section present the simplest example of a finite-volume discretization, the two-point flux-approximation (TPFA) scheme, which is used extensively throughout industry and also is the default discretization method in MRST. We will give a detailed derivation of the method and point out its advantages and shortcomings. For completeness, we also briefly outline how to discretize the time-of-flight and the stationary tracer equations.

6.4.1 Two-point flux-approximation

To keep technical details at a minimum, we will in the following without loss of generality consider the simplified single-phase flow equation

$$\nabla \cdot \vec{v} = q, \quad \vec{v} = -K\nabla p, \quad \text{in } \Omega \subset \mathbb{R}^d. \quad (6.46)$$

In classical finite-difference methods, partial differential equations are approximated by replacing the derivatives with appropriate divided differences between point-values on a discrete set of points in the domain. Finite-volume methods, on the other hand, have a more physical motivation and are derived from conservation of (physical) quantities over cell volumes. Thus, in a finite-volume method the unknown functions are represented in terms of average values over a set of finite-volumes, over which the integrated PDE model is required to hold in an averaged sense. Although finite-difference and finite-volume methods have fundamentally different interpretation and derivation, the names are used interchangeably in the scientific literature. The main reason for this is probably that for certain low-order methods, the discrete equations derived for the cell-centered values in a mass-conservative finite-difference method are identical to the discrete equations for the cell averages in the corresponding finite-volume method. Herein, we will stick to this convention and not make a strict distinction between the two types of methods

To develop a finite-volume discretization for (6.46), we start by rewriting the equation in integral form using a single cell Ω_i in the discrete grid as control volume

$$\int_{\partial\Omega_i} \vec{v} \cdot \vec{n} ds = \int_{\Omega_i} q d\vec{x}. \quad (6.47)$$

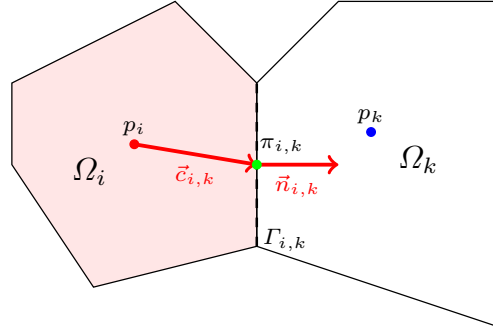


Fig. 6.9. Two cells used to define the two-point finite-volume discretization of the Laplace operator.

This is a simpler form of (6.3), where that the accumulation term has disappeared because ϕ and ρ are independent of time and the constant ρ has been eliminated.

Equation (6.47) ensures that mass is conserved for each grid cell. The next step is to use Darcy's law to compute the flux across each face of the cell,

$$v_{i,k} = \int_{\Gamma_{ik}} \vec{v} \cdot \vec{n} ds, \quad \Gamma_{i,k} = \partial\Omega_i \cap \partial\Omega_k. \quad (6.48)$$

We will refer to the faces $\Gamma_{i,k}$ as *half-faces* since they are associated with a particular grid cell Ω_i and a certain normal vector $\vec{n}_{i,k}$. However, since the grid is assumed to be matching, each interior half face will have a twin half-face $\Gamma_{k,i}$ that has identical area $A_{k,i} = A_{i,k}$ but opposite normal vector $\vec{n}_{k,i} = -\vec{n}_{i,k}$. If we further assume that the integral over the cell face in (6.48) is approximated by the midpoint rule, we use Darcy's law to write the flux as

$$v_{i,k} \approx A_{i,k} \vec{v}(\vec{x}_{i,k}) \cdot \vec{n}_{i,k} = -A_{i,k} (\mathbf{K} \nabla p)(\vec{x}_{i,k}) \cdot \vec{n}_{i,k}, \quad (6.49)$$

where $\vec{x}_{i,k}$ denotes the centroid on $\Gamma_{i,k}$. The idea is now to use a one-sided finite difference to express the pressure gradient as the difference between the pressure $\pi_{i,k}$ at the face centroid and at some point inside the cell. However, in a finite-volume method, we only know the cell averaged value of the pressure inside the cell. We therefore must make some additional assumption that will enable us to reconstruct point values that are needed to estimate the pressure gradient in Darcy's law. If we assume that the pressure is linear (or constant) inside each cell, the reconstructed pressure value π_i at the cell center is identical to the average pressure p_i inside the cell, and hence it follows that (see Figure 6.9)

$$v_{i,k} \approx A_{i,k} \mathbf{K}_i \frac{(p_i - \pi_{i,k}) \vec{c}_{i,k}}{|\vec{c}_{i,k}|^2} \cdot \vec{n}_{i,k} = T_{i,k} (p_i - \pi_{i,k}). \quad (6.50)$$

Here, we have introduced one-sided transmissibilities $T_{i,k}$ that are associated with a single cell and gives a two-point relation between the flux across a cell

face and the difference between the pressure at the cell and face centroids. We will refer to these one-sided transmissibilities as *half-transmissibilities* since they are associated with a half face.

To derive the final discretization, we impose continuity of fluxes across all faces, $v_{i,k} = -v_{k,i} = v_{ik}$ and continuity of face pressures $\pi_{i,k} = \pi_{k,i} = \pi_{ik}$. This gives us two equations,

$$T_{i,k}^{-1}v_{ik} = p_i - \pi_{ik}, \quad -T_{k,i}^{-1}v_{ik} = p_k - \pi_{ik}.$$

By eliminating the interface pressure π_{ik} , we end up with the following two-point flux-approximation (TPFA) scheme,

$$v_{ik} = [T_{i,k}^{-1} + T_{k,i}^{-1}]^{-1}(p_i - p_k) = T_{ik}(p_i - p_k). \quad (6.51)$$

where is the T_{ik} the transmissibility associated with the connection between the two cells. As the name suggests, the TPFA scheme uses two 'points', the cell averages p_i and p_k , to approximate the flux across the interface Γ_{ik} between the cells Ω_i and Ω_k . In the derivation above, the cell fluxes were parametrized in terms of the index of the neighboring cell. Extending the derivation to also include fluxes on exterior faces is trivial since we either know the flux explicitly for Neumann boundary conditions (6.23) or (6.25), or know the interface pressure for Dirichlet boundary conditions (6.24).

By inserting the expression for v_{ik} into (6.47), we see that the TPFA scheme for (6.46), in compact form, seeks a set of cell averages that satisfy the following system of equations

$$\sum_k T_{ik}(p_i - p_k) = q_i, \quad \forall \Omega_i \subset \Omega \quad (6.52)$$

This system is clearly symmetric, and a solution is, as for the continuous problem, defined up to an arbitrary constant. The system is made positive definite, and symmetry is preserved by specifying the pressure in a single point. In MRST, we have chosen to set $p_1 = 0$ by adding a positive constant to the first diagonal of the matrix $\mathbf{A} = [a_{ij}]$, where:

$$a_{ij} = \begin{cases} \sum_k T_{ik} & \text{if } j = i, \\ -T_{ij} & \text{if } j \neq i, \end{cases}$$

The matrix \mathbf{A} is sparse and will have a banded structure for structured grids (tridiagonal for 1D grids and penta- and heptadiagonal for logically Cartesian grids in 2D and 3D, respectively). The TPFA scheme is monotone, robust, and relatively simple to implement, and is currently the industry standard with reservoir simulation.

Example 6.1. To tie the links with standard finite-difference methods on Cartesian grids, we will derive the two-point discretization for a 2D Cartesian grid with isotropic permeability. Consider the flux in the x -direction between

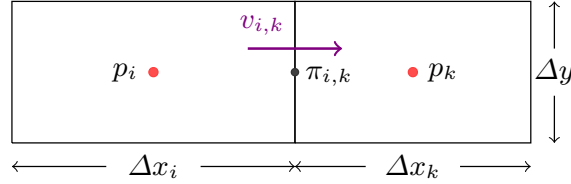


Fig. 6.10. Two cells used to derive the TPFA discretization for a 2D Cartesian grid

two cells i and k as illustrated in Figure 6.10. As above, we impose mass conservation inside each cell. For cell i this reads:

$$v_{i,k} = \Delta y \frac{(p_i - \pi_{i,k})}{(\frac{1}{2}\Delta x_i)^2} (\frac{1}{2}\Delta x_i, 0) K_i(1, 0)^T = \Delta y \frac{2K_i}{\Delta x_i} (p_i - \pi_{i,k})$$

and likewise for cell k :

$$v_{k,i} = \Delta y \frac{(p_k - \pi_{k,i})}{(\frac{1}{2}\Delta x_k)^2} (-\frac{1}{2}\Delta x_k, 0) K_k(-1, 0)^T = \Delta y \frac{2K_k}{\Delta x_k} (p_k - \pi_{k,i})$$

Next, we impose continuity of fluxes and face pressures,

$$v_{i,k} = -v_{k,i} = v_{ik}, \quad \pi_{i,k} = \pi_{k,i} = \pi_{ik}$$

which gives us two equations

$$\frac{\Delta x_i}{2K_i \Delta y} v_{ik} = p_i - \pi_{ik}, \quad -\frac{\Delta x_k}{2K_k \Delta y} v_{ik} = p_k - \pi_{ik}.$$

Finally, we eliminate π_{ik} to obtain

$$v_{ik} = 2\Delta y \left(\frac{\Delta x_i}{K_i} + \frac{\Delta x_k}{K_k} \right)^{-1} (p_i - p_k),$$

which shows that the transmissibility is given by the harmonic average of the permeability values in the two adjacent cells, as one would expect.

In [4], we showed how one could develop an efficient and self-contained MATLAB program that in approximately thirty compact lines solved the incompressible flow equation (6.46) using the two-point method outlined above. The program was designed for Cartesian grids with no-flow boundary conditions only and relied strongly on a logical ijk numbering of grid cells. For this reason, the program has limited applicability beyond highly idealized cases like the SPE10 model. However, in its simplicity, it presents an interesting contrast to the general-purpose implementation in MRST that handles unstructured grids, wells, and more general boundary conditions. The interested reader is encouraged to read the paper and try the accompanying program and example scripts that can be downloaded from

<http://folk.uio.no/kalie/matlab-ressim/>

6.4.2 Discrete div and grad operators

While the double-index notation $v_{i,k}$ and v_{ik} used in the previous section is simple and easy to comprehend when working with a single interface between two neighboring cells, it becomes more involved when we want to introduce the same type of discretizations for more complex equations than the Poisson equation for incompressible flow. To prepare for discussions that will follow later in the book, we will in the following introduce a more abstract way of writing the two-point finite-volume discretization introduced in the previous section. The idea is to introduce discrete operators for the divergence and gradient operators that mimic their continuous counterparts, which will enable us to write the discretized version of the Poisson equation (6.46) in the same form as its continuous counterpart. To this end, we start by a quick recap of the definition of unstructured grids. As discussed in detail in Section 4.4, the grid structure in MRST, consists of three objects: The *cells*, the *faces*, and the *nodes*. Each cell corresponds to a set of faces, and each face to a set of *edges*, which again are determined by the nodes. Each object has given geometrical properties (volume, areas, centroids). As before, let us denote by n_c and n_f , the number of cells and faces, respectively. To define the topology of the grid, we will mainly use two different mappings. The first mapping is given by $N : \{1, \dots, n_c\} \rightarrow \{0, 1\}^{n_f}$ and maps a cell to the set of faces that constitute this cell. In a grid structure \mathbf{G} , this is represented as the `G.cells.faces` array, where the first column that gives the cell numbers is not stored since it is redundant and instead must be computed by a call `f2cn = gridCellNo(G)`. The second mapping consists in fact of two mappings that, for a given face, give the corresponding neighboring cells, $N_1, N_2 : \{1, \dots, n_f\} \rightarrow \{1, \dots, n_c\}$. In a grid structure \mathbf{G} , N_1 is given by `G.faces.neighbors(:,1)` and N_2 by `G.faces.neighbors(:,2)`.

Let us now construct the discrete versions of the divergence and gradient operators, which we denote `div` and `grad`. The mapping `div` is a linear mapping from faces to cells. We consider a discrete flux $\mathbf{v} \in \mathbb{R}^{n_f}$. For a face f , the orientation of the flux $\mathbf{v}[f]$ is from $N_1(f)$ to $N_2(f)$. Hence, the total amount of matter leaving the cell c is given by

$$\text{div}(\mathbf{v})[c] = \sum_{f \in N(c)} \mathbf{v}[f] \mathbf{1}_{\{c=N_1(f)\}} - \sum_{f \in N(c)} \mathbf{v}[f] \mathbf{1}_{\{c=N_2(f)\}}. \quad (6.53)$$

The `grad` mapping maps \mathbb{R}^{n_c} to \mathbb{R}^{n_f} and it is defined as

$$\text{grad}(\mathbf{p})[f] = \mathbf{p}[N_2(f)] - \mathbf{p}[N_1(f)], \quad (6.54)$$

for any $\mathbf{p} \in \mathbb{R}^{n_c}$. In the continuous case, the gradient operator is the adjoint of the divergence operator (up to a sign), as we have

$$\int_{\Omega} p \nabla \cdot \vec{v} d\vec{x} + \int_{\Omega} \vec{v} \cdot \nabla p d\vec{x} = 0, \quad (6.55)$$

for vanishing boundary conditions. Let us prove that this property holds also in the discrete case. To simplify the notations, we set $S_c = \{1, \dots, n_c\}$ and $S_f = \{1, \dots, n_f\}$. For any $\mathbf{v} \in \mathbb{R}^{n_f}$ and $\mathbf{p} \in \mathbb{R}^{n_c}$, we have

$$\begin{aligned} \sum_{c \in S_c} \operatorname{div}(\mathbf{v})[c] \mathbf{p}[c] &= \sum_{c \in S_c} \mathbf{p}[c] \left(\sum_{f \in N(c)} \mathbf{v}[f] \mathbf{1}_{\{c=N_1(f)\}} - \sum_{f \in N(c)} \mathbf{v}[f] \mathbf{1}_{\{c=N_2(f)\}} \right) \\ &= \sum_{c \in S_c} \sum_{f \in S_f} \mathbf{v}[f] \mathbf{p}[c] \mathbf{1}_{\{c=N_1(f)\}} \mathbf{1}_{\{f \in N(c)\}} \\ &\quad - \sum_{c \in S_c} \sum_{f \in S_f} \mathbf{v}[f] \mathbf{p}[c] \mathbf{1}_{\{c=N_2(f)\}} \mathbf{1}_{\{f \in N(c)\}} \end{aligned} \quad (6.56)$$

We can switch the order in the sums above and obtain

$$\begin{aligned} \sum_{c \in S_c} \sum_{f \in S_f} \mathbf{v}[f] \mathbf{p}[c] \mathbf{1}_{\{c=N_1(f)\}} \mathbf{1}_{\{f \in N(c)\}} &= \\ \sum_{f \in S_f} \sum_{c \in S_c} \mathbf{v}[f] \mathbf{p}[c] \mathbf{1}_{\{c=N_1(f)\}} \mathbf{1}_{\{f \in N(c)\}}. \end{aligned}$$

For a given face f , we have that $\mathbf{1}_{\{c=N_1(f)\}} \mathbf{1}_{\{f \in N(c)\}}$ is nonzero if and only if $c = N_1(f)$ and therefore

$$\sum_{f \in S_f} \sum_{c \in S_c} \mathbf{1}_{\{c=N_1(f)\}} \mathbf{1}_{\{f \in N(c)\}} \mathbf{v}[f] \mathbf{p}[c] = \sum_{f \in S_f} \mathbf{v}[f] \mathbf{p}[N_1(f)].$$

In the same way, we have

$$\sum_{c \in S_c} \sum_{f \in S_f} \mathbf{v}[f] \mathbf{p}[c] \mathbf{1}_{\{c=N_2(f)\}} \mathbf{1}_{\{f \in N(c)\}} = \sum_{f \in S_f} \mathbf{v}[f] \mathbf{p}[N_2(f)]$$

so that (6.56) yields

$$\sum_{c \in S_c} \operatorname{div}(\mathbf{v})[c] \mathbf{p}[c] + \sum_{f \in S_f} \operatorname{grad}(\mathbf{p})[f] \mathbf{v}[f] = 0. \quad (6.57)$$

Until now, the boundary conditions have been ignored. They are included by introducing one more cell number $c = 0$ to denote the exterior. Then we can consider external faces and extend the mappings N_1 and N_2 to $S_c \cup \{0\}$ so that, if a given face f satisfies $N_1(f) = 0$ or $N_2(f) = 0$ then it is external. Note that the grad operator only defines values on internal faces. Now taking external faces into account, we obtain

$$\begin{aligned} \sum_{c \in S_c} \operatorname{div}(\mathbf{v})[c] \mathbf{p}[c] + \sum_{f \in S_f} \operatorname{grad}(\mathbf{p})[f] \mathbf{v}[f] \\ = \sum_{f \in S_f \setminus S_f} \left(\mathbf{p}[N_1(f)] \mathbf{1}_{\{N_2(f)=0\}} - \mathbf{p}[N_2(f)] \mathbf{1}_{\{N_1(f)=0\}} \right) \mathbf{v}[f], \end{aligned} \quad (6.58)$$

where \bar{S}_f denotes the set of internal and external faces. The identity (6.58) is the discrete counterpart to

$$\int_{\Omega} p \nabla \cdot \vec{v} d\vec{x} + \int_{\Omega} \vec{v} \cdot \nabla p d\vec{x} = \int_{\partial\Omega} p \vec{v} \cdot \vec{n} ds. \tag{6.59}$$

Going back to (6.46), we see that the vector $\mathbf{v} \in \mathbb{R}^{n_f}$ is a discrete approximation of the flux on faces. Given $f \in S_f$, we have

$$\mathbf{v}[f] \approx \int_{\Gamma_f} \vec{v}(x) \cdot \vec{n}_f ds,$$

where \vec{n}_f is the normal to the face f , where the orientation is given by the grid. The relation between the discrete pressure $\mathbf{p} \in \mathbb{R}^{n_c}$ and the discrete flux is given by the two-point flux approximation discussed in the previous section,

$$\mathbf{v}[f] = -\mathbf{T}[f] \mathbf{grad}(\mathbf{p})[f] \approx - \int_{\Gamma_f} \mathbf{K}(x) \nabla p \cdot \vec{n}_f ds, \tag{6.60}$$

where $\mathbf{T}[f]$ denotes the transmissibility of the face f , as defined in (6.51). Hence, the discretization of (6.46) is

$$\mathbf{div}(\mathbf{v}) = q \tag{6.61a}$$

$$\mathbf{v} = -\mathbf{T} \mathbf{grad}(\mathbf{p}). \tag{6.61b}$$

where the multiplication in (6.61b) holds element-wise.

Example 6.2. To illustrate the use of the discrete operators, let us set up and solve the classical Poisson equation on a simple box geometry,

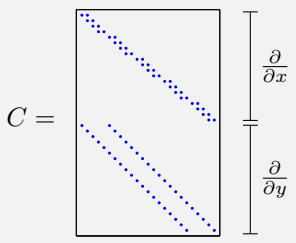
$$-\mathbf{div}(\mathbf{T} \mathbf{grad}(\mathbf{p})) = \mathbf{q}, \quad \Omega = [0, 1] \times [0, 1] \tag{6.62}$$

subject to no-flow boundary conditions with q consisting of a point source at (0,0) and a point sink at (1,1). First, we construct a small Cartesian grid

```
G = computeGeometry(cartGrid([5 5],[1 1]));
```

for which T equals a scalar multiple of the identity matrix and is therefore dropped for simplicity. The `div` and `grad` operators will be constructed as sparse matrices. To this end, we will use (6.54) and (6.57), which implies that the sparse matrix used to construct `div` is the negative transpose of the matrix that defines `grad`. Moreover, since we assume no-flow boundary conditions, we only need to let N_1 and N_2 account for internal connections:

```
N = G.faces.neighbors;
N = N(all(N ~ 0, 2), :);
nf = size(N,1);
nc = G.cells.num;
C = sparse([(1:nf)'; (1:nf)'], N, ...
           ones(nf,1)*[-1 1], nf, nc);
grad = @(x) C*x;
div = @(x) -C'*x;
```



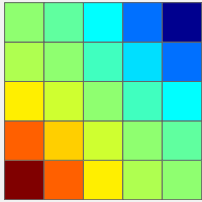
Once we have the discrete operators, we can write (6.62) in residual form, $\mathbf{f}(\mathbf{p}) = \mathbf{A}\mathbf{p} + \mathbf{q} = 0$, and then use automatic differentiation as discussed in Section 2.7 to obtain \mathbf{A} by computing $\partial \mathbf{f} / \partial \mathbf{p}$

```

p = initVariablesADI(zeros(nc,1));
q = zeros(nc, 1);           % source term
q(1) = 1; q(nc) = -1;      % -> quarter five-spot

eq  = div(grad(p))+q;      % equation
eq(1) = eq(1) + p(1);      % make solution unique
p    = -eq.jac{1}\eq.val;  % solve equation

```

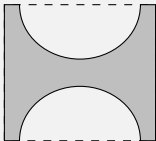


Next, we try to solve the same type of flow problem on a non-rectangular domain. That is, we still consider the unit square, but remove two half-circles of radius 0.4 centered at (0.5,0) and (0.5,1), respectively. To construct the corresponding grid, we use the fictitious grid approach from Section 4.1 (see Exercise 16 on page 83):

```

G = cartGrid([20 20],[1 1]);
G = computeGeometry(G);
r1 = sum(bsxfun(@minus,G.cells.centroids,[0.5 1]).^2,2);
r2 = sum(bsxfun(@minus,G.cells.centroids,[0.5 0]).^2,2);
G = extractSubgrid(G, (r1>0.16) & (r2>0.16));

```

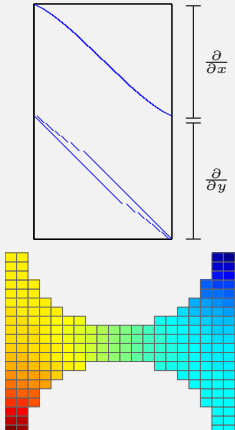


The construction of the discrete operators is agnostic to the exact layout of the grid, and since the transmissibility matrix T is still a multiple of the identity matrix, since the grid cells are equidistant squares, we can simply reuse the exact same set-up as above:

```

% Grid information
N = G.faces.neighbors;
:
% Operators
C = sparse([(1:nf)'; (1:nf)'], N, ...
          ones(nf,1)*[-1 1], nf, nc);
:
% Assemble and solve equations
p = initVariablesADI(zeros(nc,1));
q = zeros(nc, 1);
q(1) = 1; q(nc) = -1;
eq  = div(grad(p))+q;
eq(1) = eq(1) + p(1);
p    = -eq.jac{1}\eq.val;
plotCellData(G,p);

```

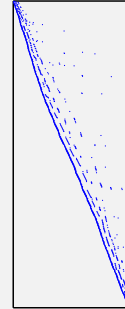


Notice that the C matrix has almost the same sparsity structure as in our first problem, except that the nonzero band now are curved since the number of cells in each column/row of the grid changes throughout the domain.

Example 6.3. To illustrate the power of the combination of an unstructured grid format and discrete differential operators, we also go through how you can use this technique to solve the Poisson equation on an unstructured grid. As an example, we use the Voronoi grid generated from the `seamount` data set shown in Figure 4.11 on page 90. Now comes the important point: *Because the discrete differential operators are defined in terms of the two general matrices N_1 and N_2 that describe the internal connections in the grid, their construction remains exactly the same as for the Cartesian grid:*

```
load seamount
G = pebi(triangleGrid([x(:) y(:)], delaunay(x,y)));
G = computeGeometry(G);

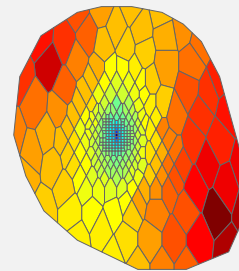
N = G.faces.neighbors;
N = N(all(N ~= 0, 2), :);
nf = size(N,1);
nc = G.cells.num;
C = sparse([(1:nf)'; (1:nf)'], N, ...
           ones(nf,1)*[-1 1], nf, nc);
grad = @(x) C*x;
```



Here, the directional derivatives do not follow the axial directions and hence C will have a general sparse structure and not the banded structure we saw for the Cartesian grids in the previous example. Likewise, because the cell centers are no longer equidistant points on a uniform mesh, the diagonal entries in the transmissibility matrix will not be the same constant for all cells and hence cannot be scaled out of the discrete system. For historical reasons, MRST only supplies a routine for computing half-transmissibilities defined in (6.50) on page 170. These are defined for *all* faces in the grid. Since we have assumed no-flow boundary conditions, we hence only need to find the half-transmissibilities associated with the *interior* faces and compute their harmonic average to get the transmissibilities defined in (6.51):

```
hT = computeTrans(G, struct('perm', ones(nc,1)));
cf = G.cells.faces(:,1);
T = 1 ./ accumarray(cf, 1 ./ hT, [G.faces.num, 1]);
T = T(all(N~=0,2),:);

p = initVariablesADI(zeros(nc,1));
q = zeros(nc, 1); q([135 282 17]) = [-1 .5 .5];
eq = div(T.*grad(p))+q;
eq(1) = eq(1) + p(1);
p = -eq.jac{1}\eq.val;
```



You may also notice that we have changed our source terms slightly so that there is now a fluid sink at the center and fluid sources to the north-west and south-east. We will return to a more detailed discussion of the computation of transmissibilities and assembly of discrete linear systems in Section 7.2

6.4.3 Time-of-flight and tracer

The transport equations (6.39) and (6.41) can be written on the common form

$$\nabla \cdot (u\vec{v}) = h(\vec{x}, u), \quad (6.63)$$

where $u = \tau$ and $h = \phi + \tau \nabla \cdot \vec{v}$ for time-of-flight and $u = C$ and $h = q_C + C \nabla \cdot \vec{v}$ for the artificial tracer.

To discretize the steady transport equation (6.63), we integrate it over a single grid cell Ω_i and use Gauss' divergence theorem to obtain

$$\int_{\partial\Omega_i} u \vec{v} \cdot \vec{n} ds = \int_{\Omega_i} h(\vec{x}, u(\vec{x})) d\vec{x}.$$

In Section 6.4.1 we discussed how to discretize the flux over an interface Γ_{ik} between two cells Ω_i and Ω_k for the case that $u \equiv 1$. To be consistent with the notation used above, we will call this flux v_{ik} . If we can define an appropriate value u_{ik} at the interface Γ_{ik} , we can write the flux across the interface as

$$\int_{\Gamma_{ik}} u \vec{v} \cdot \vec{n} ds = u_{ik} v_{ik}. \quad (6.64)$$

The obvious idea of setting $u_{ik} = \frac{1}{2}(u_i + u_k)$ gives a centered scheme that is unfortunately notoriously unstable. By inspecting the direction information is propagating in the transport equation, we can instead use the so-called upwind value

$$u_{ik} = \begin{cases} u_i, & \text{if } v_{ij} \geq 0, \\ u_k, & \text{otherwise.} \end{cases} \quad (6.65)$$

This can be thought of as adding extra numerical dispersion which will stabilize the resulting scheme so that it does not introduce spurious oscillations.

For completeness, let us also write this discretization using the abstract notation defined in the previous section. If we discretize u by a vector $\mathbf{u} \in \mathbb{R}^{n_c}$ and h by a vector function $\mathbf{h}(\mathbf{u}) \in \mathbb{R}^{n_c}$, the transport equation (6.63) can be written in the discrete form

$$\text{div}(\mathbf{u}\mathbf{v}) = \mathbf{h}(\mathbf{u}). \quad (6.66)$$

We also substitute the expression for \mathbf{v} from (6.61b) and use (6.65) to define u at each face f . Then, we define, for each face $f \in S_f$,

$$(\mathbf{u}\mathbf{v})[f] = \mathbf{u}^f[f] \mathbf{T}[f] \mathbf{grad}(\mathbf{p})[f], \quad (6.67)$$

where

$$\mathbf{u}^f[f] = \begin{cases} \mathbf{u}[N_1(f)], & \text{if } \mathbf{grad}(\mathbf{p})[f] > 0, \\ \mathbf{u}[N_2(f)], & \text{otherwise.} \end{cases} \quad (6.68)$$

Time-of-flight and tracer distributions can of course also be computed based on tracing streamlines by solving the ordinary differential equations

(6.35). The most commonly used method for tracing streamlines on hexahedral grids is a semi-analytical tracing algorithm introduced by Pollock [159], which uses analytical expressions of the streamline paths inside each cell based on the assumption that the velocity field is piecewise linear locally. Although Pollock's method is only correct for regular grids, it is often used also for highly skewed and irregular grids. Other approaches for tracing on unstructured grids and the associated accuracy are discussed in [50, 161, 94, 126, 75, 125, 103]. On unstructured polygonal grids, tracing of streamlines becomes significantly more involved. Because the general philosophy of MRST is that solvers should work independent of grid type – so that the user can seamlessly switch from structured to fully unstructured, polygonal grids – we prefer to use finite-volume methods rather than streamline tracing to compute time-of-flight and tracer distributions.

COMPUTER EXERCISES:

32. Compare the discrete differentiation operators for selected grids from Chapter 4, e.g., Exercises 16 to 18 on page 84 and Exercises 21 and 22 on page 95. Can you explain the differences?

Incompressible Solvers

A simulation model can be considered to consist of two main parts; the first part describes the reservoir rock and the second part describes the mathematical laws that govern fluid behavior. We have already discussed how to model the reservoir rock and its petrophysical properties in Chapters 3 and 4 and shown how the resulting geological models are represented in MRST using a grid object, usually called `G`, that describes the geometry of the reservoir, and a rock object, usually called `rock`, that describes petrophysical parameters. From the properties in these objects, one can compute spatial discretization operators that are generic and not tied to a particular set of flow equations as discussed in Section 6.4.2.

To form a full simulation model for porous media flow, however, we also need to introduce forcing terms and fluid properties. In MRST, the fluid behavior is represented as a fluid object that describes basic fluid properties such as density, viscosity, and compressibility. These fluid objects can then be extended to model more complex behavior for specific models, for instance to include properties like relative permeability and capillary pressure that describe the interaction between a multiphase flow interacts and a porous rock. Forcing terms other than gravity are represented similarly using objects with data structures that are specific to boundary conditions, (volumetric) source terms, and models of injection and production wells. In addition, it is convenient to introduce a state object holding the reservoir states (primary unknowns and derived quantities) like pressure, fluxes, face pressures, etc.

There are two different ways the data objects outlined above can be combined to form a full simulator. In Example 6.2, we saw how one can use discrete differential operators to write the flow equations in residual form and then employ automatic differentiation to linearize and form a linear system. Whereas this technique is elegant and will prove highly versatile for compressible flow models later in the book, it is an overkill for incompressible single-phase flow, since these equations already are linear. In this chapter we therefore outline how one can use a classic procedural approach to implement the discretized flow equations from the previous chapter. We start by outlin-

ing the data structures and constructors needed to set up fluid properties and forcing terms, and once this is done, we move on to discuss in detail how to build two-point discretizations and assemble and solve corresponding linear systems. The codes presented are simplified version of the basic flow solvers for incompressible flow that are implemented in the add-on modules `incomp` and `diagnostics` of MRST. Then at the end of the chapter, we go through a few examples and give all code lines that are necessary for full simulation setups with various driving mechanisms.

7.1 Basic data structures in a simulation model

In the previous chapter, we showed an example of a simple flow solver that did not contain any fluid properties and assumed no-flow boundary conditions and point sources as the only forcing term. In this section we will outline the basic data structures that are needed to set up more comprehensive single-phase simulation models.

7.1.1 Fluid properties

The only fluid properties we need in the basic single-phase flow equation are the viscosity and the fluid density for incompressible models and the fluid compressibility for compressible models. For more complex single-phase and multiphase models, there are other fluid and rock-fluid properties that will be needed by flow and transport solvers. To simplify the communication of fluid properties, MRST uses so-called fluid object that contain basic fluid properties as well as a few function handles that can be used to evaluate rock-fluid properties that are relevant for multiphase flow. This basic structure can be expanded further to represent more advanced fluid models.

The following shows how to initialize a simple fluid object that only requires viscosity and density as input

```
fluid = initSingleFluid('mu' , 1*centi*poise, ...
                       'rho', 1014*kilogram/meter^3);
```

After initialization, the fluid object will contain pointers to functions that can be used to evaluate petrophysical properties of the fluid:

```
fluid =
  properties: @(varargin)properties(opt,varargin{:})
  saturation: @(x,varargin)x.s
  relperm: @(s,varargin)relperm(s,opt,varargin{:})
```

Only the first function is relevant for single-phase flow, and returns the viscosity when called with a single output argument and the viscosity and the density when called with two output arguments. The other two functions can

be considered as dummy functions that can be used to ensure that the single-phase fluid object is compatible with solvers written for more advanced fluid models. The `saturation` function accepts a reservoir state as argument (see Section 7.1.2) and returns the corresponding saturation (volume fraction of the fluid phase) which will either be empty or set to unity, depending upon how the reservoir state has been initialized. The `relperm` function accepts a fluid saturation as argument and returns the relative permeability, i.e., the reduction in permeability due to the presence of other fluid phases, which is always identical to one for a single-phase model.

7.1.2 Reservoir states

To hold the dynamic state of the reservoir, MRST uses a special data structure. We will in the following refer to realizations of this structure as state objects. In its basic form, the structure contains three elements: a vector `pressure` with one pressure per cell in the model, a vector `flux` with one flux per grid face in the model, and a vector `s` with one saturation value for each cell, which should either be empty or be an identity vector since we only have a single fluid. The state object is typically initialized by a call to the following function

```
state = initResSol(G, p0, s0);
```

where `p0` is the initial pressure and `s0` is an optional parameter that gives the initial saturation (which should be identical to one for single-phase models). Notice that this initialization *does not* initialize the fluid pressure to be at hydrostatic equilibrium. If such a condition is needed, it must be enforced explicitly by the user. In the case that the reservoir has wells, one should use the alternative function:

```
state = initState(G, W, p0, s0);
```

This will give a state object with an additional field `wellSol`, which is a vector with length equal the number of wells. Each element in the vector is a structure that has two fields `wellSol.pressure` and `wellSol.flux`. These two fields are vectors of length equal the number of completions in the well and contain the bottom-hole pressure and flux for each completion.

7.1.3 Fluid sources

The simplest way to describe flow into or flow out from interior points of the reservoir is to use volumetric source terms. These source terms can be added using the following function:

```
src = addSource(src, cells, rates);
src = addSource(src, cells, rates, 'sat', sat);
```

Here, the input values are:

- **src**: structure from a prior call to `addSource` which will be updated on output or an empty array (`src==[]`) in which case a new structure is created. The structure contains the following fields:
 - **cell**: cells for which explicit sources are provided
 - **rate**: rates for these explicit sources
 - **value**: pressure or flux value for the given condition
 - **sat**: fluid composition of injected fluids in cells with `rate>0`
- **cells**: indices to the cells in the grid model in which this source term should be applied.
- **rates**: vector of volumetric flow rates, one scalar value for each cell in **cells**. Note that these values are interpreted as flux rates (typically in units of $[m^3/day]$ rather than as flux density rates (which must be integrated over the cell volumes to obtain flux rates).
- **sat**: optional parameter that specifies the composition of the fluid injected from this source. An $n \times m$ array of fluid compositions with n being the number of elements in **cells** and m is the number of fluid phases. For $m = 3$, the columns are interpreted as: 1='aqua', 2='liquid', and 3='vapor'. This field is for the benefit of multiphase transport solvers, and is ignored for all sinks (at which fluids flow *out* of the reservoir). The default value is `sat = []`, which corresponds to single-phase flow. As a special case, if `size(sat,1)==1`, then the saturation value will be repeated for all cells specified by **cells**.

For convenience, values and sat may contain a single value; this value is then used for all faces specified in the call.

There can only be a single net source term per cell in the grid. Moreover, for incompressible flow with no-flow boundary conditions, the source terms *must* sum to zero if the model is to be well posed, or alternatively sum to the flux across the boundary. If not, we would either inject more fluids than we extract, or vice versa, and hence implicitly violate the assumption of incompressibility.

7.1.4 Boundary conditions

As discussed in Section 6.3.1, all outer faces in a grid model are assumed to be no-flow boundaries in MRST unless other conditions are specified explicitly. The basic mechanism for specifying Dirichlet and Neumann boundary conditions is to use the function:

```
bc = addBC(bc, faces, type, values);
bc = addBC(bc, faces, type, values, 'sat', sat);
```

Here, the input values are:

- **bc**: structure from a prior call to `addBC` which will be updated on output or an empty array (`bc==[]`) in which case a new structure is created. The structure contains the following fields:

- **face**: external faces for which explicit conditions are set
 - **type**: cell array of strings denoting type of condition
 - **value**: pressure or flux value for the given condition
 - **sat**: fluid composition of fluids passing through inflow faces, not used for single-phase models
- **faces**: array of external faces at which this boundary condition is applied.
 - **type**: type of boundary condition. Supported values are 'pressure' and 'flux', or cell array of such strings.
 - **values**: vector of boundary conditions, one scalar value for each face in **faces**. Interpreted as a pressure value in units of [Pa] when **type** equals 'pressure' and as a flux value in units of [m³/s] when **type** is 'flux'. If the latter case, the positive values in **values** are interpreted as injection fluxes *into* the reservoir, while negative values signify extraction fluxes, i.e., fluxes *out of* the reservoir.
 - **sat**: optional parameter that specifies the composition of the fluid injected across inflow faces. Similar setup as for explained for source terms in Section 7.1.3.

There can only be a single boundary condition per face in the grid. Solvers assume boundary conditions are given on the boundary; conditions in the interior of the domain yield unpredictable results. Moreover, for incompressible flow and only Neumann conditions, the boundary fluxes *must* sum to zero if the model is to be well posed. If not, we would either inject more fluids than we extract, or vice versa, and hence implicitly violate the assumption of incompressibility.

For convenience, MRST also offers two additional routines that can be used to set Dirichlet and Neumann conditions at all outer faces in a certain direction for grids having a logical *IJK* numbering:

```
bc = pside(bc, G, side, p);
bc = fluxside(bc, G, side, flux)
```

The **side** argument is a string that much match one out of the following six alias groups:

- 1: 'West', 'XMin', 'Left'
- 2: 'East', 'XMax', 'Right'
- 3: 'South', 'YMin', 'Back'
- 4: 'North', 'YMax', 'Front'
- 5: 'Upper', 'ZMin', 'Top'
- 6: 'Lower', 'ZMax', 'Bottom'

These groups correspond to the cardinal directions mentioned as the first alternative in each group. The user should also be aware of an important difference in how fluxes are specified in **addBC** and **fluxside**. Specifying a scalar value in **addBC** means that this value will be copied to all faces the boundary condition is applied to, whereas a scalar value in **fluxside** sets the cumulative flux for all faces that make up the global side to be equal the specified value.

7.1.5 Wells

Wells are similar to source terms in the sense that they describe injection or extraction of fluids from the reservoir, but differ in the sense that they not only provide a volumetric flux rate, but also contain a model that couples this flux rate to the difference between the average reservoir in the grid cell and the pressure inside the wellbore. As discussed in Section 6.3.2, this relation can be written for each perforation as

$$v_p = J(p_i - p_f) \quad (7.1)$$

where J is the well index, p_i is the pressure in the perforated grid cell, and p_f is the flowing pressure in the wellbore. The latter can be found from the pressure at the top of the well and the density of the fluid in each perforation. For single-phase, incompressible this $p_f = p_{wh} + \rho \Delta z_f$, where p_{wh} is the pressure at the well head and Δz_f is the vertical distance from this point and to the perforation.

The structure used to represent wells in MRST, which by convention is called `W`, consists of the following fields:

- `cells`: an array index to cells perforated by this well
- `type`: string describing which variable is controlled (i.e., assumed to be fixed), either 'bhp' or 'rate'
- `val`: the target value of the well control (pressure value for `type='bhp'` or the rate for `type='rate'`).
- `r`: the wellbore radius (double).
- `dir`: a char describing the direction of the perforation, one of the cardinal directions 'x', 'y' or 'z'
- `WI`: the well index: either the productivity index or the well injectivity index depending on whether the well is producing or injecting.
- `dZ`: the height differences from the well head, which is defined as the 'highest' contact (i.e., the contact with the minimum z -value counted amongst all cells perforated by this well)
- `name`: string giving the name of the well
- `comp`: fluid composition, only used for injectors
- `refDepth`: reference depth of control mode
- `sign`: define if the well is intended to be producer or injector

Well structures are created by a call to the function

```

W = addWell(W, G, rock, cellInx);
W = addWell(W, G, rock, cellInx, 'pn', pv, ... );
```

Here, `cellInx` is a vector of indices to the cells perforated by the well, and 'pn'/pv denote one or more 'key'/value pairs that can be used to specify optional parameters that influence the well model:

- **type**: string specifying well control, 'bhp' (default) means that the well is controlled by bottom-hole pressure, whereas 'rate' means that the well is rate controlled.
- **val**: target for well control. Interpretation of this values depends upon **type**. For 'bhp' the value is assumed to be in unit Pascal, and for 'rate' the value is given in unit [m³/sec]. Default value is 0.
- **radius**: wellbore radius in meters. Either a single, scalar value that applies to all perforations, or a vector of radii, with one value for each perforation. The default radius is 0.1 m.
- **dir**: well direction. A single CHAR applies to all perforations, while a CHAR array defines the direction of the corresponding perforation.
- **innerProduct**: used for consistent discretizations discussed in Chapter 8
- **WI**: well index. Vector of length equal the number of perforations in the well. The default value is -1 in all perforations, whence the well index will be computed from available data (cell geometry, petrophysical data, etc) in grid cells containing well completions
- **Kh**: permeability times thickness. Vector of length equal the number of perforations in the well. The default value is -1 in all perforations, whence the thickness will be computed from the geometry of each perforated cell.
- **skin**: skin factor for computing effective well bore radius. Scalar value or vector with one value per perforation. Default value: 0.0 (no skin effect).
- **Comp_i**: fluid composition for injection wells. Vector of saturations. Default value: **Comp_i** = [1, 0, 0] (water injection)
- **Sign**: well type: production (**sign**=-1) or injection (**sign**=1). Default value: [] (no type specified)
- **name**: string giving the name of the well. Default value is 'Wn' where *n* is the number of this well, i.e., **n**=**numel(W)**+1

For convenience, MRST also provides the function

```
W = verticalWell(W, G, rock, I, J, K)
W = verticalWell(W, G, rock, I, K)
```

that can be used to specify vertical wells in models described by Cartesian grids or grids that have some kind of extruded structure. Here,

- **I, J**: gives the horizontal location of the well heel. In the first mode, both I and J are given and then signify logically Cartesian indices so that I is the index along the first logical direction while J is the index along the second logical direction. This mode is only supported in grids which have an underlying Cartesian (logical) structure such as purely Cartesian grids or corner-point grids.
In the second mode, only I is described and gives the *cell index* of the topmost cell in the column through which the vertical well will be completed. This mode is supported for logically Cartesian grids containing a three-component field **G.cartDims** or for otherwise layered grids which contain the fields **G.numLayers** and **G.layerSize**.

- `K`: a vector of layers in which this well should be completed. If `isempty(K)` is true, then the well is assumed to be completed in all layers in this grid column and the vector is replaced by `1:num_layers`.

7.2 Incompressible two-point pressure solver

The two-point flux-approximation scheme introduced in Section 6.4.1 is implemented as two different routines in the `incomp` module:

```
hT = computeTrans(G,rock)
```

computes the half-face transmissibilities and does not depend on the fluid model, the reservoir state, or the driving mechanisms, whereas

```
state = incompTPFA(state, G, hT, fluid, 'mech1', obj1, ...)
```

takes the complete model description as input and assembles and solves the two-point system. Here, `mech` arguments the drive mechanism ('src', 'bc', and/or 'wells') using correctly defined objects `obj`, as discussed in Sections 7.1.3–7.1.5. Notice that `computeTrans` may fail to compute sensible transmissibilities if the permeability field in `rock` is not given in SI units. Likewise, `incompTPFA` may produce strange results if the inflow and outflow specified by the boundary conditions, source terms, and wells does not sum to zero and hence violates the assumption of incompressibility. However, if fixed pressure is specified in wells or on parts of the outer boundary, there will be an outflow or inflow that will balance the net rate that is specified elsewhere. In the remains of this section, we will discuss more details of the incompressible solver and demonstrate how simple it is to implement the TPFA method on general polyhedral grid by going through the essential code lines needed to compute half-transmissibilities and solve and assemble the global system. The impatient reader can jump directly to Section 7.4, which contains several examples that demonstrate the use of the incompressible solver for single-phase flow.

To focus on the discretization and keep the discussion simple, we will not look at the full implementation of the two-point solver in `incomp`. Instead, we discuss excerpts from two simplified functions, `simpleComputeTrans` and `simpleIncompTPFA`, that are located in the `1phase` directory of the `mrst-book` module and together form a simplified single-phase solver which has been created for pedagogical purposes. The standard `computeTrans` function from `mrst-core` can be used for different representations of petrophysical parameters and includes functionality to modify the discretization by overriding the definition of cell and face centers and/or including multipliers that modify the values of the half-transmissibilities, see e.g., Sections 3.4.3 and 3.5.5. Likewise, the `incompTPFA` solver from the `incomp` module is implemented for a general, incompressible flow model with multiple fluid phases with flow driven by a general combination of boundary conditions, fluid sources, and well models.

$$T_{i,k} = A_{i,k} \mathbf{K}_i \frac{\vec{c}_{i,k} \cdot \vec{n}_{i,k}}{|\vec{c}_{i,k}|^2}$$

$$T_{ik} = [T_{i,k}^{-1} + T_{k,i}^{-1}]^{-1}$$

$$\sum_k T_{ik} (p_i - p_k) = q_i$$

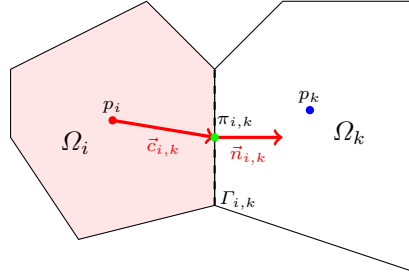


Fig. 7.1. Two-point discretization on general polyhedral cells

Assume that we have a standard grid \mathbf{G} that contains cell and face centroids, e.g., as computed by the `computeGeometry` function discussed in Section 4.4. Then, the essential code lines of `simpleComputeTrans` are as follows: First, we define the vectors $\vec{c}_{i,k}$ from cell centroids to face centroids, see Figure 7.1. To this end, we first need to determine the map from faces to cell number so that the correct cell centroid is subtracted from each face centroid.

```
hf = G.cells.faces(:,1);
hf2cn = gridCellNo(G);
C = G.faces.centroids(hf,:) - G.cells.centroids(hf2cn,:);
```

The face normals in MRST are assumed to have length equal to the corresponding face areas, and hence correspond to $A_{i,k} \vec{n}_{i,k}$ in (6.50). To get the correct sign, we look at the neighboring information that describes which cells share the face: if the current cell number is in the first column, the face normal has a positive sign. If not, it gets a negative sign:

```
sgn = 2*(hf2cn == G.faces.neighbors(hf, 1)) - 1;
N = bsxfun(@times, sgn, G.faces.normals(hf,:));
```

The permeability tensor may be stored in different formats, as discussed in Section 3.5, and we therefore use an utility function to extract it:

```
[K, i, j] = permTensor(rock, G.griddim);
```

Finally, we compute the half transmissibilities, $C^T K N / C^T C$. To limit memory use, this is done in a for-loop (which is rarely used in MRST):

```
hT = zeros(size(hf2cn));
for k=1:size(i,2),
    hT = hT + C(:,i(k)) .* K(hf2cn, k) .* N(:, j(k));
end
hT = hT ./ sum(C.*C,2);
```

The actual code has a few additional lines that perform various safeguards and consistency checks.

Once the half transmissibilities have been computed, they can be passed to the `simpleIncompTPFA` solver. The first thing this solver needs to do is adjust the half transmissibilities to account for fluid viscosity, since they were derived for a fluid with unit viscosity:

```
mob = 1./fluid.properties(state);
hT = hT .* mob(hf2cn);
```

Then we loop through all faces and compute the face transmissibility as the harmonic average of the half-transmissibilities

```
T = 1 ./ accumarray(hf, 1 ./ hT, [G.faces.num, 1]);
```

Here, we have used the MATLAB function `accumarray` which constructs an array by accumulation. A call to `a = accumarray(subs,val)` will use the subscripts in `subs` to create an array `a` based on the values `val`. Each element in `val` has a corresponding row in `subs`. The function collects all elements that correspond to identical subscripts in `subs` and stores the sum of those values in the element of `a` corresponding to the subscript. In our case, `G.cells.faces(:,1)` gives the global face number for each half face, and hence the call to `accumarray` will sum the transmissibilities of the half-faces that correspond to a given global face and store the result in the correct place in a vector of `G.faces.num` elements. The function `accumarray` is very powerful and is used a lot in MRST in place of nested for-loops. In fact, we will employ this function to loop over all the cells in the grid and collect and sum the transmissibilities of the faces of each cell to define the diagonal of the TPFA matrix:

```
nc = G.cells.num;
i = all(G.faces.neighbors ~= 0, 2);
n1 = G.faces.neighbors(i,1);
n2 = G.faces.neighbors(i,2);
d = accumarray([n1; n2], repmat(T(i),[2,1]),[ nc, 1]);
```

Now that we have computed both the diagonal and the off-diagonal element of A , the discretization matrix itself can be constructed by a straightforward call to MATLAB's `sparse` function:

```
I = [n1; n2; (1:nc)'];
J = [n2; n1; (1:nc)'];
V = [-T(i); -T(i); d]; clear d;
A = sparse(double(I), double(J), V, nc, nc);
```

Finally, we check if Dirichlet boundary conditions are imposed on the system, and if not, we modify the first element of the system matrix to (somewhat arbitrarily) fix the pressure in the first cell to zero, before we solve the system to compute the pressure:

```
A(1) = 2*A(1);
p = mldivide(A, rhs);
```

To solve the system we rely on MATLAB's default solver `mldivide`, which for a sparse system boils down to calling a direct solver from UMFPACK implementing an unsymmetric, sparse, multifrontal LU factorization add citation. While this solver is efficient for small to medium-sized systems, larger systems are more efficiently solved using more problem-specific solvers. To provide flexibility, the linear solver can be passed as a function-pointer argument to both `incompTPFA` and `simpleIncompTPFA`.

Once the pressures have been computed, we can compute pressure values at the face centroids using the half-face transmissibilities

```
fp = accumarray(G.cells.faces(:,1), p(hf2cn).*hT, [G.faces.num,1])./ ...
    accumarray(G.cells.faces(:,1), hT, [G.faces.num,1]);
```

and likewise construct the fluxes across the interior faces

```
ni = G.faces.neighbors(i,:);
flux = -accumarray(find(i), T(i).*(p(ni(:,2))-p(ni(:,1))), [nf, 1]);
```

In the code excerpts given above, we did not account for gravity forces and general Dirichlet or Neumann boundary conditions, which both will complicate the code beyond the scope of the current presentation. The interested reader should consult the actual code to work out these details.

We will short discuss several examples that demonstrate how this code can be used to solve flow problems on structured and unstructured grids. However, before doing so, we outline another flow solver from the `diagnostics` module visualizing flow patterns

7.3 Upwind solver for time-of-flight and tracer

The `diagnostics` module provides various functionality that can be used to probe a reservoir model to establish communication patterns between inflow and outflow regions, time lines for fluid movement, and various measures of reservoir heterogeneity. At the heart of this module, lies the function

```
tof = computeTimeOfFlight(state, G, rock, mech1, obj1, ...)
```

which implements the upwind, finite-volume discretization introduced in Section 6.4.3 for solving the time-of-flight equation $\vec{v} \cdot \nabla \tau = \phi$ to compute the time it takes a neutral particle to travel from the nearest fluid source or inflow boundary to each point in the reservoir. Here, the `mech` arguments specify the drive mechanism ('src', 'bc', and/or 'wells') specified in terms of specific objects `obj`, as discussed in Sections 7.1.3 to 7.1.5. The same routine can also compute tracer concentrations that can be used to define volumetric partitions if the user specifies extra input parameters. Likewise, the backward time-of-flight, i.e., the time it takes to travel from any point in the reservoir and to the nearest fluid sink or outflow boundary, can be computed from the same

equation if we change the sign of the flow field and modify the boundary conditions and/or source terms accordingly. In the following, we will go through the main parts of how this discretization is implemented.

We start by identifying all volumetric sources of inflow and outflow, which may be described as source/sink terms in `src` and/or as wells in `W`,

```
[qi,qs] = deal([]);
if ~isempty(W),
    qi = [qi; vertcat(W.cells)];
    qs = [qs; vertcat(state.wellSol.flux)];
end
if ~isempty(src),
    qi = [qi; src.cell];
    qs = [qs; src.rate];
end
```

and collect the results in a vector `q` of source terms having one value per cell

```
q = sparse(src.cell, 1, src.rate, G.cells.num, 1);
```

We also need to compute the accumulated inflow and outflow from boundary fluxes for each cell. This will be done in three steps. First, we create an empty vector `ff` with one entry per global face, find all faces that have Neumann conditions, and insert the corresponding value in the correct row

```
ff = zeros(G.faces.num, 1);
isNeu = strcmp('flux', bc.type);
ff(bc.face(isNeu)) = bc.value(isNeu);
```

For faces having Dirichlet boundary conditions, the flux is not specified and must be extracted from the solution computed by the pressure solver, i.e., from the `state` object that holds the reservoir state. We also need to set the correct sign so that fluxes *into* a cell are positive and fluxes *out of* a cell are negative. To this end, we use the fact that the normal vector of face `i` points from cell `G.faces.neighbors(i,1)` to `G.faces.neighbors(i,2)`. In other words, the sign of the flux across an outer face is correct if `neighbors(i,1)==0`, but if `neighbors(i,2)==0` we need to reverse the sign

```
isDir = strcmp('pressure', bc.type);
i = bc.face(isDir);
if ~isempty(i)
    ff(i) = state.flux(i) .* (2*(G.faces.neighbors(i,1)==0) - 1);
end
```

The last step is to sum all the fluxes across outer faces and collect the result in a vector `qb` that has one value per cell

```
is_outer = ~all(double(G.faces.neighbors) > 0, 2);
qb = sparse(sum(G.faces.neighbors(is_outer,:), 2), 1, ...
            ff(is_outer), G.cells.num, 1);
```

Here, `G.faces.neighbors(is_outer,:)`, 2) gives the index of the cell that is attached to each outer face (since the entry in one of the columns must be zero for an outer face).

Once the contributions to inflow and outflow are collected, we can start building the upwind flux discretization matrix \mathbf{A} . The off-diagonal entries are defined defined such that $A_{ji} = \max(v_{ij}, 0)$ and $A_{ij} = -\min(v_{ij}, 0)$, where v_{ij} is the flux computed by the TPFA scheme discussed in the previous section.

```
i = ~any(G.faces.neighbors==0, 2);
out = min(state.flux(i), 0);
in = max(state.flux(i), 0);
```

The diagonal entry equals the outflux minus the divergence of the velocity, which can be obtained by summing the off-diagonal rows. This will give the correct equation in all cell except for those with a positive fluid source. Here, the net outflux equals the divergence of the velocity and we hence end up with an undetermined equation. In these cells, we can as a reasonable approximation set the average time-of-flight to be equal half the time it takes to fill the cell, which means that the diagonal entry should be equal twice the fluid rate inside the cell.

```
n = double(G.faces.neighbors(i,:));
inflow = accumarray([n(:, 2); n(:, 1)], [in; -out]);
d = inflow + 2*max(q+qb, 0);
```

Having obtained diagonal and all the nonzero off-diagonal elements, we can assemble the full matrix

```
nc = G.cells.num;
A = sparse(n(:,2), n(:,1), in, nc, nc) ...
    + sparse(n(:,1), n(:,2), -out, nc, nc);
A = -A + spdiags(d, 0, nc, nc);
```

We have now established the complete discretization matrix, and time-of-flight can be computed by a simple matrix inversion

```
tof = A \ poreVolume(G,rock);
```

If there are no gravity forces and the flux has been computed by a monotone scheme, one can show that the discretization matrix A can be permuted to a lower-triangular form [140, 139]. In the general case, the permuted matrix will be block triangular with irreducible diagonal blocks. Such systems can be inverted very efficiently using a permuted back-substitution algorithm as long as the irreducible diagonal blocks are small. In our experience, MATLAB is quite good at detecting such structures and using the simple backslash (\backslash) operator is therefore efficient, even for quite large models. However, for models of real petroleum assets described on stratigraphic grids (see Chapter 4.3), it is often necessary to preprocess flux fields to get rid of numerical clutter that

would otherwise introduce large irreducible blocks inside stagnant regions. By specifying optional parameters to `computeTimeOfFlight`, the function will get rid of such small cycles in the flux field and set the time-of-flight to a prescribed upper value in all cells that have sufficiently small influx. This tends to reduce the computational cost significantly for large models with complex geology and/or significant compressibility effects.

In addition to time-of-flight, we can compute stationary tracers as discussed in Section 6.3.4. This is done by passing an optional parameter,

```
tof = computeTimeOfFlight(state, G, rock, ..., 'tracer', tr)
```

where `tr` is a cell-array of vectors that each gives the indexes of the cells that emit a unique tracer. For incompressible flow, the discretization matrix of the tracer equation is the same as that for time-of-flight, and all we need to do is to assemble the right-hand side

```
numTrRHS = numel(tr);
TrRHS = zeros(nc,numTrRHS);
for i=1:numTrRHS,
    TrRHS(tr{i},i) = 2*qp(tr{i});
end
```

Since we have doubled the rate in any cells with a positive source when constructing the matrix A , the rate on the right-hand side must also be doubled.

Now we can solve the combined time-of-flight, tracer problem as a linear system with multiple right-hand side,

```
T = A \ [poreVolume(G,rock) TrRHS];
```

which means that we essentially get the tracer for free as long as the number of tracers does not exceed the number of right-hand columns MATLAB can be handled in one solve. We will return to a more thorough discussion of the tracer partitions in the next chapter and show how these can be used to delineate connectivities within the reservoir. In the rest of this chapter, we will consider time-of-flight and streamlines as a means to study flow patterns in reservoir models.

7.4 Simulation examples

You have now been introduced to all the functionality from the `incomp` module that is necessary to solve a single-phase flow problem as well as the time-of-flight solver from the `diagnostics` module, which can be used to compute time lines in the reservoir. In following, we will discuss several examples, in which we demonstrate step-by-step how to set up a flow model, solve it, and visualize and analyze the resulting flow field. Complete codes can be found in the `1phase` directory of the `mrst-book` module.

7.4.1 Quarter five-spot

As our first example, we show how to solve $-\nabla \cdot (K\nabla p) = q$ with no-flow boundary conditions and two source terms at diagonally opposite corners of a 2D Cartesian grid covering a $500 \times 500 \text{ m}^2$ area. This setup mimics a standard quarter five-spot well pattern, which you already have encountered in Figure 6.7 on page 164 when we discussed well models. The full code is available in the script `quarterFiveSpot.m`.

We use a $n_x \times n_y$ grid with homogeneous petrophysical data, permeability of 100 mD, and porosity of 0.2:

```
[nx,ny] = deal(32);
G = cartGrid([nx,ny],[500,500]);
G = computeGeometry(G);
rock.perm = ones(G.cells.num, 1)*100*milli*darcy;
rock.poro = ones(G.cells.num, 1)*.2;
```

As we saw above, all we need to know to develop the spatial discretization is the reservoir geometry and the petrophysical properties. This means that we can compute the half transmissibilities without knowing any details about the fluid properties and the boundary conditions and/or sources/sinks that will drive the global flow:

```
hT = simpleComputeTrans(G, rock);
```

The result of this computation is a vector with one value per local face of each cell in the grid, i.e., a vector with `G.cells.faces` entries.

The reservoir is horizontal and gravity forces are therefore not active. We create a fluid with properties that are typical for water:

```
gravity reset off
fluid = initSingleFluid('mu', 1*centi*poise, ...
                       'rho', 1014*kilogram/meter^3);
```

To drive the flow, we will use a fluid source at the south-west corner and a fluid sink at the north-east corner of the model. The time scale of the problem is defined by the strength of the source term. In our case, we set the source terms such that a unit time corresponds to the injection of one pore volume of fluids. By convention, all flow solvers in MRST automatically assume no-flow conditions on all outer (and inner) boundaries if no other conditions are specified explicitly.

```
pv = sum(poreVolume(G,rock));
src = addSource([], 1, pv);
src = addSource(src, G.cells.num, -pv);
display(src)
```

The data structure used to represent the fluid sources contains three elements:

```

src =
  cell: [2x1 double]
  rate: [2x1 double]
  sat: []

```

The `src.cell` gives the cell numbers where the source term is nonzero, and the vector `src.rate` specifies the fluid rates, which by convention are positive for inflow into the reservoir and negative for outflow from the reservoir. The last data element `src.sat` specifies fluid saturations, which only has meaning for multiphase flow models and hence is set to be empty here.

To simplify communication among different flow and transport solvers, all unknowns (reservoir states) are collected in a structure. Strictly speaking, this structure need not be initialized for an incompressible model in which none of the fluid properties depend on the reservoir states. However, to avoid treatment of special cases, MRST requires that the structure is initialized and passed as argument to the pressure solver. We therefore initialize it with a dummy pressure value of zero and a unit fluid saturation since we only have a single fluid

```

state = initResSol(G, 0.0, 1.0);
display(state)

```

```

state =
  pressure: [1024x1 double]
  flux: [2112x1 double]
  s: [1024x1 double]

```

This completes the setup of the model. To solve for the pressure, we simply pass the reservoir state, grid model, half transmissibilities, fluid model, and driving forces to the flow solver, which assembles and solves the incompressible flow equation.

```

state = simpleIncompTPFA(state, G, hT, fluid, 'src', src);
display(state)

```

As explained above, `simpleIncompTPFA` solves for pressure as the primary variable and then uses transmissibilities to reconstruct the face pressure and inter-cell fluxes. After a call to the pressure solver, the `state` object is therefore expanded by a new field `facePressure` that contains pressures reconstructed at the face centroids

```

state =
  pressure: [1024x1 double]
  flux: [2112x1 double]
  s: [1024x1 double]
  facePressure: [2112x1 double]

```

Figure 7.2 shows the resulting pressure distribution. To improve the visualization of the flow field, we show streamlines. In MRST, Pollock's method [159] for semi-analytical tracing of streamlines has been implemented in the

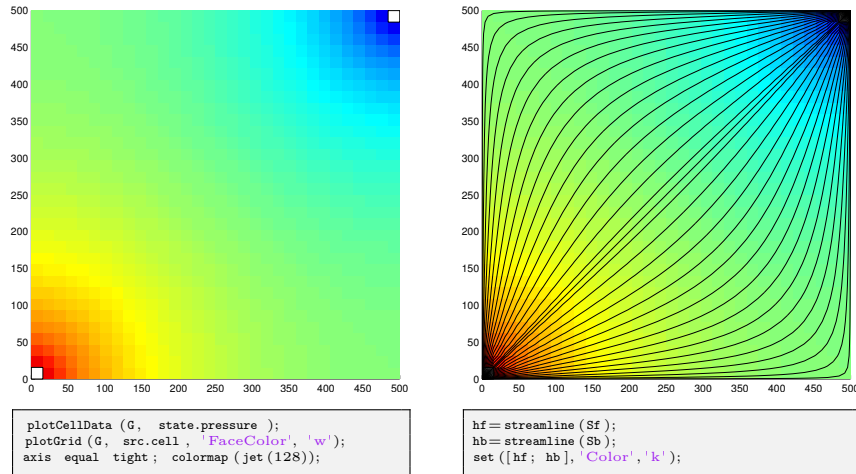


Fig. 7.2. Solution of the quarter five-spot problem on a 32×32 uniform grid. The left plot shows the pressure distribution and in the right plot we have imposed streamlines passing through centers of the cells on the NW–SE diagonal.

`streamlines` add-on module. Here, we will use this functionality to trace streamlines forward and backward, starting from the midpoint of all cells along the NW–SE diagonal in the grid

```

mrstModule add streamlines;
seed = (nx:nx-1:nx*ny).';
Sf = pollock(G, state, seed, 'substeps', 1);
Sb = pollock(G, state, seed, 'substeps', 1, 'reverse', true);

```

The `pollock` routine produces a cell array of individual streamlines that can be passed onto MATLAB's built-in `streamline` routine for plotting, as shown to the right in Figure 7.2.

To get a better picture of how fast the fluids will flow through our domain, we solve the time-of-flight equation (6.39) subject to the condition that $\tau = 0$ at the inflow, i.e., at all points where $q > 0$. For this purpose, we use the `computeTimeOfFlight` solver discussed in Section 7.3, which can compute both the forward time-of-flight from inflow points and into the reservoir,

```

toff = computeTimeOfFlight(state, G, rock, 'src', src);

```

and the backward time-of-flight from outflow points and backwards into the reservoir

```

tofb = computeTimeOfFlight(state, G, rock, 'src', src, 'reverse', true);

```

Isocontours of time-of-flight define natural time lines in the reservoir, and to emphasize this fact, the left plot in Figure 7.3 shows the time-of-flight

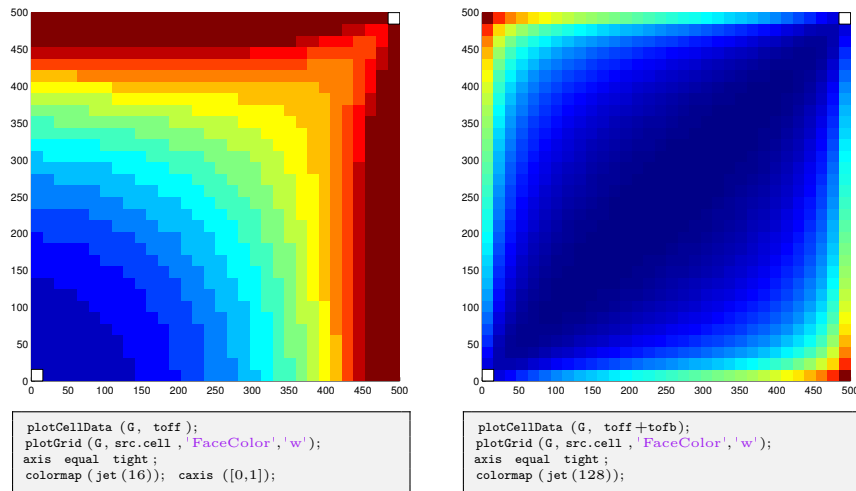


Fig. 7.3. Solution of the quarter five-spot problem on a 32×32 uniform grid. The left plot shows time-of-flight plotted with a few color levels to create a crude contouring effect. The right plot shows a plot of the total travel time to distinguish high-flow and stagnant regions.

plotted using only a few colors to make a rough contouring effect. The sum of the forward and backward time-of-flights gives the total time it takes a fluid particle to travel through the reservoir, from an inflow point to an outflow point. The total travel time can be used to visualize high-flow and stagnant regions as demonstrated in the right plot of Figure 7.3.

COMPUTER EXERCISES:

33. Run the quarter five-spot example with the following modifications:
 - a) Replace the Cartesian grid by a curvilinear grid, e.g., using `twister` or a random perturbation of internal nodes as shown in Figure 4.3.
 - b) Replace the Cartesian grid by the locally refined grid from Exercise 21 on page 95
 - c) Replace the homogeneous permeability by a heterogeneous permeability derived from the Carman–Kozeny relation (3.6)
 - d) Set the domain to be a single layer of the SPE10 model. Hint: use `SPE10_rock()` to sample the petrophysical parameters and remember to convert to SI units.

Notice that the `pollock` function may not work for non-Cartesian grids.
34. Construct a grid similar to the one in Exercise 16 on page 83, except that the domain is given a 90° flip so that axis of the cylindrical cut-outs align with the z -direction. Modify the code presented above so that you can compute a *five-spot* setup with one injector near each corner and a producer in the narrow middle section between the cylindrical cut-outs.

7.4.2 Boundary conditions

To demonstrate how to specify boundary conditions, we will go through essential code lines of three different examples; the complete scripts can be found in `boundaryConditions.m`. In all three examples, the reservoir is 50 meter thick, is located at a depth of approximately 500 meters, and is restricted to a $1 \times 1 \text{ km}^2$ area. The permeability is uniform and anisotropic, with a diagonal (1000, 300, 10) mD tensor, and the porosity is uniform and equal 0.2. In the first two examples, the reservoir is represented as a $20 \times 20 \times 5$ rectangular grid, and in the third example the reservoir is given as a corner-point grid of the same Cartesian dimension, but with an uneven uplift and four intersecting faults (as shown in the left plot of Figure 4.34):

```
[nx,ny,nz] = deal(20, 20, 5);
[Lx,Ly,Lz] = deal(1000, 1000, 50);
switch setup
  case 1,
    G = cartGrid([nx ny nz], [Lx Ly Lz]);
  case 2,
    G = cartGrid([nx ny nz], [Lx Ly Lz]);
  case 3,
    G = processGRDECL(makeModel13([nx ny nz], [Lx Ly Lz/5]));
    G.nodes.coords(:,3) = 5*(G.nodes.coords(:,3) ...
        - min(G.nodes.coords(:,3)));
end
G.nodes.coords(:,3) = G.nodes.coords(:,3) + 500;
```

Setting rock and fluid parameters, computing transmissibilities, and initializing the reservoir state can be done as explained in the previous section, and details are not included for brevity.

Linear pressure drop

In the first example (`setup=1`), we specify a Neumann condition with total inflow of $5000 \text{ m}^3/\text{day}$ on the east boundary and a Dirichlet condition with fixed pressure of 50 bar on the west boundary:

```
bc = fluxside(bc, G, 'EAST', 5e3*meter^3/day);
bc = pside (bc, G, 'WEST', 50*barsa);
```

This completes the definition of the model, and we can pass the resulting objects to the `simpleIncompTFPA` solver to compute the pressure distribution shown to the right in Figure 7.4. In the absence of gravity, these boundary conditions will result in a linear pressure drop from east to west inside the reservoir.

Hydrostatic boundary conditions

In the next example, we will use the same model, except that we now include the effects of gravity and assume hydrostatic equilibrium at the outer vertical

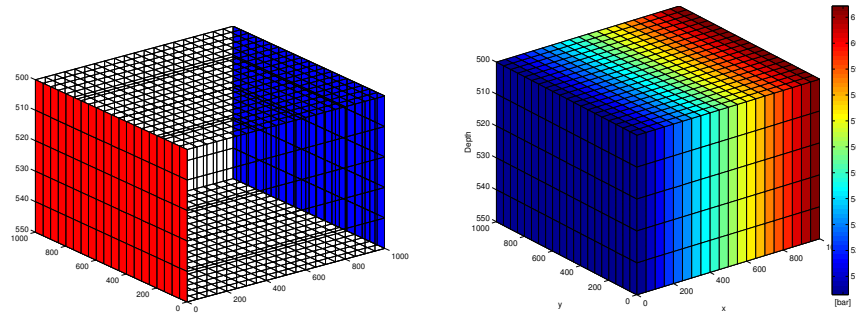


Fig. 7.4. First example of a flow driven by boundary conditions. In the left plot, faces with Neumann conditions are marked in blue and faces with Dirichlet conditions are marked in red. The right plot shows the resulting pressure distribution.

boundaries of the model. First, we initialize the reservoir state according to hydrostatic equilibrium, which is straightforward to compute if we for simplicity assume that the overburden pressure is caused by a column of fluids with the exact same density as in the reservoir:

```
state = initResSol(G, G.cells.centroids(:,3)*rho*norm(gravity), 1.0);
```

There are at least two different ways to specify hydrostatic boundary conditions. The simplest approach is to use the function `psideh`, i.e.,

```
bc = psideh([], G, 'EAST', fluid);
bc = psideh(bc, G, 'WEST', fluid);
bc = psideh(bc, G, 'SOUTH', fluid);
bc = psideh(bc, G, 'NORTH', fluid);
```

Alternatively, we can do it manually ourselves. To this end, we need to extract the reservoir perimeter defined as all exterior faces are vertical, i.e., whose normal vector have no z -component,

```
f = boundaryFaces(G);
f = f(abs(G.faces.normals(f,3))<eps);
```

To get the hydrostatic pressure at each face, we can either compute it directly by using the face centroids,

```
fp = G.faces.centroids(f,3)*rho*norm(gravity);
```

or we use the initial equilibrium that has already been established in the reservoir by can sample from the cells adjacent to the boundary

```
cif = sum(G.faces.neighbors(f,:),2);
fp = state.pressure(cif);
```

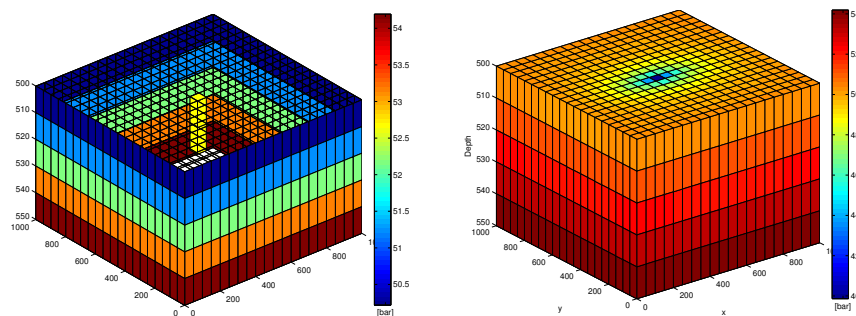


Fig. 7.5. A reservoir with hydrostatic boundary condition and fluid extracted from a sink penetrating two cells in the upper two layers of the model. The left plot shows the boundary and the fluid sink, while the right plot shows the resulting pressure distribution.

The latter may be useful if the initial pressure distribution has been computed by a more elaborate procedure than what is currently implemented in `psideh`. In either case, the boundary conditions can now be set by the call

```
bc = addBC(bc, f, 'pressure', fp);
```

To make the problem a bit more interesting, we also include a fluid sink at the midpoint of the upper two layers in the model,

```
ci = round(.5*(nx*ny-nx));
ci = [ci; ci+nx*ny];
src = addSource(src, ci, repmat(-1e3*meter^3/day,numel(ci),1));
```

The boundary conditions and source terms are shown to the left in Figure 7.5 and the resulting pressure distribution to the right. The fluid sink will cause a pressure draw-down, which will have an ellipsoidal shape because of the anisotropy in the permeability field.

Conditions on non-rectangular domain

In the last example, we consider a case where the outer boundary of the reservoir is not a simple hexahedron. In such cases, it may not be as simple as above to determine the exterior faces that lie on the perimeter of the reservoir. In particular, faults having a displacement may give exterior faces at the top and bottom of the model that are not part of what one would call the reservoir perimeter when setting boundary conditions other than no-flow. Likewise, other geological processes like erosion may cause gaps in the model that lead to exterior faces that are not part of the natural perimeter. This is illustrated in the left plot of Figure 7.6, where we have tried to specify boundary conditions using the same procedure as in the linear pressure-drop example (Figure 7.4).

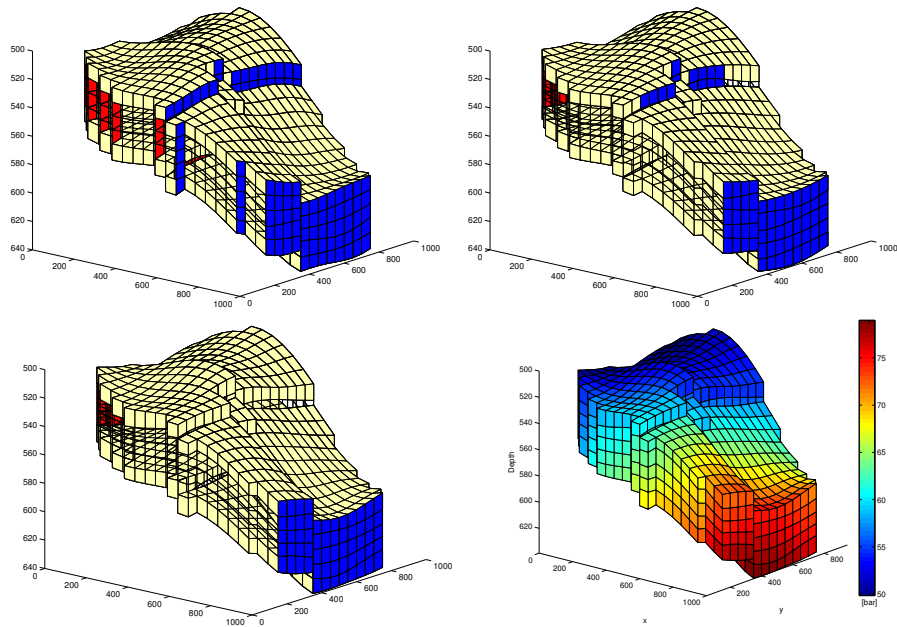


Fig. 7.6. Specifying boundary conditions along the outer perimeter of a corner-point model. The upper-left plot shows the use of `fluxside` (blue color) and `pside` (red color) to set boundary conditions on the east and west global boundaries. In the upper-right plot, the same functions have been used along with a specification of subranges in the global sides. In the lower-left plot, we have utilized user-supplied information to correctly set the conditions only along the perimeter. The lower-right plot shows the resulting pressure solution.

If the reservoir neither had faults with displacement nor holes inside its perimeter, we could use the subrange feature of `fluxside` and `pside` to restrict the boundary conditions to a subset of the global side, i.e., for our particular choice of grid parameters, set

```
bc = fluxside([], G, 'EAST', 5e3*meter^3/day, 4:15, 1:5);
bc = pside (bc, G, 'WEST', 50*barsa, 7:17, []);
```

Unfortunately, this will not work properly in the current case, as shown in the middle plot of Figure 7.6. The problem is that `fluxside` and `pside` define their 'east' sides to consist of all faces that only belong to one cell and are categorized to be on the east side of this cell.

To find the faces that are on the perimeter, we need to use expert knowledge. In our case, this amounts to utilizing the fact that the perimeter is defined as those faces that lie on the bounding box of the model. On these faces, we distribute the total flux to individual faces according to the face area. For the Neumann condition we therefore get

```
x = G.faces.centroids(f,1);
[xm,xM] = deal(min(x), max(x));
ff = f(x>xM-1e-5);
bc = addBC(bc, ff, 'flux', (5e3*meter^3/day) ...
    * G.faces.areas(ff)/ sum(G.faces.areas(ff)));
```

The Dirichlet condition can be specified in a similar manner.

COMPUTER EXERCISES:

35. Consider a 2D box with a sink at the midpoint and inflow across the perimeter specified either in terms of a constant pressure or a constant flux. Are there differences in the two solutions, and if so, can you explain why? Hint: use time-of-flight, total travel time, and/or streamlines to investigate the flow pattern.
36. Apply the production setup from Figure 7.5 on page 201, with hydrostatic boundary conditions and fluids extracted from two cells at the midpoint of the model, to the model depicted in Figure 7.6 on the preceding page.
37. Compute the flow patterns for all the bed models in data sets `BedModels1` and `BedModel2` subject to linear pressure drop first in the x and then in the y -direction. These models are examples of small-scale models constructed to model small-scale heterogeneity and compute representative properties in simulation models on a larger scale, and a linear pressure drop is the most wide-spread computational setup used for flow-based upscaling. What happens if you try to specify flux conditions?
38. Consider models from the `CaseB4` data set. Use appropriate boundary conditions to drive flow across the faults and compare flow patterns computed on the pillar and on the stair-stepped grid, as well as solutions computed for the two different model resolutions. Can you explain any differences you observe?

7.4.3 Structured versus unstructured stencils

We have so far only discussed grids that have an underlying structured cell numbering. The two-point schemes can also be applied to fully unstructured and polyhedral grids. To demonstrate this, we use the triangular grid generated from the `seamount` data set that is supplied with MATLAB, see Figure 4.8, scaled to cover a 1×1 km² area. Based on this grid, we define a non-rectangular reservoir. The reservoir is assumed to be homogeneous with an isotropic permeability of 100 mD and the resident fluid has the same properties as in the previous examples. A constant pressure of 50 bar is set at the outer perimeter and fluid is drained from a well located at (450, 500) at a constant rate of one pore volume over fifty years. (All details are found in the script `stencilComparison.m`).

We start by generating the triangular grid, which will subsequently be used to define the extent of the reservoir:

```
load seamount
T = triangleGrid([x(:) y(:)], delaunay(x,y));
[Tmin,Tmax] = deal(min(T.nodes.coords), max(T.nodes.coords));
T.nodes.coords = bsxfun(@times, ...
    bsxfun(@minus, T.nodes.coords, Tmin), 1000./(Tmax - Tmin));
T = computeGeometry(T);
```

Next, we generate two Cartesian grids that cover the same domain, one with approximately the same number of cells as the triangular grid and a 10×10 refinement of this grid that will give us a reference solution,

```
G = computeGeometry(cartGrid([25 25], [1000 1000]));
inside = isPointInsideGrid(T, G.cells.centroids);
G = removeCells(G, ~inside);
```

The function `isPointInsideGrid` implements a simple algorithm for finding whether one or more points lie inside the circumference of a grid. First, all boundary faces are extracted and then the corresponding nodes are sorted so that they form a closed polygon. Then, MATLAB's built-in function `inpolygon` can be used to check whether the points are inside this polygon or no.

To construct a radial grid centered around the point at which we will extract fluids, we start by using the same code as on page 109 to generate a set of points inside $[-1, 1] \times [-1, 1]$ that are graded radially towards the origin (see e.g., Figure 4.25),

```
P = [];
for r = exp([-3.5:.2:0, 0, .1]),
    [x,y] = cylinder(r,25); P = [P [x (1,:); y (1,:)]];
end
P = unique([P'; 0 0], 'rows');
```

The points are scaled and translated so that their origin is moved to the point (450,500), from which fluid will be extracted:

```
[Pmin,Pmax] = deal(min(P), max(P));
P = bsxfun(@minus, bsxfun(@times, ...
    bsxfun(@minus, P, Pmin), 1200./(Pmax-Pmin)), [150 100]);
```

Then, we remove all points outside of the triangular grid, before the point set is passed to two grid-factory routines to first generate a triangular and then a Voronoi grid:

```
inside = isPointInsideGrid(T, P);
V = computeGeometry( pebi( triangleGrid(P(inside,:)) ));
```

Once the grids have been constructed, the setup of the remaining part of the model will be the same in all cases. To avoid unnecessary replication of

code, we collect the grids in a cell array and use a simple for-loop to set up and simulate each model realization:

```

g = {G, T, V, Gr};
for i=1:4
    rock.poro = repmat(0.2, g{i}.cells.num, 1);
    rock.perm = repmat(100*milli*darcy, g{i}.cells.num, 1);
    hT = simpleComputeTrans(g{i}, rock);
    pv = sum(poreVolume(g{i}, rock));

    tmp = (g{i}.cells.centroids - repmat([450, 500], g{i}.cells.num, [])).^2;
    [~, ind] = min(sum(tmp, 2));
    src{i} = addSource(src{i}, ind, -.02*pv/year);

    f = boundaryFaces(g{i});
    bc{i} = addBC([], f, 'pressure', 50*barsa);

    state{i} = incompTPFA(initResSol(g{i}, 0, 1), ...
        g{i}, hT, fluid, 'src', src{i}, 'bc', bc{i}, 'MatrixOutput', true);

    [tof{i}, A{i}] = computeTimeOfFlight(state{i}, g{i}, rock, ...
        'src', src{i}, 'bc', bc{i}, 'reverse', true);
end

```

The pressure solutions computed on the four different grids are shown in Figure 7.7, while Figure 7.8 compares the sparsity patterns of the corresponding linear systems for the three coarse grids.

As expected, the Cartesian grid gives a banded matrix consisting of five diagonals that correspond to each cell and its four neighbors in the cardinal directions. Even though this discretization is not able to predict the complete draw-down at the center (the reference solution predicts a pressure slightly below 40 bar), it captures the shape of the draw-down region quite accurately; the region appears ellipsoidal because of the non-unit aspect ratio in the plot. In particular, we see that the points in the radial plot follow those of the fine-scale reference closely. The spread in the points as $r \rightarrow 300$ is not a grid-orientation effect, but the result of variations in the radial distance to the fixed pressure at the outer boundary on all four grids.

The unstructured triangular grid is more refined near the well and is hence able to predict the pressure draw-down in the near-well region more accurately. However, the overall structure of this grid is quite irregular, as can be seen from the sparsity pattern of the linear system shown in Figure 7.8, and the irregularity gives significant grid-orientation effects. This can be seen from the irregular shape of the color contours in the upper part of Figure 7.7 as well as from the spread in the scatter plot. In summary, this grid is not well suited for resolving the radial symmetry of the pressure draw-down in the near-well region. But to be fair, the grid was not generated for this purpose either.

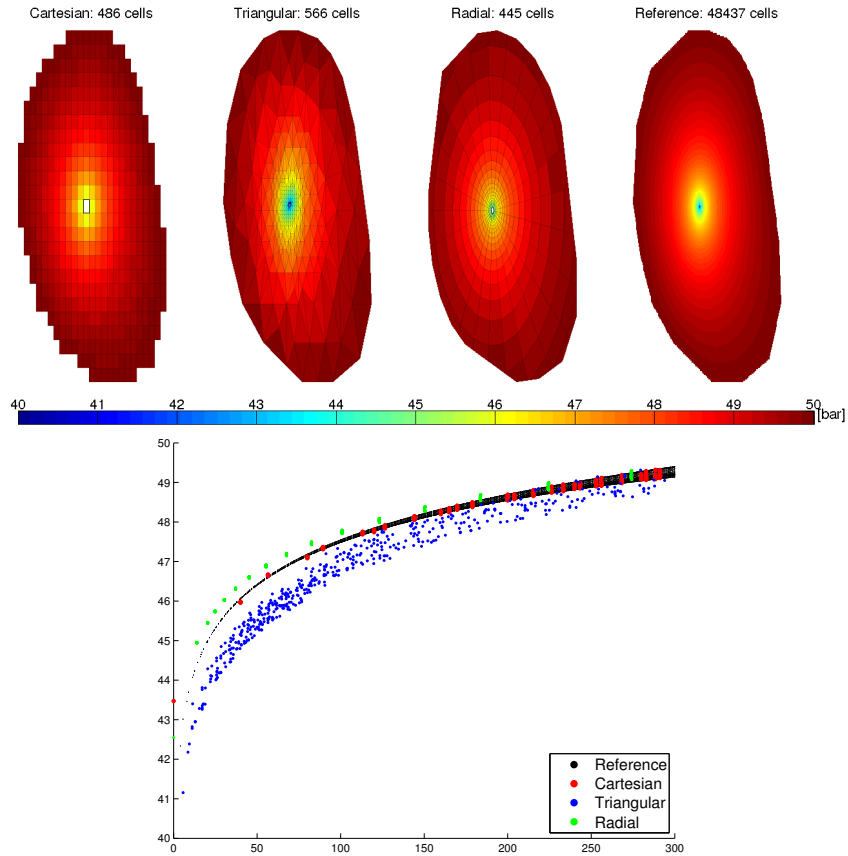


Fig. 7.7. Comparison of the pressure solution for three different grid types: uniform Cartesian, triangular, and a graded radial grid. The scattered points used to generate the triangular domain and limit the reservoir are sampled from the `seamount` data set and scaled to cover a $1 \times 1 \text{ km}^2$ area. Fluids are drained from the center of the domain, assuming a constant pressure of 50 bar at the perimeter.

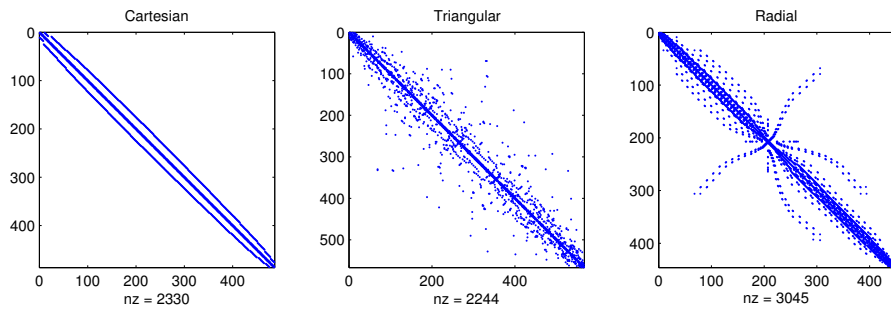


Fig. 7.8. Sparsity patterns for the TPFA stencils on the three different grid types shown in Figure 7.7.

Except for close to the well and close to the exterior boundary, the topology of the radial grid is structured in the sense that each cell has four neighbors, two in the radial direction and two in the angular direction, and the cells are regular trapezoids. This should, in principle, give a banded sparsity pattern provided that the cells are ordered starting at the natural center point and moving outward, one ring at the time. To verify this claim, you can execute the following code:

```
[~,q]=sort(state{3}.pressure);
spy(state{3}.A(q,q));
```

However, as a result of how the grid was generated, by first triangulating and then forming the dual, the cells are numbered from west to east, which explains why the sparsity pattern is so far from being a simple banded structure. While this may potentially affect the efficiency of a linear solver, it has no impact on the accuracy of the numerical approximation, which is good because of the grading towards the well and the symmetry inherent in the grid. Slight differences in the radial profile compared with the Cartesian grid(s) can mainly be attributed to the fact that the source term and the fixed pressure conditions are not located at the exact same positions in the simulations, due to the inherent difference in the discretizations.

In Figure 7.9, we also show the sparsity pattern of the linear system used to compute the reverse time-of-flight from the well and back into the reservoir. Using the default cell ordering, the sparsity pattern of each upwind matrix will appear as a less dense version of the pattern for the corresponding TPFA matrix. However, whereas the TPFA matrices represent an elliptic equation in which information propagates in both directions across cell interfaces, the upwind matrices are based on one-way connections arising from fluxes between pairs of cells that are connected in the TPFA discretization. To reveal the true nature of the system, we can permute the system by either sorting the cell pressures in ascending order (potential ordering) or using the function `dmperm` to compute a Dulmage–Mendelsohn decomposition. As pointed out in Section 7.3, the result is a lower triangular matrix, from which it is simple to see that the unidirectional propagation of information one would expect for a hyperbolic equations having only positive characteristics.

COMPUTER EXERCISES:

39. Compare the sparsity patterns resulting from the potential ordering and use of `dmperm` for both the upwind and the TPFA matrices.
40. Investigate the flow patterns in more details using forward time-of-flight, travel time, and streamlines.
41. Replace the boundary conditions by a constant influx, or set pressure values sampled from a radially symmetric pressure solution in an infinite domain.

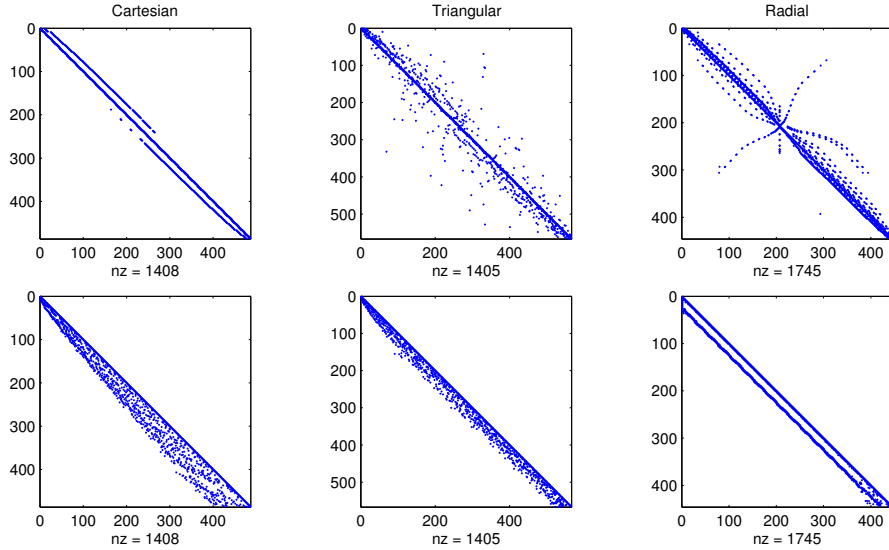


Fig. 7.9. Sparsity patterns for the upwind stencils used to compute time-of-flight on the three different grid types shown in Figure 7.7. In the lower row, the matrices have been permuted to lower-triangular form by sorting the cell pressures in ascending order.

7.4.4 Using Peaceman well models

Whereas it may be sufficient to consider flow driven by sources, sinks, and boundary conditions in many subsurface applications, the key aspect in reservoir simulation is in most cases to predict the amount of fluids that are produced and/or injected from one or more wells. As we saw in Section 6.3.2, flow in and out of a wellbore takes place on a scale that is much smaller than those of a single grid cell in typical sector and field models and is therefore commonly modeled using a semi-analytical model of the form (6.34). In this section, we will go through two examples to demonstrate how such models can be included in the simulation setup using data objects and utility functions introduced in Section 7.1.5. The first example is a highly idealized box model. In the second example we consider a realistic model of a shallow-marine reservoir taken from the SAIGUP study, see Section 3.5.5.

Box reservoir

We consider a reservoir consisting of a homogeneous $500 \times 500 \times 25$ m³ sand box with a isotropic permeability of 100 mD, represented on a regular $20 \times 20 \times 5$ Cartesian grid. The fluid is the same as in the examples above. All code lines necessary to set up the model, solve the flow equations, and visualize the results are found in the script `firstWellExample.m`.

Setting up the model is quickly done, once you have gotten familiar with MRST:

```
[nx,ny,nz] = deal(20,20,5);
G = computeGeometry( cartGrid([nx,ny,nz], [500 500 25]) );
rock.perm = repmat(100 .* milli*darcy, [G.cells.num, 1]);
fluid = initSingleFluid('mu',1*centi*poise,'rho',1014*kilogram/meter^3);
hT = computeTrans(G, rock);
```

The reservoir will be produced by a well pattern consisting of a vertical injector and a horizontal producer. The injector is located in the south-west corner of the model and operates at a constant rate of 3000 m³ per day. The producer is completed in all cells along the upper east rim and operates at a constant bottom-hole pressure of 1 bar (i.e., 10⁵ Pascal in SI units):

```
W = verticalWell([], G, rock, 1, 1, 1:nz, 'Type', 'rate', 'Comp_i', 1, ...
                'Val', 3e3/day(), 'Radius', .12*meter, 'name', 'I');
W = addWell(W, G, rock, nx : ny : nx*ny, 'Type', 'bhp', 'Comp_i', 1, ...
            'Val', 1.0e5, 'Radius', .12*meter, 'Dir', 'y', 'name', 'P');
```

In addition to specifying the type of control on the well ('bhp' or 'rate'), we also need to specify the radius and the fluid composition, which is '1' here since we have a single fluid. After initialization, the array W contains two data objects, one for each well:

Well #1:		Well #2:
cells: [5x1 double]		cells: [20x1 double]
type: 'rate'		type: 'bhp'
val: 0.0347		val: 100000
r: 0.1000		r: 0.1000
dir: [5x1 char]		dir: [20x1 char]
WI: [5x1 double]		WI: [20x1 double]
dZ: [5x1 double]		dZ: [20x1 double]
name: 'I'		name: 'P'
compi: 1		compi: 1
refDepth: 0		refDepth: 0
sign: 1		sign: []

This concludes the specification of the model. We can now assemble and solve the system

```
gravity reset on;
resSol = initState(G, W, 0);
state = incompTPFA(state, G, hT, fluid, 'wells', W);
```

The result is shown in Figure 7.10. As expected, the inflow rate decays with the distance to the injector. The flux intensity depicted in the lower-right plot is computed using the following command, which first maps the vector of face fluxes to a vector with one flux per half face and then sums the absolute value of these fluxes to get a flux intensity per cell:

```
cf = accumarray(getCellNoFaces(G), ...
               abs(faceFlux2cellFlux(G, state.flux)));
```

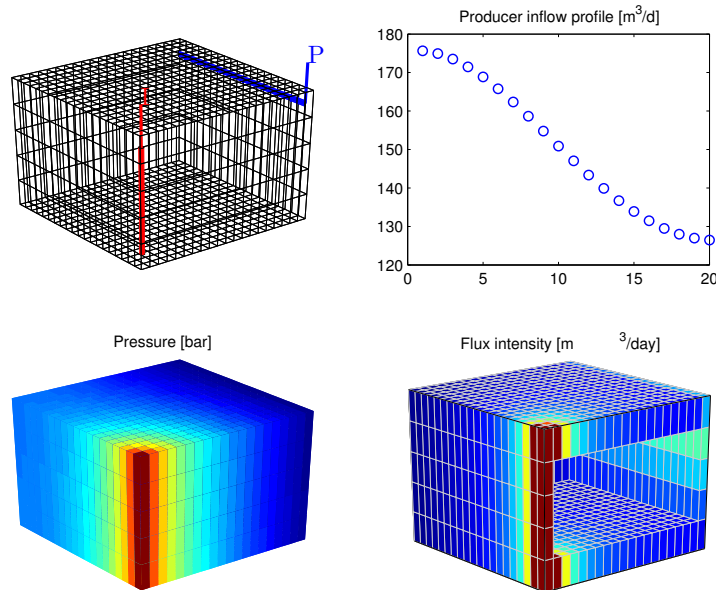


Fig. 7.10. Solution of a single-phase, incompressible flow problem inside a box reservoir with a vertical injector and a horizontal producer.

Shallow-marine reservoir

In the final example, we will return to the SAIGUP model discussed in Section 4.5. This model does not represent a real reservoir, but is one out of a large number of models that were built to be plausible realizations that contain the types of structural and stratigraphic features one could encounter in models of real clastic reservoirs. Continuing from Section 4.5, we simply assume that the grid and the petrophysical model has been loaded and processed. All details are given in the script `saigupWithWells.m`. (The script also explains how to speed up the grid processing by using two C-accelerated routines for constructing a grid from Eclipse input and computing areas, centroids, normals, volumes, etc).

The permeability input is an anisotropic tensor with zero vertical permeability in a number of cells. As a result, some parts of the reservoir may be completely sealed off from the wells. This will cause problems for the time-of-flight solver, which requires that all cells in the model must be flooded after some finite time that can be arbitrarily large. To avoid this potential problem, we assign a small constant times the minimum positive vertical permeability to the grid blocks that have zero cross-layer permeability.

```
is_pos = rock.perm(:, 3) > 0;
rock.perm(~is_pos, 3) = 1e-6*min(rock.perm(is_pos, 3));
```

Similar safeguards are implemented in most commercial simulators.

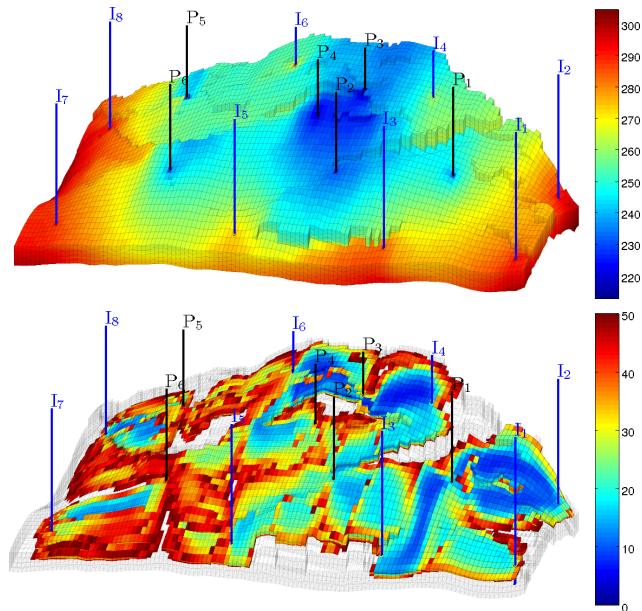


Fig. 7.11. Incompressible, single-phase simulation of the SAIGUP model. The upper plot shows pressure distribution, and the lower plot shows cells with total travel time less than fifty years.

The reservoir is produced from six producers spread throughout the middle of the reservoir; each producer operates at a fixed bottom-hole pressure of 200 bar. Pressure support is provided by eight injectors located around the perimeter, each operating at a prescribed and fixed rate. As in the previous example, the wells are described using a Peaceman model. For simplicity, all wells chosen to be vertical and are assigned using the logical ij sub-index available in the corner-point format. The following code specifies the injectors:

```

nz = G.cartDims(3);
I = [ 3, 20, 3, 25, 3, 30, 5, 29];
J = [ 4, 3, 35, 35, 70, 70,113,113];
R = [ 1, 3, 3, 3, 2, 4, 2, 3]*500*meter^3/day;
W = [];
for i = 1 : numel(I),
    W = verticalWell(W, G, rock, I(i), J(i), 1:nz, 'Type', 'rate', ...
                    'Val', R(i), 'Radius', .1*meter, 'Comp_I', 1, ...
                    'name', ['I$-', int2str(i), '$']);
end

```

The producers are specified in the same way. Figure 7.11 shows the well positions and the pressure distribution. We see a clear pressure buildup along the east, south, and west rim of the model. Similarly, there is a pressure draw-

down in the middle of the model around producers P2, P3, and P4. The total injection rate is set so that one pore volume will be injected in a little less than forty years.

Although this is a single-phase simulation, let us for a while think of our setup in terms of injection and production of different fluids (since the fluids have identical properties, we can think of a 'blue' fluid being injected into a 'black' fluid). In an ideal situation, one would wish that the 'blue' fluid would sweep the whole reservoir before it breaks through to the production wells, as this would maximize the displacement of the 'black' fluid. Even in the simple quarter five-spot examples in Section 7.4.1 (see Figure 7.3), we saw that this was not the case, and one cannot expect that this will happen here, either. The lower plot in Figure 7.11 shows all cells in which the total travel time (sum of forward and backward time-of-flight) is less than fifty years. By looking at such a plot, one can get a quite a good idea of regions in which there is very limited communication between the injectors and producers (i.e., areas without colors). If this was a multiphase flow problem, these areas would typically contain bypassed oil and be candidates for infill drilling or other mechanisms that would improve the volumetric sweep. We will come back to a more detailed discussion of flow patterns and volumetric connections in Section 9.4.2.

COMPUTER EXERCISES:

42. Change the parameter 'Dir' from 'y' to 'z' in the box example and rerun the case. Can you explain why you get a different result?
43. Switch the injector in the box example to be controlled by a bottom-hole pressure of 200 bar. Where would you place the injector to maximize production rate if you can only perforate (complete) it in five cells?
44. Consider the SAIGUP model: can you improve the well placement and/or the distribution of fluid rates. Hint: is it possible to utilize time-of-flight information?
45. Use the function `SPE10_setup` to set up an incompressible, single-phase version of the full SPE 10 benchmark. Compute pressure, time-of-flight and tracer concentrations associated with each well. Hint: You may need to replace MATLAB's standard backslash-solver by a highly-efficient iterative solver like AGMG [150, 10] to get reasonable computational performance. Also, beware that you may run out of memory if your computer is not sufficiently powerful.

Flow Diagnostics

Even for single-phase flow it is seldom sufficient to only study well responses and pressure distribution to understand the flow paths and communication patterns in a complex reservoir model. To gain a better qualitative picture of the flow taking place in the reservoir, you will typically want to know the answer to questions such as: From what region does a given producer drain? To what region does a given injector provide pressure support? Which injection and production wells are in communication? What part of the reservoir affects this communication? How much does each injector contribute to support the recovery from a given producer? Do any of the wells have back-flow? What is the sweep and displacement efficiency within a given drainage, sweep, or well-pair region? Which regions are likely to remain unswept? Likewise, you will typically also want to perform what-if and sensitivity analyzes to understand how different parameters in the reservoir model and their inherent sensitivity affect reservoir responses.

As we will see later in the book, performing a single simulation of a full reservoir model containing a comprehensive description of geology, reservoir fluids, flow physics, well controls, and coupling to surface facilities is a computationally demanding task that may require hours or even days to complete. This means that your ability to study parameter variations is limited. This is particularly at odds with modern reservoir characterization techniques, in which hundreds of equiprobable realizations may be generated to quantify uncertainty in the characterization. In this chapter, we will therefore introduce a set of simple techniques referred to as *flow diagnostics* that can be used to develop basic understanding of how the fluid flow is affected by reservoir geology and how the flow patterns in the reservoir respond to engineering controls. In their basic setup, these techniques only rely on the solution of single-phase, incompressible flow problems as discussed in the two previous chapters. (However, in parts of the presentation, we will use some simple concepts from multiphase flow that have not yet been properly introduced, but are hopefully still understandable).

In general, flow diagnostics can be defined as *simple and controlled numerical flow experiments that are run to probe a reservoir model, establish connections and basic volume estimates, and quickly provide a qualitative picture of the flow patterns in the reservoir*. Flow diagnostics can also be used to compute quantitative information about the recovery process in settings somewhat simpler than what would be encountered in an actual field, and using these techniques, you can rapidly and iteratively perturb simulation input and evaluate the resulting changes in volumetric connections and communications to build an understanding of cause and effects in your model.

Ideas similar to what will be presented in the following have previously been used within streamline simulation [54] for ranking and upscaling [88, 19, 170], identifying reservoir compartmentalization [80], rate optimization [174, 153, 90], and flood surveillance [22]. Our presentation, however, is inspired by Shahvali et al. [168] and [137], who developed the concept of flow diagnostics based on standard finite-volume discretizations.

Because of their low computational cost, flow diagnostics methods can easily be incorporated into interactive graphical tools that offer rapid and interactive screening and preprocessing capabilities. This, however, is not easy to present in book form, and if you want to see these tools in practice, you should try out some of the examples that follow MRST study the exercises presented throughout this chapter. Flow diagnostics techniques can also be utilized to post-process more comprehensive simulation methods and to perform what-if and sensitivity analyzes in parameter regions surrounding preexisting simulations. As such, flow diagnostics offers a computationally inexpensive complement and/or alternative to the use of full-featured multiphase simulations to provide flow information in various reservoir management workflows. .

9.1 Flow patterns and volumetric connections

You have already been introduced to the basic quantities that lie at the core of flow diagnostics in the two previous chapters: As you probably recall from Chapter 6.3.3, we can derive time lines that show how heterogeneity affects flow patterns for an instantaneous velocity field \vec{v} by computing

- the forward time-of-flight, defined by

$$\vec{v} \cdot \nabla \tau_f = \phi, \quad \tau_f|_{\text{inflow}} = 0, \quad (9.1)$$

which measures time it takes a neutral particle to travel to a given point in the reservoir from the nearest fluid source or inflow boundary; and

- the backward time-of-flight, defined by

$$-\vec{v} \cdot \nabla \tau_b = \phi, \quad \tau_b|_{\text{outflow}} = 0, \quad (9.2)$$

which measures the time it takes a neutral particle to travel from any point in the reservoir to the nearest fluid sink or outflow boundary.

The sum of the forward and backward time-of-flight at a given point in the reservoir gives the total residence time of an imaginary particle as it travels from the nearest fluid source or inflow boundary to the nearest fluid sink or outflow boundary. Studying iso-contours of time-of-flight will give an indication of how more complex multiphase displacements may evolve under fixed well and boundary conditions, and will reveal more information about the flow field than pressure and velocities alone. This was illustrated already in the previous chapter, where Figure 7.3 on page 198 showed time lines for a quarter five-spot flow pattern and the total residence time was used to distinguish high-flow regions from stagnant regions. Likewise, in Figure 7.11 on page 211 we used time-of-flight to identify non-targeted regions for a complex field model, that is, regions with high τ_f values that were likely to remain unswept and hence were obvious targets to investigate for placement of additional wells. Time-of-flight can also be used to derive various measures of dynamic heterogeneity, as we will see in the next section, or to compute proxies of economical measures such as net-present value for models that contain multiphase fluid information, see [137].

In similar manner, we can determine the points in the reservoir that are affected by a given fluid source or inflow boundary by solving the following injector (or inflow) tracer equation,

$$\vec{v} \cdot \nabla c_i^k = 0, \quad c_i^k|_{\text{inflow}} = 1. \quad (9.3)$$

To understand what this equation does, let us think of an imaginary painting experiment in which we inject a mass-less, non-diffusive ink of a unique color at each fluid source or point on the inflow boundary we want to trace the influence from. The ink will start flowing through the reservoir and paint every point it gets in contact with. Eventually, the fraction of different inks that flow past each point in the reservoir will reach a steady state, and by measuring these fractions, we can determine the extent to which each different ink influences a specific point. Likewise, to determine how much each point in the reservoir is influenced by a fluid sink or point on the outflow boundary, we can reverse the flow field and solve similar equations for producer (or outflow) tracers,

$$-\vec{v} \cdot \nabla c_p^k = 0, \quad c_i^k|_{\text{outflow}} = 1. \quad (9.4)$$

To summarize, the basic computation underlying flow diagnostics consists of three parts: (i) solution of a pressure equation to determine the bulk fluid movement; (ii) solution of a set of numerical tracer equations to partition the model into volumetric flow regions; and (iii) solution of time-of-flight equations to give time lines that describe the flow within each region. In the following, we will describe in more detail how these basic quantities can be combined and processed to provide more insight into flow patterns and volumetric connections in the reservoir.

9.1.1 Volumetric partitions

If all parts of the inflow (or outflow) are assigned a unique tracer value, the resulting tracer distribution should in principle produce a partition of unity for all parts of the reservoir that are in communication with the inflow (or outflow) boundary. In practice, one may not be able to obtain an exact partition of unity because of numerical errors. Based on the inflow and outflow tracers, we can further define

- drainage regions – each such region represents the reservoir volume that eventually will be drained by a given producer (or outflow boundary) given that the current flow field \vec{v} prevails until infinity;
- sweep regions – each such region represents the reservoir volume that eventually will be swept by a given injector (or inflow boundary) if the current flow conditions remain forever;
- well pairs – pairs of injectors and producers that are in communication with each other;
- well-pair regions – regions of the reservoir in which the flow between a given injector and producer takes place.

Drainage and sweep regions are typically determined by a majority vote over all tracers, while well pairs are determined by finding all injectors whose concentration is positive in one of the well completions of a given producer (or vice versa). Well-pair regions can be found by intersecting drainage and sweep regions, or alternatively by intersecting injector and producer tracers. Well-allocation factors will be discussed in more detail in Section 9.1.3 and in Chapter 10 in conjunction with single-phase upscaling.

Our default choice would be to assign a unique tracer to each injector and producer, but you can also subdivide some of the wells into multiple segments and trace the influence of each segment separately. This can, for instance, be used to determine if a (horizontal) well has cross-flow, so that fluid injected in one part of the well is drawn back into the wellbore in another part of the well, or fluids produced in one completion is pushed out again in another.

We have already encountered the function `computeTimeOfFlight` for computing time-of-flight in Section 7.3. The `diagnostics` module offers an additional utility function

```
D = computeTOFandTracer(state, G, rock, 'wells', W, ...)
```

that computes forward and backward time-of-flight, injector and producer tracers, as well as sweep and drainage regions in one go for models with flow driven by wells. These quantities are represented as fields in the structure `D`:

- `inj` and `prod` give the indices for the injection and production wells in the well structure `W`;
- `tof` is a $2 \times n$ vector with τ_f in its first and τ_b in its second column;
- `itracer` and `ptracer` contains the tracers for the injectors and producers;
- `ipart` and `ppart` hold the partitions resulting from a majority vote.

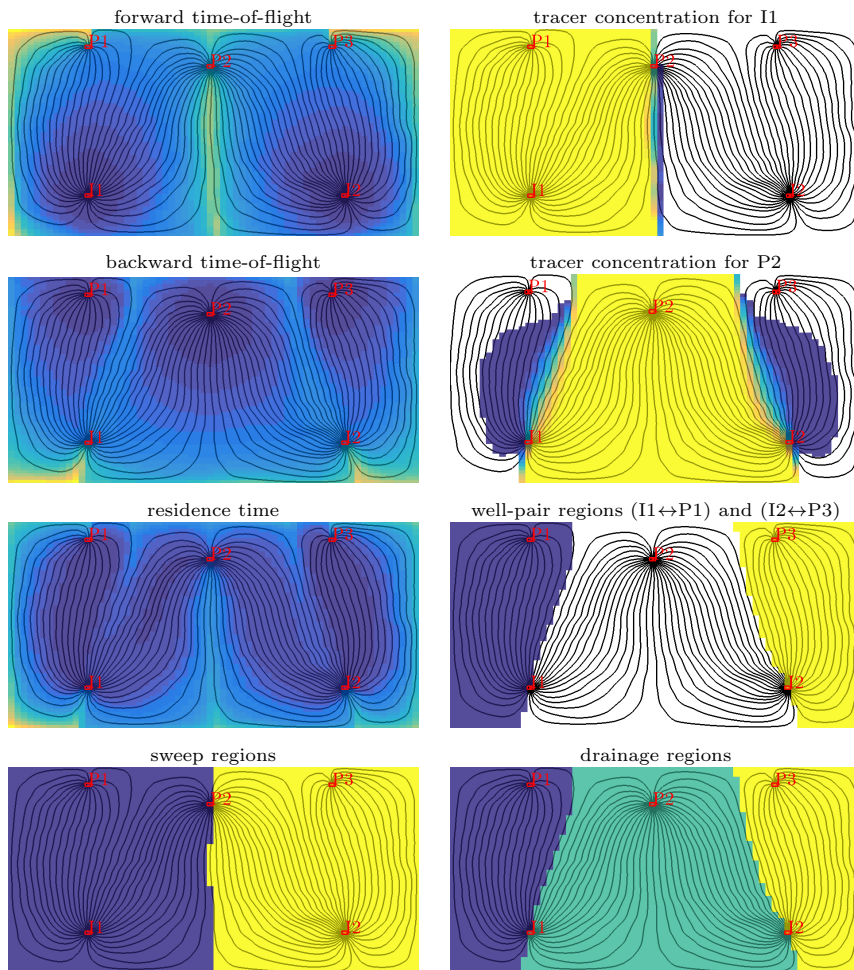


Fig. 9.1. Time-of-flight, tracer distributions, and various types of volumetric delineations for a simple case with two injectors and three producers. The source code necessary to generate the plots is given in the `showDiagnostBasic` tutorial in the `book` module.

Similar quantities can be associated with boundary conditions and/or source terms, but support for this has not yet been implemented in MRST. Well pairs can be identified by

```
WP = computeWellPairs(G, rock, W, D)
```

which also computes the pore volume of the region of the reservoir associated with each pair.

Figure 9.1 shows time-of-flight, tracer concentrations, tracer partitions and a few combinations thereof for a simple flow problem with two injectors and

three production wells. There are many other ways these basic quantities can be combined and plotted to reveal volumetric connection and provide enhanced insight into flow patterns. One can, for instance, combine sweep regions with time-of-flight to provide a simple forecasts of contacted volumes or to visualize how displacement fronts move through the reservoir. To this end, one would typically also include estimates of characteristic wave-speeds from multiphase displacement theory.

9.1.2 Time-of-flight per tracer region: improved accuracy

It is important to understand that the time-of-flight values computed by a finite-volume method like the one discussed in Chapter 6.4.3 are *volume-average values*, which cannot be compared directly with the *point values* one obtains by tracing streamlines as described in Chapter 6.3.3. Since time-of-flight is a quantity defined from a global line integral (see (6.38)), the point-wise variations can be large inside a single grid cell, in particular near flow divides and in the near-well regions, where both high-flow and low-flow streamlines converge. To improve the accuracy of the time-of-flight within each well-pair region, one can use the tracer concentrations to recompute the time-of-flight values for each tracer region,

$$\vec{v} \cdot \nabla (c_i^k \tau_f^k) = c_i^k \phi. \quad (9.5)$$

In MRST, this is done by passing the option `computeWellTOFs` to the time-of-flight solver, using a call that looks something like

```
T = computeTimeOfFlight(state, G, rock, 'wells', W, ...
                        'tracer', {W(inj).cells}, 'computeWellTOFs', true);
```

which will then append one extra column for each tracer at the end of the return parameter T.

9.1.3 Well-allocation factors

Apart from a volumetric partition of the reservoir, one is often interested in knowing how much of the inflow to a given producer can be attributed to each of the injectors, or conversely, how the 'push' from a given injector is distributed to the different producers. We will refer to this as well-allocation factors, which can be further refined so that they also describe the cumulative flow from the toe to the heel of a well. By computing the cumulative flux from the toe to the heel of the well and plotting this flux as a function of the distance from the toe (with the flux on the x -axis and distance on the y -axis) we get a plot that is reminiscent of the plot from a production-logging tool.

To formally define the well-allocation factors, we use the notation from Section 6.4.2, so that $\mathbf{x}[c]$ denotes the value of vector \mathbf{x} in cell c . Next, we let c_n^i denote the injector tracer concentration associated with well (or well

segment) number n , let \mathbf{c}_m^p denote the producer concentration associated with well number m , \mathbf{q} the vector of well fluxes, and $\{w_k^n\}_k$ the cells in which well number n is completed. Then, the cumulative factors are defined as

$$\begin{aligned} a_{nm}^i[w_\ell^n] &= \sum_{k=1}^{\ell} \mathbf{q}[w_k^n] \mathbf{c}_n^i[w_k^n] \mathbf{c}_m^p[w_k^n], \\ a_{mn}^p[w_\ell^m] &= \sum_{k=1}^{\ell} \mathbf{q}[w_k^m] \mathbf{c}_n^i[w_k^m] \mathbf{c}_m^p[w_k^m]. \end{aligned} \tag{9.6}$$

The total well-allocation factor equals the cumulative factor evaluated at the heel of the well. Well-allocation factors are computed using the function `computeWellPair` and are found as two arrays of structs, `WP.inj` and `WP.prod`, that give the allocation factors for all the injection and production wells (or segments) accounted for in the flow diagnostics. In each struct, the array `alloc` gives the a_{nm} factors, whereas the influx or outflux that cannot be attributed to another well or segment is represented in the array `ralloc`.

9.2 Measures of dynamic heterogeneity

Whereas primary recovery can be reasonably approximated using averaged petrophysical properties, secondary and tertiary recovery is strongly governed by the intrinsic variability in rock properties and geological characteristics. This variability, which essentially can be observed at all scales in the porous medium, is commonly referred to as 'heterogeneity'. As we have seen in previous chapters, both the rock's ability to store and to transmit fluids are heterogeneous. However, it is the heterogeneity in permeability that has the most pronounced effect on flow patterns and volumetric connections in the reservoir. The importance of heterogeneity has been recognized from the earliest days of petroleum production, and over the years a number of static measures have been proposed to characterize heterogeneity, such as flow and storage capacity, Lorenz coefficient, Koval factor, and Dykstra–Parson's permeability variation coefficient, to name a few; see e.g., [106] for a more comprehensive overview.

In this section, we will show how some of the static heterogeneity measures from classical sweep theory can be reinterpreted in a dynamic setting if we calculate them from the time-of-flight (and tracer partitions) associated with an instantaneous flow field [170]. Static measures describe the spatial distribution of permeability and porosity, and large static heterogeneity means that there are large (local) variations in the rock's ability to store and transmit fluids. Dynamic heterogeneity measures, on the other hand, describe the distribution of flow-path lengths and connection structure, and large heterogeneity values show that there are large variations in travel and residence times, which again tend to manifest itself in early breakthrough of injected fluids. Experience has

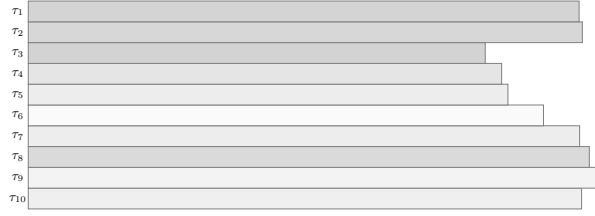


Fig. 9.2. Streamtube analogue used to define dynamic flow and storage capacity. Colors illustrate different average porosities.

shown that these measures, and particularly the dynamic Lorenz coefficient, correlates very well with forecasts of hydrocarbon recovery predicted by more comprehensive flow simulations and hence can be used as effective flow proxies in various reservoir management workflows, see [170, 168, 137]

9.2.1 Flow and storage capacity

A computation of forward and backward time-of-flight is the starting point for defining dynamic heterogeneity measures. We start by defining dynamic flow and storage capacity. To this end, we can think of the reservoir as a set of N streamtubes (non-communicating volumetric flow paths) that each has a volume V_i , a flow rate q_i , and a residence time $\tau_i = V_i/q_i$. The streamtubes are sorted so that their residence times are ascending, $\tau_1 \leq \tau_2 \leq \dots \leq \tau_N$, see Figure 9.2. Inside each streamtube, we assume a piston type displacement; think of a blue fluid pushing a red fluid from the left to the right in the figure. We then define the normalized flow capacity F_i and storage capacity Φ_i by,

$$\Phi_i = \sum_{j=1}^i V_j / \sum_{j=1}^N V_j, \quad F_i = \sum_{j=1}^i q_j / \sum_{j=1}^N q_j. \quad (9.7)$$

Here, Φ_i is the volume fraction of all streamtubes that have 'broken through' at time τ_i and F_i represent the corresponding fractional flow, i.e., the fraction of the injected fluid to the total fluid being produced. These two quantities can be plotted in a diagram as shown in Figure 9.3. From this diagram, we can also define the fractional recovery curve defined as the ratio of inplace fluid produced to the total fluid being produced; that is $(1 - F)$ plotted versus dimensionless time $t_D = d\Phi/dF$ measured in units of pore volumes injected.

To see how the F - Φ diagram can be seen as a measure of dynamic heterogeneity, we first consider the case of a completely homogeneous displacement, for which all streamtubes will break through at the same time τ . This means that, $(\Phi_i - \Phi_{i-1})/(F_i - F_{i-1}) \propto V_i/q_i$ is constant, which implies that $F = \Phi$, since both F and Φ are normalized quantities. Next, we consider a heterogeneous displacement in which all the streamtubes have the same flow rate q . Since the residence times τ_i form a monotonically increasing sequence, we have

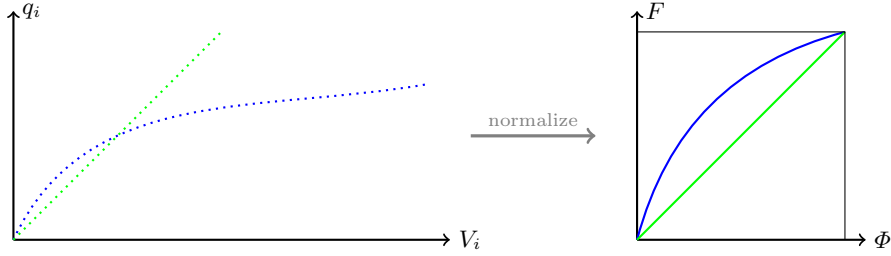


Fig. 9.3. Construction of the F - Φ diagram. The plot to the left shows flow rates q_i plotted as function of streamtube volumes V_i for a homogeneous displacement (green) and for a heterogeneous displacement (blue). The right plot shows the corresponding F - Φ diagrams, where the flow rates and the streamtube volumes have been normalized.

that $\{V_i\}$ will also be monotonically increasing. In general, $F(\Phi)$ is a concave function, where the steep initial slope corresponds to high-flow regions giving early breakthrough, whereas the flat trailing tail corresponds to low-flow and stagnant regions.

In the continuous case, we can (with a slight abuse of notation) define the storage capacity as

$$\Phi(\tau) = \int_0^\tau \phi(\vec{x}(s)) ds \quad (9.8)$$

where $\vec{x}(\tau)$ represents all streamlines whose total travel time equals τ . By assuming incompressible flow, we have that pore volume equals the flow rate times the residence time, $\phi = q\tau$, and hence we can define the flow capacity as

$$F(\tau) = \int_0^\tau q(\vec{x}(s)) ds = \int_0^\tau \frac{\phi(\vec{x}(s))}{s} ds. \quad (9.9)$$

From this, we can define *normalized, dynamic* flow and storage capacities by

$$\hat{\Phi}(\tau) = \frac{\Phi(\tau)}{\Phi(\infty)}, \quad \hat{F}(\tau) = \frac{F(\tau)}{F(\infty)}.$$

Henceforth, we will only discuss the normalized quantities and for simplicity we will also drop the hat symbol. To compute these quantities in practice, one would then have to first compute a representative set of streamlines, associate a flow rate, a pore volume, and a total travel time to each streamline, and then compute the cumulative sums as in (9.7).

Next, we consider how these concepts carry over to our grid setting where time-of-flight is computed by a finite-volume method and not by tracing streamlines. Let `pv` be an $n \times 1$ array containing the pore volume of the n cells in the grid and `tof` be an $n \times 2$ array containing the forward and backward time-of-flights. We can now compute the cumulative, normalized storage capacity `Phi` as follows:

```

t      = sum(tof,2);    % total travel time
[ts,ind] = sort(t);    % sort cells based on travel time
v      = pv(ind);      % put pore volumes in correct order
Phi    = cumsum(v);    % cumulative sum
vt     = full(Phi(end)); % total volume of region
Phi    = [0; Phi/vt];  % normalize to units of pore volumes

```

In our finite-volume formulation, we do not have direct access to the flow rate for each cell, but this can easily be computed as the ratio between pore volume and residence time if we assume incompressible flow. With this, it is straightforward to compute the cumulative, normalized flow capacity F

```

q      = v./ts;        % back out flux based on incompressible flow
ff     = cumsum(q);    % cumulative sum
ft     = full(ff(end)); % total flux computed
F      = [0; ff/ft];  % normalize and store flux

```

This is essentially what is implemented in the utility function `computeFandPhi` in the `diagnostics` module.

The result of the above calculation is that we have two sequences Φ_i and F_i that are both given in terms of the residence time τ_i . If we sort the points (Φ_i, F_i) according to ascending values of τ_i , we obtain a sequence of discrete points that describe a parametrized curve in 2D space. The first end-point of this curve is at the origin: If no fluids have entered the domain, the cumulative flow capacity is obviously zero. Likewise, full flow capacity is reached when the domain is completely filled, and since we normalize both Φ and F by their value at the maximum value of τ , this corresponds to the point (1,1). Given that both F and Φ increase with increasing values of τ , we can use linear interpolation to define a continuous, monotonic, increasing function $F(\Phi)$.

9.2.2 Lorenz coefficient and sweep efficiency

The Lorenz coefficient is a popular measure of heterogeneity, and is defined as the difference in flow capacity from that of an ideal piston-like displacement:

$$L_c = 2 \int_0^1 (F(\Phi) - \Phi) d\Phi, \quad (9.10)$$

In other words, the Lorenz coefficient is equal twice the area under the $F(\Phi)$ curve and above the line $F = \Phi$, and has values between zero for homogeneous displacement and unity for an infinitely heterogeneous displacement, see Figure 9.4. Assuming that the flow and storage capacity are given as two vectors `F` and `Phi`, the Lorenz coefficient can be computed by applying a simple trapezoid rule

```

v      = diff(Phi,1);
Lc     = 2*(sum((F(1:end-1)+F(2:end))/2.*v) - .5);

```

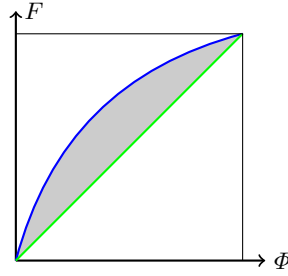


Fig. 9.4. The definition of the Lorenz coefficient from the F - Φ diagram. The green line represents a completely homogeneous displacement in which all flow paths have equal residence times, where the blue line is a heterogeneous displacement in which there is variation in the residence times. The Lorenz coefficient is defined as two times the gray area.

which is implemented in the `computeLorenz` function in the `diagnostics` module.

The F - Φ diagram can also be used to compute the *volumetric sweep efficiency* E_v , which measures how efficient injected fluids are used. Here, E_v is defined as the volume fraction of in-place fluid that has been displaced by injected fluid, or equivalently, as the ratio between the volume contacted by the displacing fluid at time t and the volume contacted at time $t = \infty$. In our streamtube analogue, only streamtubes that have not yet broken through will contribute to sweep the reservoir. Normalizing by total volume, we thus have

$$\begin{aligned} E_v(t) &= \frac{q}{V} \int_0^t [1 - F(\Phi(\tau))] d\tau \\ &= \frac{qt}{V} - \frac{q}{V} \int_0^t F(\tau) d\tau = \frac{qt}{V} - \frac{q}{V} \left[F(t)t - \int_0^F \tau dF \right] \\ &= \frac{t}{\bar{\tau}} (1 - F(t)) + \frac{1}{\bar{\tau}} \int_0^\Phi \bar{\tau} d\Phi = \Phi + (1 - F) \frac{d\Phi}{dF} = \Phi + (1 - F)t_D \end{aligned}$$

The third equality follows from integration by parts, and the fourth equality since $\bar{\tau} = V/q$ and $\tau dF = \bar{\tau} d\Phi$. Here, the quantity $d\Phi/dF$ takes the role as dimensionless time. Prior to breakthrough, $E_v = t_D$. After breakthrough, Φ is the volume of fully swept flow paths, whereas $(1 - F)t_D$ is the volume of flow paths being swept.

The implementation in MRST is quite simple and can be found in the utility function `computeSweep`. Starting from the two arrays `F` and `Phi`, we first remove any flat segments in `F` to avoid division by zero

```

inz      = true(size(F));
inz(2:end) = F(1:end-1)~=F(2:end);
F        = F(inz);
Phi      = Phi(inz);

```

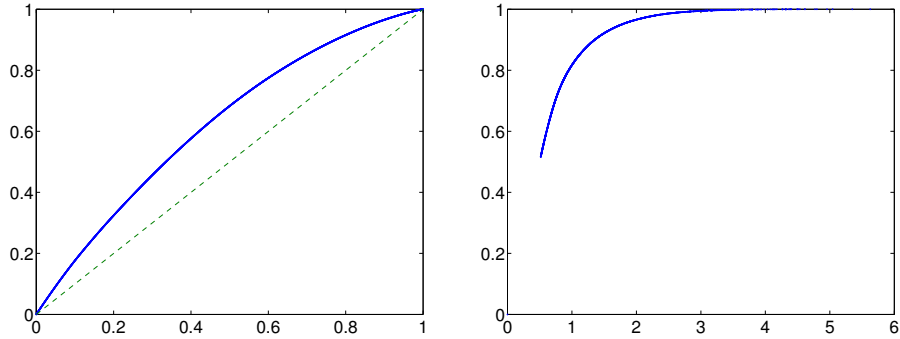


Fig. 9.5. F - Φ and sweep diagram for the simple case with two injectors and three producers, which has a Lorenz coefficient of 0.2475.

Then, dimensionless time and sweep efficiency can be computed as follows

```

tD = [0; diff(Phi)./diff(F)];
Ev = Phi + (1-F).*tD;
```

Figure 9.5 shows the F - Φ and the sweep diagram for the simple example with two injectors and three producers from Figure 9.1. For this particular setup, the Lorenz coefficient was approximately 0.25, which indicates that we can expect a mildly heterogeneous displacement with some flow paths that break through early and relatively small stagnant regions. From the diagram of the sweep efficiency, we see that 70% of the fluids in-place can be produced by injecting one pore volume and by injecting two additional pore volumes almost all the in-place fluid can be produced.

9.2.3 Summary of diagnostic curves and measures

Altogether, we have defined three different curves that can be derived from the residence/travel time. The curves shown in Figure 9.6 are visually intuitive and emphasize different characteristics of the displacement:

- The F - Φ curve is useful for assessing the overall level of displacement heterogeneity. The closer this curve is to a straight line, the better is the displacement.
- The fractional recovery curve emphasizes early-time breakthrough behavior and can have utility as a proxy for fractional recovery of the fluid in-place.
- The sweep efficiency highlights the behavior after breakthrough and has utility as a proxy for recovery factor.

The curves can be defined for the field as a total, or be associated with sector models, individual swept volumes, well-pair regions, and so on.

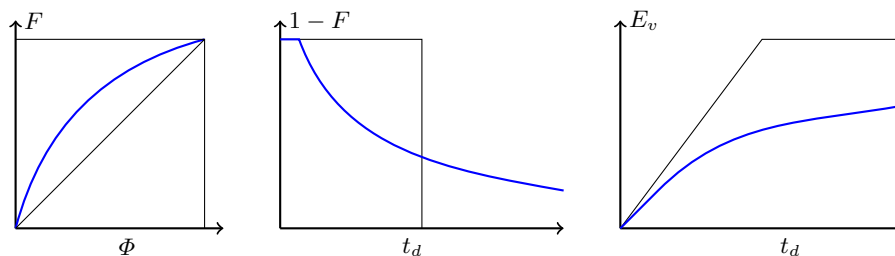


Fig. 9.6. The three basic flow diagnostics curves: F - Φ diagram, fractional recovery curve, and sweep efficiency. All quantities Φ , F , E_v , and t_D are dimensionless; t_D is given in terms of pore volumes injected (PVI).

Whereas visually intuitive information is useful in many workflows, others need measures defined in terms of real numbers. In our work, we have primarily used the Lorenz coefficient. However, dynamic analogues of other classical heterogeneity measures can be defined in a similar fashion. For instance, the dynamic Dykstra–Parsons’ coefficient is defined as

$$V_{DP} = \frac{(F')_{\Phi=0.5} - (F')_{\Phi=0.841}}{(F')_{\Phi=0.5}}, \quad (9.11)$$

where $\Phi = 0.5$ corresponds to the mean storage capacity, while $\Phi = 0.841$ is the mean value plus one standard deviation. Likewise, we can define the dynamic flow heterogeneity index,

$$F_{HI} = F(\Phi^*)/\Phi^*, \quad F'(\Phi^*) = 1, \quad (9.12)$$

Here, one can show that $(\frac{dF}{d\Phi})_i = \frac{\bar{\tau}}{\tau_i}$, where $\bar{\tau} = V/q = \sum V_i / \sum q_i$ is the average residence time for all the streamtubes. These heterogeneity measures have not yet been implemented in the `diagnostics` module.

COMPUTER EXERCISES:

51. Implement Dykstra–Parsons’ coefficient (9.11) and the flow heterogeneity index (9.12).
52. Use time-of-flight values defined per tracer region as discussed in Section 9.1.2 on page 244 to implement refined versions of the dynamic heterogeneity measures.
53. Compute heterogeneity measures for each well pair in the model with two injectors and three producers. (Original source code: `showDiagnostBasics`) Are there differences between the different regions?
54. Try to make the displacement shown in Figures 9.1 and 9.5 less heterogeneous by moving the wells and/or by changing the relative magnitude of the injection/production rates.

9.3 Case studies

The use of flow diagnostics is best explained through examples. In this section we therefore go through several cases and demonstrate various ways in which flow diagnostics can be used to enhance our understanding of flow patterns and volumetric connections, tell us how to change operational parameters such as well placement and well rates to improve recovery, etc.

9.3.1 Tarbert formation: volumetric connections

As our first example, we consider a subset of the SPE10 data set consisting of the top twenty layers of the Tarbert formation, see Section 3.5.3. We modify the original inverted five-spot well pattern by replacing the central injector by two injectors that are moved a short distance from the model center (see Figure 9.7), assume single-phase incompressible flow, and solve the corresponding flow problem. A complete description of the setup can be found in `showWellPairsSPE10.m` in the `book` module.

Given the geological model represented in terms of the structures `G` and `rock`, the wells represented by `W`, and the reservoir state by `rS`, we first compute the time-of-flight and tracer partitions:

```
D = computeTOFandTracer(rS, G, rock, 'wells', W);
```

This gives us the information we need to partition the volume into different drainage and sweep volumes. The simplest way to do this for the purpose of visualization is to use a majority vote over the injector and producer tracer partitions to determine the well that influences each cell the most as shown in Figure 9.8. The result of this majority vote is collected in `D.ppart` and `D.ipart`, respectively, and the essential commands to produce the two upper plots in Figure 9.8 are:

```
plotCellData(G,D.ipart, ...);
plotCellData(G,D.ppart,D.ppart>1, ...);
```

Since there are two injectors, we would expect to see two different sweep regions. However, in the figure there is also a small blue volume inside the triangular section bounded by I1, P1, and P2, which corresponds to an almost impermeable part of the reservoir that will not be swept by any of the injectors. The well pattern is symmetric and for a homogeneous medium we would therefore expect that the two pressure-controlled injectors would sweep symmetric volumes of equal size. For the highly heterogeneous Tarbert formation, however, the sweep regions are quite irregular and clearly not symmetric. Because of the two wells are completed in cells with very different permeability, the injection rate of I2 is approximately six times that of I1, and hence I2 will sweep a much larger region than I1. In particular, we see that I2 is the injector that contributes most to flooding the lower parts of the region near P3,

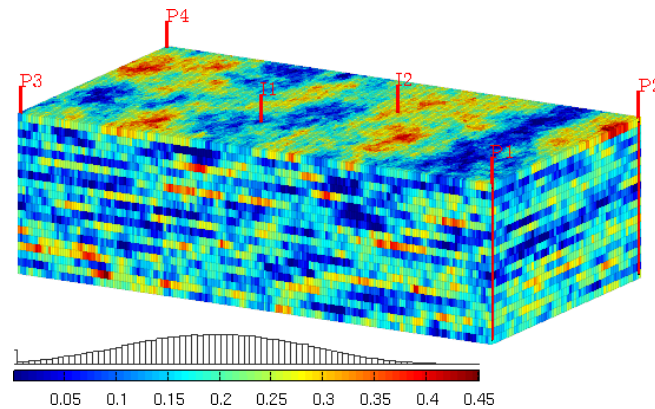


Fig. 9.7. Porosity and well positions for a model consisting of subset of the Tarbert formation in Model 2 from the 10th SPE Comparative Solution Project

even though I1 is located closer. Looking at the drainage and sweep regions in conjunction, it does not seem likely that I1 will contribute significantly to support the production from wells P1 and P2 unless we increase its rate.

When using a majority vote to determine drainage and sweep regions, we disregard the fact that there are regions that are influenced by more than one well. To visualize such regions of the reservoir, we can blend in a gray color in all cells in which more than one tracer has nonzero concentration as shown in the bottom plot of Figure 9.8. The plot is generated by the following call:

```
plotTracerBlend(G, D.ppart, max(D.ptracer, [], 2), ... );
```

Having established the injection and tracer partitions, we can identify well pairs and compute the pore volumes of the region associated with each pair:

```
WP = computeWellPairs(rS, G, rock, W, D);
pie(WP.vols, ones(size(WP.vols)));
legend(WP.pairs, 'location', 'Best');
```

To visualize the volumetric regions, we compute the tensor product of the injector and producer partitions and then compress the result to get a contiguous partition vector with a zero value signifying unswept regions:

```
p = compressPartition(D.ipart + D.ppart*max(D.ipart))-1;
plotCellData(G,p,p>0,'EdgeColor','k','EdgeAlpha',.05);
```

The result is shown in Figure 9.9, and confirms our previous observations of the relative importance of I1 and I2. Altogether, I1 contributes to sweep approximately 16% of the total pore volume, shown as the light red and the yellow regions in the 3D plot.

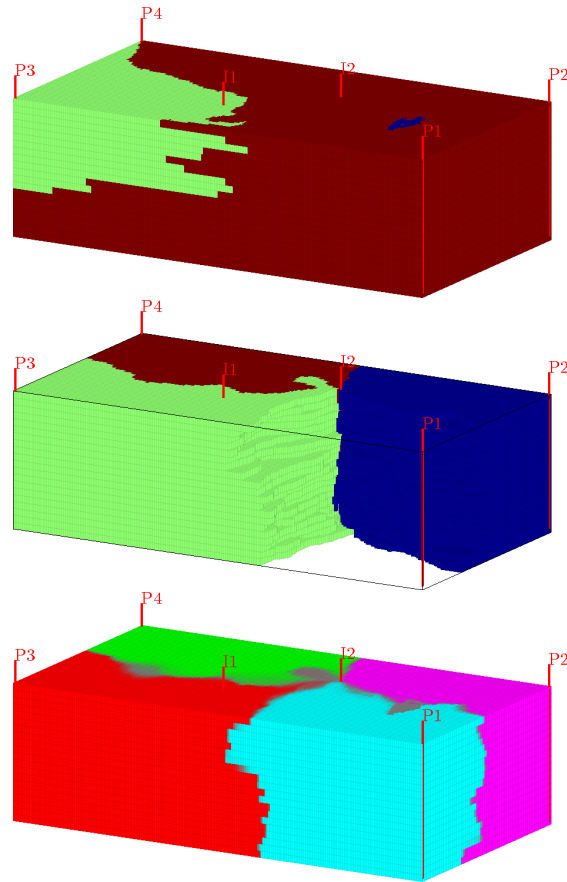


Fig. 9.8. Sweep (top) and drainage regions (middle) determined by a majority vote over injector and producer tracer partitions, respectively, for the Tarbert model. The bottom plot shows a refined tracer partition in which gray color signifies regions that are affected by multiple tracers.

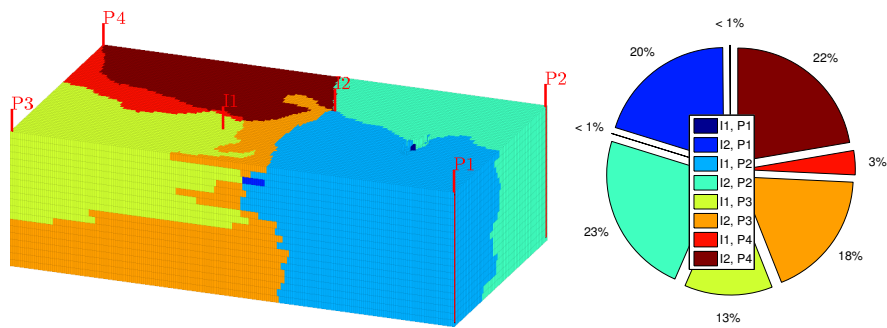


Fig. 9.9. Well-pair regions and associated fraction of the total pore volume for the upper twenty layers of the Tarbert formation.

It is also interesting to see how these volumetric connections affect the fluxes in and out of wells. To this end, we should look at the cumulative well-allocation factors, which are defined as the cumulative flux in/out of a well from bottom to top perforation of a vertical well, and from toe to heel for a deviated well. We start by computing the flux allocation manually for the two injectors (outflow fractions are given from well head and downward and hence need to be flipped):

```

for i=1:numel(D.inj)
    subplot(1,numel(D.inj),i); title(W(D.inj(i)).name);
    alloc = cumsum(flipud(WP.inj(i)).alloc,1);
    barh(flipud(WP.inj(i).z), alloc,'stacked'); axis tight
    lh = legend(W(D.prod).name,4);
    set(gca,'YDir','reverse');
end

```

Figure 9.10 shows the resulting bar plots of the cumulative allocation factors. These plots confirm and extend the understanding we have developed by studying volumetric connections: I1 will primarily push fluids towards P3. Some fluids are also pushed towards P4, and we also observe that there is almost no outflow in the top three perforations where the rock has low quality. Injection from I2, on the other hand, contributes to uphold the flux into all four producers. We also see that the overall flux is not well balanced. Producer P1 has significantly lower inflow than the P2 to P4. Alternatively, we can use the library functions `plotWellAllocationPanel(D, WP)` from the `diagnostics` module to compute and visualize the well-allocation factors for all the wells in the model, as shown in Figure 9.11.

Finally, to look more closely at the performance of the different completions along the well path, we can divide the completion intervals into bins and assign a corresponding set of pseudo-wells for which we recompute flow diagnostics. As an example, we split the completions of I1 into three bins and the completions of I2 into four bins.

```

[rSp,Wp] = expandWellCompletions(rS,W,[5, 3; 6, 4]);
Dp = computeTOfandTracer(rSp, G, rock, 'wells', Wp);

```

Figure 9.12 shows the majority-voted sweep regions for the four segments of I2; to better see the various sweep regions, the 3D plot is rotated 180 degrees compared with the other 3D plots of this model. To obtain the figure, we used the following key statements

```

plotCellData(G, Dp.ipart,(Dp.ipart>3) & (Dp.ipart<8),...);
WpP = computeWellPairs(rSp, G, rock, Wp, Dp);
avols = accumarray(WpP.pairIx(:,1),WpP.vols);
pie(avols(4:end));

```

Notice, in particular, that fluids injected in the lowest segment is the major contributor in almost half of the well's total sweep region.

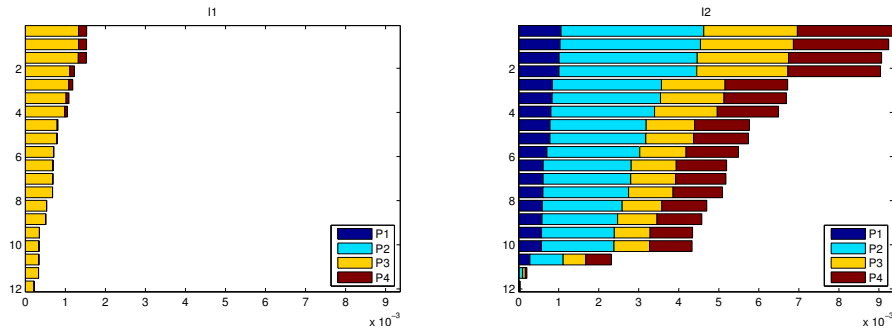


Fig. 9.10. Well-allocation factors for the two injectors of the Tarbert model.

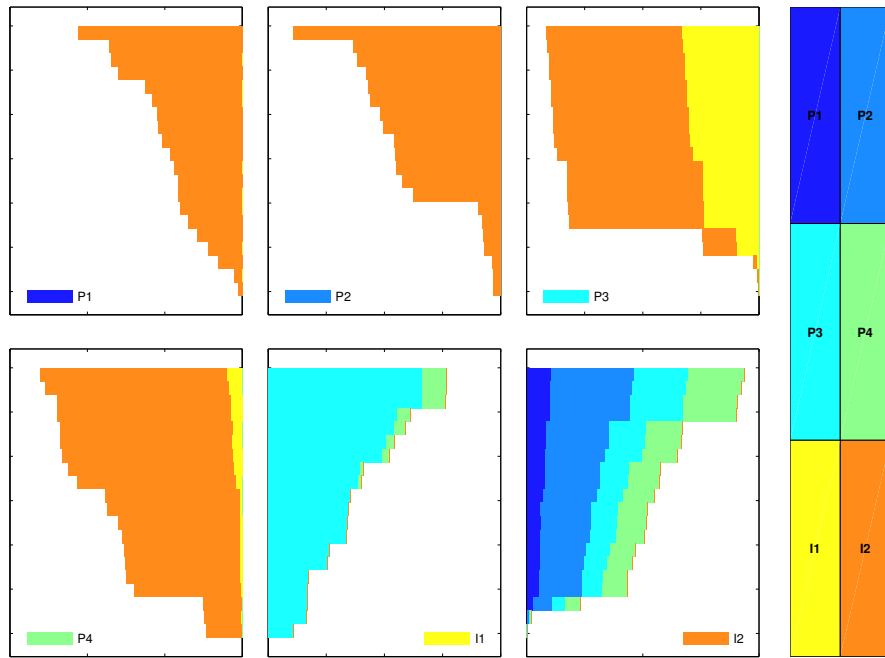


Fig. 9.11. Normalized well-allocation factors for all wells of the Tarbert model.

9.3.2 Layers of SPE10: heterogeneity and sweep improvement

In this example, we first compute the Lorenz coefficient for all layers of the SPE10 model subject to an inverted five-spot well pattern. We then pick one of the layers and show how we can balance the well allocation and improve the Lorenz coefficient and the areal sweep by moving some of the wells to regions with better sand quality.

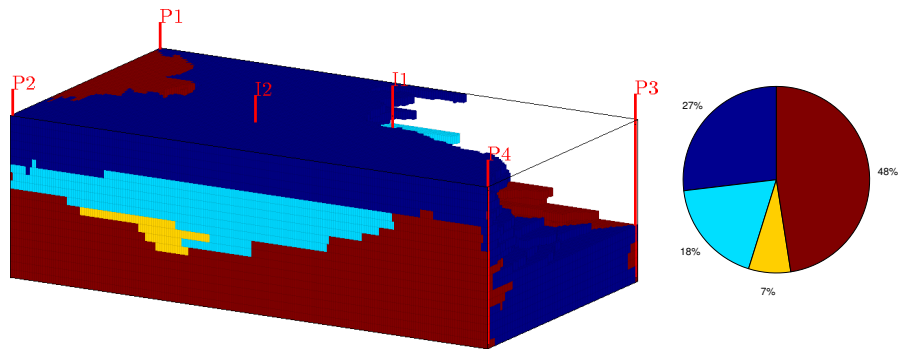


Fig. 9.12. Majority-voted sweep regions for I2 of the Tarbert case divided into four segments that each are completed in five layers of the model. (Notice that the view angle is rotate 180 degrees compared with Figure 9.8.) The pie chart shows the fraction of the total sweep region that can attributed to each segment of the well.

To compute Lorenz coefficient for all layers in the SPE10 model, we first define a suitable $60 \times 220 \times 1$ grid covering a rectangular area of $1200 \times 2200 \times 2$ ft³. Then, we loop over all the 85 layers using the following essential lines:

```

for n=1:85
    rock = SPE10_rock(1:cartDims(1),1:cartDims(2),n);
    rock.perm = convertFrom(rock.perm, milli*darcy);
    rock.poro = max(rock.poro, 1e-4);

    W = [];
    for w = 1:numel(wtype),
        W = verticalWell(..);
    end

    T = computeTrans(G, rock);
    rS = incompTPFA(initState(G, W, 0), G, T, fluid, 'wells', W);

    D      = computeTOFandTracer(rS, G, rock, 'wells', W, 'maxTOF', inf);
    [F,Phi] = computeFandPhi(poreVolume(G,rock), D.tof);
    Lc(n)  = computeLorenz(F,Phi);
end

```

Because the permeability changes for each layer, we need to recompute the transmissibility. Likewise, we regenerate the well objects to ensure correct well indices when updating the petrophysical data. Complete source code can be found in the script `computeLorenzSPE10` in the `book` module.

Figure 9.13 reports the Lorenz coefficients for all layers for a setup in which both the injector and the four producers are controlled by bottom-hole pressure. We relatively large dynamic heterogeneity and the variation among individual layers within the same formation is a result of our choice of well

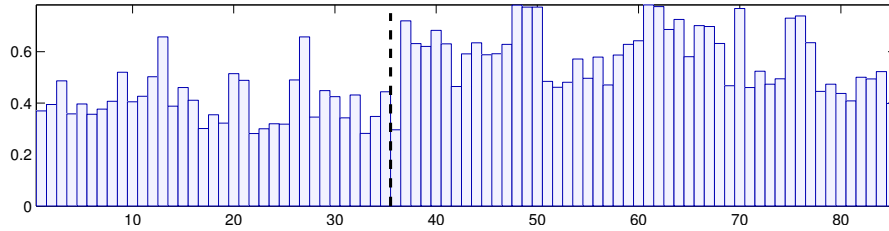


Fig. 9.13. Lorenz coefficient for each of the 85 horizontal layers of the SPE10 model subject to an inverted five-spot pattern with injector and producers controlled by bottom-hole pressure. The dashed line shows the border between the Tarbert and the Upper Ness layers.

controls. The actual injection and production rates achieved with pressure-controlled wells are very sensitive to each well being perforated in a region of good sand quality. Good sand quality is difficult to ensure when using fixed well positions, and hence pressure-controlled wells will generally accentuate heterogeneity effects. To see this, you should modify the script and rerun the case with equal rates in all the four producers.

Our somewhat haphazard placement of the wells is not what a good reservoir engineer would recommend, but serves well to illustrate our next point. Since the Lorenz coefficient generally is quite large, most of the cases would have suffered from early breakthrough if we were to use this initial well placement for multiphase fluid displacement. Let us therefore pick one of the layers and see if we can try to improve the Lorenz coefficient and hence also the sweep efficiency. Figure 9.14 shows the well allocation and the sand quality near the production wells for Layer 61, which is the layer giving the worst Lorenz coefficient. The flux allocation shows that we have a very unbalanced displacement pattern where producer P4 draws 94.5% of the flux from the injector and producers P1 and P2 together draw only 1.2%. This can be explained if by looking at the sand quality in our reservoir. Producer P1 is completed in a low-quality sand and will therefore achieve a low rate if all producers operate at the same bottom-hole pressure. Producers P2 and P3 are perforated in cells with better sand, but are both completely encapsulated in regions of low sand quality. On the other hand, producer P4 is connected to the injector through a relatively contiguous region of high-permeable sand. Likewise, the largely concave F - Φ diagram shown to the left in Figure 9.15 testifies that the displacement is strongly heterogeneous and hence be characterized by large differences in the residence time of different flow paths, or in other words, suffer from early breakthrough of the displacing fluid). Hence, we would need to large amounts of the displacing fluid to recover the hydrocarbons from the low-quality sand; this can be seen from the weakly concave sweep diagram to the right in Figure 9.15. Altogether, we should expect a very unfavorable volumetric sweep from this well placement.

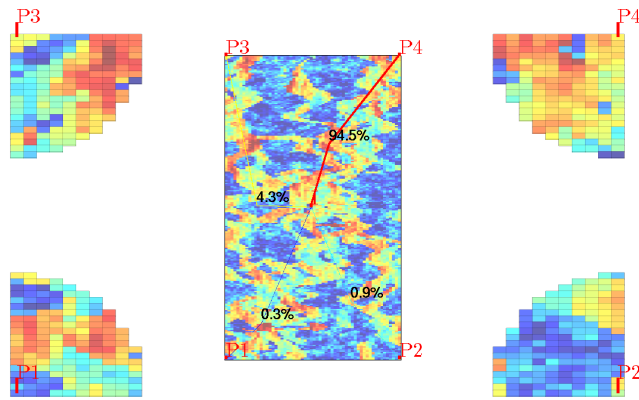


Fig. 9.14. Well configuration and flux allocation for the four well pairs with initial well configuration for Layer 61. (Red colors are good sands, while blue colors signify sands of low permeability and porosity.)

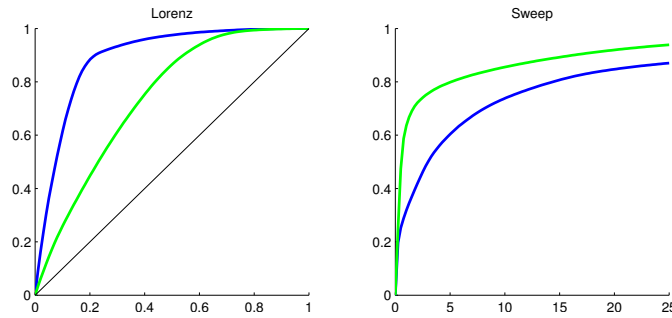


Fig. 9.15. $F-\Phi$ and sweep diagrams before (blue line) and after (green line) producers P1 to P3 have been moved to regions with better sand quality. Moving well reduces the Lorenz coefficient from 0.78 to 0.47.

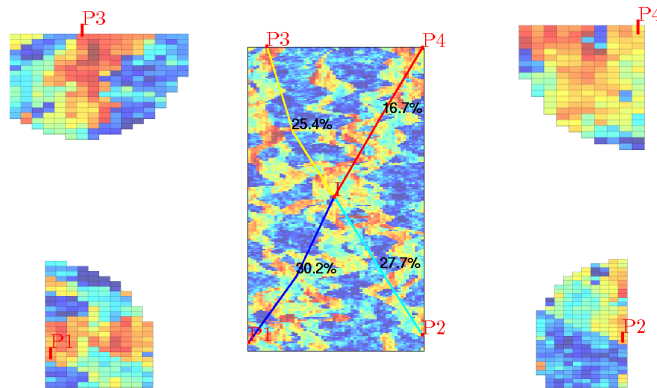


Fig. 9.16. Well configuration and flux allocation for the four well pairs after the producers P1 to P3 have been moved to regions with better sand quality.

Table 9.1. Volumetric flow rates in units 10^{-5} m³/s for each of the wells in Layer 61 of the SPE10 model.

Placement	P1	P2	P3	P4	I
Initial	-0.0007	-0.0020	-0.0102	-0.2219	0.2348
Improved	-0.0719	-0.0660	-0.0604	-0.0398	0.2381

To improve the displacement, we can try to move each of the producers to a better location; that is, we should look for cells in the vicinity of each well that have better sand quality (higher porosity and permeability) *and* are connected to the injector by more contiguous paths of good quality sands. Figure 9.16 shows the well allocation after we have made such a move of producers P1, P2, and P3. Producer P4 was already in a good location, so we do not move it. Compared with our previous setup, the well allocation is now much more balanced and which is also confirmed by the well rates reported in Table 9.1. (Notice also that the overall reservoir rate has increased slightly). In Figure 9.15, we see that the F - Φ diagram has become significantly less concave and, likewise, that the sweep diagram has become much more concave. This testifies that the variation in residence times associated with different flow paths is much smaller and we should expect a more efficient and less heterogeneous volumetric sweep.

These types of dynamic heterogeneity measures are generally easy to use as a guide when searching for optimal or improved well placement. Because of their low computational cost, the measures can be used as part of a manual, interactive search or combined with more rigorous mathematical optimization techniques. In the `diagnostics` module you can find examples that use flow diagnostics in combination with adjoint methods to determine optimal well locations and set optimal injection and production rates as discussed in more detail in [137].

COMPUTER EXERCISES:

55. Repeat the experiment using fixed rates for the producers (and possibly also for the injector). Can you explain the differences that you observe?
56. Use the interactive diagnostic tool introduced in the next section to manually adjust the bottom-hole pressures (or alternatively the production rates) to see if you can improve the sweep even further.
57. Can you devise an automated strategy that uses flow diagnostics to search for optimal five-spot patterns?
58. Cell-averaged time-of-flight values computed by a finite-volume scheme can be quite inaccurate when interpreted pointwise, particularly for highly heterogeneous media. To investigate this, pick one of the fluvial layers from SPE 10 and use the `pollock` routine from the `streamline` module to compute time-of-flight values on a 10×10 subsample inside a few selected cells. Alternatively, you can use the finite-volume method on a refined grid.

9.4 Interactive flow diagnostics tools

The examples you have encountered so far in the book have mostly been self contained in the sense that we have either discussed the code lines necessary for the example, or given reference to complete MRST scripts that can be run in batch or cell mode to produce the figures and numerical results discussed in the text. In this section, we will deviate slightly from this rule. While the ideas behind most flow diagnostics techniques are relatively simple to describe and their computation is straightforward to implement, the real strength of these techniques lies in their visual appeal and the ability for rapid user interaction. Together, MATLAB and MRST provide a wide variety of powerful visualization routines that can be used to visualize input parameters and simulation results. As you saw in the previous section, the `diagnostics` module supplies additional tools for enhanced visualization. However, using a script-based approach to visualization means that you each time need to write extra code lines to manually set color map and view angle or display various additional information such as legends, colorbars, wells, and figure titles, etc. These extra code lines have mostly been omitted in our discussion in the previous section, but if you go in and examine the accompanying scripts, you will see that a large fraction of the code lines focus on improving the visual appearance of plots. This code is repetitive and should ideally not be exposed to the user of flow diagnostics. More important, however, a script-based approach gives a static view of the data and offers limited capabilities for user interaction apart from zooming, rotating, and moving the displayed data sets. Likewise, a new script must be written and executed each time we want to look a new plot that combines various types of diagnostic data, e.g., to visualize time-of-flight or petrophysical values within a given tracer region, use time-of-flight to threshold the tracer regions, etc.

To simplify the user interface to flow diagnostics, we have integrates most of the flow-diagnostics capabilities into a graphical tool that enables you to interact more directly with your data set

```
interactiveDiagnostics(G, rock, W);
```

The script uses the standard two-point incompressible flow solver for a single-phase fluid with density 1000 kg/m^3 and viscosity 1 cP to compute a representative flow field, which is then fed to the function `computeTOFandTracer()` to compute the basic flow diagnostics quantities discussed above. Once the computation of basic flow diagnostic quantities is complete, the graphical user interface is launched, see Figure 9.17: This consists of a *plotting window* showing the reservoir model and a *control window* that contains a set workflow tabs and menus that enable you to use flow diagnostics to explore volumetric connections, flow paths, and dynamic heterogeneity measures. The control window has three different tabs. The 'region selection' tab is devoted to displaying the various kinds of volumetric regions discussed in Section 9.1.1. The 'plots' tab lets you compute F - Φ diagram, Lorenz coefficient, and the well-

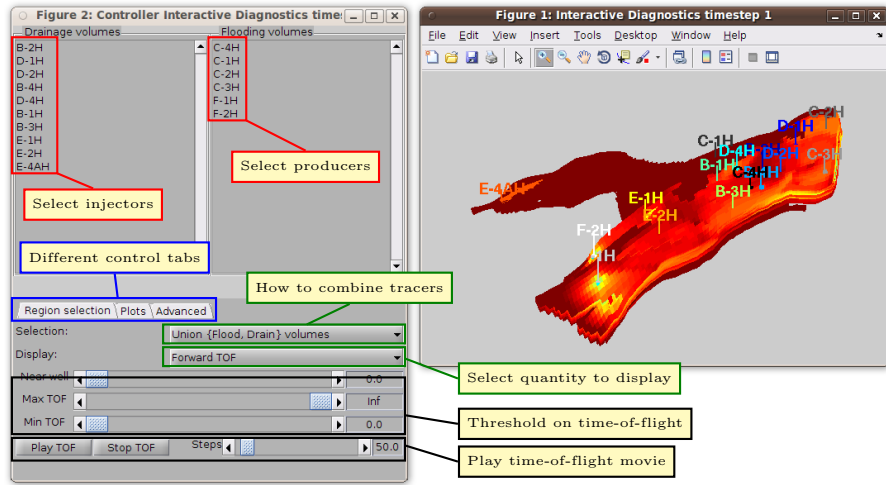


Fig. 9.17. The graphical user interface to flow diagnostics. The plotting window shows forward time-of-flight, which is the default value displayed upon startup. In the control window, we show the 'region selection' tab that lets you select which quantity to show in the plotting window, select which wells to include in the plot, specify how to combine tracer partitions to select volumetric regions, and as well as set maximum and minimum time-of-flight values to crop the volumetric regions.

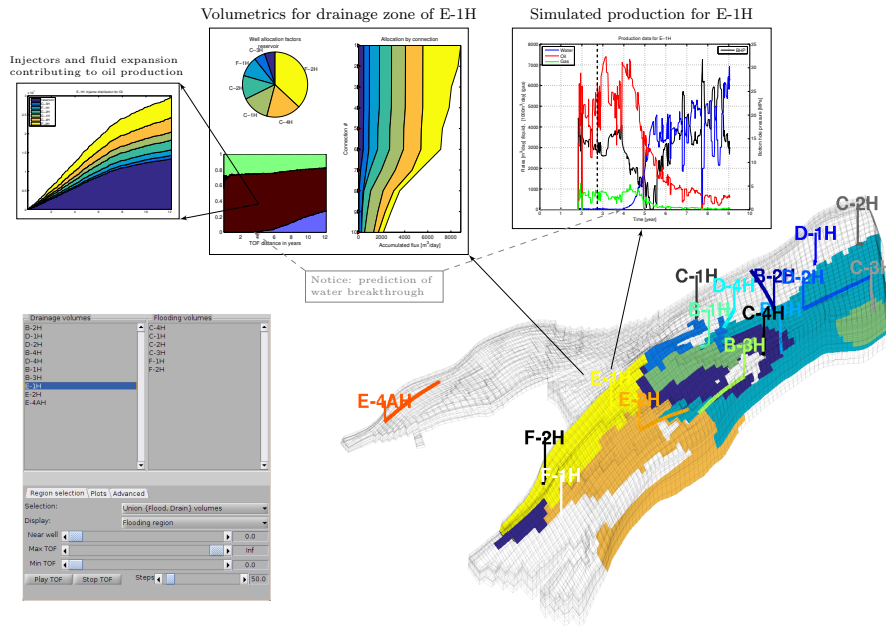


Fig. 9.18. Flow diagnostics used to post-process a three-phase, black-oil flow simulation of the Norne field.

allocation panels shown in Figure 9.11. From this tab, you can also bring up a dialog box that enables you to edit the well settings and recompute a new flow field and the resulting flow diagnostics (unless the parameter `'computeFlux'` is set to false). In the 'advanced' tab, you can control the appearance of the 3D plot by selecting whether to display grid lines, well-pair information, and well paths, set 3D lighting and transparency value, etc. This tab also allows you to export the current volumetric subset as a set of boolean cell indicators.

The regions to be displayed in the plotting window are specified by selecting a set of active wells and by choosing how the corresponding tracer partitions should be combined. That is, for a given set of 'active' wells, you can either display all cells that have nonzero injector or producer tracer, only those cells that have nonzero injector and producer tracer, only cells with nonzero producer tracer, or only cells with nonzero injector tracers. The select a set of active wells, you can either use the list of injectors and producers in the control window, or you can select an individual well by left-clicking on the well in the plotting window. In the latter case, the set of active wells will consist of the well you selected plus all other wells that this well is in communication with. Clicking on a well will also bring up a new window that displays a pie chart of the well allocation factors and a graph that displays cumulative allocation factors per connection. Figure 9.18 shows this type of visualization for a model where we also have access to the various time steps of a full multiphase simulation. In this case, we invoke the GUI by calling

```
interactiveDiagnostics(G, rock, W, 'state', state, 'computeFlux', false);
```

so that the fluxes used to compute time-of-flight and tracer partitions are extracted from the given reservoir state given in `state`. Left-click on producer E-1H, brings up a plot of the well allocation as well as a plot of the fluid distribution displayed as function of the backward time-of-flight from the well. To further investigate the flow mechanism, we can click on each fluid and get a plot of how the various injectors and fluid expansion in the reservoir contribute to push the given fluid toward the producer. In Figure 9.18 we have expanded the GUI by another function that enables us to plot the simulated well history of each well. The GUI also offers functionality to load additional cell-based data sets that can be displayed in the 3D plot:

```
interactiveDiagnostics(G, rock, W, celldata);
interactiveDiagnostics(G, rock, W, celldata, 'state', state);
```

The GUI also has more functionality for post-processing simulations with multiple time steps, but this is beyond the scope of the current presentation.

In the following we will use the interactive GUI to study a few reservoir models. This means, in particular, that the scripts that accompany the case studies in this section do not reproduce all figures directly as was the case for the script-based approach presented in the previous section. Instead, you will have to perform several manual actions specified in the scripts to reproduce some of the figures.

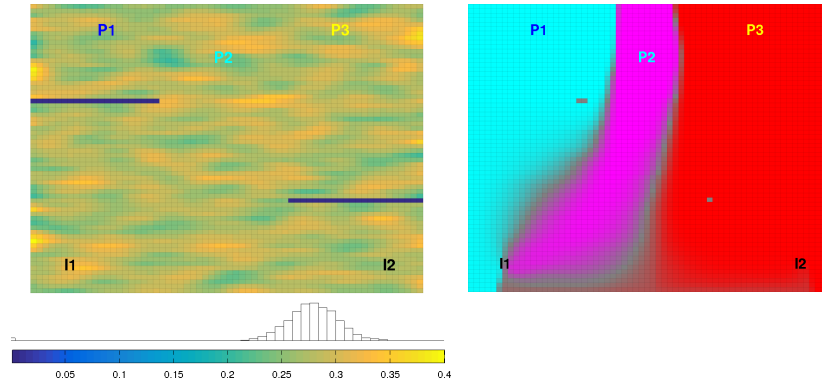


Fig. 9.19. A simple 2D reservoir with two injectors and three producers. The left plot shows porosity and the right plot the corresponding producer tracer partition.

9.4.1 Simple 2D example

As our first example, we will use a slightly modified version of the setup used from Figure 9.1, in which we have introduced two low-permeable zones that will play the role of sealing faults, moved the two injectors slightly to the south, and switched all wells from rate to pressure control. The resulting reservoir model is shown in Figure 9.19, whereas specific values for the well controls are found in Table 9.2 under the label 'base case'. In our previous setup, we had a relatively symmetric well pattern in which producers P1 and P3 were supported by injectors I1 and I2, respectively, while producer P2 was supported by both injectors. This symmetry is broken by the two sealing faults, and now injector I1 also provides a significant support for producer P3. This can be inferred from the plot of the producer tracer partition: the gray area between the magenta (P2) and red (P3) regions signifies a parts of the reservoir that are drained by both producers. Since there is a relatively large gray area southeast of I1, this injector will support both P2 and P3. There is also a gray area southwest of injector I2, but since this is less pronounced, we should expect that only a small portion of the inflow of P2 can be attributed to I2. To confirm this, you can load the model in the interactive viewer (see the script `interactiveSimple`), and click on the names for each individual producer to bring up a pie chart reporting the corresponding flux allocation.

Next, we let us try to figure out to what extent this is a good well pattern or not. We can start by looking at how a displacement front would propagate if the present flow field remains constant. If the displacement front travels with a unit speed relatively to the Darcy velocity given by the flux field, the region swept by the front at time t consists of all those cell for which $\tau_f \leq t$. Using the interactive GUI as shown in Figure 9.17, you can either show swept regions by specifying threshold values manually, or use the 'Play TOF' button to play a 'movie' of how the displacement front advances through the reservoir.

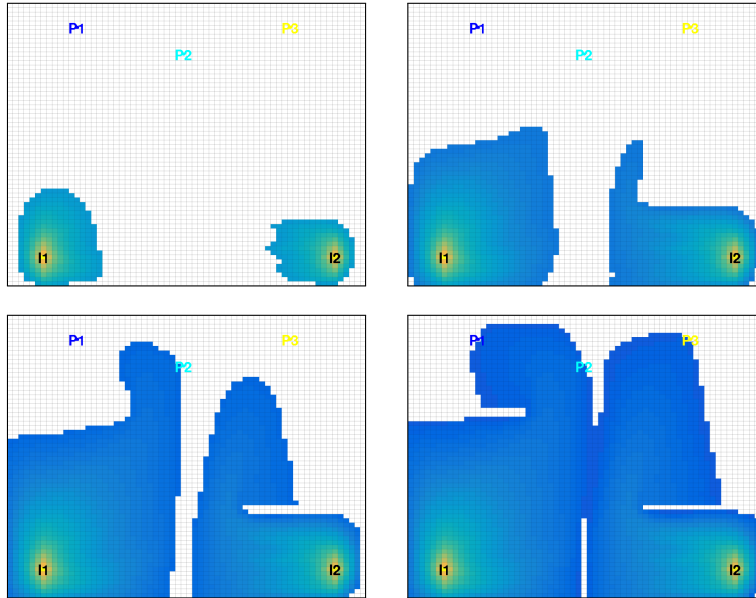


Fig. 9.20. Evolution of an imaginary displacement front illustrated by thresholding time-of-flight inside the sweep regions for the base case.

Figure 9.20 shows four snapshots of such an advancing front. We notice, in particular, how the sealing fault to the northwest of the reservoir impedes the northbound propagation of the I1 displacement front and leads to early breakthrough in P2. We also see that there is a relatively large region that is still unswept after the two displacement fronts have broken through in all three producers.

As a more direct alternative to studying snapshots of an imaginary displacement front, we can plot the residence time, i.e., the sum of the forward and backward time-of-flight, as shown in the upper-left plot in Figure 9.21. Here, we have used a nonlinear gray-map to more clearly distinguish high-flow zones (dark gray) from stagnant regions (white) and other regions of low flow (light gray). In the figure, we see that wells I1 and P2 are connected by a high-flow region, which explains the early breakthrough we observed in Figure 9.20. The existence of high-flow regions can also be seen from the $F-\Phi$ diagram and the Lorenz coefficient of 0.273.

The interactive diagnostic tool has functionality that lets you modify the well controls and if needed, add new wells or remove existing ones. We will now use this functionality to try to improve the volumetric sweep of the reservoir, much in the same way as we did manually for a layer of SPE 10 in Section 9.3.2. We start by reducing the high flow rate in the region influenced by I1 and P2. That is, we increase the pressure in P2 to, say, 130 bar to decrease the inter-well pressure drop. The resulting setup is referred to as 'Case 1', and gives

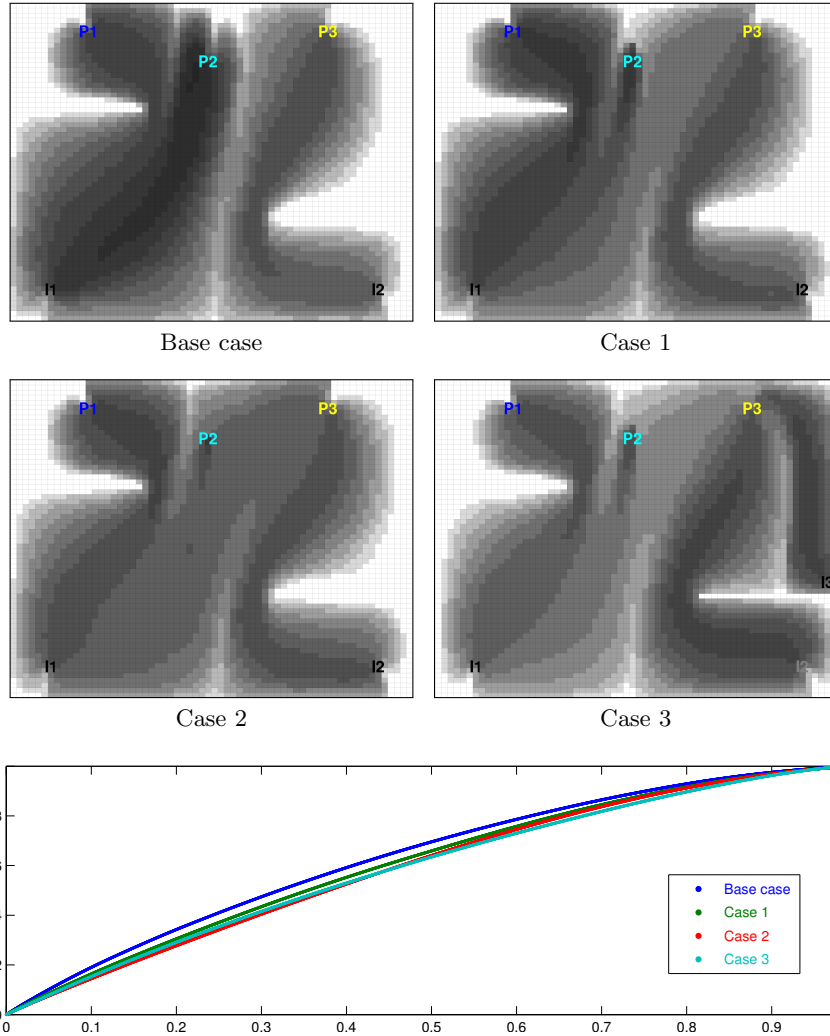


Fig. 9.21. In Cases 1 and 2, well controls have been manually adjusted from that of the base case (see Table 9.2) to equilibrate total travel time throughout the reservoir. Case 3 includes infill drilling of an additional injector. The bottom plot shows the corresponding $F-\Phi$ curves.

Table 9.2. Well controls given in terms of bottom-hole pressure [bar] for a simple 2D reservoir with five initial wells (I1, I2, P1, P2, P3) and one infill well (I3).

	I1	I2	I3	P1	P2	P3	Lorenz
Base case	200	200	—	100	100	100	0.2730
Case 1	200	200	—	100	130	80	0.2234
Case 2	200	200	—	100	130	80	0.1934
Case 3	200	220	140	100	130	80	0.1887

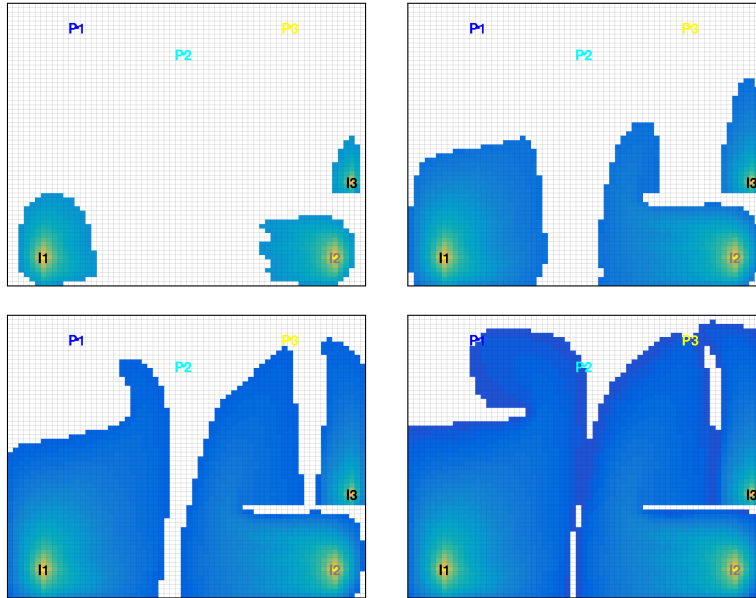


Fig. 9.22. Evolution of an imaginary displacement front illustrated by thresholding time-of-flight inside the sweep regions for Case 3.

more equilibrated flow paths, as can be seen from the Lorenz coefficient and the upper-right plot in Figure 9.21. In Case 2, we have decreased the pressure in P3 to 80 bar to increase the flow in the I2–P3 region. As a result of these two adjustments to the well pressures, we have reduced the stagnant region north of P2 and also diminished the clear flow-divide that extended from the south of the reservoir to the region between P2 and P3. To also sweep the large unswept region east of P3, we can use infill drilling to introduce a new well in the southeast of this region, just north of the sealing fault. Since the new well is quite close to the existing producer, we should assign a relatively low pressure to avoid introducing too high flow rates. In Case 3, we have chosen to let the well operate at 140 bar and at the same time we have increased the pressure in I2 to 220 bar. Figure 9.22 shows snapshots of the advancing front at the same instances in time as was used in Figure 9.20 for the base case. Altogether, the well configuration of Case 3 gives a significant increase in the swept areas and reduces the Lorenz coefficient to 0.189. It is therefore reasonable to expect that this configuration would give a better displacement if the setups were rerun with a multiphase simulator.

A more detailed description of how you should use the interactive GUI to perform the above experiments can be found in the `interactiveSimple.m` script of the `book` module. I encourage you to use the script to familiarize yourself with interactive flow diagnostics. Are you able to make further improvements?

9.4.2 SAIGUP: flow patterns and volumetric connections

The previous example was highly simplified and chosen mainly to illustrate the possibilities that lie in the interactive use of flow diagnostics. In this example, we revisit the SAIGUP case study from Section 7.4.4 on page 210 and take a closer look at the volumetric connection in this shallow-marine reservoir. We start by re-running this case study to set up the simulation model and compute a flow field:

```
saigupWithWells; close all
clearvars -except G rock W state
```

Henceforth, we only need the geological model, the description of the wells, and the reservoir state and have hence cleared all other variables and closed all plots produced by the script. With this, we are ready to launch the interactive flow diagnostics session. Since we already have computed a reservoir state, we can pass this on to the interactive GUI and hence use it in pure post-processing mode:

```
interactiveDiagnostics(G, rock, W, 'state', state, 'computeFlux', false);
```

in which we are not able to edit any well definitions and recompute fluxes.

In Figure 7.11 on page 211 we saw that although the injectors and producers are completed in all the twenty grid layers of the model, there is almost no flow in the bottom half of the reservoir. A more careful inspection shows that there is almost no flow in the upper layers in most of the reservoir either. This is a result of the fact that the best sand quality is found in the upper-middle layers of the reservoir, as shown in Figure 9.23, which compares the permeability in the full model with the permeability in cells having a residence time less than one hundred years. Because each injector is controlled by a total fluid rate, large fluid volumes will be injected in completions that are connected to good quality sand, while almost no fluid is injected into zones with low permeability and porosity. This can be seen in Figure 9.24, which shows overall and cumulative well-allocation factors for four of the injectors. Injectors I3 and I4 are completed in the southern part of the reservoir, and here low-quality sand in the bottom half of the reservoir leads to almost negligible injection rates in completions 11 to 20. In a real depletion plan, the injectors would probably not have been completed in the lower part of the sand column. Injector I5 located to the west in the reservoir is completed in a column with low permeability in the top four and the bottom layer, high permeability in Layers 6 to 9, and intermediate permeability in the remaining layers. Hence, almost no volume is injected through the top four completions, which hence are redundant. Finally, injector I6 is completed in a column with poor sand quality in the top three layers, high permeability in Layers 4 to 9, and intermediate permeability in the remaining layers.

Figure 9.24 also shows the flux allocation for all well pairs in the reservoir. In the plot, each curved line corresponds to a connection between an injector

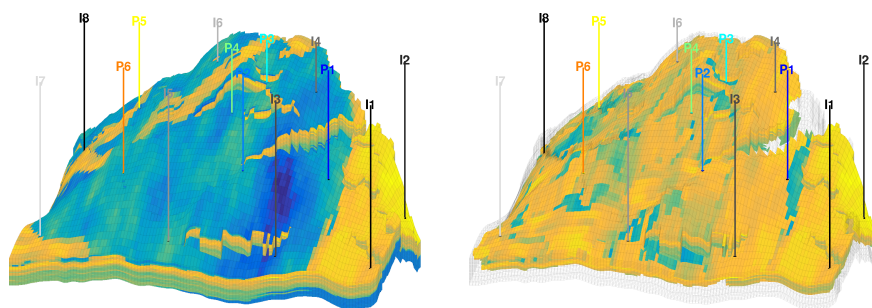


Fig. 9.23. Horizontal permeability ($\log_{10} K_x$) for the SAIGUP model. The left plot shows the full permeability field, while the right plot only shows the permeability in cells that have a total residence time less than 100 years. (The reservoir is plotted so that the north-south axis goes from left to right in the figure.)

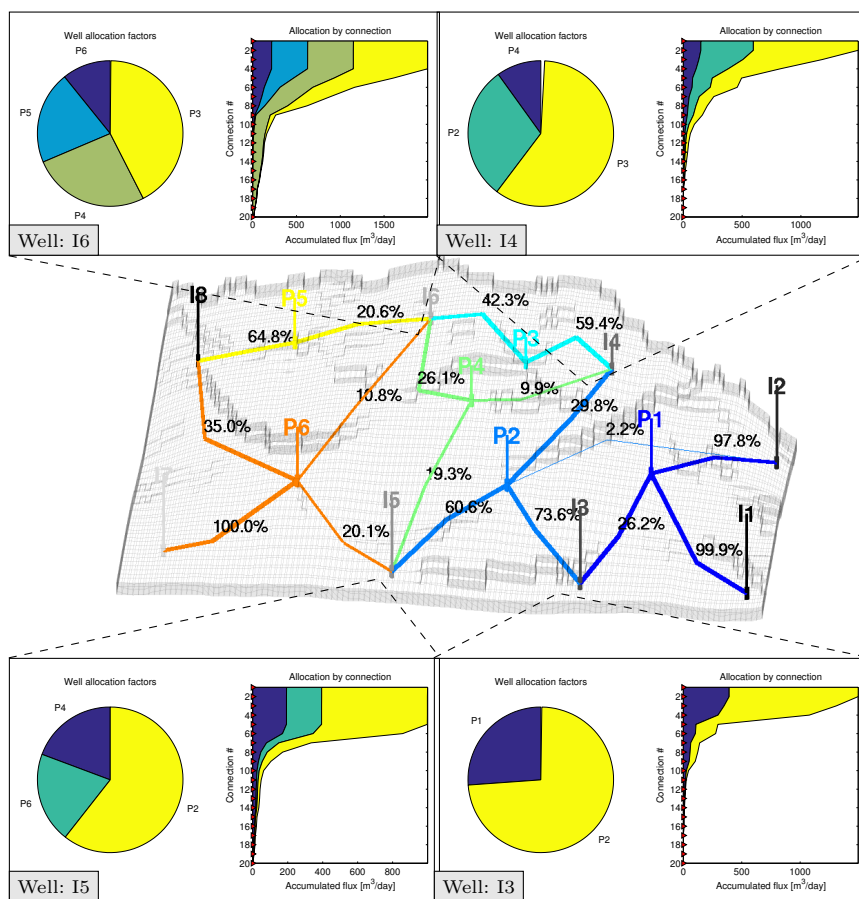


Fig. 9.24. Flux allocation for all well pairs of the SAIGUP model and well-allocation factors for injectors I3, I4, I5 and I6.

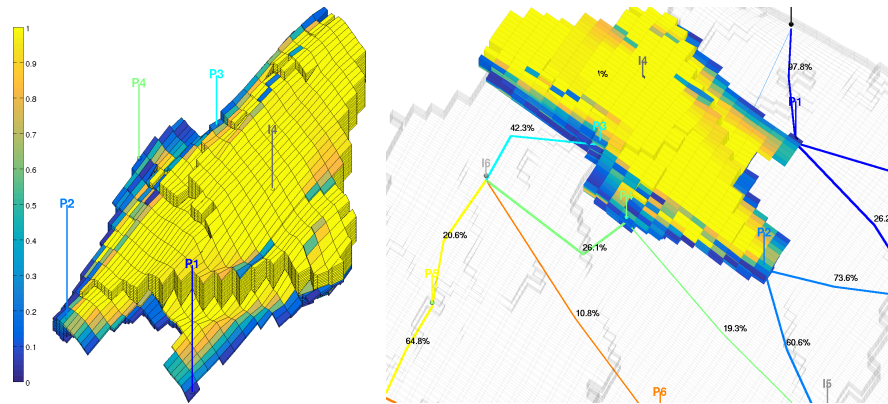


Fig. 9.25. Plot of the injector tracer region for well I4.

and a producer, where the color of the line signifies the producer and the percentage signifies the fraction of the total flux from each injector that goes to the different producers. The connections have been truncated so that only pairs that correspond to at least 1% of the flux are shown in the figure; which explains why not all the fractions sum up to unity. Let us take injector I4 as an example. Figure 9.25 shows two plots of the tracer region for this injector. From the well-allocation plots, we have already seen that I4 is connected to producers P2 to P4; (almost) all the well completions lie inside of the tracer of I4. Producer P1, on the other hand, is only completed in a single cell inside the tracer region, and this cell is in the top layer of the reservoir where the sand quality is very poor. It is therefore not clear whether P1 is actually connected to I4 or if this weak connection is a result of inaccuracies in the tracer computation. Since we only use a first-order discretization, the tracer fields will generally contain a significant amount of numerical smearing near flow divides, which here is signified by blue-green colors.

COMPUTER EXERCISES:

59. Change all the injectors to operate at a fixed bottom-hole pressure of 300 bar. Does this significantly change the flow pattern in the reservoir? Which configuration do you think is best?
60. Use the flow diagnostic tool to determine well completions in the SAIGUP model that have insignificant flow rate, eliminate these well completions, and rerun the model. Are there any apparent changes in the flux allocation and volumetric connections?
61. Consider the model given in `makeAnticlineModel.m`. Can you use flow diagnostics to suggest a better well configuration?

Upscaling Petrophysical Properties

As you have seen previously in the book, porous rock formations are typically heterogeneous at a large variety of length scales, from the micrometer scale of pore channels to the kilometer scale of petroleum reservoirs or even larger scales for aquifer systems and sedimentary basins. Describing all flow processes pertinent to hydrocarbon production or CO₂ extraction with a single model is therefore not possible. In Section 3.3 we introduced you to the concept of representative elementary volumes and mentioned various types of models that can be used for flow studies, including: flow in core samples (cm scale), bed models (meter scale), sector models, and field models (km scale). These models must be calibrated against static and dynamic data of very different spatial (and temporal) resolution: thin sections, core samples, well logs, geological outcrops, seismic surveys, well tests, production data, core flooding and other laboratory experiments, etc.

For full sized reservoirs the traditional approach has been to model geological structures with a geological model, and fluid flow with a coarser simulation model. Geological models are produced to represent the heterogeneity of the reservoir and possibly incorporate a measure of inherent uncertainty. Pore, core, and bed models are mainly designed to give input to the geological characterization and to derive flow parameters for simulation models. The process of making a geological model is generally strongly under-determined. It is therefore customary, in particular on the reservoir scale, to use *geostatistical* methods to generate plausible distributions of petrophysical properties as discussed briefly in Section 3.5. In recent years, process models that seek to mimic deposition and subsequent structural changes have also gained a lot in popularity since they tend to produce less artifacts in the geo-cellular models. Heterogeneity and correlations in petrophysical properties depend strongly on the patterns in the sedimentary deposits and flow patterns tend to be strongly affected by details in the structural architecture of the reservoir. There is therefore a general trend to build complex, high-resolution models for geological characterization to represent small-scale geological structures. Likewise, large ensembles of equiprobable models are generated to systematically

quantify model uncertainty. While high-resolution models can describe a wide variety of geological structures, there are also many structures on a finer scale than the resolution of the geological model that are thought to be important to understand the reservoir. Therefore, it is common to develop hierarchies of models that cover a wide range of physical scales to systematically propagate the effects of small-scale geological variations observed in core samples up to the reservoir scale.

On the other hand, high-resolution geological used for reservoir characterization tend to contain more volumetric cells than contemporary simulators can handle without having to resort to massively parallel high-performance computing. As a result, flow simulations are usually performed using models that contain less details than those used for geological characterization. And even if you had all the computational power you needed, there are several arguments why you still should perform simulations on coarser models. First of all, one can argue that high-resolution models contain more details than what is justified by the available data. Second, in many modeling workflows the available computational power should be spent running multiple model realizations to span the range of plausible outcomes rather than on obtaining high numerical resolution for few highly uncertain predictions. Third, because coarser models contain fewer parameters, they are simpler to calibrate to observed reservoir responses (pressure tests and production data). Finally, a coarser model may be sufficient to predict flow patterns and reservoir responses with the accuracy needed to make a certain business decision. It is perhaps tempting to believe that with future increases in computing power, one will soon be able to close the gap in resolution between models used for reservoir characterization and models used for flow simulation. The development so far, indicates that such an idea is wrong. The trend is rather that increases in computational power enable geologists and reservoir engineers to build larger and more complex models at a pace that outperforms the improvement in simulation capabilities.

For all the reasons above, there is a strong need for mathematical and numerical techniques that can be used to communicate parameters and properties between models of different spatial resolution. And – this need will persist, and maybe even grow stronger, in the foreseeable future.

Upscaling (or homogenization) refers to the process of propagating properties and parameters from a model of *high spatial resolution* to a model of *lower spatial resolution*. In this process, *heterogeneous regions* in a reservoir model are replaced by *homogeneous regions* to make up a coarser model of the same reservoir. Or, in the words of Chapter 5 on grid coarsening, upscaling is the process in which petrophysical properties in the cells that make up a coarse block are averaged into a single effective value for each coarse block, see Figure 10.1. The effective properties of the new homogeneous regions are defined so that they preserve the effects of small-scale variations in an averaged sense. How this averaging should be performed depends on the type of property to be upscaled. One distinguishes between *additive properties* that

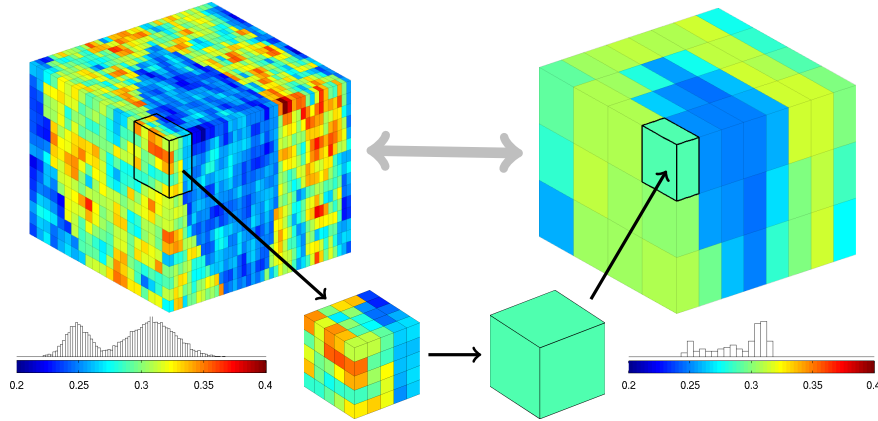


Fig. 10.1. Upscaling of petrophysical properties, here represented by porosity.

can be upscaled using simple volumetric averaging and *nonadditive properties*, for which correct averaging methods only exist in special cases and the best one can hope for in the general case is to compute accurate approximations.

Downscaling methods are used when propagating properties and parameters from a model with *low spatial resolution* to a model having *higher spatial resolution*. One can, for instance, be interested in refining coarse-scale modifications in petrophysical properties obtained during a history match on a simulation model to update the underlying geomodel. In this process, the aim is to preserve both the coarse-scale trends and the fine-scale heterogeneity structures.

10.1 Upscaling for reservoir simulation

The process of upscaling petrophysical parameters leads to many fundamental questions. For instance, do the partial differential equations that make up the flow model on the coarse scale take the same form as the equations modeling flow at the subgrid scale? And if so, how do we honor the fine-scale heterogeneities at the subgrid level. Even though upscaling has been a standard procedure in reservoir simulation for more than four decades, nobody has answered these questions rigorously, except for cases with special heterogeneous formations such as periodic or stratified media.

Homogenization is a rigorous mathematical theory for asymptotic analysis of periodic structures, see [28, 93, 85]. A relevant result states that for a periodic medium with permeability $K(\frac{x}{\epsilon})$, there exists a constant symmetric and positive-definite tensor K_0 such that the solutions p_ϵ and $v_\epsilon = -K(\frac{x}{\epsilon})\nabla p_\epsilon$ to the following elliptic problem

$$-\nabla \cdot K\left(\frac{x}{\epsilon}\right)\nabla p_\epsilon = q \quad (10.1)$$

converge uniformly as $\varepsilon \rightarrow 0$ to the corresponding solutions of a homogenized equation

$$-\nabla \cdot \mathbf{K}_0 \nabla p_0 = q. \quad (10.2)$$

This means that if we assume that the region we seek to compute an effective property for is a cell in an infinite periodic medium, then homogenization theory can be used to derive homogenized tensors for the region. The main advantage of this approach is that it provides mathematical methods to prove existence and uniqueness of the solution, and also verifies that the governing equation at the macroscopic level take the same form as the elliptic equation that governs porous media flow at the level of the representative elementary volumes (REVs). However, whether homogenization can be used for practical simulations is more debatable, in particular since natural rocks very seldom are periodic.

As you will see shortly, the most basic upscaling techniques rely on some kind of local averaging procedure in which effective properties in each grid block are calculated solely from properties within the grid block. As such, these averaging procedures do not consider coupling beyond the local domain, which in turn implies that the upscaling methods fail to account for the effect of long-range correlation and large-scale flow patterns in the reservoir unless these can be represented correctly by the forces that drive flow inside the local domain. Because different flow patterns may call for different upscaling procedures, it is generally acknowledged that global effects must also be taken into consideration to obtain robust coarse-scale simulation models.

Upscaling must also be seen in close connection with gridding and coarsening methods, as discussed in Chapters 4 and 5. Even though these questions have already been answered when making the fine-scale model, you should consider what kind of grid you want to use to represent the porous medium on the coarse scale, what resolution you need, and how you should orient your coarse blocks. To make the simulation models as accurate and robust as possible, the grid should be designed so that grid blocks capture heterogeneities on the scale of the block. This often implies that you may need significantly more blocks if you use a regular grid than if you use an unstructured polyhedral grid. You may also want to use different coarsening factors in zones of high and low flow, near and far away from wells and fluid contacts, etc. The importance of designing a good coarse grid should not be underestimated, but gridding in itself will not be discussed any further herein. Henceforth, we will instead tacitly assume that a suitable coarse grid is available and focus on upscaling techniques.

The literature on upscaling techniques is extensive, ranging from simple averaging techniques, e.g., [95], via flow-based methods that rely on local flow problems [26, 59] to more comprehensive global [144, 84] and local-global [41, 42, 73] methods. Some attempts have been made to analyze the upscaling process, e.g., [21, 189], but so far there is generally no theory or framework for assessing the quality of an upscaling technique. In fact, upscaling tech-

niques are seldom rigorously quantified with mathematical error estimates. Instead, the quality of upscaling techniques is usually assessed by comparing upscaled production characteristics with those obtained from a reference solution computed on an underlying fine grid.

In the following, we will only discuss the basic principles and try to show you how you can implement relatively simple upscaling methods and explain why some methods may work well for some flow scenarios and not for others. If you are interested in a comprehensive overview, you should consult one of the many review papers devoted to this topic, e.g., [48, 185, 21, 164, 69, 60, 61]. We start by a brief discussion of how to upscale porosity and other additive properties, before we move on to discuss upscaling permeability effects, which is the primary example of a nonadditive property. Because of the way Darcy's law has been extended to from single-phase to multiphase flow, it is common to distinguish the upscaling of absolute permeability K , which is associated with single-phase flow, and relative permeability $k_{r\alpha}$, which is the multiphase factor that absolute permeability must be multiplied with to get the effective permeability experienced by one fluid in the presence of another. Upscaling of absolute permeability is therefore often called *single-phase upscaling*, whereas upscaling of relative permeability is referred to as *multiphase upscaling*. The main parts of this chapter is devoted to permeability upscaling and to upscaling of the corresponding transmissibilities that account for permeability effects in finite-volume discretizations. As in the rest of the book, our discussion will to a large extent be driven by examples, for which complete codes can be found in the `upscaling` subdirectory of the `book` module of MRST.

10.2 Upscaling additive properties

Porosity is the simplest example of an additive property and can be upscaled through a simple volumetric average. If Ω denotes the region we want to average over, the averaged porosity value is given as

$$\phi^* = \frac{1}{\Omega} \int_{\Omega} \phi(\vec{x}) d\vec{x}. \quad (10.3)$$

Implementing the computation of this volumetric average can be a bit tricky if the coarse blocks and the fine cells are not matching. In MRST, however, we always assume that the coarse grid is given as a partition of the fine grid, as explained in Chapter 5. If \mathbf{q} denotes the vector of integers describing the coarse partition, upscaling porosity amounts to a single statement

```
crock.poro = accumarray(q,rock.poro.*C.cells.volumes)./ ...
               max(accumarray(q,G.cells.volumes),eps);
```

Here we have used `max(..,eps)` to safeguard against division by zero in the unlikely case your grid contains blocks with zero volume or your partition

vector is not contiguous. Weighting by volume is not necessary for grids with uniform cell sizes. Similar statements were used to go from the fine-scale model on the left side of Figure 10.1 to the coarse-scale model shown on the right. Complete source code is found in the script called `illustrateUpscaling.m`. Flux densities are upscaled in the same way, with cell volumes replaced by face areas.

Other additive (or volumetric) properties like net-to-gross, saturations and concentrations can be upscaled almost in the same way, except that one now should replace the bulk average in (10.3) by a *weighted* average. If n denotes net-to-gross, the correct average would be to weight with porosity, so that

$$n^* = \left[\int_{\Omega} \phi(\vec{x}) d\vec{x} \right]^{-1} \int_{\Omega} \phi(\vec{x}) n(\vec{x}) d\vec{x}. \quad (10.4)$$

and likewise for saturations. In MRST, we can compute this upscaling as follows

```
pv = rock.poro.*G.cells.volumes;
N = accumarray(q,pv.*n) ./ max(accumarray(q,pv),eps);
```

To verify that this is the correct average, we simply compute

$$\begin{aligned} \phi^* n^* &= \left[\frac{1}{\Omega} \int_{\Omega} \phi(\vec{x}) d\vec{x} \right] \left[\int_{\Omega} \phi(\vec{x}) d\vec{x} \right]^{-1} \int_{\Omega} \phi(\vec{x}) n(\vec{x}) d\vec{x} \\ &= \frac{1}{\Omega} \int_{\Omega} \phi(\vec{x}) n(\vec{x}) d\vec{x} = (\phi n)^*. \end{aligned}$$

Using the same argument, one can easily argue that concentrations should be weighted with saturations, and so on. Rock type (or flow unit), on the other hand, is not an additive property, even though it is sometimes treated almost as if it was by applying a majority vote to identify the rock type that occupies the largest volume fraction of a block. Such a simple approach is generally not robust [192] and should generally be avoided.

To get more acquainted with upscaling of additive quantities, we recommend that you try to do the following computer exercises.

COMPUTER EXERCISES:

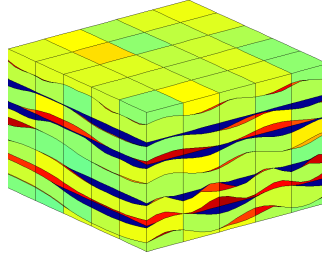
62. Construct a $8 \times 24 \times 5$ coarse partition of the SAIGUP model and upscale the additive rock properties. Verify your upscaling by computing

```
pv = accumarray(CG.partition, poreVolume(G,rock));
max(abs(pv - poreVolume(CG, crock)))
```

How would you make a coarse grid that represents the porosity better? To measure the quality of a given approximation, you can for instance use the following error measure:

```
err3 = sum(abs(rock.poro - crock3.poro(CG3.partition)))/...
      sum(rock.poro)*100;
```

63. The file `mortarTestModel` from the `BedModels1` data set describes a sedimentary bed that consists of three different facies. Construct a coarse model that has 5×5 blocks in the lateral direction and as many blocks in the vertical direction as required to preserve distinct facies layers, as shown in the plot below.



Upscale the porosity of the model. Do you think the resulting coarse grid is suitable for flow simulations? (Hint: Check the guidelines from Section 5.4.)

10.3 Upscaling absolute permeability

To study upscaling of absolute permeability, it is sufficient to consider single-phase flow in the form of a variable-coefficient, Poisson equation

$$\nabla \cdot \mathbf{K} \nabla p = 0. \quad (10.5)$$

Even with such a simple equation, the choice of what is the best method to average absolute permeability generally depends on a complex interplay between the local permeability distribution and the characteristic flow directions. In certain special cases, one can develop simple methods that average permeability correctly, but in the general case, all one can do is to develop computational methods that approximate the true effective permeability of the upscaled region. How accurate a given approximation is, will depend on the coarse grid, the specific upscaling method, the purpose for which the upscaled values are to be used, and the complexity of the fine-scale permeability distribution.

Most techniques for upscaling absolute permeability seek an averaged tensor \mathbf{K}^* that reproduces the same total flow through each homogeneous region as one would obtain if the single-pressure equation (10.5) was solved with the full fine-scale heterogeneity. In other words, if Ω is the homogeneous region to which we wish to assign an effective property \mathbf{K}^* , this property should fulfill

$$\int_{\Omega} \mathbf{K}(\vec{x}) \nabla p \, d\vec{x} = \mathbf{K}^* \int_{\Omega} \nabla p \, d\vec{x}. \quad (10.6)$$

This equation states that the net flow rate \vec{v}_Ω through Ω is related to the average pressure gradient $\nabla_\Omega p$ in Ω through the upscaled Darcy law

$$\vec{v}_\Omega = -\mathbf{K}^* \nabla_\Omega p. \quad (10.7)$$

The upscale permeability tensor \mathbf{K}^* is not uniquely defined by (10.6) for a given pressure field p , and conversely, there does not exist a unique \mathbf{K}^* so that (10.6) holds for any pressure field. This reflects that \mathbf{K}^* depends on the flow through Ω , which in turn is determined by the boundary conditions that are specified on $\partial\Omega$. The better you know the boundary conditions the homogenized region will be subject to in subsequent simulations, the more accurate estimates you can compute for the upscaled tensor \mathbf{K}^* . In fact, if you know these boundary conditions exactly, you can compute the true effective permeability. In general, you will not know these boundary conditions unless you have already solved your problem, and the best you can do is to make an educated and representative guess that aims to give reasonably accurate results for a wide range of flow scenarios. Another problem is that the even though the permeability tensor of a physical system needs to be symmetric and positive definite (i.e., $\vec{z} \cdot \mathbf{K} \vec{z} > 0$ for all nonzero \vec{z}), there is generally no guarantee that the effective permeability tensor constructed by an upscaling algorithm fulfill these properties. The possible absence of symmetry and positive definiteness shows that the single-phase upscaling problem is fundamentally ill-posed.

10.3.1 Averaging methods

The simplest way to upscale permeability is to use an analytic averaging formula. One general class of such formulas is the power average,

$$\mathbf{K}^* = A_p(\mathbf{K}) = \left(\frac{1}{|\Omega|} \int_\Omega \mathbf{K}(\vec{x})^p d\vec{x} \right)^{1/p}. \quad (10.8)$$

Here, $p = 1$ and $p = -1$ correspond to the arithmetic and harmonic means, respectively, while the geometric mean is obtained in the limit $p \rightarrow 0$ as

$$\mathbf{K}^* = A_0(\mathbf{K}) = \exp\left(\frac{1}{|\Omega|} \int_\Omega \log(\mathbf{K}(\vec{x})) d\vec{x} \right). \quad (10.9)$$

The use of power averaging can be motivated by the so-called Wiener-bounds [188], which state that for a statistically homogeneous medium, the correct upscaled permeability will be bounded above and below by the arithmetic and harmonic mean, respectively.

To motivate (10.8), we can look at the relatively simple problem of upscaling permeability within a one-dimensional domain $[0, L]$. From the flow equation (10.5) and Darcy's law, we have that

$$-(K(x)p'(x))' = 0 \quad \implies \quad v(x) = K(x)p'(x) \equiv \text{constant}$$

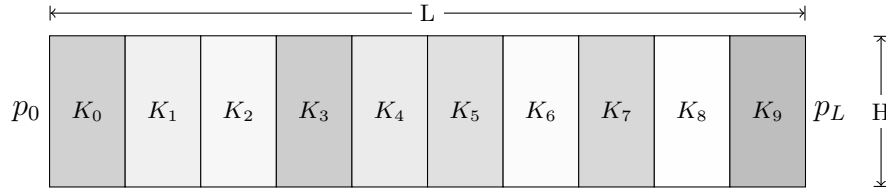


Fig. 10.2. Example of a perfectly stratified isotropic medium with layers perpendicular to the direction of the pressure drop, for which harmonic averaging is the correct way to upscale absolute permeability.

Since the upscaled permeability K^* must satisfy Darcy's law on the coarse scale, we have that $v = -K^*[p_L - p_0]/L$. Alternatively, this formula can be derived by using (10.6)

$$K^* \int_0^L p'(x) dx = K^*(p_L - p_0) \stackrel{(10.6)}{=} \int_0^L K(x) p'(x) dx = - \int_0^L v dx = -Lv.$$

We can now use (10.6) and Darcy's law to find the expression for K^*

$$\begin{aligned} \int_0^L p'(x) dx &= - \int_0^L \frac{v}{K(x)} dx \\ &= K^* \frac{p_L - p_0}{L} \int_0^L \frac{1}{K(x)} dx = K^* \left(\int_0^L p'(x) dx \right) \left(\frac{1}{L} \int_0^L \frac{1}{K(x)} dx \right), \end{aligned}$$

from which it follows that the correct way to upscale K is to use the harmonic average

$$K^* = \left(\frac{1}{L} \int_0^L \frac{1}{K(x)} dx \right)^{-1}. \quad (10.10)$$

This result is generally valid only in one dimension, but also applies to the special case of a perfectly stratified isotropic medium with layers perpendicular to the direction of pressure drop as illustrated in Figure 10.2. It is a straightforward exercise to extend the analysis above to prove that harmonic averaging is the correct upscaling in this case. (If you are familiar with Ohm's law in electricity, you probably realize that this setup is similar to that of resistors set in parallel.)

Computing the harmonic average of a permeability field is straightforward in MRST:

```

vol = G.cells.volumes;
for i=1:size(rock.perm,2)
    crock.perm(:,i) = accumarray(q,vol) ./ ...
                    accumarray(q,vol./rock.perm(:,i))
end

```

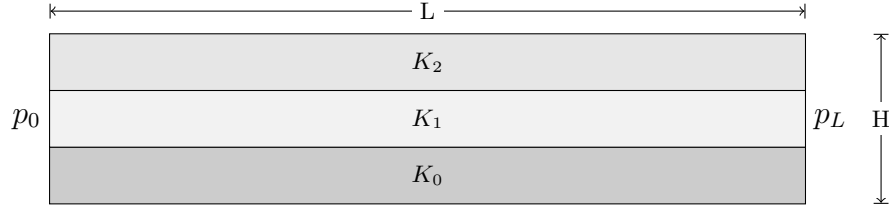


Fig. 10.3. Example of a perfectly stratified isotropic medium with layers parallel to the direction of the pressure drop, for which arithmetic averaging is the correct way to upscale absolute permeability.

where we, as in the previous section, have assumed that \mathbf{q} is a partition vector that describes the coarse grid.

Another special case is when the layers of a perfectly stratified isotropic medium are parallel to the pressure drop as shown in Figure 10.3. Since the permeability is constant along the direction of pressure drop, the pressure will be linear in the x -direction with $p(x, y) = p_0 + x(p_L - p_0)/L$. Using (10.6), we can compute

$$\begin{aligned} K^* \int_0^H \int_0^L \partial_x p(x, y) dx dy &= K^* H (p_L - p_0) \\ &= \int_0^H \int_0^L K(x, y) \partial_x p(x, y) dx dy = \frac{p_L - p_0}{L} \int_0^H \int_0^L K(x, y) dx dy, \end{aligned}$$

from which it follows that the correct upscaling is to use the arithmetic average

$$K^* = \frac{1}{LH} \int_0^H \int_0^L K(x, y) dx dy. \quad (10.11)$$

These examples show that averaging techniques can give correct upscaling in special cases, also in three dimensional space. If we now combine these two examples, we see that we can define the following upscaled permeability tensors for the isotropic media shown in Figures 10.2 and 10.3,

$$\mathbf{K}^* = \begin{bmatrix} A_{-1}^x(K) & 0 \\ 0 & A_1^x(K) \end{bmatrix} \quad \text{and} \quad \mathbf{K}^* = \begin{bmatrix} A_1^y(K) & 0 \\ 0 & A_{-1}^y(K) \end{bmatrix},$$

where the superscripts x and y on the averaging operator A from (10.8) signifies that the operator is only applied in the corresponding spatial direction. These averaged permeabilities would produce the correct net flow across the domain when these two models are subject to a pressure differential between the left and right boundaries or between the top and bottom boundaries. For other boundary conditions, however, the upscaled permeabilities will generally give incorrect flow rates.

To try to model flow in more than one direction, also for cases with less idealized heterogeneous structures modelled by a diagonal fine-scale tensor,

one can generate a diagonal permeability tensor with the following diagonal components

$$\mathbf{K}^* = \begin{bmatrix} A_1^{yz}(A_{-1}^x(\mathbf{K})) & 0 & 0 \\ 0 & A_1^{xz}(A_{-1}^y(\mathbf{K})) & 0 \\ 0 & 0 & A_1^{xy}(A_{-1}^z(\mathbf{K})) \end{bmatrix}.$$

In other words, we start by computing the harmonic average of each of the diagonal permeability components in the corresponding longitudinal direction, i.e., compute the harmonic average of K_{xx} along the x direction, and so on. Then, we compute the arithmetic average in the transverse directions, i.e., in the y and z directions for K_{xx} , and so on. This average is sometimes called the harmonic-arithmetic average and may give reasonable upscaling for layered reservoirs when the primary direction of flow is along the layers. More important, the harmonic-arithmetic average provides a tight lower bound on the effective permeability whereas the opposite method, the arithmetic-harmonic average, provides a tight upper bound.

While it is not obvious how to compute the harmonic-arithmetic average for a general unstructured grid, it is almost straightforward to use MRST to this end for rectilinear and corner-point grids. For brevity, we only show the details for the case when the grid has been partitioned uniformly in index space:

```

q = partitionUI(G, coarse);
vol = G.cells.volumes;
for i=1:size(rock.perm,2)
    dims = G.cartDims; dims(i)=coarse(i);
    qq = partitionUI(G, dims);
    K = accumarray(qq.vol)./accumarray(qq.vol./rock.perm(:,i));
    crock.perm(:,i) = accumarray(q.K(qq).*vol)./accumarray(q.vol);
end

```

The key idea in the implementation above is that to compute the harmonic average in one axial direction, we introduce a temporary partition `qq` that coincides with the coarse grid in along the given axial direction and with the original fine grid in the other axial directions. This way, the call to `accumarray` has the effect that the harmonic average is computed for one longitudinal stack of cells at the time inside each coarse block. To compute the arithmetic average, we simply map the averaged values back onto the fine grid and use `accumarray` over the original partition `q`.

The script `averagingExample1` in the `book` module shows an example of the averaging methods discussed above. The permeability field is a 45×60 sub-sample of Layer 46 from the fluvial Upper Ness formation in the SPE 10 data set. In Figure 10.4, we have compared the effective permeabilities on a 15×15 coarse grid computed by arithmetic, harmonic, and harmonic-arithmetic averaging. From the plots, we see that arithmetic averaging has a tendency to

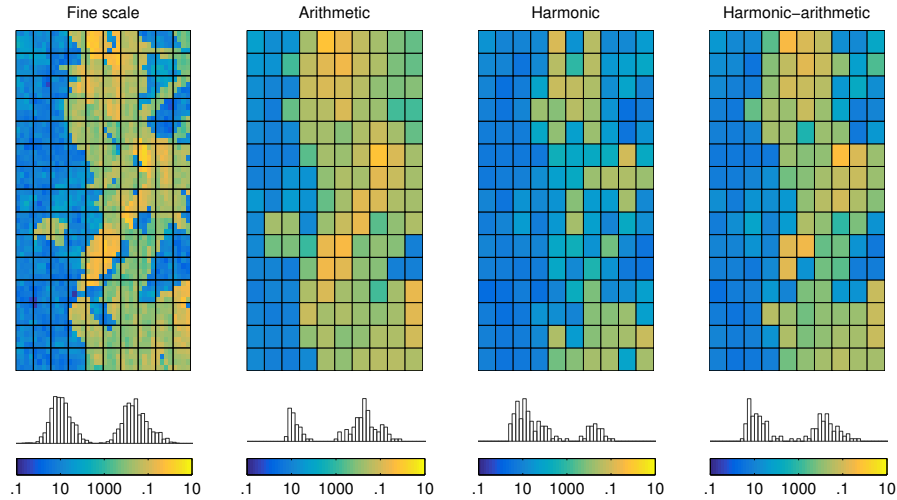


Fig. 10.4. Arithmetic, harmonic, and harmonic-arithmetic averaging applied to a 40×60 subset of Layer 46 from the SPE 10 data set.

preserve high permeability values, harmonic averaging tends to preserve small permeabilities, while harmonic-arithmetic averaging is somewhere in between.

Although simple averaging techniques like the ones discussed above can give correct upscaling in special cases, they tend to perform poorly in practice because the averages do not properly reflect the heterogeneity structures. Likewise, it is also generally difficult to determine which averaging to use since what is the best averaging method depends both on the heterogeneity of the reservoir and the prevailing flow directions. To illustrate this, we consider $8 \times 8 \times 8$ reservoir with three different permeability realizations shown in Figure 10.5. The three realizations are upscaled to a single coarse block using arithmetic, harmonic, and harmonic-arithmetic averaging. To assess the quality of the upscaling, we compare fine-scale and coarse-scale prediction of net flux across the outflow boundary for three different flow patterns: from west to east, from south to north, and from bottom to top. Complete source code for this simulation setup can be found in the script `averagingExample2` in the `book` module.

Table 10.1 reports the ratio between the outflow computed by the coarse models and the outflow computed on the original fine grid. For the layered model, arithmetic and harmonic-arithmetic averaging correctly reproduces flow in the lateral directions, whereas flow normal to the layers is correctly reproduced by harmonic and harmonic-arithmetic averaging. For the two anisotropic models from SPE 10, on the other hand, the flow rates predicted by the arithmetic and harmonic methods are generally far off. The combined harmonic-arithmetic method is more accurate, with less than 15% discrepancy for the Tarbert model and 17–76% discrepancy for the Upper

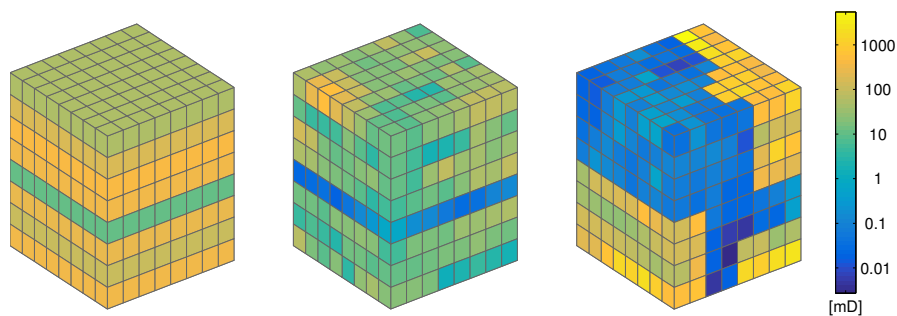


Fig. 10.5. Three models used to test the accuracy of averaging techniques. From left to right: a layered model and two subsets from the Tarbert and the Upper Ness formation, respectively, from the SPE 10 data set.

Table 10.1. Ratio between flow rate predicted by upscaled and fine-scale models for three different permeability fields, three flow scenarios, and three upscaling methods.

Model	Flow pattern	Arithmetic	Harmonic	Harm-arith
Layered	East→West	1.0000	0.2662	1.0000
	North→South	1.0000	0.2662	1.0000
	Top→Bottom	3.7573	1.0000	1.0000
Tarbert	East→West	1.6591	0.0246	0.8520
	North→South	1.6337	0.0243	0.8525
	Top→Bottom	47428.0684	0.3239	0.8588
Upper Ness	East→West	3.4060	0.0009	0.8303
	North→South	1.9537	0.0005	0.7128
	Top→Bottom	6776.8493	0.0020	0.3400

Ness model. Whether this can be considered an acceptable result will depend on the what purpose the simulation is to be used for.

COMPUTER EXERCISES:

64. Set up a set of flow simulations with different boundary conditions and/or well patterns to test the accuracy of the three effective permeability fields computed in `averagingExample1`.
65. Implement harmonic-arithmetic averaging for the SAIGUP model. (Hint: the script `cpGridHarmonic` in the `upscaling` module computes harmonic averaging for the SAIGUP model).
66. Implement the operator A_p in (10.8) as a new utility function.

10.3.2 Flow-based upscaling

In our argumentation above, we repeatedly used the simple flow problems to argue whether a particular averaging method was good or not. Taking this idea one step further, we could impose representative boundary conditions along the perimeter of each coarse block and solve the flow problem (10.5) numerically to determine fine-scale pressures and flow rates and use these to define net flow rates and average pressure gradients, which can be inverted to determine effective coarse-scale permeabilities from Darcy's law. That is, once p and v have been computed, we use the same type of argument as we used to determine the formulas for the harmonic and arithmetic averages, except that we now work with discretely defined pressures and fluxes. This raises the immediate question: what kind of boundary conditions should we use?

A number of different boundary conditions have been suggested over the years. One obvious alternative is to use three different sets of boundary conditions for each block to create a pressure drop across the coarse cell in each of the three axial directions in the same way as for the computations reported in Table 10.1 above; see Figure 10.6. By specifying sealing boundary conditions along the other boundaries, we ensure that the effective flow over the block follows the same axial direction as the pressure drop. This setup emulates how permeability is measured on core samples in the laboratory and provides us with three pairs of flow rates in 3D that can be used to compute an upscaled permeability tensor with diagonal elements

$$K_{xx} = -\frac{v_x L_x}{\Delta p_x}, \quad K_{yy} = -\frac{v_y L_y}{\Delta p_y}, \quad K_{zz} = -\frac{v_z L_z}{\Delta p_z},$$

where v_x is the net flux, L_x is the characteristic length of the block, and Δp_x is the pressure drop inside the block in the x -direction. With this method, the off-diagonal elements will always be zero by construction. Strictly speaking, the assumption of sealing boundaries is only valid in the idealized case when

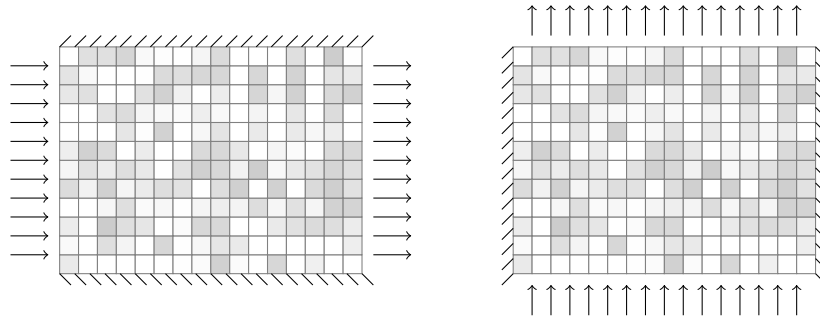


Fig. 10.6. Illustration of a simple flow-based upscaling method, solving $-\nabla \cdot (\mathbf{K} \nabla p) = 0$, with $p = 1$ and $p = 0$ prescribed along the inflow and outflow boundaries respectively, and no-flow boundary conditions elsewhere.

the permeability field is symmetric with respect to the faces of the coarse grid, i.e., if the coarse block is surrounded by mirror images of itself, and it can be shown that this method tends to introduce an upscaling bias towards low permeability values by thickening shale barriers and narrowing sand channels [98, 100].

Unless the grid block is located next to a sealing fault or an impermeable layer, it is therefore more natural to assume that the block has open boundaries so that a pressure differential applied along one of the axial directions will induce a net flow also in transverse directions. This means that the effective permeability will be a full tensor. One method to emulate open boundaries is to prescribe a constant pressure on faces perpendicular to each flow direction and linear pressure drop along the sides that are parallel to the flow direction [74, 166] so that the flow can leave or enter these sides. As for the sealing boundary, a unit pressure drop is applied in each of the axial directions. Use of linear boundary conditions is only strictly valid if the heterogeneous coarse block is embedded inside a homogeneous medium and tends to produce permeabilities with a bias towards high values [59].

Another popular option is to prescribe periodic boundary conditions [59], assuming that the grid block is sampled from a periodic medium so that the fluxes in and out of opposite boundaries will be equal. In other words, to compute the x -component of the permeability, we impose the following conditions

$$\begin{aligned} p(L_x, y, z) &= p(0, y, z) - \Delta p, & v(L_x, y, z) &= v(0, y, z), \\ p(x, L_y, z) &= p(x, 0, z), & v(x, L_y, z) &= v(x, 0, z), \\ p(x, y, L_z) &= p(x, y, 0), & v(x, y, L_z) &= v(x, y, 0). \end{aligned} \quad (10.12)$$

and similarly for the other axial directions. This approach gives a symmetric and positive definite tensor and is usually more robust than specifying sealing boundaries. Using periodic boundaries tends to give permeabilities that lie in between the lower and upper bounds computed using sealing and linear boundaries, respectively.

Let us see how two of these methods can be implemented in MRST for a rectilinear or corner-point grid. For simplicity, we assume that the d -dimensional domain to be upscaled is rectangular and represented by grid G and rock structure `rock`. We start by setting up structures representing boundary conditions,

```

bcsides = {'XMin', 'XMax', 'YMin', 'YMax', 'ZMin', 'ZMax'};
for j = 1:d;
    bcl{j} = pside([], G, bcsides{j, 1}, 0);
    bcr{j} = pside([], G, bcsides{j, 2}, 0);
end
Dp = {4*barsa, 0};
L = max(G.faces.centroids) - min(G.faces.centroids);

```

The first structure, `bcsides`, just contains name tags to locale the correct pair of boundary faces for each flow problem. The `bc1` and `bcr` structures are used to store a template of all the boundary conditions that will be used. While this is not needed in order to implement the pressure-drop method, they will come in handy when setting up the periodic boundary conditions. Finally, `Dp` and `L` contain the prescribed pressure drop and the characteristic length in each axial direction. With the data structures in place, the loop that does the upscaling for the pressure-drop method is quite simple

```

for i=1:d
    bc = addBC([], bc1{i}.face, 'pressure', Dp{1});
    bc = addBC(bc, bcr{i}.face, 'pressure', Dp{2});
    xr = incompTPFA(initResSol(G, 100*barsa, 1), G, hT, fluid, 'bc', bc);
    v(i) = sum(xr.flux(bcr{i}.face)) / sum(G.faces.areas(bcr{i}.face));
    dp(i) = Dp{1}/L(i);
end
K = convertTo(v./dp, milli*darcy);

```

That is, we loop over the axial directions and for each direction we: (i) specify a pressure from left to right, (ii) compute pressures and fluxes by solving the resulting Poisson problem, and (iii) compute average velocity v across the outflow boundary and the average pressure drop d . Finally, we can compute the effective permeability by inverting Darcy's law. The implementation described above is a key algorithmic component in steady-state upscaling of relative permeabilities for multiphase flow and is therefore offered as a separate utility function `upscalePermeabilityFixed` in the `upscaling` module.

The case with periodic boundary conditions is slightly more involved. We start by calling a routine that modifies the grid structure so that it represents a periodic domain.

```

[Gp, bcp] = makePeriodicGridMulti3d(G, bc1, bcr, Dp);
for j=1:d, ofaces{j} = bcp.face(bcp.tags==j); end

```

Technically, the grid is extended with a set of additional faces that connect cells on opposite boundaries of the domain. The routine also sets up an appropriate structure for representing periodic boundary conditions, which we use to extract the faces across which we will later compute outflow. You can find details of how the periodic grid is constructed in the source code. With the modified grid in place, the loop for computing local flow solutions reads

```

dp = Dp{1}*eye(d); nbcp = bcp;
for i=1:d
    for j=1:d, nbcp.value(bcp.tags==j)=dp(j,i); end
    xr = incompTPFA(initResSol(Gp, 100*barsa, 1), Gp, hT, fluid, 'bcp', nbcp);
    for j=1:d
        v(j,i) = sum(xr.flux(ofaces{j})) / sum(Gp.faces.areas(ofaces{j}));
    end
end

```

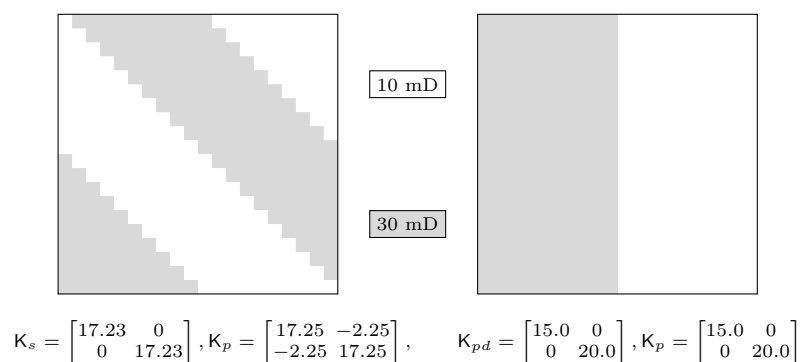


Fig. 10.7. Upscaling two isotropic permeability fields using flow-based upscaling with sealing boundaries (s) or periodic boundary conditions (p).

Inside the loop over all axial directions, the first for-loop extracts the correct pressure drop to be included in the periodic boundary conditions from the diagonal matrix \mathbf{dp} ; that is, a pressure drop along the current axial direction and zero pressure drop in the other directions. Then, we solve the flow problem and compute the average velocity across the outflow boundaries. Notice that because of the periodic conditions, we may have outflow also in the boundaries that have no associated pressure drop, which is why we may get a full-tensor permeability. Outside the loop, we compute the average pressure drop in each axial direction and invert Darcy's law to compute the permeability tensor

```
dp = bsxfun(@rdivide, dp, L);
K = convertTo(v/dp, milli*darcy)
```

The implementation described above is offered as a utility function called `upscalePermeabilityPeriodic` in the `upscaling` module. Linear boundaries are not supported in MRST, but can be implemented by combining elements from the two cases discussed above: using the function `pside` to set a pressure distribution on the boundaries parallel to the flow direction and solving a small linear system to compute the components of the effective permeability.

Whereas setting up the necessary flow problems is relatively simple when the grid corresponds to just one coarse block, it is a bit more involved to do this upscaling efficiently for many blocks at a time. In the `upscaling`, we therefore offer a utility function `upscalePerm` that computes permeability upscaling using the pressure-drop method.

Let us test the methods on a different permeability fields. Figure 10.7 shows two examples of upscaling using flow-based upscaling with sealing boundaries and periodic boundary conditions. For the case to the right, the correlation in the permeability field is along the y -direction, and both methods compute the same diagonal upscaled tensor. If we rotate the grid so that the correlation direction is along the diagonal, using pressure drop along the axial directions

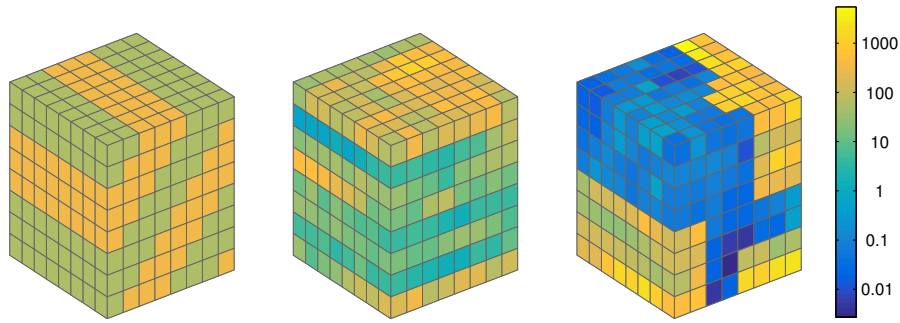


Fig. 10.8. Three models used to test the accuracy of averaging techniques. From left to right: an isotropic model with dipping layers and two subsets from the Tarbert and the Upper Ness formation, respectively, from the SPE 10 data set.

Table 10.2. Ratio between flow rate predicted by upscaled and fine-scale models for three different permeability fields, three flow scenarios, and three upscaling methods.

Model	Flow pattern	Harm-arith	Sealing	Periodic
Layered	East→West	0.78407	1.00000	1.02594
	North→South	0.49974	1.00000	1.00000
	corner→Corner	1.04273	1.30565	1.34228
Tarbert	East→West	0.86756	1.00000	0.56111
	North→South	0.89298	1.00000	0.53880
	Corner→Corner	0.00003	0.00027	39.11923
Upper Ness	East→West	0.83026	1.00000	0.40197
	North→South	0.71283	1.00000	0.28081
	Corner→Corner	0.09546	0.62377	2183.26643

with sealing boundaries still gives a diagonal tensor, whereas the periodic boundary conditions gives a full tensor. By computing the eigenvalue decomposition of this tensor, we find that the upscaled tensor is diagonal with values 15 and 19.5 if we rotate the axial directions 45 degrees clockwise. Full source code for this example can be found in the `permeabilityExample1` script.

Let us also repeat the experiment from Table 10.1 on page 283. However, since both flow-based methods will correctly reproduce flow along or orthogonal to layered media by design, we replace the layered permeability field with one having a dipping layering. Moreover, we replace the top-to-bottom pressure drop by a pressure drop between diagonally opposite corners as well as changing the sampling points from the SPE 10 model. Figure 10.8 shows the new permeability fields and Table 10.2 reports the results of the experiment. Whereas the method with sealing boundary conditions is exact by design for the first two flow fields, it gives incorrect flow rates for the diagonal flow, in particular for the Tarbert subsample. With periodic boundary conditions, we

get the exact flux when the flow direction follows regions of constant permeability from the north to the south side for the isotropic case. For the other two flow patterns, the flow directions cross dipping layers and we thus get minor deviations in the lateral direction and somewhat larger deviation for the diagonal flow. For the anisotropic subsamples, the periodic conditions generally give less accurate results than the other two methods, except for the diagonal flow on the Tarbert case.

COMPUTER EXERCISES:

67. The models in the `BedModels1` and `BedModel2` are examples of fine-scale rock models that are developed to for use in a workflow that propagates petrophysical properties from the core scale to the reservoir scale. Use the methods presented above to upscale the absolute permeability in these models.
68. Implement a method for upscaling with linear boundary conditions.
69. Estimates computed by the averaging and flow based methods have a certain ordering, from low to high values: harmonic, harmonic-arithmetic, sealing boundaries, periodic boundaries, linear boundaries, arithmetic-harmonic, and arithmetic. Make a small test suite of heterogeneity permeability fields and verify this claim.

10.4 Upscaling transmissibility

In the discrete case, the choice of an appropriate upscaling method depends on the numerical stencil used for the spatial discretization. In previous chapters we have seen that the two-point finite-volume method is the method of choice in reservoir simulation. When using this method, grid-block permeabilities are only needed to compute transmissibilities between neighboring coarse blocks. It would therefore be more convenient if we instead of computing an effective permeability tensor associated with each coarse block could compute the coarse transmissibilities associated with the interface between pairs of neighboring coarse blocks directly. These transmissibilities should be defined so that they reproduce fine-scale flow fields in an averaged sense. That is, instead of upscaled block-homogenized tensors \mathbf{K}^* , we seek block transmissibilities T_{ij}^* satisfying

$$v_{ij} = T_{ij}^* \left(\frac{1}{|\Omega_i|} \int_{\Omega_i} p \, d\vec{x} - \frac{1}{|\Omega_j|} \int_{\Omega_j} p \, d\vec{x} \right), \quad (10.13)$$

where $v_{ij} = - \int_{\Gamma_{ij}} (\mathbf{K}\nabla p) \cdot \vec{n} \, d\nu$ is the total Darcy flux across Γ_{ij} .

The upscaled transmissibilities T_{ij}^* can be computed in much the same way as we used to compute upscaled permeabilities above, see Figure 10.9. Here, we use a pressure drop to drive a flow across the interface Γ_{ij} between

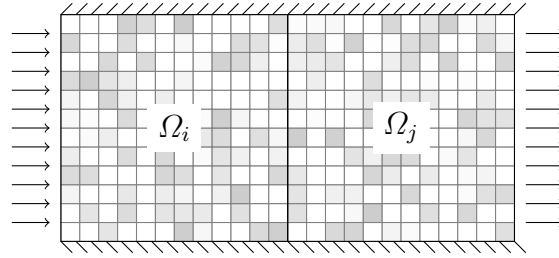


Fig. 10.9. Illustration of flow-based upscaling of transmissibility.

two coarse blocks Ω_i and Ω_j . Thus, by solving (10.5) in the two-block domain $\Omega_i \cup \Omega_j$ subject to suitable boundary conditions, we can compute the average pressures P_i and P_j in Ω_i and Ω_j and then obtain T_{ij}^* directly from the formula

$$v_{ij} = T_{ij}^*(P_i - P_j). \quad (10.14)$$

Let us see how this upscaling can be implemented in MRST. That is, we discuss how to upscale the transmissibility associated with a single interface between two grid blocks. To this end, let us assume that we have a fine grid \mathbf{G} and a coarse partition vector \mathbf{q} that subdivides the grid into two coarse blocks in the x -direction. We start by constructing a coarse-grid structure, as introduced in Section 5.2,

```
CG = generateCoarseGrid(G, q);
CG = coarsenGeometry(CG);
```

Using the data members in this structure, we can find all faces in the fine grid that lie on the interface between the coarse blocks as well as determining the correct sign to apply to the coarse-scale flux

```
i = find(~any(CG.faces.neighbors==0,2));
faces = CG.faces.fconn(CG.faces.connPos(i):CG.faces.connPos(i+1)-1);
sgn = 2*(CG.faces.neighbors(i, 1) == 1) - 1;
```

As we have seen above, there are different ways we can set up a localized flow problem that will give a flux across the interface between the two blocks. Assuming that the coarse interface will be more or less orthogonal to the x -axis, we use a pressure drop in this direction and no-flow boundary conditions on the other sides as shown in Figure 10.9:

```
bc = pside([], G, 'XMin', Dp(1));
bc = pside(bc, G, 'XMax', Dp(2));
xr = incompTPFA(initResSol(G, 100*barsa, 1), G, hT, fluid, 'bc', bc);
flux = sgn * sum(xr.flux(faces));
mu = fluid.properties();
```

All that now remains is to compute pressure values P_i and P_j associated with each coarse block before we can use (10.14) to compute the effective

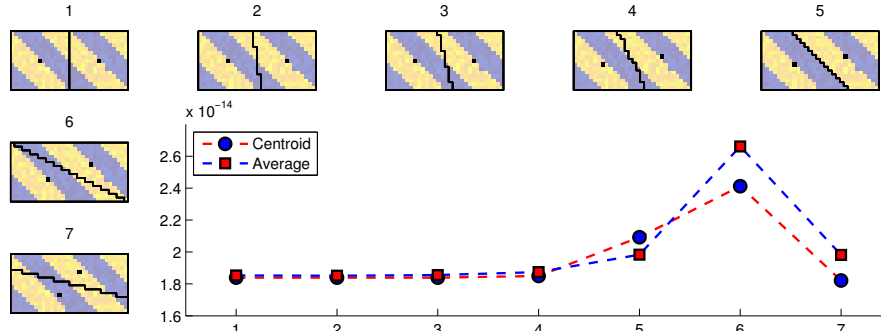


Fig. 10.10. Upscaled transmissibility computed on a series of two-block configurations using either centroid values or averaged values for the block pressures. Black dots show the location of the block centroids from which pressure values are sampled.

transmissibility Following (10.13), P_i and P_j should be defined as the average pressure inside each block

```
P = accumarray(q,xr.pressure)./accumarray(q,1);
T = mu*flux/(P(1) - P(2));
```

Here, we have assumed that all grid cells have the same size. If not, we need to weight the pressure average by cell volumes. As an alternative, we could also have used the pressure value at the block centroids, which generally will give a (slightly) different transmissibility

```
cells = findEnclosingCell(G,CG.cells.centroids);
P = xr.pressure(cells);
```

In Figure 10.10 we have used the code above to compute the transmissibility between two coarse blocks that cover a rectangular domain $[0, 200] \times [0, 100]$ m². We gradually rotate the interface between the two coarse blocks so that it goes from vertical towards being horizontal. Complete source code for the example is found in the script `transmissibilityExample1` in the `book` module. For the first four pairs of coarse blocks shown in Figure 10.10, there is only a slight difference between the transmissibilities computed using pressure values defined as block averages and pressures defined by sampling at the block centroids. The transmissibilities start to deviate as the block interface approaches the diagonal. On the other hand, whereas a pressure drop along the x -axis is a reasonable drive mechanism for the first block pairs, it is highly questionable for the last two block pairs. Let us, for instance, consider block pair number seven. If we instead apply the pressure drop along the y -axis to create a flow that is more perpendicular to the coarse interface, the transmissibility computed with block-averaged pressures changes from 2.0×10^{-14} to 8.1×10^{-14} , whereas with a pressure drop along both axial directions the value is 8.9×10^{-14} . (The latter setup is generally not well-posed as it will have singulari-

ties at the south-east and north-west corners). Depending upon what type of flow conditions the block pair will be subject to in subsequent simulations, it might be better to set a pressure drop orthogonal to the coarse-block interface or use one of the oversampling methods that will be introduced in the next section.

An important property of the upscaled transmissibilities T_{ij}^* is that they all should be positive across all interfaces that can transmit fluids since this will ensure that the TPFA scheme defined by

$$\sum_j T_{ij}^* (p_i - p_j) = q_i,$$

will reproduce the net grid block pressures $p_\ell = \frac{1}{|\Omega_\ell|} \int_{\Omega_\ell} p \, d\vec{x}$, and hence also the coarse fluxes v_{ij} . Unfortunately, there is no guarantee that the transmissibilities defined by (10.13) are positive, e.g., if the blocks are such that the chord between the cell centroids does not cross the coarse interface. However, negative transmissibilities may also occur for regular block shapes if the permeability is sufficiently heterogeneous (e.g., as in the SPE 10 model). Even worse, unique transmissibility values may not even exist, since the upscaling problem generally is not well-posed, see [189] for a more thorough discussion of existence and uniqueness. To guarantee that the resulting coarse-scale discretization is stable, one should ensure that the T_{ij}^* values are positive. A typical trick-of-the-trade is to set $T_{ij} = \max(T_{ij}, 0)$, or in other words, just ignore ill-formed connection between neighboring grid blocks. This is generally not a satisfactory solution, and one should therefore either try to change the grid, use different pressure points to define the transmissibility, or apply some kind of fall-back strategy that changes the upscaling method locally.

The `upscaling` module does not contain any simple implementation of transmissibility upscaling like the one outlined above. Instead, the module offers a routine, `upscaleTrans`, that is designed for the general case where both the coarse and the fine grids can be fully unstructured and have faces that do not align with the axial direction. To provide robust upscaling for a wide range of geological models, the routine relies on a more comprehensive approach that will be outlined briefly in the next section and also has fallback strategies to reduce the number of negative permeabilities.

10.5 Global and local-global upscaling

The methods described so far in this chapter have all be local in nature. Averaging methods derive upscaled quantities solely from the local heterogeneous structures, whereas flow-based methods try to account for flow responses by solving local flow problems with prescribed boundary conditions. These boundary conditions are the main factor that limits the accuracy of flow-based methods. In Table 10.2 on page 288, we saw how the neither of

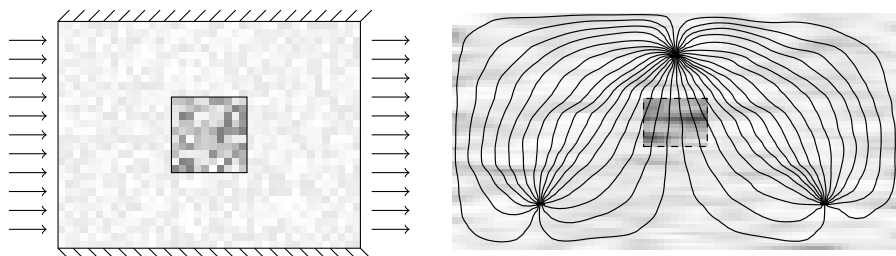


Fig. 10.11. Illustration of oversampling techniques for upscaling. The size of the grid block is exaggerated in the right plot.

the local methods were able to accurately capture the correct net flow for the anisotropic Tarbert and Upper Ness samples with boundary conditions giving diagonal flow. The main problem for flow-based techniques is, of course, that we do not know *a priori* the precise flow that will occur in a given region of the reservoir during a subsequent simulation. Thus, it is generally not possible to specify the appropriate boundary conditions for the local flow problems in a unique manner unless we already have solved the flow problem.

Improved accuracy can be obtained if you use a so-called *oversampling technique* which is sometimes referred to as an overlapping method. In oversampling methods, the domain of the local flow problem is enlarged with a border region that surrounds each grid block and boundary conditions, or other mechanisms for driving flow like wells or source terms, are specified in the region outside the domain you wish to upscale. The flow problem is then solved in the whole enlarged region, but the effective permeability tensor is only computed inside the original coarse block. This way, you lessen the impact of the localization assumption and the particular mechanism used to drive flow, and the flow across the boundaries of the coarse block is to a larger extent determined by the local heterogeneity surrounding the block. The motivation for using an oversampling technique is to better account for permeability trends that are not aligned with the grid directions and possible large-scale connectivity in the permeability fields.

To also account for global flow patterns, one can solve the pressure equation one time, or a few times, on the full geological model and sample fluxes from the global flow field and impose them as boundary conditions on the local flow problem used to upscale permeabilities or transmissibilities. In these so-called *global upscaling methods*, the pressure solution can either be computed using representative and *specific* drive mechanisms or the pressure solution can be computed using a set of *generic conditions* that e.g., flow the reservoir from east to west, north to south, and so on. From a computational point of view, this approach may seem to contradict the purpose of upscaling, but can be justified for numerical simulation of compressible and/or multiphase flow. Indeed, for such transient flows the pressure equation has to be solved

multiple times throughout the simulation, and the cost of solving the global pressure equation once (or even a few times) on a fine grid will in many cases be small compared with the cost of

Computing a global pressure solution can be avoided if one uses a so-called local-global method [41, 42, 73]. In these methods, pressure solutions obtained by solving global flow problems on a coarse grid are used to set boundary conditions for local flow problems that determine the upscaled transmissibilities. Since the initial coarse-grid computation may give quite poor boundary conditions for the local flow problems, these methods use an iterative bootstrapping procedure to gradually ensure consistency between the local and the global calculations.

Global and local-global upscaling methods may suffer from negative or anomalously large transmissibility values. To avoid these, Holden and Nielsen [84], who were among the first to study global upscaling methods, proposed an iterative process involving the solution of an optimization problem, that gradually perturbs the transmissibilities until they fall within a prescribed interval. A similar technique that avoids the solution of the fine-grid problem was presented in [144]. Chen and Durlofsky [41] observed that unphysical transmissibilities occur mainly in low-flow regions. Therefore, instead of using an optimization procedure that alters all transmissibilities in the reservoir, they proposed to use a thresholding procedure in which negative and very large transmissibilities are replaced by transmissibilities computed by a local method. Because the transmissibilities are altered only in low-flow regions, the perturbation will have limited impact on the total flow through the reservoir.

The script `upscaleTrans` offers various implementations of global transmissibility upscaling using either specific or generic mechanisms to drive flow in the full reservoir model. Whereas the generic approach enables you to tailor-make the coarse-scale model for a particular simulation setup, the generic approach will give you a more robust upscaling that is less accurate for a specific simulation setup, but need not be recomputed if you later wish to simulate setups with significant changes in the well pattern, aquifer support, and other factors that affect the global flow patterns in the reservoir. Local-global methods, however, are not yet supported in MRST. Instead, the software offers various multiscale methods [63]—including multiscale mixed finite elements [5, 152], multiscale finite volumes [130, 133], and multiscale restriction-smoothed basis [134, 135]—offering an alternative approach in which the impact of fine-scale heterogeneity is included more directly into coarse-scale flow equations.

COMPUTER EXERCISES:

70. Extend the computations reported in Table 10.2 to include oversampling methods. Does this improve the accuracy of the two flow-based methods?

71. Implement a function that performs generic global upscaling for uniform partitions of rectilinear and curvilinear grids. To drive the global flow pattern, you can use a pressure drop in each of the axial directions. How would you extend your method to more general grids and partitions?
72. Extend the `upsaling` module to include local-global upscaling methods.

10.6 Upscaling examples

In this section we will go through two examples where the methods discussed above are used to upscale full reservoir models. In doing so, we will also introduce you to a simple form of flow diagnostics [168, 137] that can be used to assess the accuracy of a single-phase upscaling.

10.6.1 Flow diagnostics quality measure

As we have mentioned several times already, a challenging problem with upscaling is to predict upfront whether the upscaling will be accurate or not. To partially answer this question and give an indication of the quality of the upscaling, we suggest to compare the cumulative well-allocation factors computed using the fine-scale and the upscaled models. As shown in Section 9.1.3 on page 244, a well-allocation factor is the percentage of the flux in or out of a completion that can be attributed to a pair of injection and production wells.

To compute these factors, we need to first compute a global, single-phase pressure solution for the specific well pattern we want to investigate. We then use the resulting flow field to compute numerical tracer partitions as discussed in Sections 6.3.4 and 7.3 that can subsequently be used to subdivide the reservoir volume into subvolumes associated with pairs of injection and production wells as discussed in Section 9.1. Global methods tend to compute at least one fine-scale pressure solution as part of the upscaling procedure, but if a global solution is not available for the specific well pattern, it is generally not very expensive to compute compared with the cost of the flow-based upscaling procedure. The same goes for the computation of a coarse-scale flow field and tracer distributions on the fine and the upscaled model.

To improve the predictive power of well-allocation factors, we may have to subdivide each well into two or more segments that each consist of a connected set of completion cells. This way, we can measure the communication between different parts of the wells, which is particularly important if the model to be upscaled includes layers or geological objects with significantly different permeabilities.

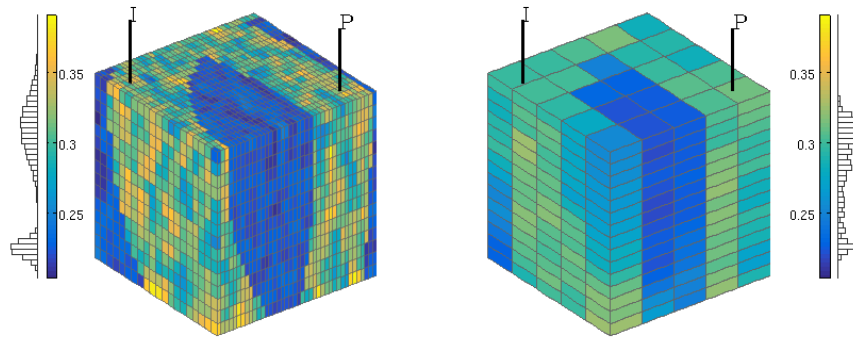


Fig. 10.12. Porosity distribution in a model with two different rock types before and after upscaling.

10.6.2 Model with two rock types

We start by considering a small rectangular model that contains two facies with contrasting petrophysical properties. An injector and a producer are placed diagonally opposite each other and completed mainly in the high-permeable parts of the model. Both wells operate at a fixed rate that amounts to the injection/production of 0.2 pore volumes per year, and to avoid potential problems with cross-flow, gravity forces are neglected. The fine grid consists of $40 \times 20 \times 15$ cells, which we seek to upscale to a coarse $5 \times 5 \times 15$ model. That is, we upscale by a factor 8×4 in the lateral direction and leave the vertical layers in an attempt to preserve the vertical communication in the model as accurately as possible. To this end, we use the `upscalePerm` function, which upscales permeability using the flow-based method from Section 10.3.2 with sealing boundary conditions. Figure 10.12 shows the porosities of the fine and the coarse model. Complete source code for this example can be found in the script `upscalingExample1` of the `book` module.

To get an indication of the accuracy of this upscaling, we will look at the cumulative well-allocation factors introduced above. For this particular model, we have only one producer and one injector, and to better measure the communication within the reservoir, we subdivide each well into two segments, an upper and a lower segments, so that we altogether will have four well-pairs whose well-allocation factors can be used to verify the quality of the upscaling. The 3D plots in Figure 10.13 show the injection and tracer partitions defined as regions with tracer concentration larger than 0.5. The resulting well-allocation factors are shown in Figure 10.14. For each well segment, we plot a bar chart of the cumulative flux in/out of the completions that make up the segment, from bottom to top. In the plots, each well segment is assigned the same unique color that was used in Figure 10.13 and

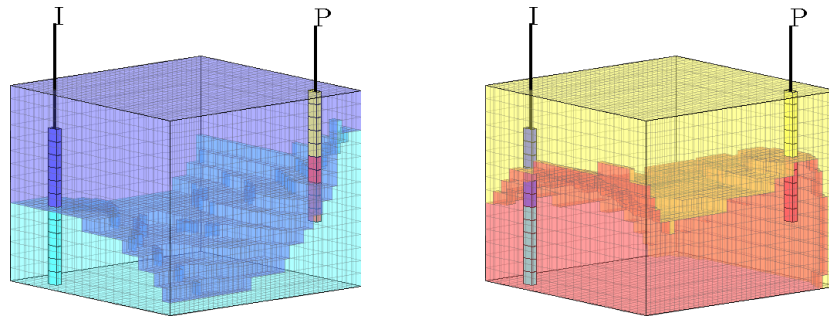


Fig. 10.13. Volumetric subdivision into injector-producer pairs by majority vote. The left plot shows the regions flooded by the upper and lower parts of the injector shown in blue and cyan, respectively. The right plot shows the drainage regions of the upper and lower half of the producer shown in yellow and red, respectively. In both plots, each cell is assigned to the completion that has the highest concentration value.

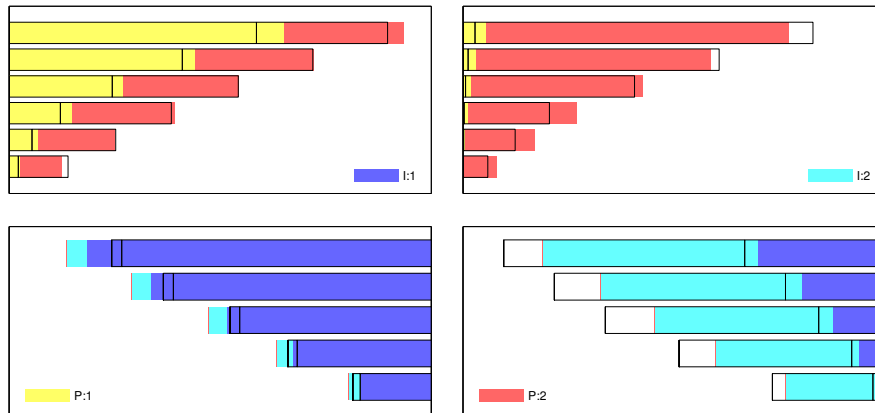


Fig. 10.14. Normalized cumulative well-allocation factors for the four well completions in the two-facies model. The color bars show well-allocation factors computed on a coarse model upscaled using `upscalePerm`, while the black lines show the same factors computed on the original model. The colored bars and the black lines should coincide if the upscaled model reproduces the flux allocation correctly.

each bar is subdivided into the fraction of the total in/outflux that belongs to the different well-pairs the segment is part of.

The bar charts at the top of Figure 10.14 show the allocation factors computed by the upscaled model for the upper half of the injector (I:1, upper-left plot), the lower part of the injector (I:2, upper-right plot), the upper part of the producer (P:1, lower-left plot), and the lower part of the producer (P:2, lower-right plot). The solid lines denote the same quantities computed for the

fine-scale model. The closer the color bars and the solid lines are, the better is the upscaling.

To explain how this type of flow diagnostics should be interpreted, let us look at the lower-left bar chart, which reports the allocation factors or the upper-half of the injector (P:1, yellow color). Here, the blue color signifies the flux that can be attributed to I:1, i.e., the upper-half of the injector, while the cyan color signifies the flux that can be attributed to I:2. Because the colored bars are mostly blue, the inflow into the upper half of the injector is predominantly associated with the I:1–P:1 pair. In other words, P:1 is mainly supported by the upper half of the injector and hardly in contact with the lower part. This trend is confirmed by looking at the upper-right bar chart, which shows that the inflow in the lower half of the injector mainly contributes to production in the lower part of the injector. The flooded volumes shown to the left in Figure 10.13 confirm that fluid injected from I:2 will mainly sweep the volume surrounding the lower of I:2. Similarly, the drainage regions in the plot to the right show that the drainage region of P:1 only engulfs the upper parts of I:1. The flooded regions of I:2, on the other hand, engulfs both P:2 and the lower parts of P:1, and hence the segment of the well will contribute flux to both segments of the producer, as shown in the upper-left chart of Figure 10.14. Likewise, the drainage region from P:2 engulfs both I:2 and the lower part of I:1 and hence is supported by flux from both the injector segments, as shown in the lower-right chart of Figure 10.14.

So, what does the flow diagnostics tell us about our upscaled model? First of all, the upscaling does obviously not fully reproduce the volumetric connections of the fine-scale model. Looking at well-allocation factors for the producers in the bottom row of Figure 10.14, we see that the upscaled model predicts too much flux in the upper segment (P:1, yellow color, left chart) since the colorbars exceed the solid lines at the top. Likewise, in the lower segment of the producer (P:2, red color, right chart), we get too low flux. Altogether, the allocation factors seem to suggest that the main problems are that the upscaled model misses some of the vertical communication and exaggerates the connection between I:1 and P:1. We could obviously have used a single number to measure the overall discrepancy in flux allocation, but in our opinion you will benefit more from a graphical presentation like this as it may help you to identify the cause of the mismatch between the upscaled and the original model.

To develop a better coarse model, we can upscale transmissibilities and well indices using a global method. For a given flow scenario, like the one above with fixed well positions and constant well controls, one can determine a set of transmissibilities and well indices that will reproduce a single pressure step exactly. This may seem desirable, but has the disadvantage that the linear system becomes negative definite, which in turn may lead to unphysical solutions away from the scenario used for upscaling. To span a reasonable set of global flow directions, we will instead use generic boundary conditions that pressurize the reservoir from east to west, from north to south, and from top

to bottom. There are several different ways these three global flow fields can be combined to compute a transmissibility values for each coarse face, see e.g., [96]. Here, we use a simple strategy suggested by [105], in which we pick the one among the three flow field that gives the largest flux across a given coarse face and insert this into (10.14) to compute the transmissibility associated with this face. A rationale for this choice is that the accuracy of the coarse model is most sensitive to the choice of transmissibilities in high-flow regions.

The well indices are upscaled using the following formula (see (6.27) on page 162)

$$J_i^* = Q_i / (P_i - p_w) \quad (10.15)$$

where Q_i is the sum over rates of all the perforations inside block i , P_i is the average block pressure, and p_w is the pressure inside the well. To obtain representative flow fields, we solve $n_w - 1$ pressure equations, where n_w is the number of wells. Each solution is computed by setting a positive pressure in one well and zero pressure in all the other wells. To combine the flow fields, we can either use the same strategy as for the transmissibilities and pick the solution that gives the largest well rate, or as we will do in the current example, add all well rates and divide by the sum of the corresponding pressure drops.

The approach outlined above has been implemented in the function `upscaleTrans`. Unfortunately, there is no guarantee that the upscaled transmissibilities are not negative. To avoid creating an ill-conditioned discretization matrix, we therefore set all negative transmissibilities to zero, thereby blocking the corresponding coarse face for flow. This is in our experience an acceptable solution as long as the upscaled transmissibilities are only intended for a specific scenario, like herein, since negative transmissibilities tend to appear because flow is tangential to the coarse interface or as a result of numerical noise in regions with very low flow. If your upscaling, on the other hand, aims to serve a more general purpose with varying well patterns and/or boundary conditions, you would need to implement a more sophisticated strategy that falls back to a local flow-based method, an averaging method, or a combination of these.

Figure 10.15 shows the resulting match in well-allocation factors, which is significantly better than when using a simple permeability upscaling. In part, this is a result of improved transmissibilities, and in part because we now have upscaled the well indices.

10.6.3 SPE10 with six wells

You have already encountered Model 2 from the 10th SPE Comparative Solution Project multiple times throughout the book. Because of its simple grid and strong heterogeneity and the fact that it is freely available online, this data set has become a community benchmark that is used for many different purposes. The original aim of the project was to “compare upgridding and upscaling approaches and the ability to predict performance of a waterflood

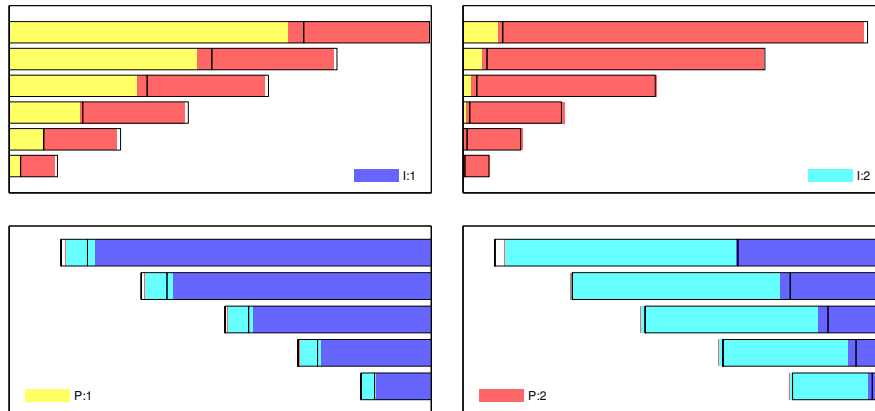


Fig. 10.15. Normalized cumulative well-allocation factors for the four well completions in the two-facies model. The color bars show well-allocation factors computed on a coarse model upscaled using `upscaleTrans`, while the black lines show the same factors computed on the original model.

through a million cell geological model”, and in [49] you can read about the relative merits of the various methods used in the upscaling studies that were submitted to the project by August 2000. In short, the study showed that the data set is generally very difficult to upscale accurately using single-phase methods and that the best results are generally obtained by methods that also account for multiphase effects. Later, however, quite good results have been obtained using local-global and multiscale methods, see e.g., [2].

In this example, we will compare the ability of four different upscaling methods to accurately predict single-phase flow. That is, we consider two averaging methods (harmonic and harmonic-arithmetic) and a local flow-based upscaling with sealing boundary conditions for upscaling permeability, and the global upscaling method discussed at the end of the previous example for upscaling transmissibilities and well indices. (However, unlike in the previous example, we use maximum flow rate to determine both transmissibilities and well indices). Full source code can be found in the script `upscalingExample2`.

We start by considering the Tarbert formation, which can be found in the upper 35 layers of model. To upscale this Cartesian grid model, we choose a coarsening factor of $10 \times 10 \times 3$, and to get an even number of cell layers inside each grid block, we extend the model slightly by repeating the top layer so that the fine-scale model altogether has $220 \times 60 \times 36 = 475\,200$ cells. To get a slightly more interesting well pattern, we replace the original five-spot pattern with a pattern consisting of producers in the four corners of the model and two injectors located near the center of the model, see Figure 10.16. All four wells operate at a fixed bottom-hole pressure of 200 bar for the producers and 500 bar for the injectors. In Figure 10.17, we verify whether the well-allocation

rates predict by the four upscaling methods for injector I2 reproduce the fine-scale results or not. This well has significant communication with all four producers and hence is more difficult to match than injector I1, which mainly communicates with P3 and P4.

Harmonic averaging not surprisingly gives well rates that are far from the fine-scale targets. As explained in Section 10.3.1, the harmonic mean has a bias against smaller values and tends to underestimate the effective permeability. Since all wells are controlled by bottom-hole pressure, too low permeability means too low well rates. If the wells were controlled by total rate, as in the previous example, the well rates predicted by the harmonic average would have been more correct, but the predicted pressure build-up around the injector and the pressure draw-down in the producers would both be too high.

Comparing the local, flow-based method to the harmonic-arithmetic averaging method, we see that the latter is significantly more accurate. By design, the flow-based method should give accurate prediction of flow along the axial directions of the grid. Here, however, we have flow that is strongly affected by heterogeneity and mostly goes in the lateral, diagonal direction and hence the harmonic-arithmetic method seems to be more suited, in particular if we consider the computational time of the two methods. In our current implementation, the flow-based method extracts a subgrid and assembles and inverts three local matrices for each coarse block. The computational overhead of this procedure is significant since each new local solve incurs full start-up cost. The result is that the function `upscalePerm` has orders of magnitude higher computational cost than the harmonic-arithmetic averaging, which is implemented using a few highly efficient calls to `accumarray`.

Using the global upscaling method, we get almost exact reproduction of the fine-scale well-allocation factors. The plots may be a bit deceiving because of the areas where the colorbars extend beyond the solid lines representing the fine-scale well-allocation. However, bear in mind that the bars and lines represent *cumulative* factors, and thus we should only look at the discrepancy at the top of each colorbar, and if you look closely, you will see that here the match is excellent. There are two reasons for this: On one hand, using global flow field will ensure that each upscaling problem has more representative boundary conditions used for localization and hence can better account for correlations in the heterogeneity that extend beyond the block. On the other hand, the global method includes upscaling of well indices that can have a significant impact on the well rates that determine the flux allocation. In passing, we also note that although the computational cost of the global method is significantly lower than that of the local method, primarily since we here have been able to utilize a highly efficient multigrid solver for the global flow problems and avoid solving a long sequence of small problems that each have a large start-up cost.

For completeness, we also include the results of a similar study for the whole SPE 10 model, see Figure 10.18. This includes the fluvial Upper Ness formation, which is notoriously difficult to upscale accurately and we also see

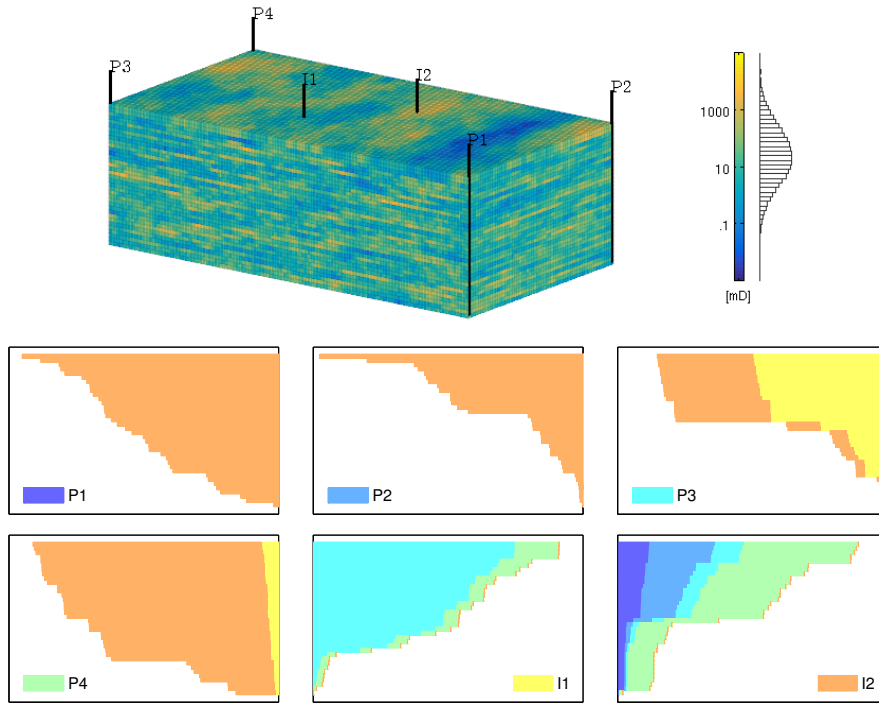


Fig. 10.16. Model of the Tarbert formation with six wells, two central injectors and four peripheral producers. The 3D plot shows lateral permeability distribution, while the bar charts shows normalized cumulative well-allocation factors.

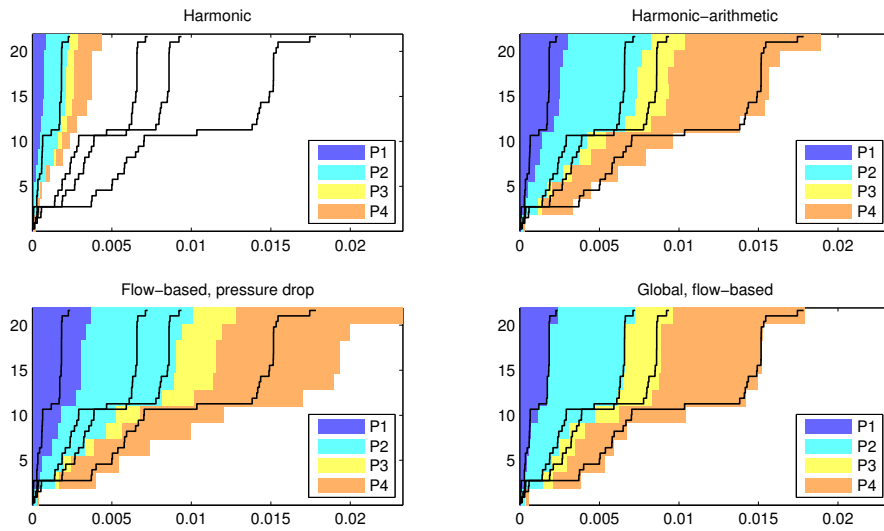


Fig. 10.17. Well-allocation factors for injector I2 in the Tarbert model computed on four different coarse models.

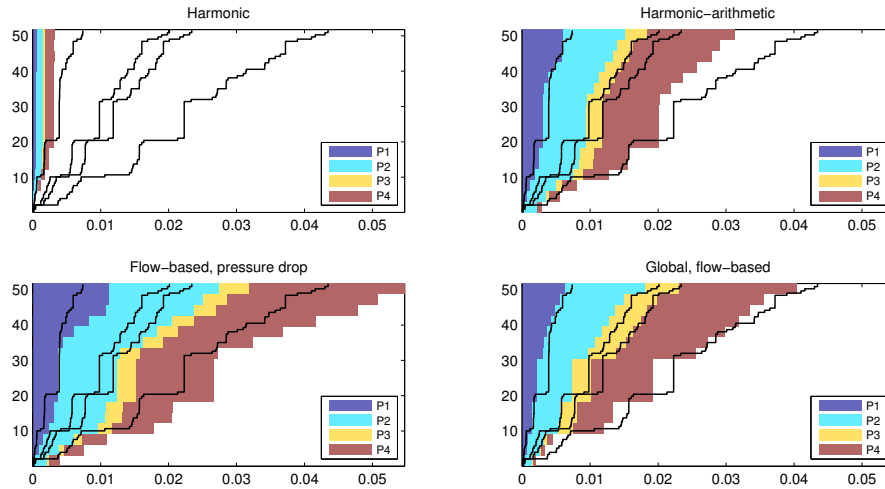


Fig. 10.18. Well-allocation factors for injector I2 in the full SPE 10 model computed on four different coarse models.

that the harmonic-arithmetic and the global method are no longer as accurate as for the Tarbert formation. For this 1.1 million grid cell model, an efficient iterative solver like AGMG is indispensable to be able to compute the fine-scale solution and perform a global upscaling in MATLAB.

10.6.4 General advice and simple guidelines

Through the various examples in this chapter, we have tried and hopefully succeeded to convince you that accurate and robust upscaling is a difficult problem and that there is no single upscaling method that is unequivocally better than the others. This is one motivation for the tremendous so-called multiscale methods have received in recent years since these methods offer a promise of a more systematic and consistent way of bringing the impact of small-scale heterogeneity variations into simulations on a coarser scale.

What is the best upscaling method for a specific project will depend on many factors. The most important factor is probably what you intend to use the upscaled model for. If you are upscaling for a specific scenario, it is strongly recommended to use a method that employs specific global information as this generally will enable you to perform more aggressive coarsening. If, on the other hand, the upscaled model is to be used to simulate a large variety of scenarios, or some yet unspecified scenario, you should pick a technique that is as robust as possible. What this technique is, will depend on the type of heterogeneity you are facing, the flow patterns that exist in a reservoir, and so on. For relatively homogeneous reservoirs with flow patterns that mainly follow the axial directions, a simple averaging technique may be sufficient, whereas techniques that utilize some kind of global information are

recommend for highly heterogeneous reservoirs with strong contrasts and large variations in correlation lengths. Other determining factors include the time and the computer resources you have available for upscaling, the number of petrophysical realizations you need to upscale, the required upscaling factor, etc.

Irregardless of your situation, it is generally recommended that you try different upscaling and grid coarsening methods. Start by simple averaging methods that have a low computational cost and can quickly give you a first estimate of the upscaling uncertainty or more generally the uncertainty in the petrophysical properties. Check to see if there are features in your model that need to be resolved by adapting the coarse grid and ensure that you do not create a coarse grid that will give problems for subsequent flow simulations, see e.g., the discussion in Section 5.4. Then you can gradually move towards more sophisticated upscaling methods. For local methods, you should try both sealing and linear pressure boundaries to provide lower and upper bounds. You may also need to check the use of oversampling methods to lessen the impact of boundary conditions used for localization.

At all stages, you should use representative single-phase simulations to validate your upscaled model against the original fine-scale model. To this end, we strongly recommend that you use various kinds of flow diagnostics like the well-allocation factors discussed in the examples above, tracer partitions that give you the volumetric connections between inflow and outflow, time-of-flight that gives time lines for displacement fronts, and so on. Herein, we have computed these quantities using finite-volume discretizations that are available in MRST, but these flow diagnostic measures can also be computed using streamline simulation [53], which is generally a very efficient tool for comparing geomodels and upscaled simulation models. Whether you choose one or the other, is not that important. What is important, is that you stick to using single-phase flow physics to avoid mixing in the effect of multiphase flow parameters like variations in relative permeabilities and capillary pressures, which need to be upscaled by other means.

Compressible Flow

Single-Phase Flow and Rapid Prototyping

In previous chapters we have outlined and explained in detail how to discretize and solve incompressible flow problems. For multiphase problems we used a fractional-flow formulation combined with a sequential solution approach in which flow and transport were computed in consecutive substeps. Sequential formulations are popular in academia and for research purposes, but are less used for practical simulation in industry. To the extent simulations are used in practical reservoir engineering, they are mainly based on compressible equations discretized by so-called fully-implicit discretizations in which flow and transport are solved as a coupled system. This approach is very robust and particularly useful for problems with large variations in time constants or strong coupling between different types of flow mechanisms.

As a prequel to the discussion of compressible multiphase flow models that comes later in the book, this chapter will teach you how to discretize the basic equations for single-phase, compressible flow and explain in detail how you can use this discretization to develop compact, but yet efficient simulators. To this end, we will rely heavily on the library for automatic differentiation (AD) that was briefly introduced Section 2.7 and discrete differential and averaging operators. As briefly discussed in Section 6.4.2, these discrete operators enable you to implement discretized flow equations in a form that is compact and close to their mathematical description, while use of automatic differentiation ensures that no analytical derivatives have to be programmed explicitly as long as the discrete flow equations and constitutive relationships are implemented as a sequence of algebraic operations. In MRST, discrete operator and automatic differentiation is combined with a flexible grid structure, a highly vectorized and interactive scripting language, and a powerful graphical environment. This is in our opinion the main reason why the software has proved to be a particularly efficient tool for developing new computational methods and workflow tools. In this chapter, we try to substantiate this claim by showing several examples of rapid prototyping by extending the single-phase model to include pressure-dependent viscosity, non-Newton fluid behavior, and temperature effects. Complete scripts for all the examples can be found in the `ad-1ph` subdirectory of the `book` module.

12.1 Implicit discretization

As our basic model, we consider the single-phase continuity equation,

$$\frac{\partial}{\partial t}(\phi\rho) + \nabla \cdot (\rho\vec{v}) = q, \quad \vec{v} = -\frac{K}{\mu}(\nabla p - g\rho\nabla z). \quad (12.1)$$

The primary unknown is usually the fluid pressure p . Additional equations are supplied to provide relations between p and the other quantities in the equation, e.g., by specifying $\phi = \phi(p)$, an equation-of-state $\rho = \rho(p)$ for the fluid, and so on; see the discussion in Section 6.2. (Notice that q is defined slightly differently in (12.1) than in (6.5)).

Using the discrete operators introduced in Section 6.4.2, the basic implicit discretization of (12.1) reads

$$\frac{(\phi\rho)^{n+1} - (\phi\rho)^n}{\Delta t^n} + \text{div}(\rho\mathbf{v})^{n+1} = \mathbf{q}^{n+1}, \quad (12.2a)$$

$$\mathbf{v}^{n+1} = -\frac{K}{\mu^{n+1}}[\text{grad}(\mathbf{p}^{n+1}) - g\rho^{n+1}\text{grad}(z)]. \quad (12.2b)$$

Here, $\phi \in \mathbb{R}^{n_c}$ denotes the vector with one porosity value per cell, \mathbf{v} is the vector of fluxes per face, and so on. The superscript refers to discrete times at which one wishes to compute the unknown reservoir states and Δt denotes the distance between two such consecutive points in time.

In many cases of practical interest it is possible to simplify (12.2). For instance, if the fluid is only slightly compressible, several terms can be neglected so that the nonlinear equation reduces to a linear equation in the unknown pressure p^{n+1} ,

$$\frac{\mathbf{p}^{n+1} - \mathbf{p}^n}{\Delta t^n} - \frac{1}{c_t\mu\phi}\text{div}(\mathbf{K}\text{grad}(\mathbf{p}^{n+1})) = \mathbf{q}^n. \quad (12.3)$$

However, this is not always possible and for generality we assume that ϕ and ρ depend nonlinearly on p so that (12.2) gives rise to a nonlinear system of equations that needs to be solved in each time step. As we will see later in this chapter, the viscosity may also depend on pressure, flow velocity, and/or temperature, which adds further nonlinearity to the system.

In the following, we will mainly work with discretized equations written in residual form. As an example, the residual form of (12.3) reads

$$\mathbf{p}^{n+1} - \frac{\Delta t^n}{c_t\mu\phi}\text{div}(\mathbf{K}\text{grad}(\mathbf{p}^{n+1})) - \mathbf{p}^n - \Delta t^n\mathbf{q}^n = 0.$$

If we now collect all the discrete equations that make up our model, we can write the resulting system of nonlinear equations in short vector form as

$$\mathbf{F}(\mathbf{x}^{n+1}; \mathbf{x}^n) = \mathbf{0}, \quad (12.4)$$

where \mathbf{x}^{n+1} is the vector of unknown state variables at the next time step and the vector of current states \mathbf{x}^n can be seen as a parameter.

Nonlinear systems of discrete equations like (12.4) that arise from the discretization of partial differential equations are typically solved by Newton's method. The main computational cost of solving a nonlinear PDE often lies in solving the linear systems involved in each Newton iteration. For a discretized equation on vector form, $\mathbf{F}(\mathbf{x}) = \mathbf{0}$, the approximate solution \mathbf{x}^{i+1} in the $(i + 1)$ -th iteration is obtained from

$$\frac{\partial \mathbf{F}(\mathbf{x}^i)}{\partial \mathbf{x}^i} \delta \mathbf{x}^{i+1} = -\mathbf{F}(\mathbf{x}^i), \quad \mathbf{x}^{i+1} \leftarrow \mathbf{x}^i + \delta \mathbf{x}^{i+1}. \quad (12.5)$$

Here, $\mathbf{J}(\mathbf{x}^i) = \partial \mathbf{F}(\mathbf{x}^i) / \partial \mathbf{x}^i$ is the Jacobian matrix, while $\delta \mathbf{x}^{i+1}$ is referred to as the *Newton update* at iteration number $i + 1$. Theoretically, the Newton process exhibits quadratic convergence under certain smoothness and differentiability requirements on \mathbf{F} . Obtaining such convergence in practice, however, will crucially depend on having a sufficiently accurate Jacobian matrix. Computing the Jacobian matrix can typically be broken down to differentiation of elementary operations and functions. Nevertheless, if \mathbf{F} represents a set of complex equations, analytical derivation and subsequent coding of the Jacobian can be very time-consuming and prone to errors. Fortunately, computing Jacobians is a good candidate for automation using automatic differentiation.

The idea of using automatic differentiation to develop reservoir simulators is not new. This technique was introduced in an early version of the commercial Intersect simulator [55], but has mainly been pioneered through a reimplementation of the GPRS research simulator [37]. The new simulator, called AD-GPRS is primarily based on fully implicit formulations [183, 193, 182] in which independent variables and residual equations are AD structures implemented using ADETL, a library for forward-mode AD realized by expression templates in C++ [191, 190]. This way, the Jacobi matrices needed in the nonlinear Newton-type iterations can be constructed from the derivatives that are implicitly computed when evaluating the residual equations. In [111], the authors discuss how to use the alternative backward-mode differentiation to improve computational efficiency.

12.2 A simulator based on automatic differentiation

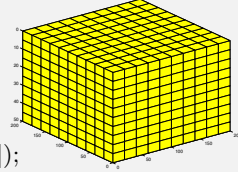
We will now present step-by-step how you can use the AD class in MRST to implement an implicit solver for the compressible, single-phase continuity equation (12.1). In particular, we revisit the discrete spatial differentiation operators from 6.4.2 and introduce additional discrete averaging operators that together enable us to write the discretized equations in an abstract residual form that resembles the semi-continuous form of the implicit discretization in (12.2). Starting from this residual form, it is relatively simple to obtain a linearization using automatic differentiation and set up a Newton iteration.

12.2.1 Model setup and initial state

For simplicity, we consider a homogeneous box-model:

```
[nx,ny,nz] = deal( 10, 10, 10);
[Lx,Ly,Lz] = deal(200, 200, 50);
G = cartGrid([nx, ny, nz], [Lx, Ly, Lz]);
G = computeGeometry(G);

rock.perm = repmat(30*milli*darcy, [G.cells.num, 1]);
rock.poro = repmat(0.3, [G.cells.num, 1]);
```



Beyond this point, our implementation is agnostic to details about the grid, except when we specify well positions on page 345, which would typically have involved a few more code lines for a complex corner-point model like the SAIGUP or the Norne models discussed in Sections 4.5 and 4.3.1.

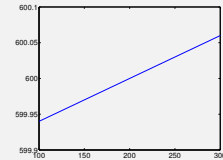
We assume a constant rock compressibility c_r . Accordingly, the pore volume p_v of a grid cell obeys the differential equation¹ $c_r p_v = dp_v/dp$ or

$$p_v(p) = p_{v_r} e^{c_r(p-p_r)}, \quad (12.6)$$

where p_{v_r} is the pore volume at reference pressure p_r . To define the relation between pore volume and pressure, we use an anonymous function:

```
cr = 1e-6/barsa;
p_r = 200*barsa;
pv_r = poreVolume(G, rock);

pv = @(p) pv_r .* exp( cr * (p - p_r) );
```

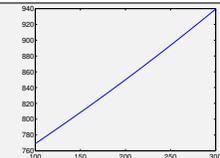


The fluid is assumed to have a constant viscosity, $\mu = 5$ cP. As for the rock, we assume a constant fluid compressibility c resulting in the differential equation $c\rho = d\rho/dp$ for the fluid density. Accordingly,

$$\rho(p) = \rho_r e^{c(p-p_r)}, \quad (12.7)$$

where ρ_r is the density at reference pressure p_r . With this set, we can define the equation-of-state for the fluid:

```
mu = 5*centi*poise;
c = 1e-3/barsa;
rho_r = 850*kilogram/meter^3;
rhoS = 750*kilogram/meter^3;
rho = @(p) rho_r .* exp( c * (p - p_r) );
```



¹ To make a closer correspondence between the computer code and the mathematical equation, we deliberately violate the advice of never using a compound symbol to denote a single mathematical quantity.

```

show = true(G.cells.num,1);
cellInx = sub2ind(G.cartDims, ...
    [I-1; I-1; I; I; I(1:2)-1], ...
    [J ; J; J; J; nperf + [2;2]], ...
    [K-1; K; K; K-1; K(1:2)-[0; 1]]);
show(cellInx) = false;
plotCellData(G,p_init/barsa, show, ...
    'EdgeColor','k');
plotWell(G,W, 'height',10);
view(-125,20), camproj perspective

```

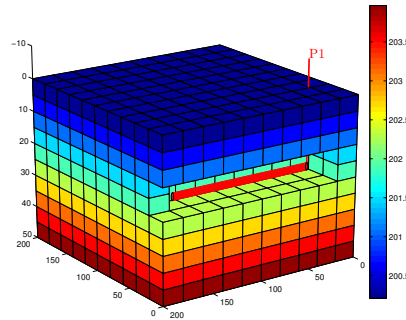


Fig. 12.1. Model with initial pressure and single horizontal well.

The assumption of constant compressibility will only hold for a limited range of temperatures. Surface conditions are not inside the validity range of the constant compressibility assumption. We therefore set the fluid density ρ_S at surface conditions separately since we will need it later to evaluate surface volume rate in our model of the well, which here is a horizontal wellbore perforated in eight cells:

```

nperf = 8;
I = repmat(2, [nperf, 1]);
J = (1:nperf).' + 1;
K = repmat(5, [nperf, 1]);
cellInx = sub2ind(G.cartDims, I, J, K);
W = addWell([], G, rock, cellInx, 'Name', 'producer', 'Dir', 'x');

```

Assuming the reservoir is initially at equilibrium implies that we must have $dp/dz = g\rho(p)$. In our simple setup, this differential equation can be solved analytically, but for demonstration purposes, we use one of MATLAB's built-in ODE-solvers to compute the hydrostatic distribution numerically, relative to a fixed datum point $p(z_0) = p_r$, where we without lack of generality have set $z_0 = 0$ since the reservoir geometry is defined relative to this height:

```

gravity reset on, g = norm(gravity);
[z_0, z_max] = deal(0, max(G.cells.centroids(:,3)));
equil = ode23(@(z,p) g .* rho(p), [z_0, z_max], p_r);
p_init = reshape(deval(equil, G.cells.centroids(:,3)), [], 1);

```

This finishes the model setup, and at this stage we plot the reservoir with well and initial pressure as shown in Figure 12.1.

12.2.2 Discrete operators and equations

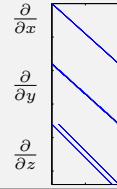
We are now ready to discretize the model. As seen in Section 6.4.2, the discrete version of the divergence operator is a linear mapping from the set of faces to the set of cells, and for a flux field, it sums the outward fluxes for each cell.

The discrete gradient operator maps from the set of cells to the set of faces, and for a pressure-field, it computes the pressure increase between neighboring cells of each face. Because of our assumption of no-flow boundary conditions (except at the well), we restrict the flow equations to the interior faces of the grid and start by computing the map between interior faces and cells

```
N = double(G.faces.neighbors);
intInx = all(N ~ 0, 2);
N = N(intInx, :);
```

In MATLAB notation with N defined as above, it follows that $\mathbf{grad}(\mathbf{x}) = \mathbf{x}(N(:,2)) - \mathbf{x}(N(:,1)) = \mathbf{C}\mathbf{x}$, where the matrix \mathbf{C} is defined in the code below. As a linear mapping, the discrete `div`-function is simply the negative transpose of `grad`; this follows from the discrete version of the Gauss–Green theorem, (6.57). In addition, we define an *average*-mapping that for each face computes the arithmetic average of the neighboring cells, which we will need to evaluate density values at grid faces:

```
n = size(N,1);
C = sparse([(1:n)'; (1:n)'], N, ...
           ones(n,1)*[-1 1], n, G.cells.num);
grad = @(x) C*x;
div = @(x) -C'*x;
avg = @(x) 0.5 * (x(N(:,1)) + x(N(:,2)));
```



This is all we need to define the spatial discretization for a homogeneous medium on a grid with cubic cells. To also account for cell geometries and heterogeneities in the spatial discretization, we use the `MRST`-function `computeTrans`, which we have seen in Section 7.2 computes the half transmissibilities associated with the two-point flux-approximation (TPFA) discretization. This means that we need to take the harmonic average to obtain face-transmissibilities, i.e., for neighboring cells i and j , $T_{ij} = (T_{i,j}^{-1} + T_{j,i}^{-1})^{-1}$ as in (6.51).

```
hT = computeTrans(G, rock);           % Half-transmissibilities
cf = G.cells.faces(:,1);
nf = G.faces.num;
T = 1 ./ accumarray(cf, 1 ./ hT, [nf, 1]); % Harmonic average
T = T(intInx);                       % Restricted to interior
```

Having defined the necessary discrete operators, we are in a position to use the basic implicit discretization from (12.2). We start with Darcy's law (12.2b), which for each face f can be written

$$\vec{v}[f] = -\frac{\mathbf{T}[f]}{\mu} (\mathbf{grad}(p) - g \rho_a[f] \mathbf{grad}(z)), \quad (12.8)$$

where the density at the interface is evaluated using the arithmetic average

$$\rho_a[f] = \frac{1}{2}(\rho[N_1(f)] + \rho[N_2(f)]). \quad (12.9)$$

Similarly, we can write the continuity equation for each cell c as

$$\frac{1}{\Delta t} \left[(\phi(\mathbf{p})[c] \rho(\mathbf{p})[c])^{n+1} - (\phi(\mathbf{p})[c] \rho(\mathbf{p})[c])^n \right] + \text{div}(\rho_a \mathbf{v})[c] = \mathbf{0}. \quad (12.10)$$

The two residual equations (12.8) and (12.10) are implemented as anonymous functions of pressure:

```
gradz = grad(G.cells.centroids(:,3));
v = @p - (T/mu).*( grad(p) - g*avg(rho(p)).*gradz );

presEq = @p,p0,dt (1/dt)*(pv(p).*rho(p) - pv(p0).*rho(p0)) ...
          + div( avg(rho(p)).*v(p) );
```

In the code above, $\mathbf{p0}$ is the pressure field at the *previous* time step (i.e., \mathbf{p}^n), while \mathbf{p} is the pressure at the *current* time step (\mathbf{p}^{n+1}). Having defined the discrete expression for Darcy-fluxes, we can check that this is in agreement with our initial pressure field by computing the magnitude of the flux, $\text{norm}(\mathbf{v}(\mathbf{p}_{\text{init}})) \cdot \text{day}$. The result is $1.5 \times 10^{-6} \text{ m}^3/\text{day}$, which should convince us that the initial state of the reservoir is sufficiently close to equilibrium.

12.2.3 Well model

The production well will appear as a source term in the pressure equation. We therefore need to define an expression for flow rate in all cells in which the well is connected to the reservoir (which we will refer to as well connections). Inside the well, we assuming instantaneous flow so that the pressure drop is always hydrostatic. For a horizontal well, the hydrostatic term is zero and could obviously be disregarded, but we include it for completeness and as a robust precaution, in case we later want to reuse the code with a different well path. Approximating the fluid density in the well as constant, computed at bottom-hole pressure, the pressure $\mathbf{p}_c[w]$ in connection w of well $N_w(w)$ is given by

$$\mathbf{p}_c[w] = \mathbf{p}_{bh}[N_w(w)] + g \Delta \mathbf{z}[w] \rho(\mathbf{p}_{bh}[N_w(w)]), \quad (12.11)$$

where $\Delta \mathbf{z}[w]$ is the vertical distance from the bottom-hole to the connection. We use the standard Peaceman model introduced in Section 6.3.2 to relate the pressure at the well connection to the average pressure inside the grid cell. Using the well-indices provided in \mathbf{w} , the mass flow-rate at connection c is then given by

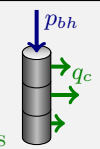
$$\mathbf{q}_c[w] = \frac{\rho(\mathbf{p}[N_c(w)])}{\mu} \text{WI}[w] (\mathbf{p}_c[w] - \mathbf{p}[N_c(w)]), \quad (12.12)$$

where $\mathbf{p}[N_c(w)]$ is the pressure in the cell $N_c(w)$ containing connection w . In our code, this model is implemented as follows:

```

wc = W(1).cells; % connection grid cells
WI = W(1).WI; % well-indices
dz = W(1).dz; % depth relative to bottom-hole

p_conn = @(bhp) bhp + g*dz.*rho(bhp); %connection pressures
q_conn = @(p, bhp) WI .* (rho(p(wc)) / mu) .* (p_conn(bhp) - p(wc));
    
```



We also include the total volumetric well-rate at surface conditions as a free variable. This is simply given by summing all mass well-rates and dividing by the surface density:

```

rateEq = @(p, bhp, qS) qS - sum(q_conn(p, bhp))/rhoS;
    
```

With free variables p , bhp , and qS , we are now lacking exactly one equation to close the system. This equation should account for *boundary conditions* in the form of a well-control. Here, we choose to control the well by specifying a fixed bottom-hole pressure

```

ctrlEq = @(bhp) bhp - 100*barsa;
    
```

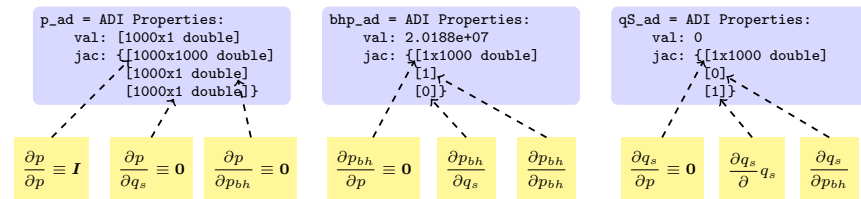
12.2.4 The simulation loop

What now remains is to set up a simulation loop that will evolve the transient pressure. We start by initializing the AD variables. For clarity, we append `_ad` to all variable names to distinguish them from doubles. The initial bottom-hole pressure is set to the corresponding grid-cell pressure.

```

[p_ad, bhp_ad, qS_ad] = initVariablesADI(p_init, p_init(wc(1)), 0);
    
```

This gives the following AD pairs that make up the unknowns in our system:



To solve the global flow problem, we will have to stack all the equations into one big system for which we can compute the Jacobian and perform a Newton update. We therefore set indices for easy access to individual variables in the stack:

```

[p_ad, bhp_ad, qS_ad] = initVariablesADI(p_init, p_init(wc(1)), 0);
nc = G.cells.num;
[pIx, bhpIx, qSIx] = deal(1:nc, nc+1, nc+2);
    
```

Next, we set parameters to control the time steps in the simulation and the iterations in the Newton solver:

```
numSteps = 52;           % number of time-steps
totTime = 365*day;      % total simulation time
dt       = totTime / numSteps; % constant time step
tol      = 1e-5;        % Newton tolerance
maxits   = 10;          % max number of Newton its
```

Simulation results from all time steps are stored in a structure `sol`. For efficiency, this structure is preallocated and initialized so that the first entry is the initial state of the reservoir:

```
sol = repmat(struct('time', [], 'pressure', [], 'bhp', [], ...
                  'qS', []), [numSteps + 1, 1]);
sol(1) = struct('time', 0, 'pressure', double(p_ad), ...
               'bhp', double(bhp_ad), 'qS', double(qS_ad));
```

We now have all we need to set up the time-stepping algorithm, which consists of an outer and an inner loop. The outer loop updates the time step, advances the solution one step forward in time, and stores the result in the `sol` structure. This procedure is repeated until we reach the desired final time:

```
t = 0; step = 0;
while t < totTime,
    t = t + dt; step = step + 1;
    fprintf('\nTime step %d: Time %.2f -> %.2f days\n', ...
           step, convertTo(t - dt, day), convertTo(t, day));
    % Newton loop
    resNorm = 1e99;
    p0 = double(p_ad); % Previous step pressure
    nit = 0;
    while (resNorm > tol) && (nit <= maxits)
        : % Newton update
        :
        resNorm = norm(res);
        nit     = nit + 1;
        fprintf(' Iteration %3d: Res = %.4e\n', nit, resNorm);
    end
    if nit > maxits, error('Newton solves did not converge')
    else % store solution
        sol(step+1) = struct('time', t, 'pressure', double(p_ad), ...
                           'bhp', double(bhp_ad), 'qS', double(qS_ad));
    end
end
```

The inner loop performs the Newton iteration by computing and assembling the Jacobian of the global system and solving the linearized residual equation to compute an iterative update. The first step to this end is to evaluate the residual for the flow pressure equation and add source terms from wells:

```

eq1    = presEq(p_ad, p0, dt);
eq1(wc) = eq1(wc) - q_conn(p_ad, bhp_ad);

```

Most of the lines we have implemented so far are fairly standard, except perhaps for the definition of the residual equations as anonymous functions, and equivalent statements can be found in almost any computer program solving this type of time-dependent equation by an implicit method. Now, however, comes what is normally the tricky part: linearization of the equations that make up the whole model and assembly of the resulting Jacobian matrices to generate the Jacobian for the full system. And here you have the magic of automatic differentiation – *you do not have to do this at all!* The computer code necessary to evaluate all the Jacobians has been defined implicitly by the functions in the AD class in MRST that overloads the elementary operators used to define the residual equations. The calling sequence is obviously more complex than the one depicted in Figure 2.6 on page 33, but the operators used are in fact only the three elementary operators plus, minus, and multiply applied to scalars, vectors, and matrices, as well as element-wise division by a scalar. When the residuals are evaluated using the anonymous functions defined above, the AD library also evaluates the derivatives of each equation with respect to each independent variable and collects the corresponding sub-Jacobians in a list. To form the full system, we simply evaluate the residuals of the remaining equations (the rate equation and the equation for well control) and concatenate the three equations into a cell array:

```

eqs = {eq1, rateEq(p_ad, bhp_ad, qS_ad), ctrlEq(bhp_ad)};
eq  = cat(eqs{:});

```

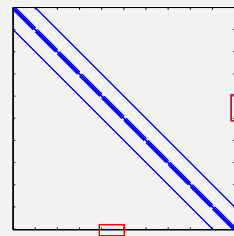
In doing this, the AD library will correctly combine the various sub-Jacobians and set up the Jacobian for the full system. Then, we can extract this Jacobian, compute the Newton increment, and update the three primary unknowns:

```

J    = eq.jac{1}; % Jacobian
res  = eq.val;   % residual
upd  = -(J \ res); % Newton update

% Update variables
p_ad.val = p_ad.val + upd(pIx);
bhp_ad.val = bhp_ad.val + upd(bhpIx);
qS_ad.val = qS_ad.val + upd(qSIx);

```



The sparsity pattern of the Jacobian is shown in the plot to the left of the code for the Newton update. The use of a two-point scheme on a 3D Cartesian grid gives a Jacobi matrix that has a heptadiagonal structure, except for the off-diagonal entries in the two red rectangles that arise from the well equation and correspond to derivatives of this equation with respect to cell pressures.

Figure 12.2 shows a plot of the dynamics of the solution. Initially, the pressure is in hydrostatic equilibrium as shown in Figure 12.1. As the well

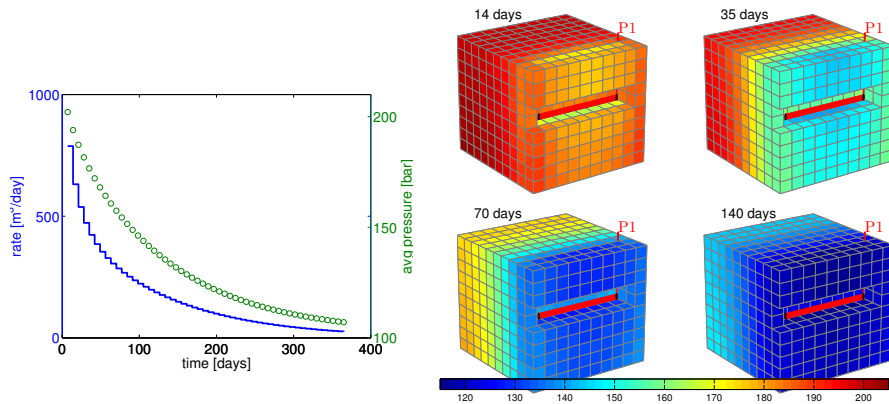


Fig. 12.2. Time evolution of the pressure solution for the compressible single-phase problem. The plot to the left shows the well rate (blue line) and average reservoir pressure (green circles) as function of time, and the plots to the right show the pressure after two, five, ten, and twenty pressure steps.

starts to drain the reservoir, there is a draw-down in the pressure near the well which gradually propagates from the well and outward. As a result, the average pressure inside the reservoir is reduced, which again causes a decay in the production rate.

COMPUTER EXERCISES:

73. Apply the compressible pressure solver introduced above to the quarter five-spot problem discussed in Section 7.4.1.
74. Apply the compressible pressure solver to the three different grid models studied in Section 7.4.3 that were derived from the `seamount` data set. Replace the fixed boundary conditions by a no-flow condition.
75. Use the implementation introduced in Section 12.2 as a template to develop a solver for slightly compressible flow (12.3). More details about this model can be found on page 158 in Section 6.2. How large can c_f be before the assumptions in the slightly compressible model become inaccurate? Use different heterogeneities, well placements, and/or model geometries to investigate this question in more detail.
76. Extend the compressible solver in to incorporate other boundary conditions than no flow.
77. Try to compute time-of-flight by extending the equation set to also include the time-of-flight equation (6.39). Hint: the time-of-flight and the pressure equations need not be solved as a coupled system.
78. Same as above, except that you should try to reuse the solver introduced in Section 7.3. Hint: you must first reconstruct fluxes from the computed pressure and then construct a state object to communicate with the TOF solver.

12.3 Pressure-dependent viscosity

One particular advantage of using automatic differentiation in combination with the discrete differential and averaging operators is that it simplifies the testing of new models and alternative computational approaches. In this section, we discuss two examples that hopefully demonstrate this aspect.

In the model discussed in the previous section, the viscosity was assumed to be constant. However, in the general case the viscosity will increase with increasing pressures and this effect may be significant for the high pressures seen inside a reservoir. To illustrate, we introduce a linear dependence, rather than the exponential pressure-dependence used for the pore volume (12.6) and the fluid density (12.7). That is, we assume that the viscosity is given by

$$\mu(p) = \mu_0 [1 + c_\mu(p - p_r)]. \quad (12.13)$$

Having a pressure dependence means that we have to change two parts of our discretization: the approximation of the Darcy flux across a cell face (12.8) and the flow rate through a well connection (12.12). Starting with the latter, we evaluate the viscosity using the same pressure as was used to evaluate the density, i.e.,

$$\mathbf{q}_c[w] = \frac{\rho(\mathbf{p}[N_c(w)])}{\mu(\mathbf{p}[N_c(w)])} \text{WI}[w] (\mathbf{p}_c[w] - \mathbf{p}[N_c(w)]). \quad (12.14)$$

For the Darcy flux (12.8), we have two choices: either use a simple arithmetic average as in (12.9) to approximate the viscosity at each cell face,

$$\mathbf{v}[f] = - \frac{\mathbf{T}[f]}{\mu_a[f]} (\mathbf{grad}(\mathbf{p}) - g \rho_a[f] \mathbf{grad}(z)), \quad (12.15)$$

or replace the quotient of the transmissibility and the face viscosity by the harmonic average of the mobility $\lambda = K/\mu$ in the adjacent cells. Both choices introduce changes in the structure of the discrete nonlinear system, but because we are using automatic differentiation, all we have to do is code the corresponding formulas. Let us look at the details of the implementation in MRST, starting with the arithmetic approach.

Arithmetic average

First, we introduce a new anonymous function to evaluate the relation between viscosity and pressure:

```
[mu0,c_mu] = deal(5*centi*poise, 2e-3/barsa);
mu = @(p) mu0*(1+c_mu*(p-p_r));
```

Then, we can replace the definition of the Darcy flux (changes marked in red):

```
v = @(p) -(T./mu(avg(p))).*( grad(p) - g*avg(rho(p)).*gradz );
```

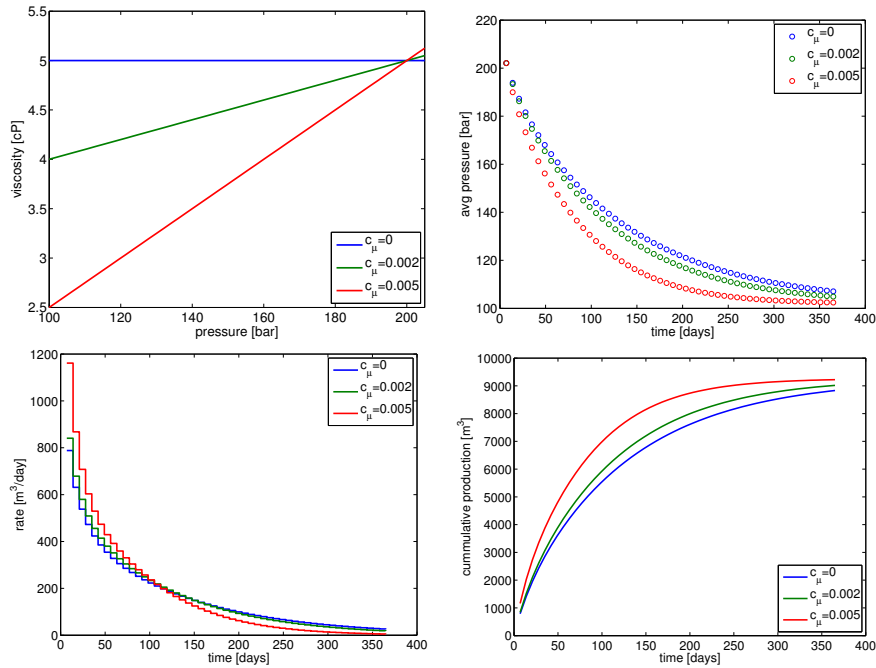


Fig. 12.3. The effect of increasing the degree of pressure-dependence for the viscosity.

and similarly for flow rate through each well connection:

$$q_{\text{conn}} = @(\text{p}, \text{bhp}) \text{ WI} \cdot (\text{rho}(\text{p}(\text{wc})) ./ \text{mu}(\text{p}(\text{wc}))) \cdot (\text{p}_{\text{conn}}(\text{bhp}) - \text{p}(\text{wc}));$$

In Figure 12.3 we illustrate the effect of increasing the pressure dependence of the viscosity. Since the reference value is given at $p = 200$ bar which is close to the initial pressure inside the reservoir, the more we increase c_μ , the lower μ will be in the pressure draw-down zone near the well. Therefore, we see a significantly higher initial production rate for $c_\mu = 0.005$ than for $c_\mu = 0$. On the other hand, the higher value of c_μ , the faster the draw-down effect of the well will propagate into the reservoir, inducing a reduction in reservoir pressure that eventually will cause production to cease. In terms of overall production, a stronger pressure dependence may be more advantageous as it leads to a higher total recovery and higher cumulative production early in the production period.

Face mobility: harmonic average

A more correct approximation is to write Darcy's law based on mobility instead of using the quotient of the transmissibility and an averaged viscosity:

$$\mathbf{v}[f] = -\mathbf{A}[f] (\text{grad}(\mathbf{p}) - g \rho_a[f] \text{grad}(\mathbf{z})). \quad (12.16)$$

The face mobility $\mathbf{A}[f]$ can be defined in the same way as the transmissibility is defined in terms of the half transmissibilities using harmonic averages. That is, if $\mathbf{T}[f, c]$ denotes the half transmissibility associated with face f and cell c , the face mobility $\mathbf{A}[f]$ for face f can be written as

$$\mathbf{A}[f] = \left(\frac{\mu[N_1(f)]}{\mathbf{T}[f, N_1(f)]} + \frac{\mu[N_2(f)]}{\mathbf{T}[f, N_2(f)]} \right)^{-1}. \quad (12.17)$$

In MRST, the corresponding code reads:

```
hf2cn = getCellNoFaces(G);
nhf   = numel(hf2cn);
hf2f  = sparse(double(G.cells.faces(:,1)),(1:nhf)',1);
hf2if = hf2f(intInx,:);
fmob  = @(mu,p) 1./(hf2if*(mu(p(hf2cn))./hT));

v = @(p) -fmob(mu,p).*( grad(p) - g*avg(rho(p)).*gradz );
```

Here, `hf2cn` represents the maps N_1 and N_2 that enable us to sample the viscosity value in the correct cell for each half-face transmissibility, whereas `hf2if` represents a map from half faces (i.e., faces seen from a single cell) to global faces (which are shared by two cells). The map has a unit value in row i and column j if half face j belongs to global face i . Hence, premultiplying a vector of half-face quantities by `hf2if` amounts to summing the contributions from cells $N_1(f)$ and $N_2(f)$ for each global face f .

Using the harmonic average for a homogeneous model should produce simulation results that are identical (to machine precision) to those produced by using arithmetic average. With heterogeneous permeability, there will be small differences in the well rates and averaged pressures for the specific parameters considered herein. For sub-samples of the SPE 10 data set, we typically observe maximum relative differences in well rates of the order 10^{-3} .

COMPUTER EXERCISES:

79. Investigate the claim that the difference between using an arithmetic average of the viscosity and a harmonic average of the fluid mobility is typically small. To this end, you can for instance use the following sub-sample from the SPE10 data set: `rock = SPE10_rock(41:50,101:110,1:10)`

12.4 Non-Newtonian fluid

Viscosity is the material property that measures a fluid's resistance to flow, i.e., the resistance to a change in shape, or to the movement of neighboring portions of the fluid relative to each other. The more viscous a fluid is, the less

easily it will flow. In Newtonian fluids, the shear stress or the force applied per area tangential to the force, at any point is proportional to the strain rate (the symmetric part of the velocity gradient) at that point and the viscosity is the constant of proportionality. For non-Newtonian fluids, the relationship is no longer linear. The most common nonlinear behavior is shear thinning, in which the viscosity of the system decreases as the shear rate is increased. An example is paint, which should flow easily when leaving the brush, but stay on the surface and not drip once it has been applied. The second type of nonlinearity is shear thickening, in which the viscosity increases with increasing shear rate. A common example is the mixture of cornstarch and water. If you search YouTube for “cornstarch pool” you can view several spectacular videos of pools filled with this mixture. When stress is applied to the mixture, it exhibits properties like a solid and you may be able to run across its surface. However, if you go too slow, the fluid behaves more like a liquid and you fall in.

Solutions of large polymeric molecules are another example of shear-thinning liquids. In enhanced oil recovery, polymer solutions may be injected into reservoirs to improve unfavorable mobility ratios between oil and water and improve the sweep efficiency of the injected fluid. At low flow rates, the polymer molecule chains tumble around randomly and present large resistance to flow. When the flow velocity increases, the viscosity decreases as the molecules gradually align themselves in the direction of increasing shear rate. A model of the rheology is given by

$$\mu = \mu_\infty + (\mu_0 - \mu_\infty) \left(1 + \left(\frac{K_c}{\mu_0} \right)^{\frac{2}{n-1}} \dot{\gamma}^2 \right)^{\frac{n-1}{2}}, \quad (12.18)$$

where μ_0 represents the Newtonian viscosity at zero shear rate, μ_∞ represents the Newtonian viscosity at infinite shear rate, K_c represents the consistency index, and n represents the power-law exponent ($n < 1$). The shear rate $\dot{\gamma}$ in a porous medium can be approximated by

$$\dot{\gamma}_{\text{app}} = 6 \left(\frac{3n+1}{4n} \right)^{\frac{n}{n-1}} \frac{|\vec{v}|}{\sqrt{K\phi}}. \quad (12.19)$$

Combining (12.18) and (12.19), we can write our model for the viscosity as

$$\mu = \mu_0 \left(1 + \bar{K}_c \frac{|\vec{v}|^2}{K\phi} \right)^{\frac{n-1}{2}}, \quad \bar{K}_c = 36 \left(\frac{K_c}{\mu_0} \right)^{\frac{2}{n-1}} \left(\frac{3n+1}{4n} \right)^{\frac{2n}{n-1}}, \quad (12.20)$$

where we for simplicity have assumed that $\mu_\infty = 0$.

Rapid prototyping

In the following, we show how easy it is to extend the simulator developed in the previous sections to model this non-Newtonian fluid behavior (see `nonNewtonianCell.m`). To simulate injection, we increase the bottom-hole pressure to 300 bar. Our rheology model has parameters:

```

mu0 = 100*centi*poise;
nmu = 0.3;
Kc = .1;
Kbc = (Kc/mu0)^(2/(nmu-1))*36*((3*nmu+1)/(4*nmu))^(2*nmu/(nmu-1));

```

In principle, we could continue to solve the system using the same primary unknowns as before. However, it has proved convenient to write (12.20) in the form $\mu = \eta \mu_0$ and introduce η as an additional unknown. In each Newton step, we start by solving the equation for the shear factor η exactly for the given pressure distribution. This is done by initializing an AD variable for η , but not for p in `etaEq` so that this residual now only has one unknown, η . This will take out the implicit nature of Darcy's law and hence reduce the nonlinearity and simplify the solution of the global system.

```

while (resNorm > tol) && (nit < maxits)

% Newton loop for eta (shear multiplier)
[resNorm2,nit2] = deal(1e99, 0);
eta_ad2 = initVariablesADI(eta_ad.val);
while (resNorm2 > tol) && (nit2 <= maxits)
    eeQ = etaEq(p_ad.val, eta_ad2);
    res = eeQ.val;
    eta_ad2.val = eta_ad2.val - (eeQ.jac{1} \ res);
    resNorm2 = norm(res);
    nit2 = nit2+1;
end
eta_ad.val = eta_ad2.val;

```

Once the shear factor has been computed for the values in the previous iterate, we can use the same approach as earlier to compute a Newton update for the full system. (Here, `etaEq` is treated as a system with two unknowns, p and η .)

```

eq1 = presEq(p_ad, p0, eta_ad, dt);
eq1(wc) = eq1(wc) - q_conn(p_ad, eta_ad, bhp_ad);
eqs = {eq1, etaEq(p_ad, eta_ad), ...
    rateEq(p_ad, eta_ad, bhp_ad, qS_ad), ctrlEq(bhp_ad)};
eq = cat(eqs{:});
upd = -(eq.jac{1} \ eq.val); % Newton update

```

To finish the solver, we need to define the flow equations and the extra equation for the shear multiplier. The main question to this end is: how should we compute $|\vec{v}|$? One solution could be to define $|\vec{v}|$ on each face as the flux divided by the face area. In other words, use a code like

```

phiK = avg(rock.perm.*rock.poro)./G.faces.areas(intInx).^2;
v = @(p, eta) -(T./(mu0*eta)).*( grad(p) - g*avg(rho(p)).*gradz );
etaEq = @(p, eta) eta - (1 + Kbc*v(p,eta).^2./phiK).^((nmu-1)/2);

```

Although simple, this approach has three potential issues: First, it does not tell us how to compute the shear factor for the well perforations. Second, it disregards contributions from any tangential components of the velocity field. Third, the number of unknowns in the linear system increases by almost a factor six since we now have one extra unknown per internal face. The first issue is easy to fix: To get a representative value in the well cells, we simply average the η values from the cells' faces. If we now recall how the discrete divergence operator was defined, we realize that this operation is almost implemented for us already: if $\text{div}(\mathbf{x}) = -\mathbf{C}' * \mathbf{x}$ computes the discrete divergence in each cell of the field \mathbf{x} defined at the faces, then $\text{cavg}(\mathbf{x}) = 1/6 * \text{abs}(\mathbf{C})' * \mathbf{x}$ computes the average of \mathbf{x} for each cell. In other words, our well equation becomes:

```
wavg = @(eta) 1/6*abs(C(:,W.cells))'*eta;
q_conn = @(p, eta, bhp) ...
WI .* (rho(p(wc)) ./ (mu0*wavg(eta))) .* (p_conn(bhp) - p(wc));
```

The second issue would have to be investigated in more detail and this is not within the scope of this book. The third issue is simply a disadvantage.

To get a method that consumes less memory, we can compute one η value per cell. Using the following formula, we can compute an approximate velocity \vec{v}_i at the center of cell i

$$\vec{v}_i = \sum_{j \in N(i)} \frac{v_{ij}}{V_i} (\vec{c}_{ij} - \vec{c}_i), \quad (12.21)$$

where $N(i)$ is the map from cell i to its neighboring cells, v_{ij} is the flux between cell i and cell j , \vec{c}_{ij} is the centroid of the corresponding face, and \vec{c}_i is the centroid of cell i . For a Cartesian grid, this formula simplifies so that an approximate velocity can be obtained as the sum of the absolute value of the flux divided by the face area over all faces that make up a cell. Using a similar trick as we used to compute η in well cells above, our implementation follows trivially. We first define the averaging operator to compute cell velocity

```
aC = bsxfun(@rdivide, 0.5*abs(C), G.faces.areas(intInx));
cavg = @(x) aC*x;
```

In doing so, we also rename our old averaging operator `avg` as `favg` to avoid confusion and make it more clear that this operator maps from cell values to face values. Then we can define the needed equations:

```
phiK = rock.perm.*rock.poro;
gradz = grad(G.cells.centroids(:,3));
v = @(p, eta)
    -(T./(mu0*favg(eta)).*( grad(p) - g*favg(rho(p)).*gradz ));
etaEq = @(p, eta)
    eta - ( 1 + Kbc* cavg(v(p,eta)).^2 ./phiK ).^((nmu-1)/2);
presEq = @(p, p0, eta, dt) ...
    (1/dt)*(pv(p).*rho(p) - pv(p0).*rho(p0)) + div(favg(rho(p)).*v(p, eta));
```

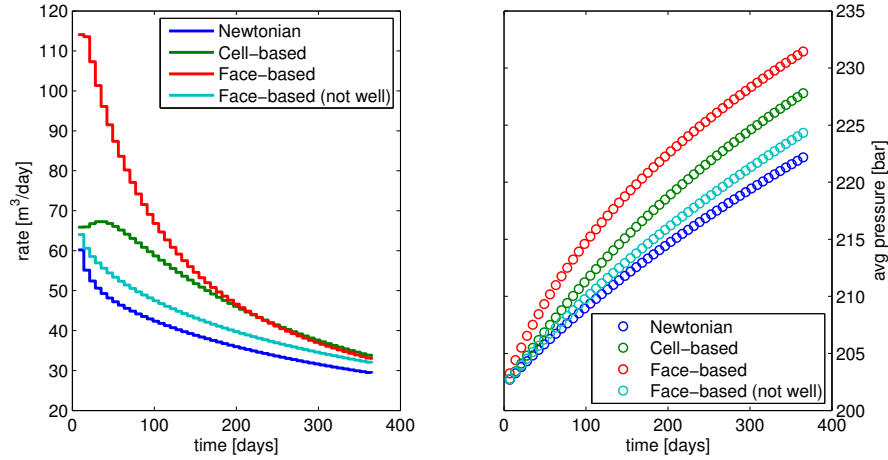


Fig. 12.4. Single-phase injection of a highly viscous, shear-thinning fluid computed by four different simulation methods: (i) fluid assumed to be Newtonian, (ii) shear multiplier η computed in cells, (iii) shear multiplier computed at faces, and (iv) shear multiplier computed at faces, but $\eta \equiv 1$ used in well model.

With this approach the well equation becomes particularly simple since all we need to do is to sample the η value from the correct cell:

```
q_conn = @(p, eta, bhp) ...
    WI .* (rho(p(wc)) ./ (mu0*eta(wc))) .* (p_conn(bhp) - p(wc));
```

A potential drawback of this second approach is that it may introduce numerical smearing, but this will, on the other hand, most likely increase the robustness of the resulting scheme.

In Figure 12.4 we compare the predicted flow rates and average reservoir pressure for two different fluid models: one that assumes that the fluid is a standard Newtonian fluid (i.e., $\eta \equiv 1$) and one that models shear thinning, which has been computed by both methods discussed above. With shear thinning, the higher pressure in the injection well causes a decrease in the viscosity which leads to significantly higher injection rates than for the Newtonian fluid and hence a higher average reservoir pressure. Perhaps more interesting is the large discrepancy in the rates and pressures predicted by the face-based and the cell-based simulation algorithms. If we in the face-based method disregard the shear multiplier q_conn , the predicted rate and pressure build-up is smaller than what is predicted by the cell-based method and closer to the Newtonian fluid case. We take this as evidence that the differences between the cell and the face-base methods to a large extent can be explained by differences in the discretized well models and their ability to capture the formation and propagation of the strong initial transient. To further back this up, we have included results from a simulation with ten times as many time steps in

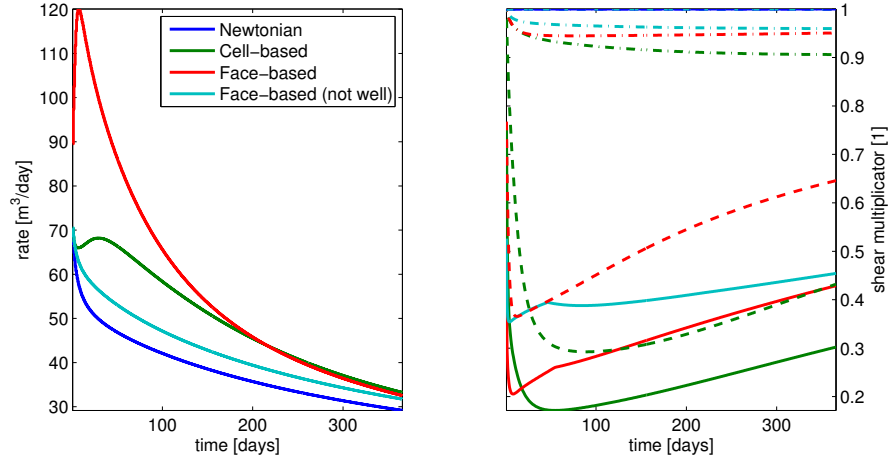


Fig. 12.5. Single-phase injection of a highly viscous, shear-thinning fluid; simulation with $\Delta t = 1/520$ year. The right plot shows the evolution of η as a function of time: solid lines show $\min(\eta)$ over all cells, dashed lines $\min(\eta)$ over the perforated cells, and dash-dotted lines average η value.

Figure 12.5, which also includes plots of the evolution of $\min(\eta)$ as a function of time. Whereas the face-based method predicts a large, immediate drop in viscosity in the near-well region, the viscosity drop predicted by the cell-based method is much smaller during the first 20–30 days. This results in a delay in the peak in the injection rate and a much smaller injected volume.

We leave the discussion here. The parameters used in the example were chosen quite haphazardly to demonstrate a pronounced shear-thinning effect. Which method is the most correct for real computations, is a question that goes beyond the current scope, and could probably best be answered by verifying against observed data for a real case. Our point here, was mainly to demonstrate the capability of rapid prototyping that comes with the use of MRST. However, as the example shows, this lunch is not completely free: you still have to understand features and limitations of the models and discretizations you choose to prototype.

COMPUTER EXERCISES:

80. Investigate whether the large differences observed in Figures 12.4 and 12.5 between the cell-based and face-based approaches to the non-Newtonian flow problem is a result of insufficient grid resolution.
81. The non-Newtonian fluid example has a strong transient during the first 30–100 days. Try to implement adaptive time steps that utilizes this fact. Can you come up with a strategy that automatically chooses good time steps?

12.5 Thermal effects

As another example of rapid prototyping, we extend the single-phase flow model (12.1) to account for thermal effects. That is, we assume that $\rho(p, T)$ is now a function of pressure and temperature T and extend our model to also include conservation on energy,

$$\frac{\partial}{\partial t} [\phi \rho] + \nabla \cdot [\rho \vec{v}] = q, \quad \vec{v} = -\frac{\mathbf{K}}{\mu} [\nabla p - g\rho \nabla z] \quad (12.22a)$$

$$\frac{\partial}{\partial t} [\phi \rho E_f(p, t) + (1 - \phi) E_r] + \nabla \cdot [\rho H_f \vec{v}] - \nabla \cdot [\kappa \nabla T] = q_e \quad (12.22b)$$

Here, the rock and the fluid are assumed to be in local thermal equilibrium. In the energy equation (12.22b), E_f is energy density per mass of the fluid, $H_f = E_f + p/\rho$ is enthalpy density per mass, E_r is energy per volume of the rock, and κ is the heat conduction coefficient of the rock. Fluid pressure p and temperature T are used as primary variables.

As in the original isothermal simulator, we must first define constitutive relationships that express the various physical quantities in terms of the primary variables. The energy equation includes heating of the solid rock, and we therefore start by defining a quantity that keeps track of the solid volume, which also depends on pressure:

```
sv = @ (p) G.cells.volumes - pv(p);
```

For the fluid model, we use

$$\begin{aligned} \rho(p, T) &= \rho_r [1 + \beta_T (p - p_r)] e^{-\alpha (T - T_r)}, \\ \mu(p, T) &= \mu_0 [1 + c_\mu (p - p_r)] e^{-c_T (T - T_r)}, \end{aligned} \quad (12.23)$$

where $\rho_r = 850 \text{ kg/m}^3$ is the density and $\mu_0 = 5 \text{ cP}$ is the viscosity of the fluid at reference conditions with pressure $p_r = 200 \text{ bar}$ and temperature $T_r = 300 \text{ K}$. The constants are $\beta_T = 10^{-3} \text{ bar}^{-1}$, $\alpha = 5 \times 10^{-3} \text{ K}^{-1}$, $c_\mu = 2 \times 10^{-3} \text{ bar}^{-1}$, and $c_T = 10^{-3} \text{ K}^{-1}$. This translates to the following code:

```
mu0 = 5*centi*poise;
cmup = 2e-3/barsa;
cmut = 1e-3;
T_r = 300;
mu = @ (p,T) mu0*(1+cmup*(p-p_r)).*exp(-cmut*(T-T_r));

beta = 1e-3/barsa;
alpha = 5*1e-3;
rho_r = 850*kilogram/meter^3;
rho = @ (p,T) rho_r .* (1+beta*(p-p_r)) .* exp(-alpha*(T-T_r));
```

We use a simple linear relation for the enthalpy, which is based on the thermodynamical relations that give

$$dH_f = c_p dT + \left(\frac{1 - \alpha T_r}{\rho} \right) dp, \quad \alpha = - \frac{1}{\rho} \frac{\partial \rho}{\partial T} \Big|_p, \quad (12.24)$$

where $c_p = 4 \times 10^3$ J/kg. The corresponding code for the enthalpy and energy densities reads:

```
Cp = 4e3;
Hf = @(p,T) Cp*T+(1-T_r*alpha).*(p-p_r)./rho(p,T);
Ef = @(p,T) Hf(p,T) - p./rho(p,T);
Er = @(T) Cp*T;
```

We defer discussing the details of these new relationships and only note that it is important that the thermal potentials E_f and H_f are consistent with the equation-of-state $\rho(p, T)$ to get a physically meaningful model.

Having defined all constitutive relationships in terms of anonymous functions, we can set up the equation for mass conservation and Darcy's law (with transmissibility renamed to T_p to avoid name clash with temperature):

```
v = @(p,T) -(Tp./mu(avg(p),avg(T))).*(grad(p) - avg(rho(p,T)).*gdz);
pEq = @(p,T,p0,T0,dt) ...
      (1/dt)*(pv(p).*rho(p,T) - pv(p0).*rho(p0,T0)) ...
      + div( avg(rho(p,T)).*v(p,T) );
```

The energy equation (12.22b) is a bit more complicated. The accumulation and the heat-conduction terms are on the same form as the operators appearing in (12.22a) and can hence be discretized in the same way. This means that we use a rock object to compute transmissibilities for κ instead of K :

```
tmp = struct('perm',4*ones(G.cells.num,1));
hT = computeTrans(G, tmp);
Th = 1 ./ accumarray(cf, 1 ./ hT, [nf, 1]);
Th = Th(intInx);
```

The remaining term in (12.22b), $\nabla \cdot [\rho H_f \vec{v}]$, represents advection of enthalpy and has a differential operator on the same form as the transport equations discussed in Section 6.4.3 and must hence be discretized by an upwind scheme. To this end, we introduce a new discrete operator that will compute the correct upwind value for the enthalpy density,

$$\text{upw}(\mathbf{H})[f] = \begin{cases} \mathbf{H}[N_1(f)], & \text{if } \mathbf{v}[f] > 0, \\ \mathbf{H}[N_2(f)], & \text{otherwise.} \end{cases} \quad (12.25)$$

With this, we can set up the energy equation on residual form

```
upw = @(x,flag) x(N(:,1)).*double(flag)+x(N(:,2)).*double(~flag);

hEq = @(p, T, p0, T0, dt) ...
      (1/dt)*(pv(p).*rho(p,T) .*Ef(p,T) + sv(p).*Er(T) ...
      - pv(p0).*rho(p0,T0).*Ef(p0,T0) - sv(p0).*Er(T0)) ...
      + div( upw(Hf(p,T),v(p,T)>0).*avg(rho(p,T)).*v(p,T) ) ...
      + div( -Th.*grad(T));
```

and are thus almost done. As a last technical detail, we must also make sure that the energy transfer in injection and production wells is modelled correctly using appropriate upwind values:

```

qw      = q_conn(p_ad, T_ad, bhp_ad);
eq1     = pEq(p_ad, T_ad, p0, T0, dt);
eq1(wc) = eq1(wc) - qw;
hq      = Hf(bhp_ad, bhT) .* qw;
Hcells  = Hf(p_ad, T_ad);
hq(qw<0) = Hcells(wc(qw<0)) .* qw(qw<0);
eq2     = hEq(p_ad, T_ad, p0, T0, dt);
eq2(wc) = eq2(wc) - hq;

```

Here, we evaluate the enthalpy using *cell values* for pressure and temperature for production wells (for which $qw < 0$) and pressure and temperatures at the *bottom hole* for injection wells.

What remains, are trivial changes to the iteration loop to declare the correct variables as AD structures, evaluate the discrete equations, collect their residuals, and update the state variables. These details can be found in the complete code given in `singlePhaseThermal.m` and have been left out for brevity.

Understanding thermal expansion

Except for the modifications discussed above, the setup is the exact same as in Section 12.2. That is, the reservoir is a $200 \times 200 \times 50 \text{ m}^3$ rectangular box with homogeneous permeability of 30 mD, constant porosity 0.3, and a rock compressibility of 10^{-6} bar^{-1} , realized on a $10 \times 10 \times 10$ Cartesian grid. The reservoir is realized on a $10 \times 10 \times 10$ Cartesian grid. Fluid is drained from a horizontal well perforated in cells with indices $i = 2, j = 2, \dots, 9$, and $k = 5$, and operating at a constant bottom-hole pressure of 100 bar. Initially, the reservoir has constant temperature of 300 K and is in hydrostatic equilibrium with a datum pressure of 200 bar specified in the uppermost cell centroids.

In the same way as in the isothermal case, the open well will create a pressure draw-down that propagates into the reservoir. As more fluid is produced from the reservoir, the pressure will gradually decay towards a steady state with pressure values between 101.2 and 104.7 bar. Figure 12.6 shows that the simulation predicts a faster pressure draw-down, and hence a faster decay in production rates, if thermal effects are taken into account.

The change in temperature of an expanding fluid will not only depend on the initial and final pressure, but also on the type of process in which the temperature is changed:

- In a *free expansion*, the internal energy is preserved and the fluid does no work. That is, the process can be described by the following differential:

$$\frac{dE_f}{dp} \Delta p + \frac{dE_f}{dT} \Delta T = 0. \quad (12.26)$$

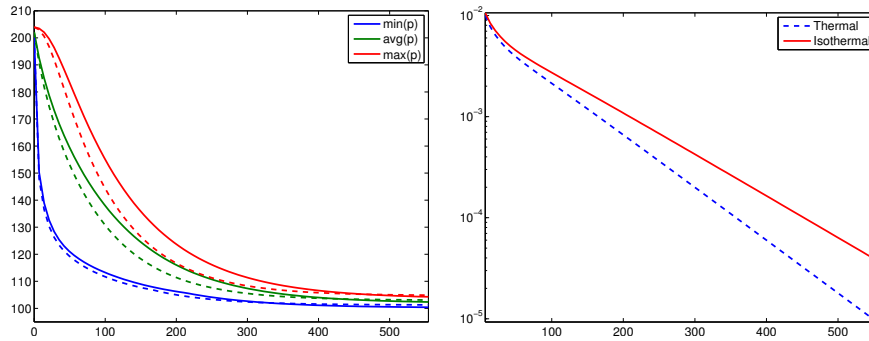


Fig. 12.6. To the left, time evolution for pressure for an isothermal simulation (solid lines) and a thermal simulation with $\alpha = 5 \cdot 10^{-3}$ (dashed lines). To the right, decay in production rate at the surface.

When the fluid is an ideal gas, the temperature is constant, but otherwise the temperature will either increase or decrease during the process depending on the initial temperature and pressure.

- In a reversible process, the fluid is in thermodynamical equilibrium and does positive work while the temperature decreases. The linearized function associated with this *adiabatic expansion* reads,

$$dE + \frac{p}{\rho V} dV = dE + p d\left(\frac{1}{\rho}\right) = 0. \quad (12.27)$$

- In a Joule–Thomson process, the enthalpy remains constant while the fluid flows from higher to lower pressure under steady-state conditions and without change in kinetic energy. That is,

$$\frac{dH_f}{dp} \Delta p + \frac{dH_f}{dT} \Delta T = 0. \quad (12.28)$$

Our case is a combination of these three processes and their interplay will vary with the initial temperature and pressure as well as with the constants in the fluid model for $\rho(p, T)$. To better understand a specific case, we can use (12.26) to (12.28) to compute the temperature change that would take place for an observed pressure draw-down if only one of the processes took place. Computing such linearized responses for thermodynamical functions is particularly simple using automatic differentiation. Assuming we know the reference state (p_r, T_r) at which the process starts and the pressure p_e after the process has taken place, we initialize the AD variables and compute the pressure difference:

```
[p,T] = initVariablesADI(p_r,T_r);
dp     = p_e - p_r;
```

Then we can solve (12.26) or (12.28) for ΔT and use the result to compute the temperature change resulting from a free expansion or a Joule–Thomson expansion:

```

E = Ef(p,T);
dEdp = E.jac{1};
dEdT = E.jac{2};
Tfr = T_r - dEdp*dp/dEdT;

hf = Hf(p,T);
dHdp = hf.jac{1};
dHdT = hf.jac{2};
Tjt = T_r - dHdp*dp/dHdT;

```

The temperature change after a reversible (adiabatic) expansion is not described by a total differential. In this case we have to specify that p should be kept constant. This is done by replacing the AD variable p by an ordinary variable `double(p)` in the code at the specific places where p appears in front of a differential, see (12.27).

```

E = Ef(p,T) + double(p)./rho(p,T);
dEdp = hf.jac{1};
dEdT = hf.jac{2};
Tab = T_r - dEdp*dp/dEdT;

```

The same kind of manipulation can be used to study alternative linearizations of systems of nonlinear equations and the influence of neglecting some of the derivatives when forming Jacobians.

To illustrate how the interplay between the three processes can change significantly and lead to quite different temperature behavior, we will compare the predicted evolution of the temperature field for $\alpha = 5 \times 10^{-n}$, $n = 3, 4$, as shown in Figures 12.7 and 12.8. The change in behavior between the two figures is associated with the change in sign of $\partial E/\partial p$,

$$dE = \left(c_p - \frac{\alpha T}{\rho} \right) dT + \left(\frac{\beta_T p - \alpha T}{\rho} \right) dp, \quad \beta_T = \frac{1}{\rho} \frac{\partial \rho}{\partial p} \Big|_T. \quad (12.29)$$

In the isothermal case and for $\alpha = 5 \times 10^{-4}$, we have that $\alpha T < \beta_T p$ so that $\partial E/\partial p > 0$. The expansion and flow of fluid will cause an instant heating near the well-bore, which is what we see in the initial temperature increase for the maximum value in Figure 12.7. The Joule–Thomson coefficient $(\alpha T - 1)/(c_p \rho)$ is also negative, which means that the fluid gets heated if it flows from high pressure to low pressure in a steady-state flow. This is seen by observing the temperature in the well perforations. The fast pressure drop in these cells causes an almost instant cooling effect, but soon after we see a transition in which most of the cells with a well perforation start having the highest temperature in the reservoir because of heating from the moving fluids. For $\alpha = 5 \times 10^{-3}$, we have that $\alpha T > \beta_T p$ so that $\partial E/\partial p < 0$ and likewise the

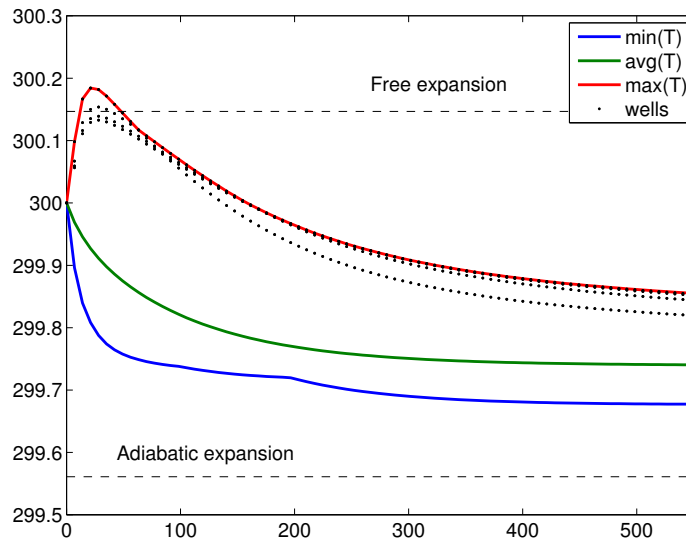
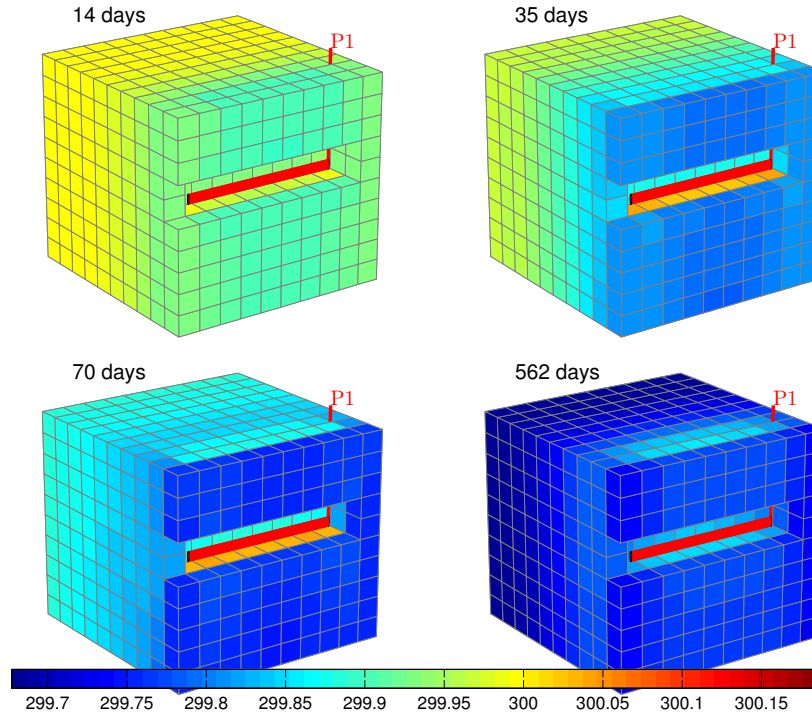


Fig. 12.7. Time evolution of temperature for a compressible, single-phase problem with $\alpha = 5 \cdot 10^{-4}$. The upper plots show four snapshots of the temperature field. The lower plot shows minimum, average, maximum, and well-perforation values.

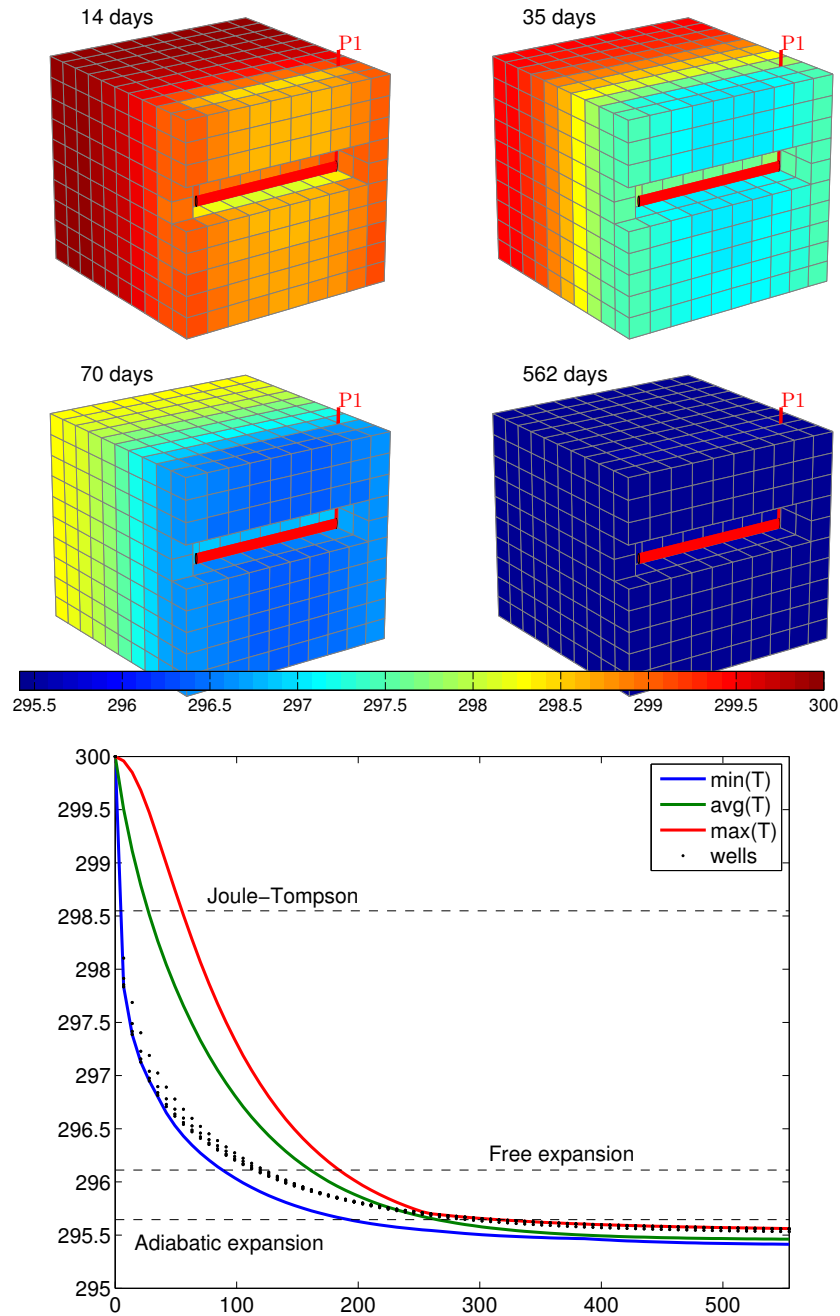


Fig. 12.8. Time evolution of temperature for a compressible, single-phase problem with $\alpha = 5 \cdot 10^{-3}$. The upper plots show four snapshots of the temperature field. The lower plot shows minimum, average, maximum, and well-perforation values.

Joule–Thomson coefficient is positive. The moving fluids will induce a cooling effect and hence the minimum temperature is observed at the well for a longer time. The weak kink in the minimum temperature curve is the result of the point of minimum temperature moving from being at the bottom front side to the far back of the reservoir. The cell with lowest temperature is where the fluid has done most work, neglecting heat conduction. In the beginning this is the cell near the well since the pressure drop is largest there. Later it will be the cell furthest from the well since this is where the fluid can expand most.

Computational performance

The observant reader may have realized that the code presented above contains a number of redundant function evaluations that may potentially add significantly to the overall computational cost: In each nonlinear iteration we keep re-evaluating quantities that depend on `p0` and `T0` even though these stay constant for each time step. This can easily be avoided by moving the definition of the anonymous functions evaluating the residual equations inside the outer time loop. The main contribution to potential computational overhead, however, comes from repeated evaluations of fluid viscosity and density. Because each residual equation is defined as an anonymous function, `v(p,T)` appears three times for each residual evaluation, once in `pEq` and twice in `hEq`. This, in turn, translates to three calls to `mu(avg(p),avg(T))` and *seven* calls to `rho(p,T)`, and so on. In practice, the number of actual function evaluations is smaller since the MATLAB interpreter most likely has some kind of built-in intelligence to spot and reduce redundant function evaluations. Nonetheless, to cure this problem, we can move the computations of residuals inside a function so that the constitutive relationships can be computed one by one and stored in temporary variables. The disadvantage is that we increase the complexity of the code and move one step away from the mathematical formulas describing the method. This type of optimization should therefore only be introduced after the code has been profiled and redundant function evaluations have proved to have a significant computational cost.

COMPUTER EXERCISES:

82. Perform a more systematic investigation of how changes in α affect the temperature and pressure behavior. To this end, you should change α systematically, e.g., from 0 to 10^{-2} . What is the effect of changing β , the parameters c_μ and c_T for the viscosity, or c_p in the definition of enthalpy?
83. Use the MATLAB profiling tool to investigate to what extent the use of nested anonymous functions causes redundant function evaluations or introduces other types of computational overhead. Hint: to profile the CPU usage, you can use the following call sequence

```
profile on, singlePhaseThermal; profile off; profile report
```

Try to modify the code as suggested above to reduce the CPU time. How low can you get the ratio between the cost of constructing the linearized system and the cost of solving it?

References

- [1] J. E. Aarnes. On the use of a mixed multiscale finite element method for greater flexibility and increased speed or improved accuracy in reservoir simulation. *Multiscale Model. Simul.*, 2(3):421–439, 2004. ISSN 1540-3459. doi:[10.1137/030600655](https://doi.org/10.1137/030600655).
- [2] J. E. Aarnes, V. Kippe, and K.-A. Lie. Mixed multiscale finite elements and streamline methods for reservoir simulation of large geomodels. *Adv. Water Resour.*, 28(3):257–271, 2005. doi:[10.1016/j.advwatres.2004.10.007](https://doi.org/10.1016/j.advwatres.2004.10.007).
- [3] J. E. Aarnes, S. Krogstad, and K.-A. Lie. A hierarchical multiscale method for two-phase flow based upon mixed finite elements and nonuniform coarse grids. *Multiscale Model. Simul.*, 5(2):337–363, 2006. ISSN 1540-3459. doi:[10.1137/050634566](https://doi.org/10.1137/050634566).
- [4] J. E. Aarnes, T. Gimse, and K.-A. Lie. An introduction to the numerics of flow in porous media using Matlab. In G. Hasle, K.-A. Lie, and E. Quak, editors, *Geometrical Modeling, Numerical Simulation and Optimisation: Industrial Mathematics at SINTEF*, pages 265–306. Springer Verlag, Berlin Heidelberg New York, 2007. doi:[10.1007/978-3-540-68783-2_9](https://doi.org/10.1007/978-3-540-68783-2_9).
- [5] J. E. Aarnes, S. Krogstad, and K.-A. Lie. Multiscale mixed/mimetic methods on corner-point grids. *Comput. Geosci.*, 12(3):297–315, 2008. ISSN 1420-0597. doi:[10.1007/s10596-007-9072-8](https://doi.org/10.1007/s10596-007-9072-8).
- [6] I. Aavatsmark. An introduction to multipoint flux approximations for quadrilateral grids. *Comput. Geosci.*, 6:405–432, 2002. doi:[10.1023/A:1021291114475](https://doi.org/10.1023/A:1021291114475).
- [7] I. Aavatsmark and R. Klausen. Well index in reservoir simulation for slanted and slightly curved wells in 3d grids. *SPE J.*, 8(01):41–48, 2003.
- [8] I. Aavatsmark, T. Barkve, Ø. Bøe, and T. Mannseth. Discretization on non-orthogonal, curvilinear grids for multi-phase flow. *Proc. of the 4th European Conf. on the Mathematics of Oil Recovery*, 1994.
- [9] J. H. Abou-Kassem, S. M. Farouq-Ali, and M. R. Islam. *Petroleum Reservoir Simulations*. Elsevier, 2013.

- [10] AGMG. Iterative solution with AGgregation-based algebraic MultiGrid, 2012. <http://homepages.ulb.ac.be/~ynotay/AGMG/>.
- [11] I. Akervoll and P. Bergmo. A study of Johansen formation located offshore Mongstad as a candidate for permanent CO₂ storage. In *European Conference on CCS Research, Development and Demonstration. 10–11 February 2009, Oslo, Norway*, 2009.
- [12] M. B. Allen, G. A. Behie, and J. A. Trangenstein. *Multiphase flow in porous media: mechanics, mathematics, and numerics*. Lecture notes in engineering. Springer-Verlag, 1988. ISBN 9783540967316.
- [13] F. O. Alpak, M. Pal, and K.-A. Lie. A multiscale method for modeling flow in stratigraphically complex reservoirs. *SPE J.*, 17(4):1056–1070, 2012. doi:[10.2118/140403-PA](https://doi.org/10.2118/140403-PA).
- [14] J. Alvestad, K. Holing, K. Christoffersen, O. Stava, et al. Interactive modelling of multiphase inflow performance of horizontal and highly deviated wells. In *European Petroleum Computer Conference*. Society of Petroleum Engineers, 1994.
- [15] O. Andersen, S. Gasda, and H. Nilsen. Vertically averaged equations with variable density for CO₂ flow in porous media. *Transp. Porous Media*, pages 1–33, 2014. ISSN 0169-3913. doi:[10.1007/s11242-014-0427-z](https://doi.org/10.1007/s11242-014-0427-z).
- [16] O. Andersen, H. M. Nilsen, and K.-A. Lie. Reexamining CO₂ storage capacity and utilization of the Utsira Formation. In *ECMOR XIV – 14th European Conference on the Mathematics of Oil Recovery, Catania, Sicily, Italy, 8-11 September 2014*. EAGE, 2014. doi:[10.3997/2214-4609.20141809](https://doi.org/10.3997/2214-4609.20141809).
- [17] O. Andersen, K.-A. Lie, and H. M. Nilsen. An open-source toolchain for simulation and optimization of aquifer-wide CO₂ storage. *Energy Procedia*, :1–10, 2015. The 8th Trondheim Conference on Capture, Transport and Storage.
- [18] T. Arbogast, L. C. Cowsar, M. F. Wheeler, and I. Yotov. Mixed finite element methods on nonmatching multiblock grids. *SIAM J. Num. Anal.*, 37(4):1295–1315, 2000.
- [19] H. Ates, A. Bahar, S. El-Abd, M. Charfeddine, M. Kelkar, and A. Datta-Gupta. Ranking and upscaling of geostatistical reservoir models using streamline simulation: A field case study. *SPE Res. Eval. Eng.*, 8(1): 22–32, 2005. doi:[10.2118/81497-PA](https://doi.org/10.2118/81497-PA).
- [20] K. Aziz and A. Settari. *Petroleum Reservoir Simulation*. Elsevier Applied Science Publishers, London and New York, 1979.
- [21] J. Barker and S. Thibeau. A critical review of the use of pseudorelative permeabilities for upscaling. *SPE Reservoir Engineering*, 12(2):138–143, 1997. doi:[10.2118/35491-PA](https://doi.org/10.2118/35491-PA).
- [22] R. P. Batycky, M. R. Thieles, R. O. Baker, and S. H. Chugh. Revisiting reservoir flood-surveillance methods using streamlines. *SPE Res. Eval. Eng.*, 11(2):387–394, 2008. doi:[10.2118/95402-PA](https://doi.org/10.2118/95402-PA).

- [23] J. Bear. *Dynamics of Fluids in Porous Media*. Dover, 1988. ISBN 0-486-45355-3.
- [24] J. Bear. *Hydraulics of Groundwater*. Dover, 2007. ISBN 0-486-65675-6.
- [25] J. Bear and Y. Bachmat. *Introduction to Modeling of Transport Phenomena in Porous Media*. Theory and Applications of Transport in Porous Media. Springer, 1990. ISBN 9780792305576.
- [26] S. H. Begg, R. R. Carter, and P. Dranfield. Assigning effective values to simulator gridblock parameters for heterogeneous reservoirs. *SPE Res. Eng.*, 4(4):455–463, 1989.
- [27] L. Beirao da Veiga, K. Lipnikov, and G. Manzini. *The Mimetic Finite Difference Method for Elliptic Problems*, volume 11 of *MS&A – Modeling, Simulation and Applications*. Springer, 2014. doi:[10.1007/978-3-319-02663-3](https://doi.org/10.1007/978-3-319-02663-3).
- [28] A. Benesoussan, J.-L. Lions, and G. Papanicolaou. *Asymptotic Analysis for Periodic Structures*. Elsevier Science Publishers, Amsterdam, 1978.
- [29] C. H. Bischof, H. M. Bücker, B. Lang, A. Rasch, and A. Vehreschild. Combining source transformation and operator overloading techniques to compute derivatives for MATLAB programs. In *Proceedings of the Second IEEE International Workshop on Source Code Analysis and Manipulation (SCAM 2002)*, pages 65–72, Los Alamitos, CA, USA, 2002. IEEE Computer Society. doi:[10.1109/SCAM.2002.1134106](https://doi.org/10.1109/SCAM.2002.1134106).
- [30] D. Braess. *Finite elements: Theory fast solvers and applications in solid mechanics*. Cambridge University Press, Cambridge, 1997.
- [31] S. C. Brenner and L. R. Scott. *The mathematical theory of finite element methods*, volume 15 of *Texts in Applied Mathematics*. Springer-Verlag, New York, 1994.
- [32] M. Brewer, D. Camilleri, S. Ward, and T. Wong. Generation of hybrid grids for simulation of complex, unstructured reservoirs by a simulator with mpfa. In *SPE Reservoir Simulation Symposium, 23-25 February, Houston, Texas, USA, 2015*. doi:[10.2118/173191-MS](https://doi.org/10.2118/173191-MS).
- [33] F. Brezzi and M. Fortin. *Mixed and Hybrid Finite Element Methods*, volume 15 of *Springer Series in Computational Mathematics*. Springer-Verlag, New York, 1991. ISBN 0-387-97582-9.
- [34] F. Brezzi, K. Lipnikov, and V. Simoncini. A family of mimetic finite difference methods on polygonal and polyhedral meshes. *Math. Models Methods Appl. Sci.*, 15:1533–1553, 2005. doi:[10.1142/S0218202505000832](https://doi.org/10.1142/S0218202505000832).
- [35] R. H. Brooks and A. T. Corey. Properties of porous media affecting fluid flow. *J. Irrigation Drainage Div.*, 92(2):61–90, 1966.
- [36] E. Buckingham. *Studies on the movement of soil moisture*. Number 38. United States. Bureau of Soils, 1907.
- [37] H. Cao. *Development of techniques for general purpose simulators*. PhD thesis, Stanford University, 2002.
- [38] Cayuga Research. Admat. URL <http://www.cayugaresearch.com/admat.html>. [Online; accessed 15-04-2014].

- [39] G. Chavent and J. Jaffre. *Mathematical models and finite elements for reservoir simulation*. North Holland, 1982.
- [40] G. Chavent and J. Jaffré. *Mathematical models and finite elements for reservoir simulation: single phase, multiphase and multicomponent flows through porous media*. Studies in Mathematics and its Applications. Elsevier, 1986.
- [41] Y. Chen and L. J. Durlofsky. Adaptive local-global upscaling for general flows in heterogeneous formations. *Transport Porous Media*, 51:343–366, 2003.
- [42] Y. Chen, L. J. Durlofsky, M. Gerritsen, and X. H. Wen. A coupled local-global upscaling approach for simulating flow in highly heterogeneous formations. *Adv. Water Resour.*, 26:1041–1060, 2003.
- [43] Z. Chen. Formulations and numerical methods of the black oil model in porous media. *SIAM J. Numer. Anal.*, 38(2):489–514, 2000. doi:[10.1137/S0036142999304263](https://doi.org/10.1137/S0036142999304263).
- [44] Z. Chen. *Reservoir Simulation: Mathematical Techniques in Oil Recovery*. Society for Industrial and Applied Mathematics, Philadelphia, PA, USA, 2007.
- [45] Z. Chen and R. E. Ewing. Comparison of various formulations of three-phase flow in porous media. *J. Comput. Phys.*, 132(2):362–373, 1997. doi:[10.1006/jcph.1996.5641](https://doi.org/10.1006/jcph.1996.5641).
- [46] Z. Chen and T. Y. Hou. A mixed multiscale finite element method for elliptic problems with oscillating coefficients. *Math. Comp.*, 72:541–576, 2003. doi:[10.1090/S0025-5718-02-01441-2](https://doi.org/10.1090/S0025-5718-02-01441-2).
- [47] Z. Chen, G. Huan, and Y. Ma. *Computational methods for multiphase flows in porous media*, volume 2 of *Computational Science and Engineering*. Society of Industrial and Applied Mathematics (SIAM), 2006. doi:[10.1137/1.9780898718942](https://doi.org/10.1137/1.9780898718942).
- [48] M. A. Christie. Upscaling for reservoir simulation. *J. Pet. Tech.*, 48(11):1004–1010, 1996. doi:[10.2118/37324-MS](https://doi.org/10.2118/37324-MS).
- [49] M. A. Christie and M. J. Blunt. Tenth SPE comparative solution project: A comparison of upscaling techniques. *SPE Reservoir Eval. Eng.*, 4:308–317, 2001. doi:[10.2118/72469-PA](https://doi.org/10.2118/72469-PA). Url: <http://www.spe.org/csp/>.
- [50] C. Cordes and W. Kinzelbach. Continuous groundwater velocity fields and path lines in linear, bilinear, and trilinear finite elements. *Water Resour. Res.*, 28(11):2903–2911, 1992.
- [51] H. P. G. Darcy. *Les Fontaines Publiques de la Ville de Dijon*. Dalmont, Paris, 1856.
- [52] A. Datta-Gupta and M. J. King. A semianalytic approach to tracer flow modeling in heterogeneous permeable media. *Adv. Water Resour.*, 18:9–24, 1995.
- [53] A. Datta-Gupta and M. J. King. *Streamline Simulation: Theory and Practice*, volume 11 of *SPE Textbook Series*. Society of Petroleum Engineers, 2007.

- [54] A. Datta-Gupta and M. J. King. *Streamline Simulation: Theory and Practice*, volume 11 of *SPE Textbook Series*. Society of Petroleum Engineers, 2007.
- [55] D. DeBaun, T. Byer, P. Childs, J. Chen, F. Saaf, M. Wells, J. Liu, H. Cao, L. Pianelo, V. Tilakraj, P. Crumpton, D. Walsh, H. Yardumian, R. Zorzynski, K.-T. Lim, M. Schrader, V. Zapata, J. Nolen, and H. A. Tchelepi. An extensible architecture for next generation scalable parallel reservoir simulation. In *SPE Reservoir Simulation Symposium, 31 January–2 February, The Woodlands, Texas, USA*, 2005. doi:[10.2118/93274-MS](https://doi.org/10.2118/93274-MS).
- [56] C. V. Deutsch and A. G. Journel. *GSLIB: Geostatistical software library and user's guide*. Oxford University Press, New York, 2nd edition, 1998.
- [57] X. Y. Ding and L. S. K. Fung. An unstructured gridding method for simulating faulted reservoirs populated with complex wells. In *SPE Reservoir Simulation Symposium, 23-25 February, Houston, Texas, USA*, 2015. doi:[10.2118/173243-MS](https://doi.org/10.2118/173243-MS).
- [58] J. Douglas Jr, D. W. Peaceman, and H. H. Rachford Jr. A method for calculating multi-dimensional immiscible displacement. *Trans. AIME*, 216:297–308, 1959.
- [59] L. J. Durlofsky. Numerical calculations of equivalent gridblock permeability tensors for heterogeneous porous media. *Water Resour. Res.*, 27(5):699–708, 1991.
- [60] L. J. Durlofsky. Upscaling of geocellular models for reservoir flow simulation: A review of recent progress, 2003. Presented at 7th International Forum on Reservoir Simulation Bühl/Baden-Baden, Germany, June 23–27, 2003.
- [61] L. J. Durlofsky. Upscaling and gridding of fine scale geological models for flow simulation, 2005. Presented at 8th International Forum on Reservoir Simulation Iles Borromees, Stresa, Italy, June 20–24, 2005.
- [62] M. G. Edwards and C. F. Rogers. A flux continuous scheme for the full tensor pressure equation. *Proc. of the 4th European Conf. on the Mathematics of Oil Recovery*, 1994.
- [63] Y. Efendiev and T. Y. Hou. *Multiscale Finite Element Methods*, volume 4 of *Surveys and Tutorials in the Applied Mathematical Sciences*. Springer Verlag, New York, 2009.
- [64] G. Eigestad, H. Dahle, B. Hellevang, W. Johansen, K.-A. Lie, F. Riis, and E. Øian. Geological and fluid data for modelling CO₂ injection in the Johansen formation, 2008. URL <http://www.sintef.no/Projectweb/MatMorA/Downloads/Johansen>.
- [65] G. Eigestad, H. Dahle, B. Hellevang, F. Riis, W. Johansen, and E. Øian. Geological modeling and simulation of CO₂ injection in the Johansen formation. *Comput. Geosci.*, 13(4):435–450, 2009. doi:[10.1007/s10596-009-9153-y](https://doi.org/10.1007/s10596-009-9153-y).

- [66] T. Ertekin, J. H. Abou-Kassem, and G. R. King. *Basic applied reservoir simulation*, volume 7 of *SPE Textbook Series*. Society of Petroleum Engineers Richardson, TX, 2001.
- [67] R. E. Ewing, R. D. Lazarov, S. L. Lyons, D. V. Papavassiliou, J. Pasciak, and G. Qin. Numerical well model for non-Darcy flow through isotropic porous media. *Comput. Geosci.*, 3(3-4):185–204, 1999. doi:[10.1023/A:1011543412675](https://doi.org/10.1023/A:1011543412675).
- [68] J. R. Fanchi. *Principles of applied reservoir simulation*. Gulf Professional Publishing, 2005.
- [69] C. L. Farmer. Upscaling: a review. *Int. J. Numer. Meth. Fluids*, 40(1–2):63–78, 2002. doi:[10.1002/fld.267](https://doi.org/10.1002/fld.267).
- [70] M. Fink. Automatic differentiation for Matlab. MATLAB Central, 2007. URL <http://www.mathworks.com/matlabcentral/fileexchange/15235-automatic-differentiation-for-matlab>. [Online; accessed 15-04-2014].
- [71] S. A. Forth. An efficient overloaded implementation of forward mode automatic differentiation in MATLAB. *ACM Trans. Math. Software*, 32(2):195–222, 2006.
- [72] L. S. K. Fung, X. Y. Ding, , and A. H. Dogru. Unconstrained voronoi grids for densely spaced complex wells in full-field reservoir simulation. *SPE J.*, 19(5):803–815, 2014. doi:[10.2118/163648-PA](https://doi.org/10.2118/163648-PA).
- [73] M. Gerritsen and J. V. Lambers. Integration of local-global upscaling and grid adaptivity for simulation of subsurface flow in heterogeneous formations. *Comput. Geosci.*, 12(2):193–208, 2008. doi:[10.1007/s10596-007-9078-2](https://doi.org/10.1007/s10596-007-9078-2).
- [74] D. Guérillot, J. L. Rudkiewicz, C. Ravenne, D. Renard, and A. Galli. An integrated model for computer aided reservoir description: From outcrop study to fluid flow simulations. *Oil & Gas Science and Technology*, 45(1):71–77, 1990.
- [75] H. Hægland, H. K. Dahle, K.-A. Lie, and G. T. Eigestad. Adaptive streamline tracing for streamline simulation on irregular grids. In P. Binning, P. Engesgaard, H. Dahle, G. Pinder, and W. Gray, editors, *Proceedings of the XVI International Conference on Computational Methods in Water Resources*, Copenhagen, Denmark, 18–22 June 2006. URL <http://proceedings.cmrw-xvi.org/>.
- [76] H. Hajibeygi and H. A. Tchelepi. Compositional multiscale finite-volume formulation. *SPE J.*, 19(2):316–326, 2014. doi:[10.2118/163664-PA](https://doi.org/10.2118/163664-PA).
- [77] H. B. Hales. A method for creating 2-d orthogonal grids which conform to irregular shapes. *SPE J.*, 1(2):115–124, 1996. doi:[10.2118/35273-PA](https://doi.org/10.2118/35273-PA).
- [78] V. L. Hauge. *Multiscale Methods and Flow-based Gridding for Flow and Transport in Porous Media*. PhD thesis, Norwegian University of Science and Technology, 2010. URL <http://ntnu.diva-portal.org/smash/get/diva2:400507/FULLTEXT02>.

- [79] V. L. Hauge, K.-A. Lie, and J. R. Natvig. Flow-based coarsening for multiscale simulation of transport in porous media. *Comput. Geosci.*, 16(2):391–408, 2012. doi:[10.1007/s10596-011-9230-x](https://doi.org/10.1007/s10596-011-9230-x).
- [80] Z. He, H. Parikh, A. Datta-Gupta, J. Perez, and T. Pham. Identifying reservoir compartmentalization and flow barriers from primary production using streamline diffusive time of flight. *SPE J.*, 7(3):238–247, June 2004. doi:[10.2118/88802-PA](https://doi.org/10.2118/88802-PA).
- [81] R. Helmig. *Multiphase flow and transport processes in the subsurface: a contribution to the modeling of hydrosystems*. Environmental engineering. Springer, 1997. ISBN 9783540627036.
- [82] S. T. Hilden, K.-A. Lie, and X. Raynaud. Steady state upscaling of polymer flooding. In *ECMOR XIV – 14th European Conference on the Mathematics of Oil Recovery, Catania, Sicily, Italy, 8-11 September 2014*. EAGE, 2014. doi:[10.3997/2214-4609.20141802](https://doi.org/10.3997/2214-4609.20141802).
- [83] H. Holden and N. Risebro. *Front Tracking for Hyperbolic Conservation Laws*, volume 152 of *Applied Mathematical Sciences*. Springer, New York, 2002.
- [84] L. Holden and B. F. Nielsen. Global upscaling of permeability in heterogeneous reservoirs; the output least squares (ols) method. *Trans. Porous Media*, 40(2):115–143, 2000.
- [85] U. Hornung. *Homogenization and porous media*. Springer-Verlag, New York, 1997.
- [86] H. Hoteit and A. Firoozabadi. Numerical modeling of two-phase flow in heterogeneous permeable media with different capillarity pressures. *Adv. Water Resour.*, 31(1):56–73, 2008. doi:[10.1016/j.advwatres.2007.06.006](https://doi.org/10.1016/j.advwatres.2007.06.006).
- [87] M. K. Hubbert. Darcy’s law and the field equations of the flow of underground fluids. *Petrol. Trans., AIME*, 207:22–239, 1956.
- [88] E. Idrobo, M. Choudhary, and A. Datta-Gupta. Swept volume calculations and ranking of geostatistical reservoir models using streamline simulation. In *SPE/AAPG Western Regional Meeting*, Long Beach, California, USA, 19–23 June 2000. SPE 62557.
- [89] M. R. Islam, S. H. Mousavizadegan, S. Mustafiz, and J. H. Abou-Kassem. *Advanced Petroleum Reservoir Simulations*. John Wiley & Sons, Inc., 2010. ISBN 9780470650684. doi:[10.1002/9780470650684](https://doi.org/10.1002/9780470650684).
- [90] O. Izgec, M. Sayarpour, and G. M. Shook. Maximizing volumetric sweep efficiency in waterfloods with hydrocarbon f - ϕ curves. *Journal of Petroleum Science and Engineering*, 78(1):54–64, 2011. doi:[10.1016/j.petrol.2011.05.003](https://doi.org/10.1016/j.petrol.2011.05.003).
- [91] P. Jenny, C. Wolfsteiner, S. H. Lee, and L. J. Durlofsky. Modeling flow in geometrically complex reservoirs using hexahedral multiblock grids. *SPE J.*, 7(2), 2002. doi:[10.2118/78673-PA](https://doi.org/10.2118/78673-PA).
- [92] P. Jenny, S. H. Lee, and H. A. Tchelepi. Multi-scale finite-volume method for elliptic problems in subsurface flow simulation. *J. Comput. Phys.*, 187:47–67, 2003. doi:[10.1016/S0021-9991\(03\)00075-5](https://doi.org/10.1016/S0021-9991(03)00075-5).

- [93] V. V. Jikov, S. M. Kozlov, and O. A. Oleinik. *Homogenization of differential operators and integral functionals*. Springer–Verlag, New York, 1994.
- [94] E. Jimenez, K. Sabir, A. Datta-Gupta, and M. J. King. Spatial error and convergence in streamline simulation. *SPE J.*, 10(3):221–232, June 2007.
- [95] A. Journal, C. Deutsch, and A. Desbarats. Power averaging for block effective permeability. In *SPE California Regional Meeting, 2-4 April, Oakland, California*, SPE 15128, 1986.
- [96] M. Karimi-Fard and L. J. Durlofsky. Accurate resolution of near-well effects in upscaled models using flow-based unstructured local grid refinement. *SPE J.*, 17(4):1084–1095, 2012. doi:[10.2118/141675-PA](https://doi.org/10.2118/141675-PA).
- [97] G. Karypis and V. Kumar. A fast and high quality multilevel scheme for partitioning irregular graphs. *SIAM J. Sci. Comp.*, 20(1):359–392, 1998. doi:[10.1137/S1064827595287997](https://doi.org/10.1137/S1064827595287997).
- [98] M. King, D. MacDonald, S. Todd, and H. Leung. Application of novel upscaling approaches to the Magnus and Andrew reservoirs. In *European Petroleum Conference, 20-22 October, The Hague, Netherlands*, SPE 50643, 1998.
- [99] M. J. King and A. Datta-Gupta. Streamline simulation: A current perspective. *In Situ*, 22(1):91–140, 1998.
- [100] M. J. King and M. Mansfield. Flow simulation of geologic models. *SPE Res. Eval. Eng.*, 2(4):351–367, 1999. doi:[10.2118/57469-PA](https://doi.org/10.2118/57469-PA).
- [101] V. Kippe, J. E. Aarnes, and K.-A. Lie. A comparison of multiscale methods for elliptic problems in porous media flow. *Comput. Geosci.*, 12(3):377–398, 2008. ISSN 1420-0597. doi:[10.1007/s10596-007-9074-6](https://doi.org/10.1007/s10596-007-9074-6).
- [102] R. A. Klausen and A. F. Stephansen. Mimetic MPFA. In *Proc. 11th European Conference on the Mathematics of Oil Recovery, 8-11 Sept., Bergen, Norway*, number A12. EAGE, 2008.
- [103] R. A. Klausen, A. F. Rasmussen, and A. Stephansen. Velocity interpolation and streamline tracing on irregular geometries. *Comput. Geosci.*, 16:261–276, 2012. doi:[10.1007/s10596-011-9256-0](https://doi.org/10.1007/s10596-011-9256-0).
- [104] S. Krogstad, K.-A. Lie, O. Møyner, H. M. Nilsen, X. Raynaud, and B. Skaflestad. MRST-AD – an open-source framework for rapid prototyping and evaluation of reservoir simulation problems. In *SPE Reservoir Simulation Symposium, 23-25 February, Houston, Texas*, 2015. doi:[10.2118/173317-MS](https://doi.org/10.2118/173317-MS).
- [105] S. Krogstad, X. Raynaud, and H. M. Nilsen. Reservoir management optimization using well-specific upscaling and control switching. *Comput. Geosci.*, 2015. doi:[10.1007/s10596-015-9497-4](https://doi.org/10.1007/s10596-015-9497-4).
- [106] L. W. Lake. *Enhanced Oil Recovery*. Prentice-Hall, 1989.
- [107] S. H. Lee, P. Jenny, and H. A. Tchelepi. A finite-volume method with hexahedral multiblock grids for modeling flow in porous media. *Comput. Geosci.*, 6(3-4):353–379, 2002. ISSN 1420-0597. Locally conservative numerical methods for flow in porous media.

- [108] O. Leeuwenburgh and R. Arts. Distance parameterization for efficient seismic history matching with the ensemble kalman filter. In *ECMOR XIII - 13th European Conference on the Mathematics of Oil Recovery*. EAGE, 2012. doi:[10.3997/2214-4609.20143176](https://doi.org/10.3997/2214-4609.20143176).
- [109] O. Leeuwenburgh, E. Peters, and F. Wilschut. Towards an integrated workflow for structural reservoir model updating and history matching. In *SPE EUROPEC/EAGE Annual Conference and Exhibition, 23-26 May, Vienna, Austria, 2011*. doi:[10.2118/143576-MS](https://doi.org/10.2118/143576-MS).
- [110] M. C. Leverett. Capillary behavior in porous solids. *Trans. AIME*, 142: 159–172, 1941. doi:[10.2118/941152-G](https://doi.org/10.2118/941152-G).
- [111] X. Li and D. Zhang. A backward automatic differentiation framework for reservoir simulation. *Comput. Geosci.*, pages 1–14, 2014. doi:[10.1007/s10596-014-9441-z](https://doi.org/10.1007/s10596-014-9441-z).
- [112] K. Lie, S. Krogstad, I. S. Ligaarden, J. R. Natvig, H. Nilsen, and B. Skaflestad. Open-source MATLAB implementation of consistent discretisations on complex grids. *Comput. Geosci.*, 16:297–322, 2012. ISSN 1420-0597. doi:[10.1007/s10596-011-9244-4](https://doi.org/10.1007/s10596-011-9244-4). URL <http://dx.doi.org/10.1007/s10596-011-9244-4>.
- [113] K.-A. Lie. *The MATLAB Reservoir Simulation Toolbox (MRST)*. Stanford University, May 2015. URL http://jolts.stanford.edu/108/the_matlab_reservoir_simulation_toolbox_mrst. Jolts – Just-in-time online learning tools.
- [114] K.-A. Lie. *MRST: Grids and Petrophysical Data*. Stanford University, May 2015. URL http://jolts.stanford.edu/109/mrst_grids_and_petrophysical_data. Jolts – Just-in-time online learning tools.
- [115] K.-A. Lie, S. Krogstad, I. S. Ligaarden, J. R. Natvig, H. M. Nilsen, and B. Skaflestad. Discretisation on complex grids – open source MATLAB implementation. In *Proceedings of ECMOR XII–12th European Conference on the Mathematics of Oil Recovery*, Oxford, UK, 6–9 September 2010. EAGE.
- [116] K.-A. Lie, J. R. Natvig, and H. M. Nilsen. Discussion of dynamics and operator splitting techniques for two-phase flow with gravity. *Int. J Numer. Anal. Mod. (Special issue in memory of Magne Espedal)*, 9(3): 684–700, 2012.
- [117] K.-A. Lie, J. R. Natvig, S. Krogstad, Y. Yang, and X.-H. Wu. Grid adaptation for the Dirichlet–Neumann representation method and the multiscale mixed finite-element method. *Comput. Geosci.*, 18(3):357–372, 2014. doi:[10.1007/s10596-013-9397-4](https://doi.org/10.1007/s10596-013-9397-4).
- [118] K.-A. Lie, H. M. Nilsen, O. Andersen, and O. Møyner. A simulation workflow for large-scale CO₂ storage in the Norwegian North Sea. In *ECMOR XIV – 14th European Conference on the Mathematics of Oil Recovery, Catania, Sicily, Italy, 8-11 September 2014*. EAGE, 2014. doi:[10.3997/2214-4609.20141877](https://doi.org/10.3997/2214-4609.20141877).

- [119] K.-A. Lie, H. M. Nilsen, O. Andersen, and O. Møyner. A simulation workflow for large-scale CO₂ storage in the Norwegian North Sea. *Comput. Geosci.*, :1–16, 2015. doi:[10.1007/s10596-015-9487-6](https://doi.org/10.1007/s10596-015-9487-6).
- [120] I. S. Ligaarden. Well models for mimetic finite difference methods and improved representation of wells in multiscale methods. Master’s thesis, University of Oslo, 2008. URL <http://www.duo.uio.no/sok/work.html?WORKID=77236>.
- [121] K. Lipnikov, M. Shashkov, and I. Yotov. Local flux mimetic finite difference methods. *Numer. Math.*, 112(1):115–152, 2009. ISSN 0029-599X. doi:[10.1007/s00211-008-0203-5](https://doi.org/10.1007/s00211-008-0203-5). URL <http://dx.doi.org/10.1007/s00211-008-0203-5>.
- [122] I. Lunati and S. H. Lee. An operator formulation of the multiscale finite-volume method with correction function. *Multiscale Model. Simul.*, 8(1):96–109, 2009. doi:[10.1137/080742117](https://doi.org/10.1137/080742117).
- [123] B. Mallison, C. Sword, T. Viard, W. Milliken, and A. Cheng. Unstructured cut-cell grids for modeling complex reservoirs. *SPE J.*, 2014. doi:[10.2118/163642-PA](https://doi.org/10.2118/163642-PA).
- [124] T. Manzocchi et al. Sensitivity of the impact of geological uncertainty on production from faulted and unfaulted shallow-marine oil reservoirs: objectives and methods. *Petrol. Geosci.*, 14(1):3–15, 2008.
- [125] S. F. Matringe and M. G. Gerritsen. On accurate tracing of streamlines. In *SPE Annual Technical Conference and Exhibition*, Houston, Texas, USA, 26-29 September 2004. SPE 89920.
- [126] S. F. Matringe, R. Juanes, and H. A. Tchelepi. Streamline tracing on general triangular or quadrilateral grids. *SPE J.*, 12(2):217–233, June 2007.
- [127] C. C. Mattax and R. L. Dalton, editors. *Reservoir Simulation*, volume 13 of *SPE Monograph Series*. Society of Petroleum Engineers, 1990. ISBN 978-1-55563-028-7.
- [128] W. McIlhagga. Automatic differentiation with Matlab objects. MATLAB Central, mar 2010. URL <http://www.mathworks.com/matlabcentral/fileexchange/26807-automatic-differentiation-with-matlab-objects>. [Online; accessed 15-04-2014].
- [129] R. Merland, G. Caumon, B. Lvy, and P. Collon-Drouaillet. Voronoi grids conforming to 3d structural features. *Comput. Geosci.*, 18(3-4):373–383, 2014. doi:[10.1007/s10596-014-9408-0](https://doi.org/10.1007/s10596-014-9408-0).
- [130] O. Møyner. Multiscale finite-volume methods on unstructured grids. Master’s thesis, Norwegian University of Science and Technology, Trondheim, 2012. URL <http://daim.idi.ntnu.no/masteroppgave?id=7377>.
- [131] O. Møyner. Construction of multiscale preconditioners on stratigraphic grids. In *ECMOR XIV – 14th European Conference on the Mathematics of Oil Recovery, Catania, Sicily, Italy, 8-11 September 2014*. EAGE, 2014. doi:[10.3997/2214-4609.20141775](https://doi.org/10.3997/2214-4609.20141775).

- [132] O. Møyner and K.-A. Lie. A multiscale two-point flux-approximation method. *J. Comput. Phys.*, 275:273–293, 2014. doi:[10.1016/j.jcp.2014.07.003](https://doi.org/10.1016/j.jcp.2014.07.003).
- [133] O. Møyner and K.-A. Lie. The multiscale finite-volume method on stratigraphic grids. *SPE J.*, 19(5):816–831, 2014. doi:[10.2118/163649-PA](https://doi.org/10.2118/163649-PA).
- [134] O. Møyner and K.-A. Lie. A multiscale method based on restriction-smoothed basis functions suitable for general grids in high contrast media. In *SPE Reservoir Simulation Symposium held in Houston, Texas, USA, 23–25 February 2015*, 2015. doi:[10.2118/173256-MS](https://doi.org/10.2118/173256-MS). SPE 173265-MS.
- [135] O. Møyner and K.-A. Lie. A multiscale restriction-smoothed basis method for high contrast porous media represented on unstructured grids. *J. Comput. Phys.*, 2015. submitted.
- [136] O. Møyner and K.-A. Lie. A multiscale restriction-smoothed basis method for compressible black-oil models. *SPE J.*, 2015. submitted.
- [137] O. Møyner, S. Krogstad, and K.-A. Lie. The application of flow diagnostics for reservoir management. *SPE J.*, 20(2):306–323, 2014. doi:[10.2118/171557-PA](https://doi.org/10.2118/171557-PA).
- [138] M. Muskat and R. D. Wyckoff. *The flow of homogeneous fluids through porous media*, volume 12. McGraw-Hill New York, 1937.
- [139] J. R. Natvig and K.-A. Lie. Fast computation of multiphase flow in porous media by implicit discontinuous Galerkin schemes with optimal ordering of elements. *J. Comput. Phys.*, 227(24):10108–10124, 2008. doi:[10.1016/j.jcp.2008.08.024](https://doi.org/10.1016/j.jcp.2008.08.024).
- [140] J. R. Natvig, K.-A. Lie, B. Eikemo, and I. Berre. An efficient discontinuous Galerkin method for advective transport in porous media. *Adv. Water Resour.*, 30(12):2424–2438, 2007. doi:[10.1016/j.advwatres.2007.05.015](https://doi.org/10.1016/j.advwatres.2007.05.015).
- [141] J. R. Natvig, B. Skaflestad, F. Bratvedt, K. Bratvedt, K.-A. Lie, V. Laptev, and S. K. Khataniar. Multiscale mimetic solvers for efficient streamline simulation of fractured reservoirs. *SPE J.*, 16(4):880–888, 2011. doi:[10.2018/119132-PA](https://doi.org/10.2018/119132-PA).
- [142] J. R. Natvig, K.-A. Lie, S. Krogstad, Y. Yang, and X.-H. Wu. Grid adaptation for upscaling and multiscale methods. In *Proceedings of ECMOR XIII–13th European Conference on the Mathematics of Oil Recovery*, Biarritz, France, 10–13 September 2012. EAGE.
- [143] R. Neidinger. Introduction to automatic differentiation and MATLAB object-oriented programming. *SIAM Review*, 52(3):545–563, 2010. doi:[10.1137/080743627](https://doi.org/10.1137/080743627).
- [144] B. F. Nielsen and A. Tveito. An upscaling method for one-phase flow in heterogeneous reservoirs; a Weighted Output Least Squares (WOLS) approach. *Comput. Geosci.*, 2:92–123, 1998.

- [145] H. M. Nilsen, K.-A. Lie, and O. Andersen. Robust simulation of sharp-interface models for fast estimation of CO₂ trapping capacity. 2015. URL <http://folk.uio.no/kalie/papers/co2lab-2.pdf>.
- [146] H. M. Nilsen, K.-A. Lie, and O. Andersen. Fully implicit simulation of vertical-equilibrium models with hysteresis and capillary fringe. *Comput. Geosci.*, :, 2015.
- [147] H. M. Nilsen, K.-A. Lie, and O. Andersen. Analysis of CO₂ trapping capacities and long-term migration for geological formations in the Norwegian North Sea using MRST-co2lab. *Computers & Geoscience*, 79: 15–26, 2015. doi:[10.1016/j.cageo.2015.03.001](https://doi.org/10.1016/j.cageo.2015.03.001).
- [148] H. M. Nilsen, K.-A. Lie, O. Møyner, and O. Andersen. Spill-point analysis and structural trapping capacity in saline aquifers using MRST-co2lab. *Computers & Geoscience*, 75:33–43, 2015. doi:[10.1016/j.cageo.2014.11.002](https://doi.org/10.1016/j.cageo.2014.11.002).
- [149] J. Nordbotten, I. Aavatsmark, and G. Eigestad. Monotonicity of control volume methods. *Numer. Math.*, 106(2):255–288, 2007. doi:[10.1007/s00211-006-0060-z](https://doi.org/10.1007/s00211-006-0060-z).
- [150] Y. Notay. An aggregation-based algebraic multigrid method. *Electron. Trans. Numer. Anal.*, 37:123–140, 2010.
- [151] P.-E. Øren, S. Bakke, and O. J. Arntzen. Extending predictive capabilities to network models. *SPE J.*, 3(4):324–336, 1998.
- [152] M. Pal, S. Lamine, K.-A. Lie, and S. Krogstad. Validation of the multi-scale mixed finite-element method. *Int. J. Numer. Meth. Fluids*, 77(4): 206–223, 2015. doi:[10.1002/flid.3978](https://doi.org/10.1002/flid.3978).
- [153] H.-Y. Park and A. Datta-Gupta. Reservoir management using streamline-based flood efficiency maps and application to rate optimization. In *Proceedings of the SPE Western North American Region Meeting*, 7-11 May 2011, Anchorage, Alaska, USA, 2011. doi:[10.2118/144580-MS](https://doi.org/10.2118/144580-MS).
- [154] D. W. Peaceman. Interpretation of well-block pressures in numerical reservoir simulation with nonsquare grid blocks and anisotropic permeability. *Soc. Petrol. Eng. J.*, 23(3):531–543, 1983. doi:[10.2118/10528-PA](https://doi.org/10.2118/10528-PA). SPE 10528-PA.
- [155] D. W. Peaceman. *Fundamentals of Numerical Reservoir Simulation*. Elsevier Science Inc., New York, NY, USA, 1991. ISBN 0444415785.
- [156] D. W. Peaceman et al. Interpretation of well-block pressures in numerical reservoir simulation. *Soc. Petrol. Eng. J.*, 18(3):183–194, 1978.
- [157] P.-O. Persson and G. Strang. A simple mesh generator in matlab. *SIAM Review*, 46(2):329–345, 2004. doi:[10.1137/S0036144503429121](https://doi.org/10.1137/S0036144503429121).
- [158] G. F. Pinder and W. G. Gray. *Essentials of Multiphase Flow in Porous Media*. John Wiley & Sons, Hoboken, New Jersey, USA, 2008.
- [159] D. W. Pollock. Semi-analytical computation of path lines for finite-difference models. *Ground Water*, 26(6):743–750, 1988.
- [160] D. K. Ponting. Corner point geometry in reservoir simulation. In P. King, editor, *Proceedings of the 1st European Conference on Math-*

- ematics of Oil Recovery, Cambridge, 1989*, pages 45–65, Oxford, July 25–27 1989. Clarendon Press.
- [161] M. Prevost, M. G. Edwards, and M. J. Blunt. Streamline tracing on curvilinear structured and unstructured grids. *SPE J.*, 7(2):139–148, June 2002.
- [162] A. F. Rasmussen and K.-A. Lie. Discretization of flow diagnostics on stratigraphic and unstructured grids. In *ECMOR XIV – 14th European Conference on the Mathematics of Oil Recovery, Catania, Sicily, Italy, 8-11 September 2014*. EAGE, 2014. doi:[10.3997/2214-4609.20141844](https://doi.org/10.3997/2214-4609.20141844).
- [163] P. A. Raviart and J. M. Thomas. A mixed finite element method for second order elliptic equations. In I. Galligani and E. Magenes, editors, *Mathematical Aspects of Finite Element Methods*, pages 292–315. Springer-Verlag, Berlin – Heidelberg – New York, 1977.
- [164] P. Renard and G. De Marsily. Calculating equivalent permeability: a review. *Adv. Water Resour.*, 20(5):253–278, 1997.
- [165] L. A. Richards. Capillary conduction of liquids through porous mediums. *Journal of Applied Physics*, 1(5):318–333, 1931. doi:[10.1063/1.1745010](https://doi.org/10.1063/1.1745010).
- [166] P. Samier. A finite element method for calculation transmissibilities in n-point difference equations using a non-diagonal permeability tensor. In Guérillot, editor, *2nd European Conference on the Mathematics of Oil Recovery*, pages 121–130. Editions TECHNIP, 1990.
- [167] T. Sandve, I. Berre, and J. Nordbotten. An efficient multi-point flux approximation method for discrete fracturematrix simulations. *J. Comput. Phys.*, 231(9):3784 – 3800, 2012. doi:[10.1016/j.jcp.2012.01.023](https://doi.org/10.1016/j.jcp.2012.01.023).
- [168] M. Shahvali, B. Mallison, K. Wei, and H. Gross. An alternative to streamlines for flow diagnostics on structured and unstructured grids. *SPE J.*, 17(3):768–778, 2012. doi:[10.2118/146446-PA](https://doi.org/10.2118/146446-PA).
- [169] L. F. Shampine, R. Ketzschner, and S. A. Forth. Using AD to solve BVPs in MATLAB. *ACM Trans. Math. Software*, 31(1):79–94, 2005.
- [170] G. Shook and K. Mitchell. A robust measure of heterogeneity for ranking earth models: The F-Phi curve and dynamic Lorenz coefficient. In *SPE Annual Technical Conference and Exhibition, 4-7 October, New Orleans, Louisiana*, 2009. doi:[10.2118/124625-MS](https://doi.org/10.2118/124625-MS).
- [171] SINTEF ICT. The MATLAB Reservoir Simulation Toolbox: Numerical CO₂ laboratory, Oct. 2014. URL <http://www.sintef.no/co2lab>.
- [172] H. L. Stone. Rigorous black oil pseudo functions. In *SPE Symposium on Reservoir Simulation, 17-20 February, Anaheim, California*. Society of Petroleum Engineers, 1991. doi:[10.2118/21207-MS](https://doi.org/10.2118/21207-MS).
- [173] Technische Universität Darmstadt. Automatic Differentiation for Matlab (ADiMat). URL <http://www.adimat.de/>. [Online; accessed 15-04-2014].
- [174] M. R. Thiele and R. P. Batycky. Water injection optimization using a streamline-based workflow. In *Proceedings of the SPE Annual Technical*

- Conference and Exhibition*, 5-8 October 2003, Denver, Colorado, 2003. doi:[10.2118/84080-MS](https://doi.org/10.2118/84080-MS).
- [175] G. W. Thomas. *Principles of hydrocarbon reservoir simulation*. IHRDC, Boston, MA, Jan 1981.
- [176] Tomlab Optimization Inc. Matlab Automatic Differentiation (MAD). URL <http://matlabad.com/>. [Online; accessed 15-04-2014].
- [177] S. M. Toor, M. G. Edwards, A. H. Dogru, and T. M. Shaalan. Boundary aligned grid generation in three dimensions and cvd-mpfa discretization. In *SPE Reservoir Simulation Symposium, 23-25 February, Houston, Texas, USA*, 2015. doi:[10.2118/173313-MS](https://doi.org/10.2118/173313-MS).
- [178] J. A. Trangenstein and J. B. Bell. Mathematical structure of the black-oil model for petroleum reservoir simulation. *SIAM J. Appl. Math.*, 49(3):749–783, 1989. ISSN 0036-1399.
- [179] E. Ucar, I. Berre, and E. Keilegavlen. Simulation of slip-induced permeability enhancement accounting for multiscale fractures. In *Fourtieth Workshop on Geothermal Reservoir Engineering, Stanford University, Stanford, California, January 26–28, 2015*, 2015.
- [180] M. T. van Genuchten. Closed-form equation for predicting the hydraulic conductivity of unsaturated soils. *Soil Science Soc. America J.*, 44(5):892–898, 1980. doi:[10.2136/sssaj1980.03615995004400050002x](https://doi.org/10.2136/sssaj1980.03615995004400050002x).
- [181] A. Verma. ADMAT: Automatic differentiation in MATLAB using object oriented methods. In *SIAM Interdisciplinary Workshop on Object Oriented Methods for Interoperability*, pages 174–183, 1999.
- [182] D. V. Voskov and H. A. Tchelepi. Comparison of nonlinear formulations for two-phase multi-component eos based simulation. *J. Petrol. Sci. Engrg.*, 82-83(0):101–111, 2012. ISSN 0920-4105. doi:[10.1016/j.petrol.2011.10.012](https://doi.org/10.1016/j.petrol.2011.10.012).
- [183] D. V. Voskov, H. A. Tchelepi, and R. Younis. General nonlinear solution strategies for multiphase multicomponent eos based simulation. In *SPE Reservoir Simulation Symposium, 2–4 February, The Woodlands, Texas*, 2009. doi:[10.2118/118996-MS](https://doi.org/10.2118/118996-MS).
- [184] Y. Wang, H. Hajibeygi, and H. A. Tchelepi. Algebraic multiscale solver for flow in heterogeneous porous media. *J. Comput. Phys.*, 259:284–303, 2014. doi:[10.1016/j.jcp.2013.11.024](https://doi.org/10.1016/j.jcp.2013.11.024).
- [185] X.-H. Wen and J. J. Gómez-Hernández. Upscaling hydraulic conductivities in heterogeneous media: An overview. *J. Hydrol.*, (183):ix–xxxii, 1996.
- [186] J. A. Wheeler, M. F. Wheeler, and I. Yotov. Enhanced velocity mixed finite element methods for flow in multiblock domains. *Comput. Geosci.*, 6(3-4):315–332, 2002. doi:[10.1023/A:1021270509932](https://doi.org/10.1023/A:1021270509932).
- [187] M. F. Wheeler, T. Arbogast, S. Bryant, J. Eaton, Q. Lu, M. Peszynska, and I. Yotov. A parallel multiblock/multidomain approach for reservoir simulation. In *SPE Reservoir Simulation Symposium, 14-17 February, Houston, Texas*, pages 51–61, 1999. doi:[10.2118/51884-MS](https://doi.org/10.2118/51884-MS).

- [188] O. Wiener. *Abhandlungen der Mathematisch*. PhD thesis, Physischen Klasse der Königlichen Sächsischen Gesellschaft der Wissenschaften, 1912.
- [189] X. H. Wu, Y. Efendiev, and T. Y. Hou. Analysis of upscaling absolute permeability. *Discrete Contin. Dyn. Syst. Ser. B*, 2(2):185–204, 2002.
- [190] R. Younis. *Advances in Modern Computational Methods for Nonlinear Problems; A Generic Efficient Automatic Differentiation Framework, and Nonlinear Solvers That Converge All The Time*. PhD thesis, Stanford University, Palo Alto, California, 2009.
- [191] R. Younis and K. Aziz. Parallel automatically differentiable data-types for next-generation simulator development. In *SPE Reservoir Simulation Symposium, 26–28 February, Houston, Texas, USA*, 2007. doi:[10.2118/106493-MS](https://doi.org/10.2118/106493-MS). SPE 106593-MS.
- [192] P. Zhang, G. E. Pickup, and M. A. Christie. A new upscaling approach for highly heterogenous reservoirs. In *SPE Reservoir Simulation Symposium, 31 January-2 February, The Woodlands, Texas*, SPE 93339, 2005.
- [193] Y. Zhou, H. A. Tchelepi, and B. T. Mallison. Automatic differentiation framework for compositional simulation on unstructured grids with multi-point discretization schemes. In *SPE Reservoir Simulation Symposium, 21-23 February, The Woodlands, Texas*, 2011. doi:[10.2118/141592-MS](https://doi.org/10.2118/141592-MS). SPE 141592-MS.